UNIVERSITY OF CALIFORNIA
RIVERSIDE

Search for Standard Model Production of Four Top Quarks in the Opposite-Sign Dilepton Final States in Proton-proton Collisions at $\sqrt{s} = 13$ TeV

A Dissertation submitted in partial satisfaction
of the requirements for the degree of

Doctor of Philosophy

in

Physics

by

Long Wang

September 2019

Dissertation Committee:

Professor Stephen Wimpenny, Co-Chairperson
Professor Robert Clare, Co-Chairperson
Professor Owen Long

The Dissertation of Long Wang is approved:

Committee Co-Chairperson

Committee Co-Chairperson

University of California, Riverside

Acknowledgments

I am grateful to my advisors Prof. Steve Wimpenny and Prof. Robert Clare, without whose help, I would not have been here.

To my family for all the support.

ABSTRACT OF THE DISSERTATION

Search for Standard Model Production of Four Top Quarks in the Opposite-Sign Dilepton Final States in Proton-proton Collisions at $\sqrt{s} = 13$ TeV

by

Long Wang

Doctor of Philosophy, Graduate Program in Physics
University of California, Riverside, September 2019
Professor Stephen Wimpenny, Co-Chairperson
Professor Robert Clare, Co-Chairperson

This dissertation presents a search for the Standard Model production of four top quarks ($pp \rightarrow t\bar{t}t\bar{t}$) using events with opposite-sign dilepton ($\mu^+\mu^-$, $\mu^\pm e^\mp$, or e^+e^-)+jets signatures. The data used in this analysis are from proton-proton collisions at a center-of-mass energy $\sqrt{s} = 13$ TeV recorded by the CMS detector at LHC during year 2016. The total integrated luminosity of the data corresponds to $35.8\,\text{fb}^{-1}$. A multivariate analysis method is used to discriminate $t\bar{t}t\bar{t}$ signal events from background events based on global event and jet properties. No significant deviation is observed in data from the prediction of the background. An upper limit is set on the cross section of Standard Model $t\bar{t}t\bar{t}$ production to be 64 fb at 95% confidence level. A combination of the measurements with results from single-lepton (μ, e)+jets final states and a previous measurement from the CMS experiment is performed and the combined cross section measurement is 13^{+11}_{-9} fb, with an observed signal significance of 1.4 standard deviations.

Contents

List of Figures

List of Tables

Chapter 1

Introduction to Standard Model

1.1 Foreword

Ever since the dawn of human civilization has this question been asked: "What is the world made up of?" The ancient philosophers came up with many ideas. Some said it's made up of air, fire, water and earth, some extended the list with metal or space, and some said it is made of microscopic hard balls. Nobody can prove their assertion, but there is one thing in common, they all believed there should be something elementary out there that made up matter. Followed by the inevitable failure of generations of alchemists' attempts to transmute base metals into gold, people started to think that the elementary thing might be different for each material. The discovery of periodic table of elements greatly helped people's understanding of the material world, but most importantly, the periodic feature promotes people to logically think that there might be substructures of these elements. When J. J. Thomson discovered electron [1] while he was studying the properties of cathode ray at the end of the nineteenth century, the door to a modern understanding of the material

world finally opened. Ernest Rutherford's experiments [2] colliding atoms with electrons in the beginning of twentieth century not only identified the structure of atoms with a nucleus surrounded by electrons, but most importantly, the way to a very effective and successful approach to probe the inner structure of atoms. Along with the huge breakthrough of novel experimental results, innovative theories aimed at explaining their behavior were also flourishing. The legends began with Planck's ingenious idea of quantization of energy. Based on Planck's theory, Niels Bohr built a mathematical description of atoms using a semi-classical model saying that electrons orbit the nucleus in fixed orbits [3]. Einstein renovated Planck's theory by proposing the concept of photons that depicts the particle nature of long considered waves of light [4]. Shortly after, de Broglie brought up his hypothesis of the wave nature of electrons and very soon extended it to all matter [5]. Thanks to Erwin Schrödinger, Werner Heisenberg, Max Born and many others' great works, the early quantum mechanics that describes how the basic elements interact with each other(via electromagnetic force) was profoundly conceived. After Chadwick's discovery of neutrons in 1932 [6], Heisenberg and others quickly developed a nuclear model consisting of protons and neutrons, and a new interaction(strong interaction) was brought into the picture. The development of quantum electrodynamics (QED) successfully combined quantum mechanics and special relativity in describing electromagnetism and served as an example in the mathematical formalism of physical theory. In the meantime, studies of nuclei revealed countless new particles, which were grouped and named baryons (now known made up of three quarks) and mesons (made up of quark and anti-quark). The periodic features of baryons and mesons promotes the understanding of a more fundamental particle - the quark. Quantum Chromodynamics

(QCD), analogous to QED, was soon developed to describe the interactions between the quarks. Following the discoveries of leptons and quarks from collider experiments, and the discovery of vector bosons ($W^{\pm}, Z$) [7], the mathematical formalisms that describe these particles were incorporated into one self-consistent theory, the Standard Model.

1.2 Standard Model

The Standard Model of particle physics is built upon the tremendous experimental and theoretical discoveries over the past century. It is the most precise and well-tested field theory and it describes almost all of the present understanding of the fundamental constituents of matter. It encompasses the weak, electromagnetic and strong interactions between these constituents. The beauty of Standard Model lies in its symmetry.

1.2.1 Constituents

Figure 1.1 shows the fundamental particles in the Standard Model. There are two types of basic particles, fermions and bosons. These are differentiated via a fundamental physical quantity named spin. Fermions are the basic particles which have a half-integer spin while bosons have an integer spin. The material world around us is made of the elementary fermions, gauge bosons and their anti-particles. There are two types of elementary fermions, the quarks and the leptons. Each type consists of 6 members (12 including their counter part of anti-particles), which are paired into three generations. The gauge bosons are the particles associated with the interaction fields, through the exchange of which forces emerge.

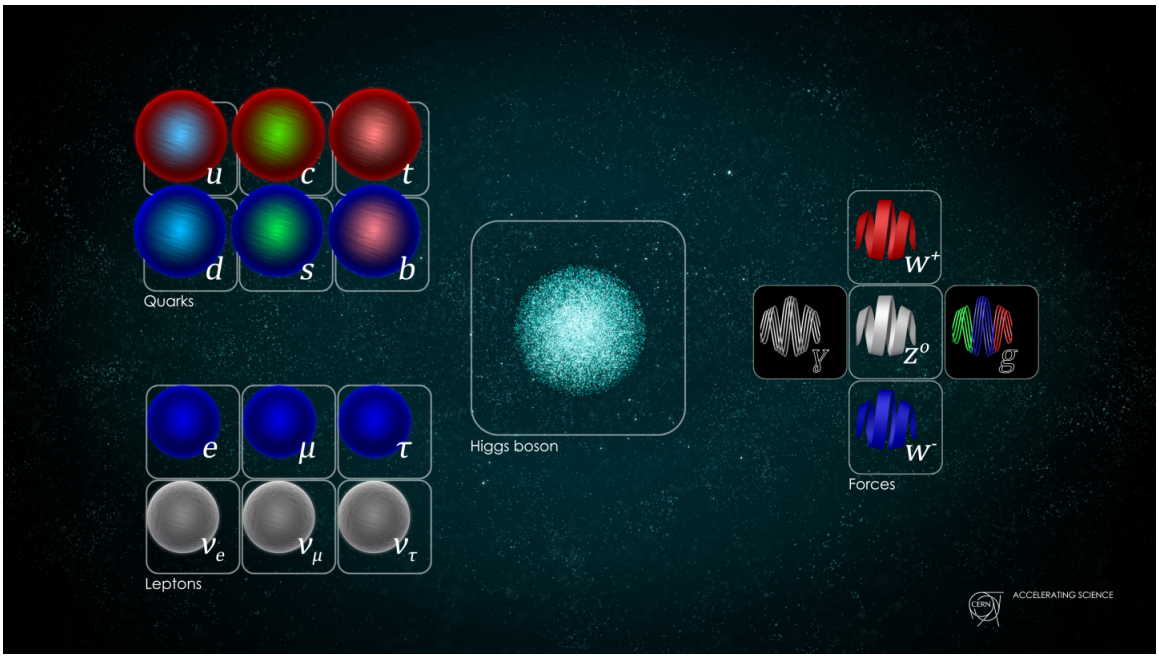

Figure 1.1: Particles of the Standard Model Physics. (Image: Daniel Dominguez/CERN)

1.2.1.1 Leptons

The three generations of leptons and their basic quantities are listed in Table 1.1. The first generation consists of electron, its associated neutrino, and their corresponding ant-particles. The muon makes up the second generation and the tau the third generation. Each generation (flavor) of leptons differ from the other generations only in its mass and life time. Heavier leptons decay into lighter leptons following the conservation of the lepton number and electric charge conservation rules. The quantum numbers of charge and lepton number of anti-leptons are those of the leptons times -1. Equation 1.1 exemplifies the laws in the decays of muon to electron.

$$\mu^- \rightarrow \nu_\mu + e^- + \bar{\nu_e} \tag{1.1}$$

All leptons are treated as point-like particles in the Standard Model as no experiment or evidence ever shows otherwise.

Table 1.1: Properties of leptons

Name	Spin ($\hbar$)	Charge (e)	L_e	L_{mu}	L_τ	Mass (MeV/c^2)
Electron(e^-)	$\frac{1}{2}$	-1	1	0	0	0.511
Electron neutrino(ν_e)		0	1	0	0	< 0.002
Muon(mu^-)		-1	0	1	0	105.658
Muon neutrino(ν_μ)		0	0	1	0	< 0.19
Tau(τ^-)		-1	0	0	1	1776.86
Tau neutrino(ν_τ)		0	0	0	1	< 18.2

1.2.1.2 Quarks

The six flavors of quarks form into 3 generations. the lightest up and down quarks are the first generation, the charm and strange quarks are the second generation and the heaviest top and bottom quarks are the third generation. Quarks have not only electric charges but also color charges, denoted symbolically by R ($\bar{\text{R}}$), G ($\bar{\text{G}}$), and B ($\bar{\text{B}}$). This is a most distinctive feature from leptons. All particles states observed in nature are symmetric in the R, G, B space, evidenced by the fact that isolated quarks are never observed in experiments. The properties of quarks are listed in Table 1.2.

The baryon number B defined for each quark is $+\frac{1}{3}$. Equations 1.2, 1.3 define hypercharge (Y) and electric charge (Q) for each quark.

$$Y = B + S + C + T + B' \tag{1.2}$$

$$Q = I_\mathfrak{z} + \frac{1}{2}Y \tag{1.3}$$

where S is strangeness number, C is charm number, T is topness number, B' is bottomness number and I_3 is the third component of isospin.

Table 1.2: Properties of quarks.

Name	Spin ($\hbar$)	Charge (e)	I_3	C	S	T	$B\prime$	Mass [1] GeV/c^2
u	$\frac{1}{2}$	$+\frac{2}{3}$	$+\frac{1}{2}$	0	0	0	0	$0.0022^{+0.0005}_{-0.0004}$
d		$-\frac{1}{3}$	$-\frac{1}{2}$	0	0	0	0	$0.0047^{+0.0005}_{-0.0003}$
c		$+\frac{2}{3}$	0	+1	0	0	0	$1.275^{+0.025}_{-0.035}$
s		$-\frac{1}{3}$	0	0	−1	0	0	$0.095^{+0.009}_{-0.003}$
t		$+\frac{2}{3}$	0	0	0	+1	0	$173.0^{+0.4}_{-0.4}$
b		$-\frac{1}{3}$	0	0	0	0	−1	$4.18^{+0.04}_{-0.03}$

1.2.2 Interactions

There are 4 types of fundamental interactions in nature as we know it. The gravitational interaction is related to space-time curvature. The electromagnetic interaction is induced by the electric charge. The weak interaction is induced by weak hypercharge, and the strong interaction is induced by color charge. The Standard Model excludes gravitational interaction from consideration because it is extremely insignificant (10^{24} times weaker than weak interaction, the famous hierarchy problem) on the scale of particle level. Table 1.3 [8] is a brief summary of properties of the three interactions under consideration.

Table 1.3: Properties of the fundamental interaction fields

Interaction	Mediator Boson	Charge Name	Range	Typical Lifetime (s)	Coupling Strength α_i
Strong	Gluon (g)	Color	1 fm	10^{-23}	1
EM	Photon (γ)	Electric Charge (e)	∞	$10^{-20} \sim 10^{-16}$	10^{-2}
Weak	W^+, W^- and Z		10^{-3} fm	10^{-12} or longer	10^{-6}

In Standard Model the interactions are dictated by local gauge symmetries. The electromagnetic interaction is represented by the $U(1)$ gauge group. The Lagrangian of the interacting field of QED in equation 1.4 can be easily obtained by imposing the local gauge invariance requirement on the free fermion Lagrangian.

$$\mathcal{L} = \bar{\psi}(i\gamma^{\mu}\partial_{\mu} - m)\psi + e\bar{\psi}\gamma^{\mu}A_{\mu}\psi - \frac{1}{4}F_{\mu\nu}F^{\mu\nu} \tag{1.4}$$

here A_{μ} is the photon field and field strength tensor $F_{\mu\nu} = \partial_{\mu}A_{\nu} - \partial_{\nu}A_{\mu}$.

Quite like an analogue of the electromagnetic interaction, the strong interaction is described by the $SU(3)_C$ non-abelian gauge group of phase transformations on the quark color fields. Equation 1.5 is the local gauge invariant QCD Lagrangian for interacting colored quarks and vector gluons.

$$\mathcal{L} = \bar{q}(i\gamma^{\mu}\partial_{\mu} - m)q - g(\bar{q}\gamma^{\mu}T_a q)G^a_{\mu} - \frac{1}{4}G^a_{\mu\nu}G^{\mu\nu}_a \tag{1.5}$$

where g is coupling strength parameter, T_a is a set of 8 generators of the $SU(3)$ group, G^a_{μ} are the eight vector gluon fields, and $G^a_{\mu\nu} = \partial_{\mu}G^a_{\nu} - \partial_{\nu}G^a_{\mu} - gf_{abc}G^b_{\mu}G^c_{\nu}$, where f_{abc} are the structure constants of the group. The self-interacting term of gluon fields in the Lagrangian shows that gluons themselves carry color charge.

The mathematical formalism of the weak interaction in the Standard Model is unified with electromagnetic interaction in the $SU(2)_L \times U(1)_Y$ local gauge invariant group as electroweak interaction. The subscript L is used to denote that local gauge transformation is invariant on the left-handed fermions and Y denotes the weak hypercharge. The mass terms in the Lagrangian of electroweak interaction is interpreted by the so-called "Spontaneous Symmetry Breaking" which states the global symmetry of the physical system is

hidden at the system's ground state. The unphysical fields related to massless Goldstone boson in the Lagrangian are corrected by the "Higgs mechanism", which exploits a particular choice of gauge transformation to recover the set of real fields of the Lagrangian. The choice of the Higgs field is such that the $W^{\pm}$ and Z are massive and the photon remains massless. This choice also helps maintain the renormalizable feature of the gauge theory. The masses of $W^{\pm}$ and Z bosons [9] are measured to be:

$$M_W = 80.379 \pm 0.012\,\mathrm{GeV}$$

$$M_Z = 91.1876 \pm 0.0021\,\mathrm{GeV}$$

which are in impressive agreement with the predictions of the Standard Model. On 4 July 2012, the ATLAS and CMS experiments at CERN's Large Hadron Collider announced the observation of a new particle consistent with the Higgs boson in the mass region around $125\,\mathrm{GeV}$ [10].

Standard Model has been proved to be the most precise theory there is. So far all the experimental results are consistent with the Standard Model predictions. But it is still incomplete in the sense that it incorporates only three out of the four fundamental interactions, and excludes gravity. It also cannot answer what dark matter is, why antimatter is so much less prevalent than matter in our universe, etc. It becomes clearer and clearer that the Standard Model is only a close approximation of a more fundamental theory at a certain scale. The top quark, with its mass by far the heaviest among all quarks and leptons, and its extremely short lifetime in contrast to the lighter quarks, serves as a perfect window for searching physics beyond the Standard Model.

Chapter 2

Top Quark Physics

2.1 Top Quark in the Standard Model

Discovered in 1996 [11], the top quark, with charge $Q = +\frac{2}{3}e$, is one of the third generation of quarks. The electroweak gauge model depicts left-handed top quark as the $+\frac{1}{2}$ member of the weak-isospin doublet with a bottom quark, and right-handed top quark as an $SU(2)_L$ singlet. The top quark mass is generated by the quark's coupling to the Higgs field (Yukawa coupling) as shown in equation 2.1:

$$\mathcal{L}^{quark}_{Yukawa} = -\left[\tilde{G}_{ij}\bar{\mu}_{iR}\tilde{\Phi}^{\dagger}\begin{pmatrix} u_j \\ d_j \end{pmatrix}_L + G_{ij}\bar{d}_{iR}\Phi^{\dagger}\begin{pmatrix} u_j \\ d_j \end{pmatrix}_L + h.c.\right] \tag{2.1}$$

where u_j and d_j are the weak eigenstates of the (u, c, t) and (d, s, b) quarks respectively, R denotes the right-handed quark singlet and L denotes the left-handed quark doublet, Φ is the isospon doublet arrangement of four real scalar fields. The top quark is the only fundamental particle whose Yukawa coupling to the Higgs boson is order of unity. The equation also shows mixing between quarks of different generations in weak eigenstates.

When transformed to mass eigenstates, the mixing between quarks is then described via the Cabbibo-Kobayashi- Maskawa (CKM) matrix in equation 2.2.

$$\begin{pmatrix} V_{ud} & V_{us} & V_{ub} \\ V_{cd} & V_{cs} & V_{cb} \\ V_{td} & V_{ts} & V_{tb} \end{pmatrix} = \begin{pmatrix} 0.97446 & 0.22452 & 0.00365 \\ 0.22438 & 0.97359 & 0.04214 \\ 0.00896 & 0.04133 & 0.999105 \end{pmatrix} \tag{2.2}$$

The strong interaction of top quarks with other color charged particles are dictated by the QCD theory as described in Section 1.2.2.

2.2 Top Quark Properties

2.2.1 Top quark production

There are two basic modes of top quark production in a hadronic collider depending on the nature of interactions the top quark goes through:

- top pair ($t\bar{t}$) production via strong interaction,
- single top quarks production via electroweak interactions.

2.2.1.1 $t\bar{t}$ pair production

At the Larger Hadron Collider (LHC) of the European Organization for Nuclear Research (CERN), the collisions of two highly energized protons can be described by perturbative QCD using the parton model. The colliding hadron (in LHC case, a proton) is treated as a composition of partons with varying fractions x of the proton's longitudinal momentum p_A, ie. the momentum of parton i is $p_i = x_i \times p_A$. The cross section of $t\bar{t}$

production from the collision of proton A and B is then given by the parton longitudinal momentum distribution functions (PDFs) $f_i(x_i, \mu^2)$ and the hard scattering cross section $\hat{\sigma}_{ij}$ of participating partons i and j:

$$\sigma(pp \to t\bar{t}) = \sum_{i,j=q,\bar{q},g} \int dx_i dx_j f_{i,A}(x_i, \mu^2) f_{j,B}(x_j, \mu^2) \times \hat{\sigma}_{ij}(ij \to t\bar{t}, \hat{s}, \mu^2) \tag{2.3}$$

where $\hat{s} = x_i x_j s$ is the effective center-of-mass energy squared for the corresponding partons. The modeling of the calculation in this way is called factorization and is shown in Figure 2.1. The parton distribution function, $f_i(x_i, \mu^2)$ can be interpreted as the probability density for finding a parton i with longitudinal momentum fraction x_i in the proton, when probed at a factorization scale μ_F. The PDFs and parton-parton cross section depend on the factorization scale μ_F and the renormalization scale μ_R, another artificial scale which is used to remove the ultraviolet divergence in higher order parton-parton cross section calculations of pQCD. At higher order of the perturbation series, the dependence on μ_F and μ_R decreases. The observable hadronic cross section must not depend on the choice of μ_F and μ_R.

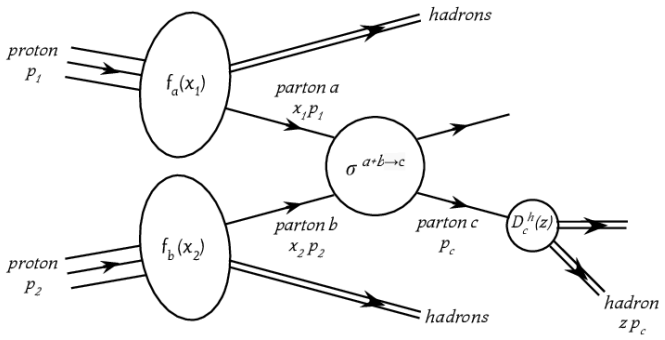

Figure 2.1: Scheme of pQCD factorization

Figure 2.2 gives the lowest order diagrams of $t\bar{t}$ production in parton model. The PDFs are extracted from measurements in deep inelastic scattering experiments where either

electrons, positrons or neutrinos collide with nucleons. Figure 2.3 shows examples of the PDFs derived from measurements from the HERA experiments at the energy scale relevant for LHC. At the energy threshold for $t\bar{t}$ production with proton-proton collision at $\sqrt{s} = 13$ TeV, the typical value of $x \sim \frac{2m_t}{\sqrt{s}} \sim 0.025$. From figure 2.3 we can see that the particle distribution function of the gluons is the largest (there is a scale of 0.05 on the figure). Thus at the LHC $t\bar{t}$ production is vastly dominated by gluon-gluon fusion, of about 90%, and the quark-antiquark annihilation production of $t\bar{t}$ takes about 10%.

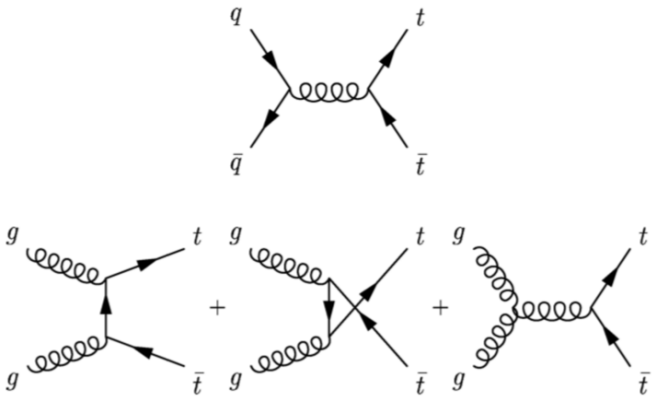

Figure 2.2: $t\bar{t}$ production at lowest order via strong interaction. top: quark-antiquark annihilation, bottom: gluon fusion

Predictions of the top quark pair production total cross sections at the LHC at next-to-next-to leading order (NNLO) assuming a top-quark mass of 172.5 GeV/c^2 are listed in Table 2.1.

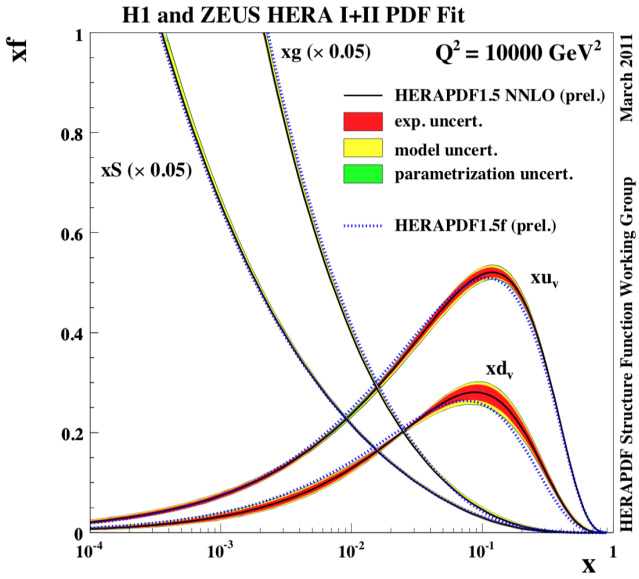

Figure 2.3: The parton distribution functions from HERAPDF1.5 NNLO at $Q^2 = 10000\text{GeV}^2$, a region relevant for LHC

Table 2.1: Predictions of the top quark pair production total cross sections at the LHC at next-to-next-to leading order. The first uncertainty is from scale dependence and the second from parton distribution functions.

$\sqrt{s}$ (TeV)	$\sigma_{t\bar{t}}$ (pb)
7	$177.3^{+4.6+9.0}_{-6.0-9.0}$
8	$252.9^{+6.4+11.5}_{-8.6-11.5}$
13	$831.8^{+19.8+35.1}_{-29.2-35.1}$
14	$984.5^{+23.2+41.3}_{-34.7-41.3}$

2.2.1.2 Single top production

Top quarks can also be produced singly via electroweak production. The small elements value of V_{td} and V_{ts} in CKM matrix suggests the top quark production channels involving Wtd or Wts vertices are strongly suppressed. Thus it's sufficient to only consider

the production channel involving the Wtb vertex. Based on the kinematic feature of the W boson, this production channel can be divided into three different channels:

- ***t*-channel**: This is similar to heavy flavor quark production via charged current deep inelastic scattering, it happens when a virtual W boson interacts with a sea b quark. Since the b quark originates from gluon splitting into $b\bar{b}$ pairs, this process is also referred to W-gluon fusion. The lowest order Feynman diagram for this channel is shown in Figure 2.4 a). W-gluon fusion is the dominant single top quark production process at the LHC, as at the energy threshold of top production, gluon PDFs dominates within all partons. This channel is sensitive to new physics like flavor-changing neutral currents.

- ***s*-channel**: Similar to the Drell-Yan process but for a highly energized W boson coming from the fusion of two quarks of one $SU(2)$ weak-isospin doublet. Figure 2.4 b) shows the lowest order Feynman diagram of this channel. The advantage of this channel is that the predicted cross section can be well calculated because the quark PDFs are better known than the gluon PDFs that contribute to the other channels. The disadvantage is that this channel has very large backgrounds which makes it very difficult to observe at LHC.

- tW **associated production**: In this channel the top quark is produced in association with an on-shell W boson via $gb \to tW^-$. The lowest order Feynman diagram for this process is shown in Figure 2.4 c) and d).

Table 2.2 listed the predicted total cross sections at NNLO accuracy at the LHC for the

Table 2.2: Predicted total cross sections at NNLO accuracy at the LHC for different single top quark production processes.

$\sqrt{s}$ (TeV)	$\sigma^{t+\bar{t}}_{t-\text{channel}}$ (pb)	$\sigma^{69\%t+31\%\bar{t}}_{s-\text{channel}}$ (pb)	$\sigma^{t+\bar{t}}_{tW}$ (pb)
7	$64.0^{+0.77}_{-0.38}$	$4.5^{+0.2}_{-0.2}$	$15.1^{+1.2}_{-1.2}$
8	$84.6^{+1.0}_{-0.51}$	$5.5^{+0.2}_{-0.2}$	$22.1^{+1.5}_{-1.5}$
13	$215^{+2.1}_{-1.3}$	NA	NA
14	$245^{+2.7}_{-1.3}$	NA	NA

above three single top quark production processes, assuming $m_t = 172.5$ GeV/c^2.

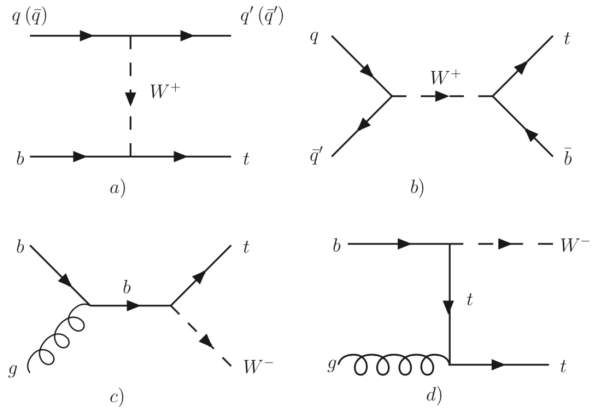

Figure 2.4: $t\bar{t}$ Lowest order Feynman diagrams for single top quark production. a) t-channel; b) s-channel; c) and d) tW associated production.

2.2.2 Top quark mass

Like all of the other fermions, the top quark mass value is not predicted by the standard model. Single quarks are unobservable due to color confinement. But since top quark does not hadronize (see section 2.2.3), it is natural to consider it as a very short lived bare fermion. At the LHC the top quark mass can be measured directly. Three main

methods are typically used in the direct measurement: a) template method, b) matrix element method and c) Ideogram method. In the template method kinematic distributions of reconstructed decay product sensitive to top quark mass from MC simulations assuming different top quark masses M_{top} are fitted to the distributions observed in data. The matrix element method exploits the likelihood to observe a sample of candidate events. The probability for the production of such sample is determined by the leading order matrix element incorporating all possible relevant parton processes with differential cross section values assuming different values of M_{top}. A likelihood fit would determine the best value of top quark mass. The ideogram method is somewhat a hybrid version of the previous two methods. An initial kinematic fit is performed, then functions that quantify how well the event agrees with a specific top quark mass value are used in the likelihood fit to determine the best M_{top} value. The latest direct measurement of top quark mass from CMS run II [12] is:

$$m_t(GeV/c^2) = 172.25 \pm 0.08(stat + JSF) \pm 0.62(syst)$$

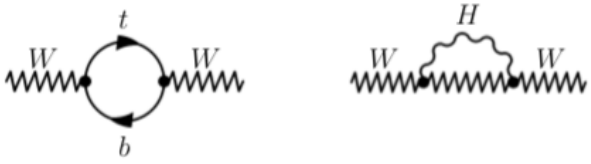

Figure 2.5: Diagrams of one loop radiative corrections to the W propagator from top mass and Higgs mass

The top quark mass can also be measured indirectly. Even though not directly predicted by SM, it is a very important parameter in the calculation of radiative corrections

to electroweak processes. The SM relates the masses of top quark, W boson and Higgs boson through the radiative corrections, as sketched in Figure 2.5. In SM electroweak theory, the W boson mass can be expressed as:

$$m_W^2 = \frac{\pi\alpha}{\sqrt{2}G_F \sin^2\theta_W(1-\Delta r)} \tag{2.4}$$

where α is electromagnetic coupling constant, G_F is Fermi constant, Δr is radiative corrections from top quark and Higgs boson. Top quark contributes to the Δr via one-loop diagrams by

$$(\Delta r)_{top} \approx -\frac{3G_F}{8\sqrt{2}\pi^2 \tan^2\theta_W} m_t^2 \tag{2.5}$$

and Higgs boson contributes to the Δr via one-loop diagram by

$$(\Delta r)_{Higgs} \approx \frac{3G_F m_W^2}{8\sqrt{2}\pi^2}\left(ln\frac{m_H^2}{m_Z^2} - \frac{5}{6}\right) \tag{2.6}$$

In the above two equations, the leading m_t dependence is quadratic while leading m_H dependence is logarithmic meaning much weaker. This feature can be used to predict the top quark mass from electroweak precision measurements. On the other hand, with precise direct measurements of the top quark mass and the W boson mass, the mass of the SM Higgs boson can also be predicted.

2.2.3 Top quark decay

The top quark width corrected to first order QCD is given by equation 2.7:

$$\Gamma_t = \frac{G_F m_t^3}{8\pi\sqrt{2}}\left(1-\frac{M_W^2}{m_t^2}\right)^2\left(1+2\frac{M_W^2}{m_t^2}\right)\left[1-\frac{2\alpha_s}{3\pi}\left(\frac{2\pi^2}{3}-\frac{5}{2}\right)\right] \tag{2.7}$$

where m_t is the top quark pole mass. For a value of $m_t = 172.5$ GeV/c^2 the width is $\Gamma_t = 1.3$ GeV/c^2. This large decay width corresponds to a very short life time $\tau_t = 1/\Gamma_t \approx 0.5 \times 10^{24}$

s, which is smaller than the typical hadronization time $\tau_{hadr} = 1/\Lambda_{QCD} \approx 2 \times 10^{24}$s. Thus the top quark will decay before it can couple to other quarks to form hadrons.

With a mass larger than the Wb threshold, and $|V_{tb}| \sim 1$, $|V_{td}| \sim 0, |V_{ts}| \sim 0$, top quark decay is completely dominated by $t \to bW^+$ process. For the leading pair production process, the final states are determined solely by the decay modes of W boson. They can be categorized into the following three distinct channels:

- **All hadronic**: $t\bar{t} \to W^+bW^-\bar{b} \to q\bar{q}'bq''\bar{q}'''\bar{b}$;
- **l+jets**: $t\bar{t} \to W^+bW^-\bar{b} \to q\bar{q}'bl^-\bar{\nu}_l\bar{b} + l^+\nu_l bq''\bar{q}'''\bar{b}$;
- **dilepton**: $t\bar{t} \to W^+bW^-\bar{b} \to l^+\nu_l bl'^-\bar{\nu}_{l'}\bar{b}$;

Contributions to the total $t\bar{t}$ decay from these channels are shown in Figure 2.6 assuming universality of leptons.

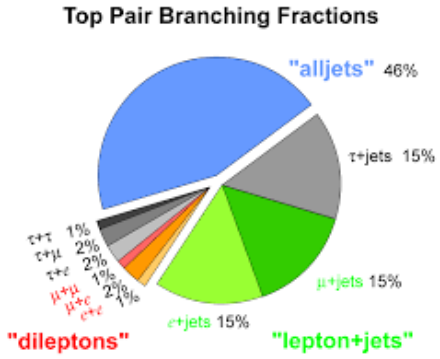

Figure 2.6: $t\bar{t}$ decay branching fractions of different channels.

2.3 Four Tops

Many new physics models [13, 14, 15, 16, 17, 18] predict an enhanced coupling to top quarks, which is particularly relevant for top quark related processes with small cross sections that are not yet observed. The $t\bar{t}t\bar{t}$ production, with many top quarks in the final state, is sensitive to these additional contributions, making it an interesting channel to probe several extensions of the Standard Model, like supersymmetry, extra dimensions and top-compositeness.

2.3.1 SM $t\bar{t}t\bar{t}$ production

In the Standard Model, $t\bar{t}t\bar{t}$ final states are produced via the scattering of either two gluons or one quark and the corresponding anti-quark at the leading order in perturbative QCD theory. Figure 2.7 shows two representative Feynman diagrams illustrating typical contributions to four top quark production at leading order in the SM. The predicted cross section for $t\bar{t}t\bar{t}$ production at next-to-leading order (NLO) is $\sigma^{SM}_{t\bar{t}t\bar{t}} = 9.2$ fb at $\sqrt{s} = 13$ TeV [19, 20]. Recently a new paper [21] updated this value using calculations which also take account EW effects. This gives a value of $\sigma^{SM}_{t\bar{t}t\bar{t}} = 12.0$ fb at $\sqrt{s} = 13$ TeV. At this value, current experiments at LHC are starting to be sensitive to the $t\bar{t}t\bar{t}$ signal, making it a perfect opportunity to study this process.

2.3.2 $t\bar{t}t\bar{t}$ decay modes

Since top quark decays dominantly by $t \to bW^+$ process, the $t\bar{t}t\bar{t}$ decay mode can also be classified into different channels with different final state signatures depending on

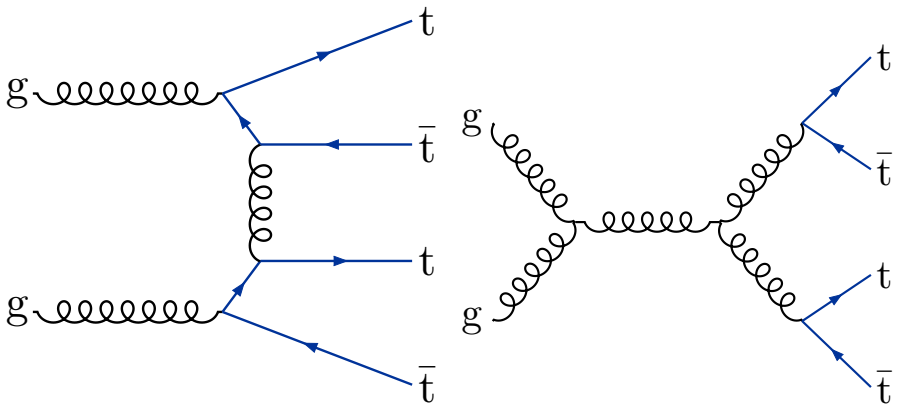

Figure 2.7: Representative diagrams for $t\bar{t}t\bar{t}$ production at the lowest order in the SM.

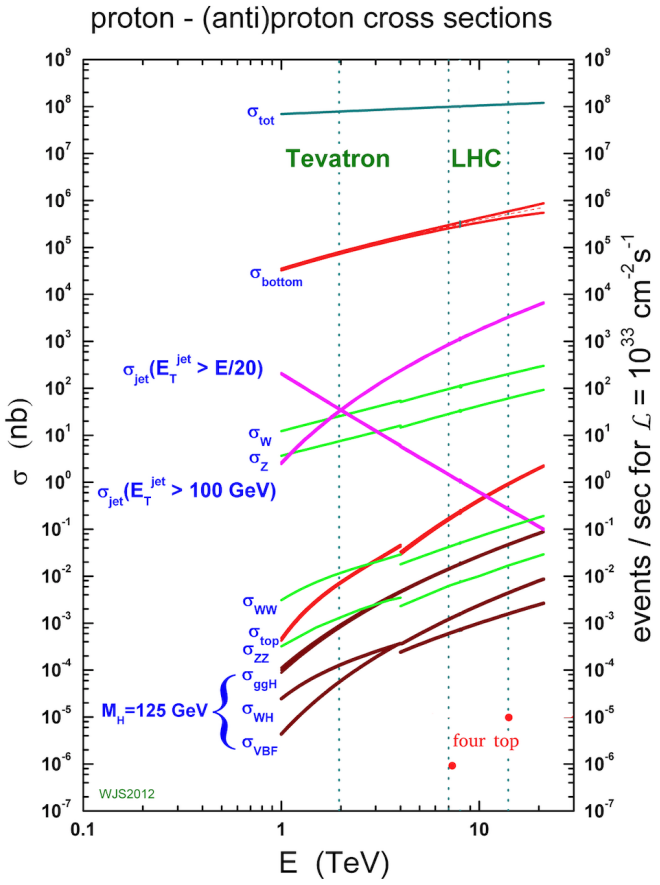

Figure 2.8: Cross section for different processes in proton-proton collision at LHC.

the number of leptonic W decay:

- Fully Leptonic channel: 4 leptons, 4 hard b quarks from top parent quarks, 4 neutrinos contribution to missing transverse energy (MET).
- Trilepton channel: 3 leptons, 4 hard b quarks from top parent quark, 2 hard jets from W hadronically decay, 3 neutrinos contribution to MET.
- Dilepton channel: 2 leptons, 4 hard b quarks from top parent quark, 4 hard jets from W hadronically decay, 2 neutrinos contribution to MET.
- Single lepton channel: 1 leptons, 4 hard b quarks from top parent quark, 6 hard jets from W hadronically decay, 1 neutrinos contribution to MET.
- All hadronic channel: no leptons, 4 hard b quarks from top parent quark, 8 hard jets from W hadronically decay, small to none MET.

Assuming the unitarity of leptons, the fraction of each decay mode is charted in Figure 2.9. Of the dilepton channel, it can be further divided into opposite sign (OS) channel which takes up 2/3 of the dilepton channel and same sign (SS) channel which takes up 1/3 of the dilepton channel.

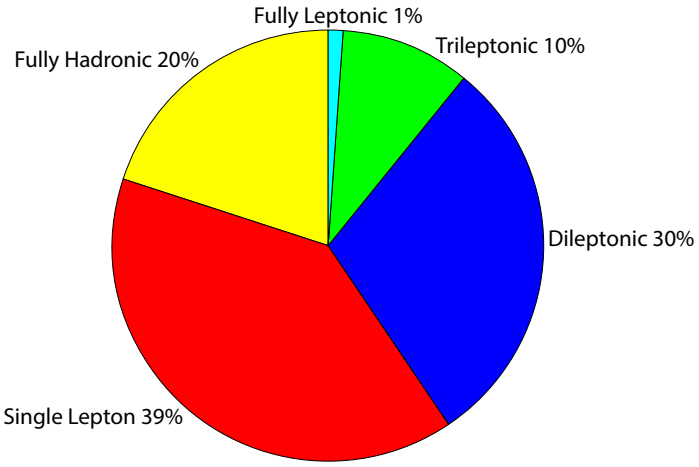

Figure 2.9: Cross section for different processes in proton-proton collision at LHC.

Chapter 3

Experimental Setup

3.1 The CERN Large Hadron Collider

The Large Hadron Collider (LHC) at the European Center for Particle Physics (CERN) is the largest and most powerful particle accelerator in the world [22]. It was built as an addition to the series of accelerators and infrastructure that already existed at CERN. Inherited from the Large Electron Positron collider (LEP), the tunnel of LHC has a circumference of about 27 km, a diameter of 3.8 m, buried 50-175 m below the ground of the French-Swiss border right next to the city of Geneva. The limited space in the tunnel promoted a novel design with two beam pipes concentrated inside a common yoke, as shown in Figure 3.1. Two particle beams are injected in the beam pipes and accelerated by the radio frequency system, util their speeds are close to the speed of light. The beams move in opposite directions and they are made to collide head-on at four interaction regions. The key to guide the beams along the accelerator ring is the use of superconducting electromagnets which operate at a temperature below -271.3 ^{o}C. 1232 dipole bending magnets are used to

direct the beams, and 392 quadrupole magnets are used to focus the beams. A third type of magnet is also used to squeeze the beam just prior to collision in order to increase the chances of collisions. The magnetic field required to achieve the design energy of 7 TeV for each beam is 8.3 Tesla, derived from Equation 3.1.

$$E\,[\mathrm{GeV}] \approx 0.3B\,[\mathrm{T}]\,R\,[\mathrm{m}] \tag{3.1}$$

A key parameter of the LHC, or any accelerator, is instantaneous Luminosity. This is defined as the number of collisions occurred per cm^2 per second in the detector, as shown in Equation 3.2.

$$L \sim \frac{fN_1N_2}{4\pi\sigma_x\sigma_y} \tag{3.2}$$

where N_i is the number of protons in each of the two crossing bunches, σ is the cross section of the bunch in x and y components, f is the bunches crossing frequency. In the case of the LHC, $f \sim 40 \times 10^6$ Hz, $N_i \sim 1.15 \times 10^{11}$ and $\sigma \sim 16 \times 10^{-4}$cm, giving an instantaneous luminosity of $L \sim 10^{34}\mathrm{cm}^{-2}s^{-1}$.

The integral of instantaneous luminosity over time is called integrated luminosity, calculated by $\mathrm{L} = \int L\,\mathrm{d}t$. And it measures the size of the collected data set. The event number of a certain process is thus given by Equation 3.3:

$$N = \sigma \times \mathrm{L} \tag{3.3}$$

where σ is the cross section for that process.

The LHC isn't a stand-alone machine to accelerate protons. For beam stability and budgetary reasons, 6 other accelerators are used sequentially to accelerate proton beams

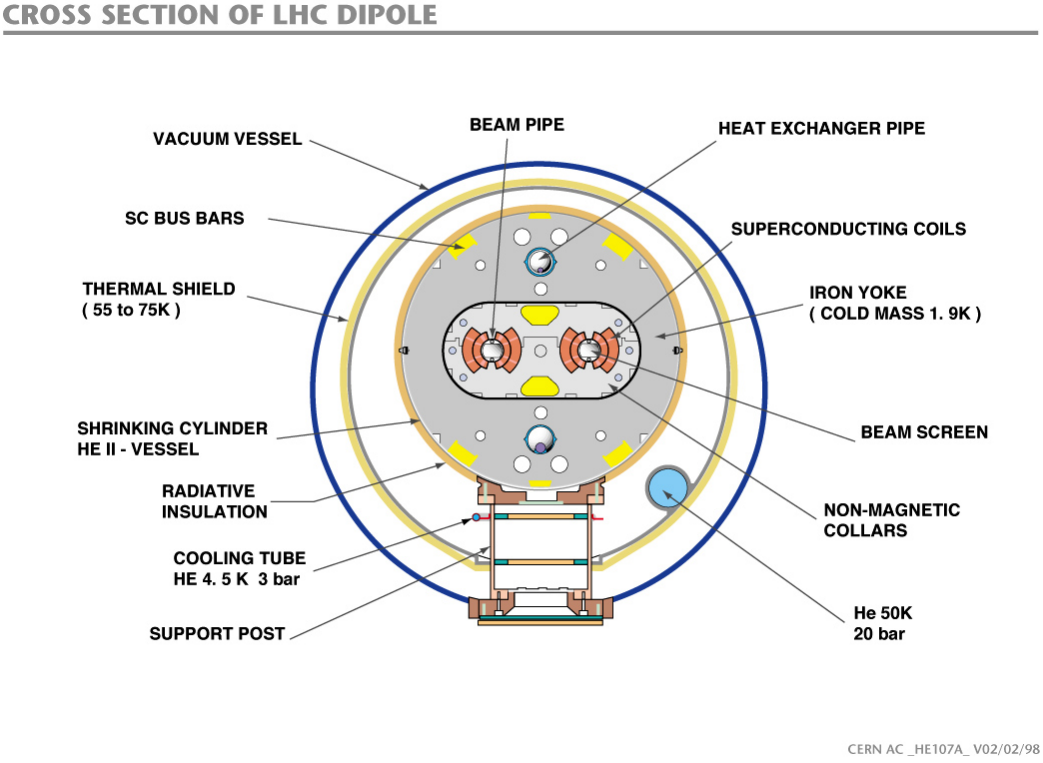

Figure 3.1: Cross section of LHC dipole

before they are injected into the LHC. Protons are produced by the 90 keV duoplasmatron source, and extracted into a Radio Frequency Quadrupole to be accelerated to 750 keV. After that, the protons will go through the linear accelerator (Linac II) where their energies are raised to 50 MeV. Next in line is the Proton Synchrotron Booster (PSB), where the protons are accelerated to 1.4 GeV and the beam intensity is increased, resulting in high luminosity needed for the LHC. Beams from PSB are transferred to the Proton Synchrotron (PS) where they are further accelerated to 26 GeV. The PS is also responsible for creating the 25 ns spacing bunch structure of beams for the LHC. The bunches from PS are passed to the Super Proton Synchrotron (SPS) before they finally reach the LHC. The SPS is to accelerate beam bunches to 450 GeV and insert the bunch trains into the LHC at just the

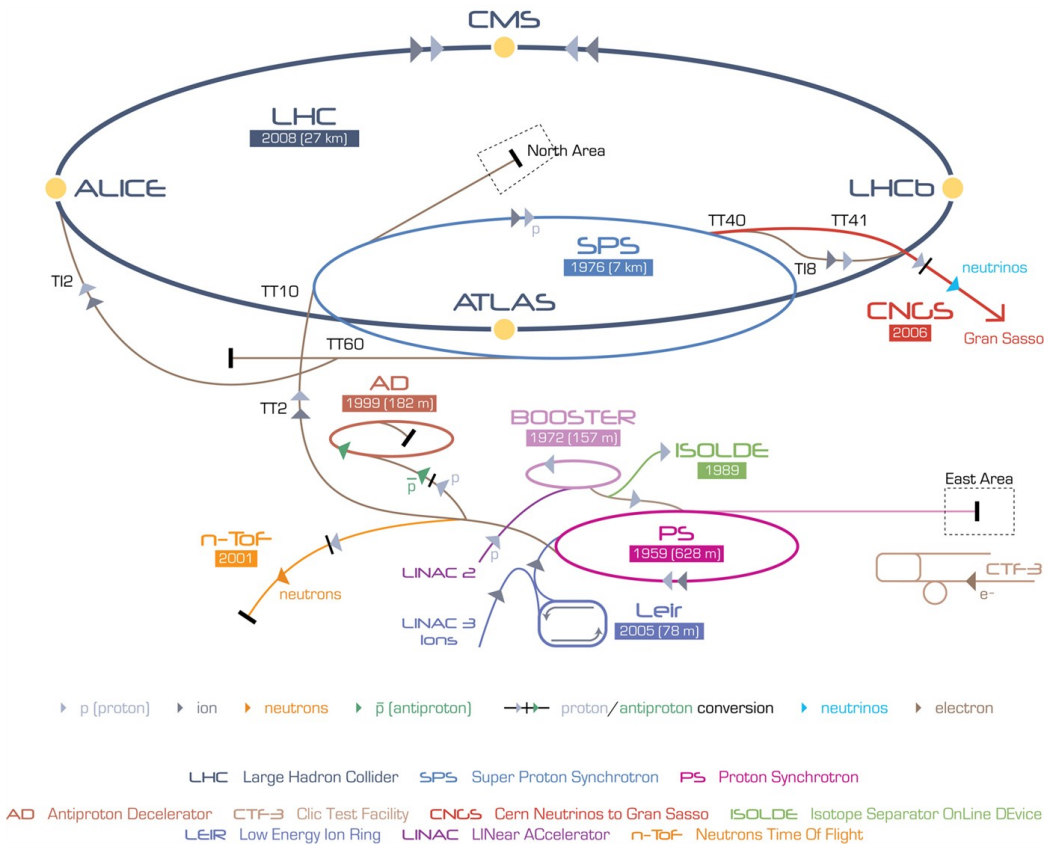

Figure 3.2: The LHC injector chain

right place to ensure the collision happens in the center of the detectors. Figure 3.2 is a schematic drawing of the LHC injector chain.

Currently there are 7 experiments at the LHC, the four big experiments: A Toroidal LHC ApparatuS (ATLAS), the Compact Muon Solenoid (CMS), A Large Ion Collider Experiment (ALICE) and Large Hadron Collider beauty (LHCb) experiment. Three small experiments TOTEM, LHCf and MoEDAL complete the list. The two biggest experiments, ATLAS and CMS, use independently designed general-purpose detectors to investigate a wide range of physics and provide data to cross-check each other. The ALICE experiment has a specialized heavy-ion detector designed to study the physics of strongly

interacting matter at extreme energy densities. The LHCb experiment specializes in the studies of the differences between matter and antimatter by studying b quark physics. The Total, elastic and diffractive cross-section measurement (TOTEM), located in the forward regions of the CMS detector, studies particles thrust forward by the collisions in LHC that are otherwise inaccessible by the four big LHC experiments. The Large Hadron Collider forward (LHCf) experiment, seated along the beamline on on both sides of the ATLAS collision point, uses particles thrown forward by LHC collisions to simulate cosmic rays. The Monopole and Exotics Detector at the LHC (MoEDAL), deployed around the same intersection region as the LHCb detector, is designed to search directly for the magnetic monopole and highly ionizing Stable Massive Particles predicted by theories beyond the Standard Model.

3.2 The Compact Muon Solenoid Experiment

The Compact Muon Solenoid (CMS) [23] is designed to operate in the LHC conditions of high pile-up and high radiation level, and to provide good lepton identification and measurement over a wide range of particle momentum. The design of CMS [24], illustrated in Figure 3.3, meets all these requirements. An essential feature of CMS is its high-field superconducting solenoid. The presence of a strong magnet field allows CMS to accurately measure the momentum of charged particles and to unambiguously determine the charge of particles when their paths are well reconstructed from tracking systems. To exploit different properties of particles, CMS consists of layers of different material grouped into sub-systems, each with a specific purpose. Moving outward from the central axis of

CMS, these systems are: the inner tracking system, the electromagnetic calorimeter, the hadron calorimeter, the superconducting solenoid and the muon systems. Figure 3.4 shows a picture of the CMS detector in life size comparing to the man standing in front of it. The detector is 21m×15m×15m in dimension. It weighs 14,000 tons and is located 100m underground in France between Jura mountain and Lake Geneva.

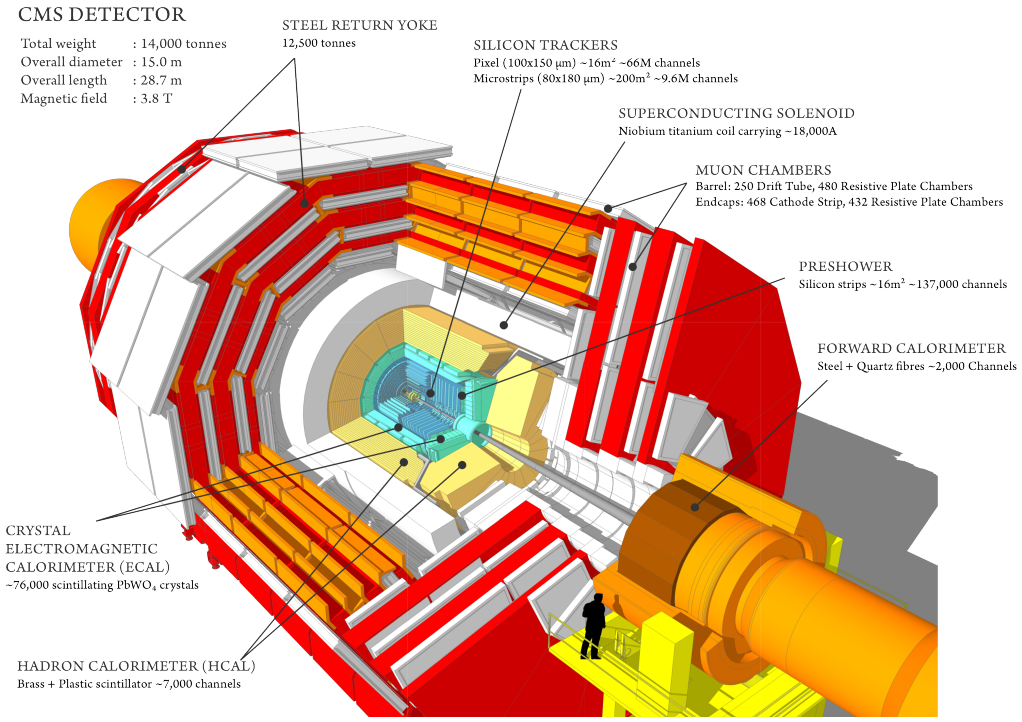

Figure 3.3: Sectional view of the CMS detector.

The coordinate system adopted by CMS has the origin point located at the collision point in the center of the detector. The x-axis as chosen to point radically from the origin point to the center of the LHC ring and y-axis points vertically upward. thus the z-axis points along the pipeline direction geologically toward Jura mountain. The azimuth angle

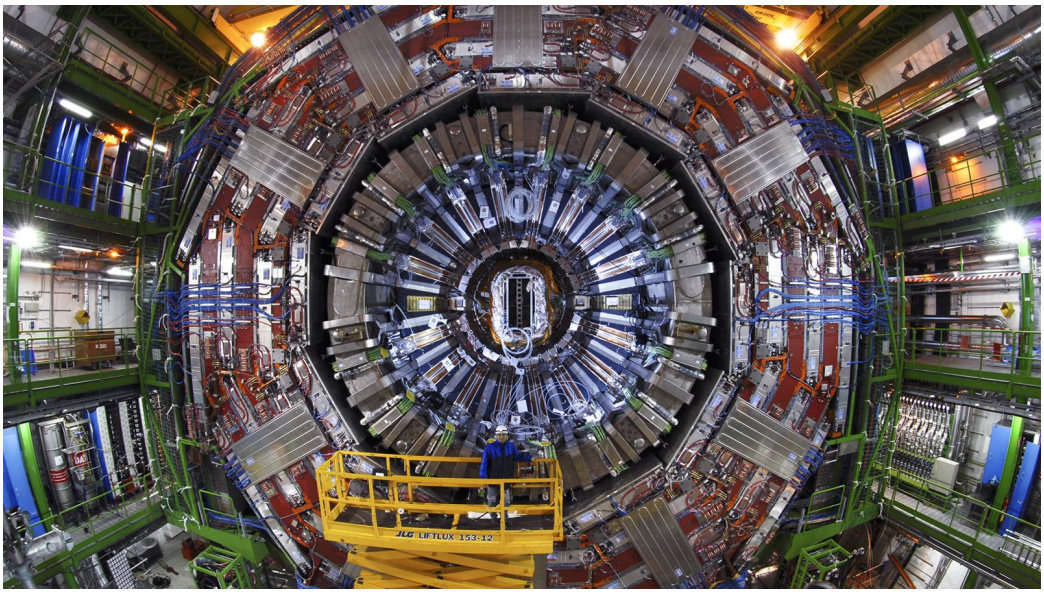

Figure 3.4: Photograph of the CMS detector

ϕ is measured from the x-axis in the $x-y$ plane and the radius $r = \sqrt{x^2+y^2}$ is the radial distance from the measured point to the z-axis. The polar angle θ is measured from the z-axis, and pseudorapidity is defined as $\eta = -\ln\tan(\theta/2)$, to characterize the boost of the particle along the longitudinal axis. An angular distance between two particles is defined as $\Delta R = \sqrt{(\Delta\eta)^2 + (\Delta\phi)^2}$. The transverse momentum p_T and E_T are computed from the vector components of momentum and energy in the $x-y$ plane. The imbalance of energy in the transverse plane due to non-interacting particles is denoted as E_T^{miss}, which is equal to the magnitude of the vector sum of all the transverse momenta by definition 3.4.

$$E_T^{miss} = |-\sum \vec{p}_T| \tag{3.4}$$

3.2.1 Superconducting solenoid magnet

A distinguishing feature of the CMS detector is its superconducting magnet. This has a free bore of 6 m diameter and is 12.5 m long, enclosed inside a 10 000 ton return yoke through which flux is returned. The solenoid provides a field of 4 T along the z direction within its volume. Outside of it, the flux returned through the iron yoke which generates a uniformed 2 T magnetic field. The operating temperature of the 4-layer winding Nb-Ti superconductor is below 4.6 K.

3.2.2 Inner tracking system

To meet the goal of finding interesting physics signature, the inner tracking system is designed to to provide a precise and efficient reconstruction of the trajectory of charged particles with high p_T, and a precise measurement of secondary vertices and impact parameters. The trajectory measurement combined with EM calorimeter or muon system information provides the essential information needed for electron and muon identification and the measurement of the particle momenta. The tracker also precisely reconstructs secondary vertices and measures the impact parameters that are crucial to the efficient tagging of heavy flavor particles. A precise trajectory requires high granularity of the tracking system, and the high bunch crossing rate requires a fast response detector to keep track of events. Also, being closest to the center of the collision requires the detector to be able to withstand a high radiation level. A silicon based tracker is used to satisfy these requirements. The CMS tracker consists of a silicon pixel detector and a silicon strip tracker. A schematic drawing of the tracking system in the r-z plane is shown in Figure 3.5.

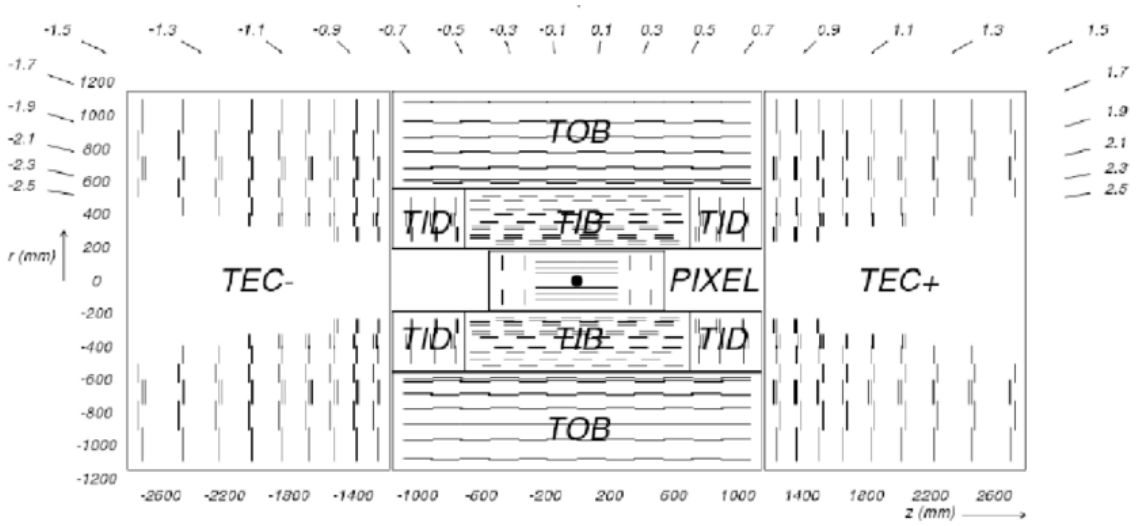

Figure 3.5: Schematic drawing of the CMS tracker in the r-z plane. Each line represents a detector module.

3.2.2.1 The Silicon Pixel System

The pixel system is composed of three concentric cylindrical barrel layers (BPix) at radii of 4.4, 7.3 and 10.2 cm surrounding the interaction point and two disks (FPix) on each side (endcap) at $z = \pm$ 34.5 and $z = \pm$ 46.5 cm. The detectors have an area of about 1 m^2 and cover the pseudorapidity range $-2.5 < \eta < 2.5$. In total 66 million pixel cells are used, each of size 100×150 μm^2. The large magnetic field shifts the motion of induced charges due to the Lorentz effect, causing several pixels to share the deposited charge. With charge interpolation between pixels, the spacial resolution of pixel detector is improved to 15−20 μm. The pixel detector is essential for reconstructing interaction vertices and displaced vertices from b and τ decays, and forming seed tracks for outer track reconstruction.

3.2.2.2 The Silicon Strip Detectors

The silicon strip tracker has three sub-detectors. The Tracker Inner Barrel and Disks (TIB/TID) populate the radial region between 20 cm and 55 cm using 4 barrel layers and 3 disks in each endcap. The spacial resolution TIB/TID are $23-35$ μm, depending on the strip sensors in each layer of disk. The Tracker Outer Barrel (TOB) surrounds TIB/TID and covers the region out to a radius of 116 cm. It has 6 layers with single point resolution of 53 μm for layers 1 to 4, 35 μm for layers 5 and 6. The Tracker EndCaps (TEC+/TEC-) consist of of 9 disks in each endcap, covering the region of 124 cm $< |z| <$ 282 cm and 22.5 cm $< r <$ 113.5 cm. As shown in Figure 3.5, the first two layers or rings in each sub-detector have back-to-back modules to deliver stereo hits for providing an extra co-ordinate in the position measurement. Together the three sub-detectors cover a pseudorapidity $|\eta| < 2.5$ for precise track measurement.

3.2.3 Electromagnetic calorimeter

To measure the energies of the electromagnetic particles emerging from the collision, the hermetic homogeneous electromagnetic calorimeter (ECAL) is installed outside of the silicon tracking system. In CMS the lead tungstate ($PbWO_4$) crystal is chosen as the active material for the ECAL because of its high density, radiation-hardness, short radiation length ($X_0 = 0.89$ cm), and small Moliére radius (2.2 cm). In addition, about 80% of scintillation light is dispersed in 25 ns, giving it a fast-response in preparation for the next bunch crossing beams. The properties of small light yield, temperature sensitivity, limited radiation damage are allowed for by applying optimal photodetectors, a precise tempera-

ture control and a light monitoring system. The ECAL has 3 components in its layout: the barrel part (EB), the endcap part (EE) and a preshower detector (ES) right before EE, as shown in Figure 3.6.

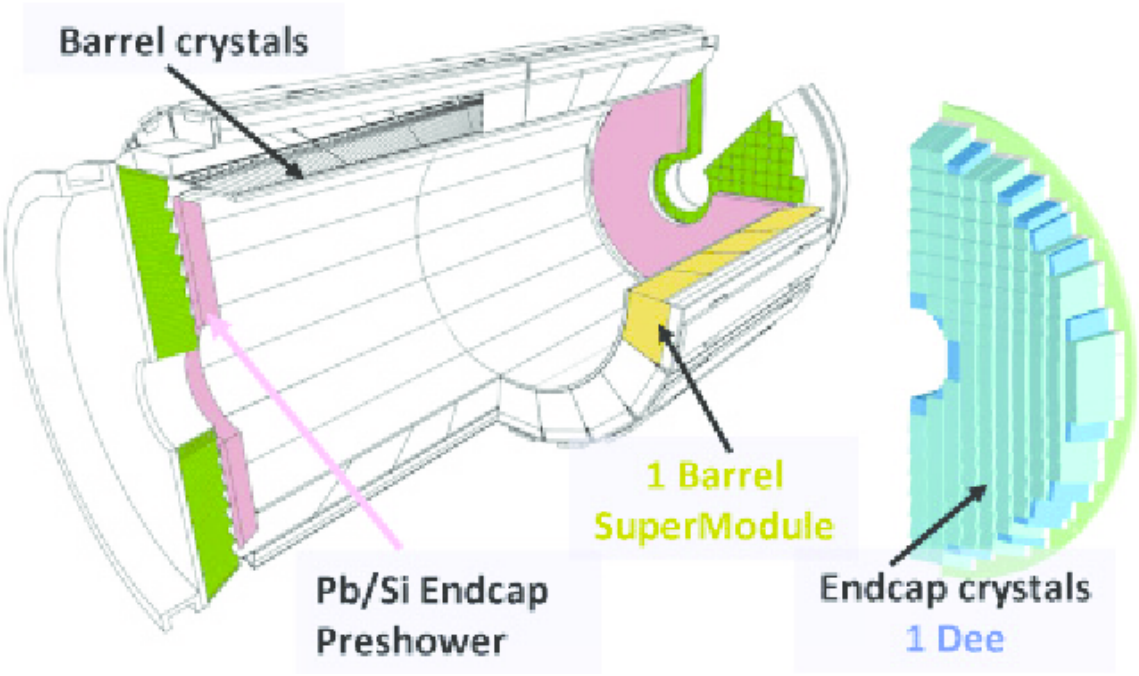

Figure 3.6: Schematic view of the CMS electromagnetic calorimeter.

EB: With a 360-fold granularity in ϕ and (2×85)-fold in η, the EB covers the pseudorapidity range $\eta < 1.479$ with 61,200 $PbWO_4$ crystals in total. Each crystal is properly aligned with a cross section of about $22{\times}22$ mm^2 ($26{\times}26$ mm^2) at the front (rear) face and a length of 230 mm ($25.8 \times X_0$). Avalanche photodiodes are attached to the end of each crystal.

EE: The endcap ECAL covers a pseudorapidity range of $1.479 < \eta < 3.0$. Each crystal has a cross section of $28.62{\times}28.62$ mm^2 ($30{\times}30$ mm^2) at the front (rear) face and a length of 220 mm ($24.7 \times X_0$).Vacuum phototriodes are attached to the end of each crystal

due to different level of magnetic field and radiation intensity.

ES: The preshower detector is used to distinguish interesting high-energy photon signatures from two closely-spaced lower-energy photons coming from the decays of neutral pions. With this goal in mind, the preshower detector is designed as a sampling calorimeter with two layers of lead and two layers of silicon strip sensors. Comparing to the 30 mm wide ECAL crystals, the strips are 2 mm wide making it possible to pinpoint the position of a trespassing particle.

Electrons and photons emerged from the collision will be stopped at ECAL and their energy will be measured. The energy resolution for electrons is p_{T} and η dependent. From $Z \rightarrow e^{+}e^{-}$ process it is measured to be $\sim 2.5\%$ in the barrel and $\sim 4.7\%$ in the endcaps.

3.2.4 Hadron calorimeter

The hadron calorimeter (HCAL) is designed to measure the directions and energies of hadrons that are made of quarks and gluons and indirectly determine the missing transverse energy, E_T^{miss}, from non-interacting particles that are crucial signatures in many new physics model predictions. Information from HCAL will also help in the identification of electrons, photons and muons when combined with tracker, ECAL and the muon system.

Figure 3.7 shows a schematic of the CMS hadron calorimeter, which is a sampling detector with alternating layers of brass absorber plates and plastic scintillator tiles. Wavelength shifting fibres are connected to the scintillator tiles to readout light emitted by the scintillation material when the secondary particles, that are created in cascade when the hadron particle from collision hits the brass absorber plate, pass through. In order to

contain all the hadrons inside HCAL, the HCAL modules are built as thickly as possible and it fills the space between ECAL and the magnetic solenoid.

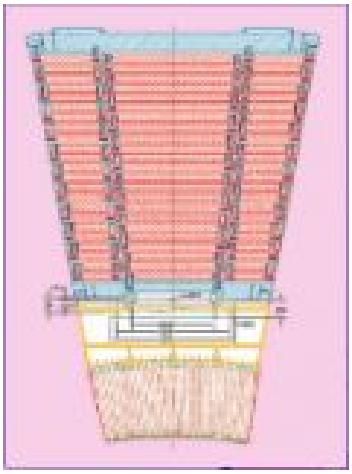

Figure 3.7: HCAL module showing sampling layers.

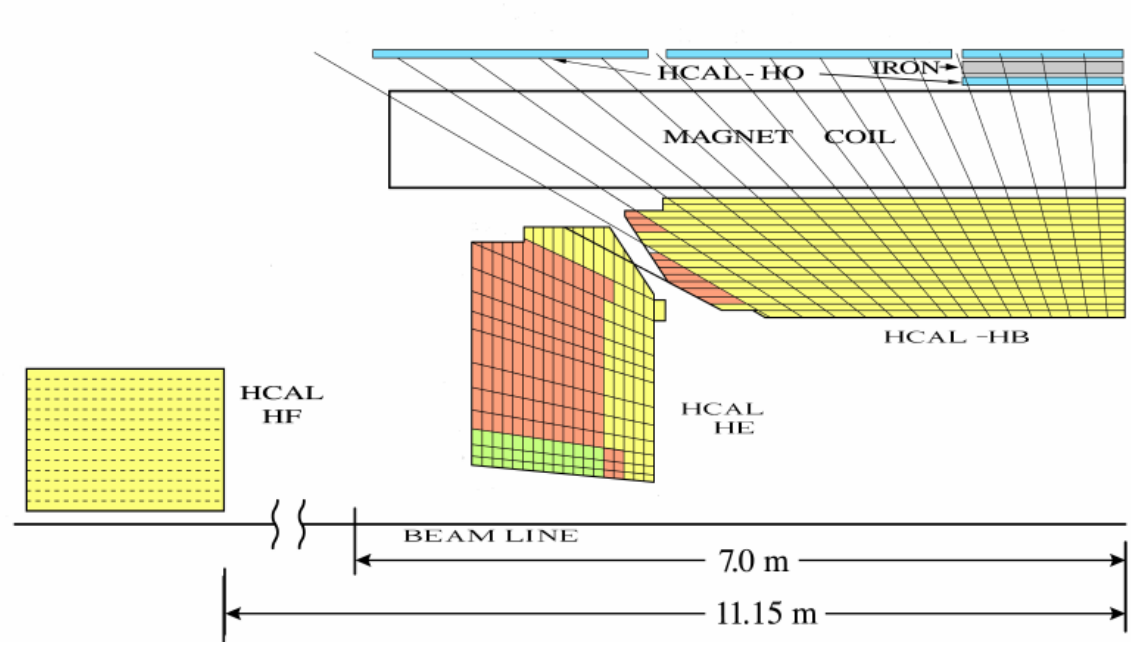

Figure 3.8: Quarter view of the CMS hadron calorimeter layout.

The HCAL has four sections: hadron barrel (HB) covers $|\eta| < 1.3$, hadron endcap (HE) covers $1.3 < |\eta| < 3$, hadron outer (HO) covers $|\eta| < 1.3$ and hadron forward (HF) covers $3 < |\eta| < 5$. HO is installed right after the solenoid, utilizing the solenoid coil as an additional absorber to ensure adequate sampling depth in the central pseudorapidity region, and to provide enough stopping power for hadronic showers. In the region $|\eta| > 3$, HF experiences an extremely high particle flux. The sampling material here is chosen as steel and quartz fibres with a two-length configuration of the readout fibres to distinguish between the showers generated by electrons and photons from those coming from hadrons. An EM shower deposits most energy in the first 22 cm of the steel absorber. Figure 3.8 shows the layout of HCAL in CMS in a quarter view.

3.2.5 The muon system

Many interesting physics processes have a muon or muons in their final states. Because they are massive and only undergo electroweak interactions, muons are the only ones that can pass through the tracker, calorimeter system and the magnetic solenoid with hardly any energy loss. Thus a robust and precise measurement of muon is of central importance to CMS.

The CMS muon system is designed for the purpose of muon identification, momentum measurement and trigger capability. The iron return yoke interspersed with muon chambers provides a nearly uniformed 2 Tesla magnetic field in the barrel region. This gives good muon momentum resolution and unambiguous charge identification. There are three sub-detectors composing the muon system: the Drift Tubes (DT) in the barrel region, the Cathode Strip Chambers (CSC) in the two endcap regions and the Resistive Plate Cham-

Table 3.1: Some properties of the CMS muon system in the year 2016.

Muon subsystem	DT	CSC	RPC
$\|\eta\|$	0.0-1.2	0.9-2.4	0.0-1.9
number of chambers	250	540	Barrel 480 Endcap 576
spatial resolution	100μm	$50-140\mu$m	$0.8-1.3$cm
time resolution	2 ns	3 ns	1.5 ns

bers (RPC) in both barrel and endcap regions [25]. A comparison on the performance of these three detectors are given in Table 3.1 [26].

3.2.5.1 DT

The DT sub-system has 4 stations which form concentric cylinders in the detector barrel: 3 inner layers have 60 drift chambers each and the outer layer has 70. Each drift tube chamber is made of 2 SuperLayers (SL) measuring the bending coordinate $(r-\phi)$ and 1 SuperLayer measuring the track angle $(r-z)$. Each SL is a group of four consecutive cell layers staggered by half a cell, giving DT a spatial resolution improvement and time-tagging capability. The layout of DT SLs and schematic drawing of a DT cell is shown in Figure 3.9.

3.2.5.2 CSC

The CSC sub-system has 8 stations on the two endcaps, 4 on each side. In each station there are 2 or 3 (on $\pm$ME1) rings of chambers. The CSC detectors are multiwire proportional chambers with the function of precision endcap muon measurement and muon trigger. Each CSC chambers is comprised of 6 anode wire planes interleaved among 7

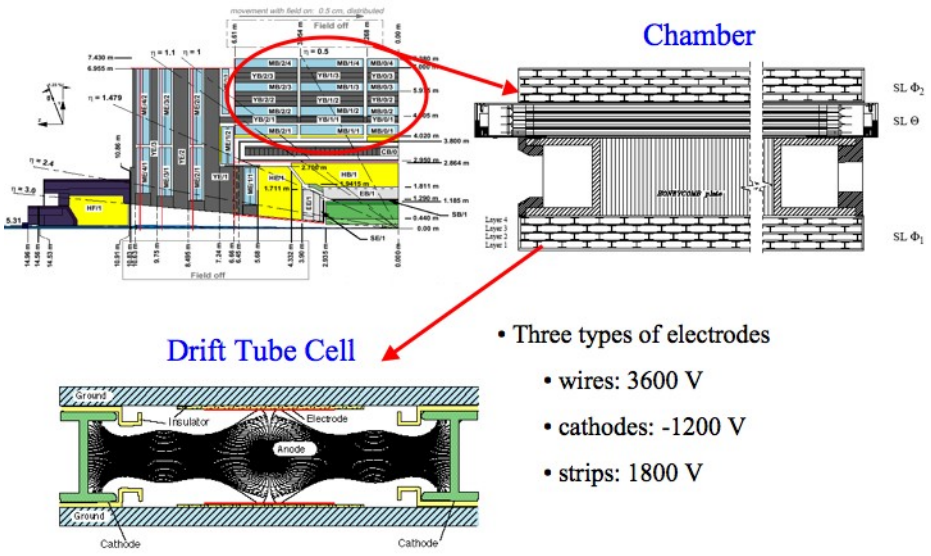

Figure 3.9: Schematic drawing of DT SuperLayers and DT cell.

cathode panels. Figure 3.10 shows the layout of CSC panels and a schematic view of a single gap illustrating the principle of CSC working.

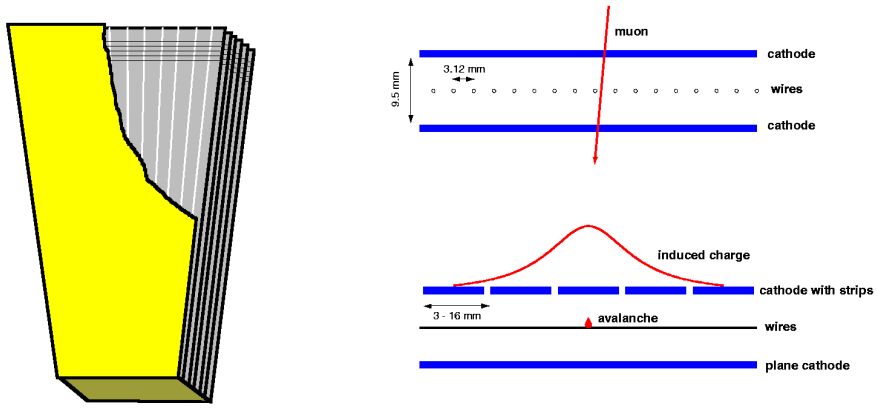

Figure 3.10: Schematic drawing of CSC chamber and working principle.

3.2.5.3 RPC

Placed right in front of every DT and CSC chamber, the RPCs are used as dedicated muon trigger device due to it high time resolution. The adequate spatial resolution also allows it to contribute to muon identification and reconstruction alongside the DTs and CSCs. The CMS RPCs are gaseous parallel plate detectors working in avalanche mode with 2 gaps formed by two parallel bakelite electrodes with a common copper readout strips in between, as shown in Figure 3.11

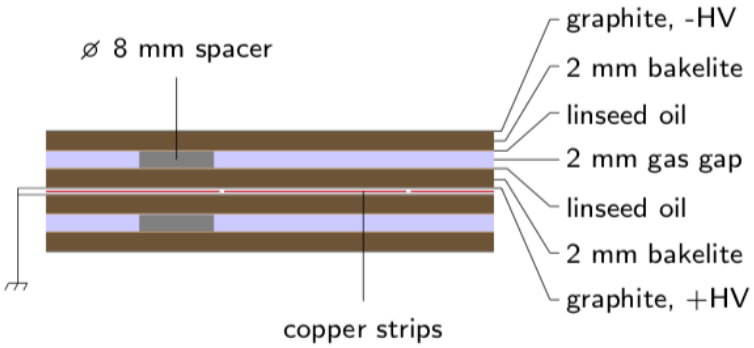

Figure 3.11: A cross-section view of the CMS RPC.

3.2.6 Trigger and Data acquisition system

The LHC provides proton beams with bunch crossing intervals of 25 ns. In CMS, for each crossing of the bunches, about 20 collisions (pile-up interactions) happens. Thus, the collision rate at CMS detector is $\sim \frac{20}{25\times10^{-9}} \sim 800$ MHz. Current technology doesn't allow us to read out and store information from every event that happens during the bunch crossing. Most of the events are produced via low-energy glancing collisions and are less likely to reveal interesting physics. The trigger system is designed to reduce the recording rate, while keeping the highly energetic interesting events. The CMS trigger system consists of two levels, the Level-1 (L1) Trigger and the High-Level Trigger (HLT). The L1 trigger is hardware dependent. It uses local fast trigger information from calorimeters and muon system to reduce incoming data rate to 100 kHz and puts the information onto the computers that make up the HLT system. Figure 3.12 depicts the architecture of the L1 trigger. The HLT is a software filter that runs on the recorded data from L1 with certain algorithms and

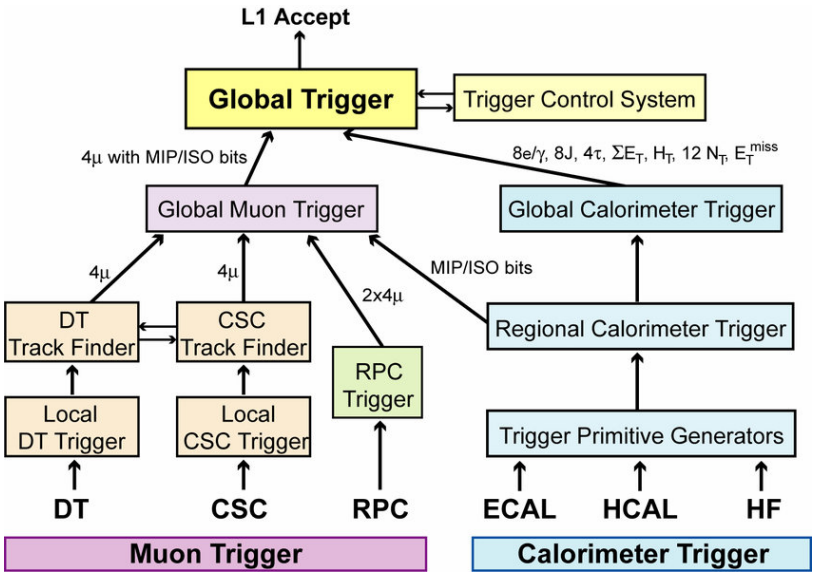

Figure 3.12: Architecture of the L1 trigger.

streamline them to a reduced rate of a few hundred Hz for physics analysis.

The CMS Data Acquisition (DAQ) system is designed to meet the requirement of sustaining a data input rate of 100 kHz from L1 trigger, and can still provide enough computer power for HLT to filter them with dedicated physics selections and store into streams of Data. Figure 3.13 shows a schematic view of the CMS DAQ system.

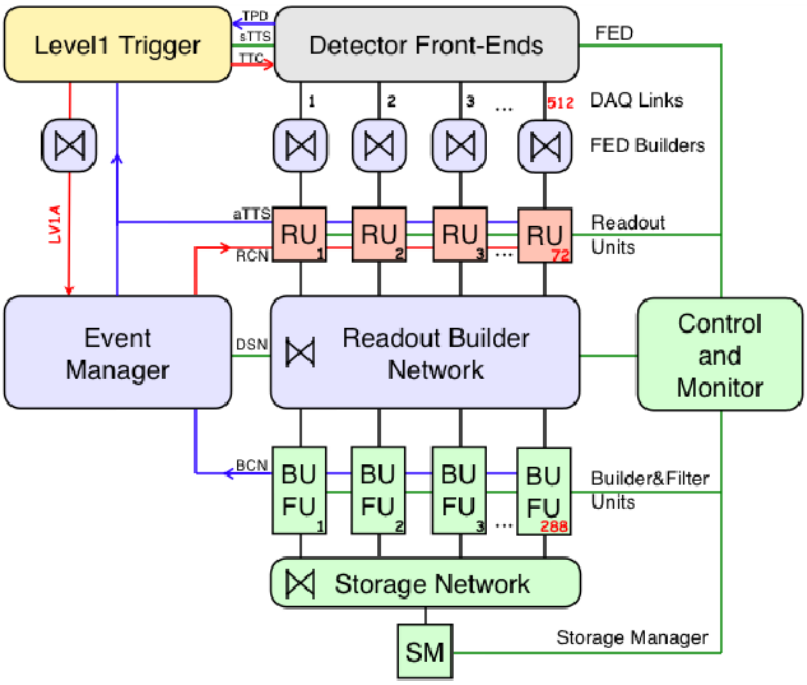

Figure 3.13: Architecture of the CMS DAQ.

Chapter 4

Event Reconstruction and Object Identification

With a functionality-based highly segmented structure detailed in the previous section 3.2, the CMS detector is able to collect signals (elements) from collision events as follows. Particles emerge from the proton-proton collision points (vertices) and enter the inner tracker system, in which charged-particles leave signals (hits) in the different layers. These are to be used to measure the trajectories of the charged hadrons. The electric charge and momentum of each charged particle is measured by combining the magnetic field and the reconstructed tracks. In the ECAL electrons and photons induce electromagnetic showers which are fully absorbed, while charged and neutral hadrons will induce hadronic showers which are not only in the ECAL but will also enter into the HCAL. Electromagnetic showers are found by grouping the energy deposits in neighboring ECAL cells to form clusters from which directions and energies of these particles can be determined. The charged and

neutral hadrons are fully absorbed in the HCAL and the corresponding energy clusters are used to determine their energy and directions. Muons and neutrinos barely interact with materials in the previous layers and pass right though. The layers of muon system record hits from the muons and provide additional track information for standalone muon charge and momentum measurement. Neutrinos leave the detector without interaction and their presence is inferred by the observation of transverse imbalance in the energy flow in the detector. These signatures are sketched in Figure 4.1.

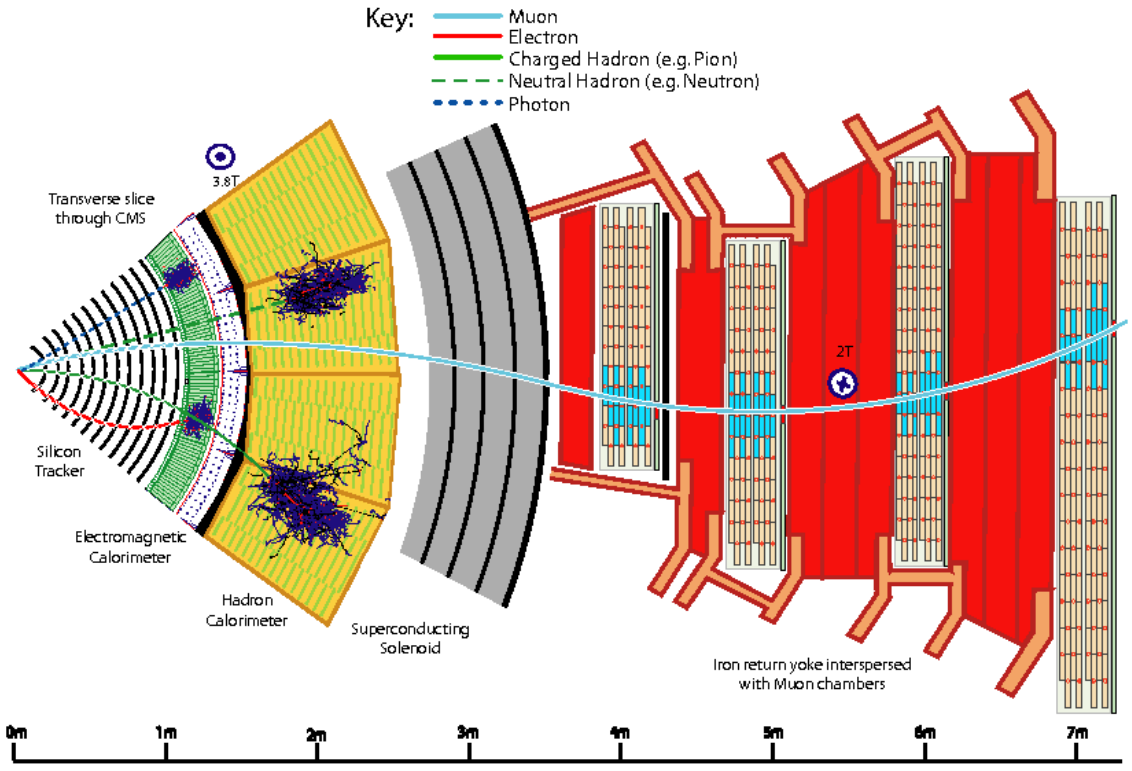

Figure 4.1: A sketch of different particles interacting with the CMS detector from a transverse view.

The physics objects used in this analysis are reconstructed via a particle-flow (PF)

algorithm [27] that identifies each final-state particle by linking PF elements (tracks and clusters) from different sub-detectors and reconstructs the particle properties by combining the corresponding measurements. The software used for reconstructing the physics objects and for performing this analysis is CMSSW_80X, a C++ based framework with modularized architecture to process the event data.

4.1 PF elements reconstruction

4.1.1 Tracks and vertices

The charged-particle track reconstruction in CMS utilizes a combinatorial track finding method based on the Kalman Filtering (KF) algorithm [28]. This has three steps:

1. **Seed generation:** The few hits in the pixel detector that are compatible with a charged-particle trajectory are used as track seeds;

2. **Trajectory building:** Starting from a coarse estimate of track parameters from the seed, the KF method is used to gather hits in the successive tracker layers until all of the tracker information is used;

3. **Final track fit:** The trajectory is refitted with a KF track fit to reduce bias from early stages, and to determine the origin, transverse momentum and direction of the charged particle.

The PF tracks are reconstructed by applying this combinatorial track finder iteratively. After each iteration the hits associated to the reconstructed trajectory are removed, and the remaining hits are used in the next iteration to form new seeds and tracks with relaxed

quality criteria. In this way the ambiguity arising from random hit-to-seed association is resolved and tracking efficiency is increased. In order to be more adaptive to the electron tracks, where the electron radiates a photon via the bremsstrahlung processes, a Gaussian-sum filter (GSF) [29] is used instead of KF for the trajectory fitting.

Muon tracks in the muon system are reconstructed by firstly clustering the hits in the DT or CSC detectors into segments, which are then used as seeds to build the trajectory by gathering the corresponding hits from the DT, CSC and RPC detectors. These fitted tracks are called standalone-muon tracks.

In each bunch crossing there are many incidences of proton-proton collisions within the detector live time. These are referred to as pileup. In order to correctly associate each reconstructed track to its true interaction origin, a primary-vertex reconstruction is performed. First, the selected tracks that appear to originate from the same interaction vertex based on a deterministic annealing (DA) algorithm [30] are clustered together to give a primary-vertex candidate. The candidates with at least two associated tracks are fitted using an adaptive vertex fitter to give the best estimation of vertex location parameters, covariance matrix and indicators for the success of the fit. The primary vertex in an event is then chosen to be the candidate with the highest sum of p_T^2 and the highest value of the indicator.

4.1.2 Calorimeter clusters

The PF clustering algorithm is done in calorimeter sub-detectors via two steps. First, the calorimeter cells with energy deposits above a threshold and larger than neighboring cells are identified as cluster seeds. The neighboring cells are defined as either 4 cells

that share common sides with the seed cell, or 8 cells including the 4 cells sharing common corners with the seed cell. Then, from the cluster seeds, topological clusters are grown to aggregate cells that are neighbors of the cells already included in the cluster, and have energy deposits larger than twice the noise level. Topological clusters are reconstructed with an expectation maximization algorithm that models the energy deposits in M individual cells from the N Gaussian energy deposits standing for N cluster seeds. The position and energy deposits of the cluster can then be analytically determined from a maximum-likelihood fit.

4.2 PF candidate identification

4.2.1 Link algorithm

Particles that emerge from the collision point normally pass through many layers of the CMS detector and leave traces in several sub-detectors. Thus a given particle may have several PF elements. To better reconstruct the particle using the overall information from the detector, a link algorithm is used to connect PF elements of the same particle.

To link a track to the cluster, the inner track is extrapolated from the last hit position in the inner tracker system into the calorimeters at a depth of the expected maximum value of the longitudinal EM shower profile in ECAL or one interaction length in HCAL. If the extrapolated position falls within a cluster, the link between the track and the cluster is established. If several tracks are linked to the same cluster, or several clusters are linked to the same track, the link with the smallest distance between the extrapolated track position and the cluster position in the (η, ϕ) plane is kept. Tangents to the GSF tracks are also extrapolated from the intersection points between the track and each layer of the tracker.

If the extrapolated position of track tangent falls within a ECAL cluster, the cluster is linked to the track as a photon emitted by electron bremsstrahlung. Tracks that are most likely to originate from photon conversion into e^+e^- are also linked together with dedicated conversion finder algorithm. If the converted photon is compatible with the GSF track tangents extrapolation, each of these tracks will also be linked to the original track. The preshower-ECAL or ECAL-HCAL cluster-to-cluster links are also established If the cluster position in preshower or ECAL falls within the envelope of ECAL or HCAL clusters. Last, links between inner tracks and tracks from the muon system are also established for muon identification.

4.2.2 Muons

PF muon candidates are reconstructed and identified first in the sequence. Three types of muons are reconstructed based on the linking procedure:

- Standalone Muon: These are reconstructed from the standalone-muon tracks mentioned in the previous section 4.1.
- Global Muon (*outside-in*): If the standalone-muon track can be linked to an inner track, these two tracks are combined and fit to from a global-muon track. This is reconstructed as a global muon.
- Tracker Muon (*inside-out*): By extrapolating preselected inner tracks to the muon system, if at least one muon segment match the extrapolated track, it qualifies as a tracker muon track thus is reconstructed as a tracker muon.

Then, the PF muon candidates are selected from the global muons or tracker muons follow-

ing a particular set of selection criteria making use of information from other sub-detectors such as energy deposition in calorimeters.

After the identification of muons, the associated PF elements are removed to prevent their further use in the identification of other particles.

4.2.3 Electrons

The reconstruction of electron candidates uses PF elements from inner tracker and the ECAL. First, the electron candidate is seeded from two complementary methods, namely ECAL-based and track-based measurement. All the clusters that are linked to either the ECAL supercluster seed or the GFS track seed or one of its tangents are associated with the candidate. Tracks linked to these clusters are also associated to the candidate if their correspondingly linked HCAL clusters have energy deposits compatible to the electron hypothesis. Tracks and clusters from a photon conversion to e^+e^- that is linked to the GSF tangent are associated to the candidate as well. The total collection of clusters is used to determine the energy of the electron candidate and the GSF track used to determine the momentum and direction. The electron candidates that meet a set of identification criteria are selected as PF electrons.

Isolated PF photons, which are not used in this analysis, are also reconstructed during this step by using the ECAL clusters that are not linked to any tracks or clusters. Again, all tracks and clusters used in this step to reconstruct the electron and isolated photon candidates are removed from the rest of PF elements.

4.2.4 Hadrons and jets

After the identification of muons, electrons and isolated photons together with the removal of their associated PF elements, the remaining particles are neutral and charged hadrons (from fragmentation and hadronization of quarks), and non-isolated photons (from π^0 decays). Non-isolated photons are reconstructed from ECAL clusters that are not linked to any HCAL clusters. Neutral hadrons are reconstructed from the HCAL clusters that are not linked to any tracks. The HCAL clusters, ECAL clusters and tracks that are linked give rise to charged hadrons.

Instead of directly using the hadrons and non-isolated photons, jets that are clustered from these reconstructed PF particles are typically used.

The jets used in this analysis are reconstructed using the anti-k_{T} clustering algorithm [31, 32]. First two distances are defined:

$$d_{ij} = \min(p_{Ti}^{2p}, p_{Tj}^{2p}) \frac{\Delta_{ij}^2}{R^2}$$

$$d_{iB} = p_{Ti}^{2p}$$

where d_{ij} is the distance between two entities (PF particles, pseudojets) i and j, d_{iB} is the distance between i and the beam, $\Delta_{ij}^2 = (y_i - y_j)^2 + (\phi_i - \phi_j)^2$ and p_{Ti}^{2p}, y_i and ϕ_i are the transverse momentum, rapidity and azimuth of entity (PF particles, pseudojets) i, respectively. R is a distance parameter. In this analysis $R = 0.4$ is used. For the anti-k$_T$ algorithm $p = -1$.

After removing PF candidates from non-primary vertices, iterative steps are done to find the minimum between d_{ij} and d_{iB}. If d_{ij} is the minimum, particle j is clustered with entity i as a single entity for the next iteration. If d_{iB} is minimum, entity i is considered a

jet and all its PF particle constituents removed from the event. This procedure is repeated until all PF particles are clustered into jets.

Chapter 5

Data Collection and Monte Carlo Simulation

5.1 Data

The real data events used for this analysis were collected by the CMS detector during 2016, and correspond to an integrated luminosity of 35.8 fb^{-1}. All of the data and simulations were processed using the 80X version of the CMS software. The analysis is performed using the MiniAOD processing of the single muon, electron muon, double muon and double electron streams. The event yields from each stream are summarized in terms of data period or "epoch" in Table 5.1 and 5.2.

Table 5.1: Data streams and event yields in Epoch B-G.

Data stream	No. of Events	Luminosity (fb^{-1})
Epoch B		
/SingleMuon/Run2016B-03Feb2017_ver2-v2/MINIAOD	153057533	
/SingleElectron/Run2016B-03Feb2017_ver2-v2/MINIAOD	237978795	
/MuonEG/Run2016B-03Feb2017_ver2-v2/MINIAOD	31630645	5.75
/DoubleMuon/Run2016B-03Feb2017_ver2-v2/MINIAOD	78121439	
/DoubleEG/Run2016B-03Feb2017_ver2-v2/MINIAOD	135727853	
Epoch C		
/SingleMuon/Run2016C-03Feb2017-v1/MINIAOD	64717887	
/SingleElectron/Run2016C-03Feb2017-v1/MINIAOD	93326612	
/MuonEG/Run2016C-03Feb2017-v1/MINIAOD	14782465	2.57
/DoubleMuon/Run2016C-03Feb2017-v1/MINIAOD	26691804	
/DoubleEG/Run2016C-03Feb2017-v1/MINIAOD	45523415	
Epoch D		
/SingleMuon/Run2016D-03Feb2017-v1/MINIAOD	96656522	
/SingleElectron/Run2016D-03Feb2017-v1/MINIAOD	146495180	
/MuonEG/Run2016D-03Feb2017-v1/MINIAOD	23211016	4.25
/DoubleMuon/Run2016D-03Feb2017-v1/MINIAOD	33279135	
/DoubleEG/Run2016D-03Feb2017-v1/MINIAOD	52423936	
Epoch E		
/SingleMuon/Run2016E-03Feb2017-v1/MINIAOD	87361180	
/SingleElectron/Run2016E-03Feb2017-v1/MINIAOD	113169792	
/MuonEG/Run2016E-03Feb2017-v1/MINIAOD	21705106	4.01
/DoubleMuon/Run2016E-03Feb2017-v1/MINIAOD	27025565	
/DoubleEG/Run2016E-03Feb2017-v1/MINIAOD	47328819	
Epoch F		
/SingleMuon/Run2016F-03Feb2017-v1/MINIAOD	65046116	
/SingleElectron/Run2016F-03Feb2017-v1/MINIAOD	70143285	
/MuonEG/Run2016F-03Feb2017-v1/MINIAOD	15897519	3.10
/DoubleMuon/Run2016F-03Feb2017-v1/MINIAOD	20178195	
/DoubleEG/Run2016F-03Feb2017-v1/MINIAOD	33972061	
Epoch G		
/SingleMuon/Run2016G-03Feb2017-v1/MINIAOD	147945188	
/SingleElectron/Run2016G-03Feb2017-v1/MINIAOD	152098594	
/MuonEG/Run2016G-03Feb2017-v1/MINIAOD	33572944	7.54
/DoubleMuon/Run2016G-03Feb2017-v1/MINIAOD	44581133	
/DoubleEG/Run2016G-03Feb2017-v1/MINIAOD	76538894	

Table 5.2: Data streams and event yields in Epoch H.

Data stream	No. of Events	Luminosity (fb^{-1})
Epoch H (V2)		
/SingleMuon/Run2016H-03Feb2017_ver2-v1/MINIAOD	166747359	
/SingleElectron/Run2016H-03Feb2017_ver2-v1/MINIAOD	123900492	
/MuonEG/Run2016H-03Feb2017_ver2-v1/MINIAOD	28042696	8.39
/DoubleMuon/Run2016H-03Feb2017_ver2-v1/MINIAOD	46809814	
/DoubleEG/Run2016H-03Feb2017_ver2-v1/MINIAOD	80546340	
Epoch H (V3)		
/SingleMuon/Run2016H-03Feb2017_ver3-v1/MINIAOD	4389901	
/SingleElectron/Run2016H-03Feb2017_ver3-v1/MINIAOD	3189661	
/MuonEG/Run2016H-03Feb2017_ver3-v1/MINIAOD	769984	0.22
/DoubleMuon/Run2016H-03Feb2017_ver3-v1/MINIAOD	1218668	
/DoubleEG/Run2016H-03Feb2017_ver3-v1/MINIAOD	2022709	

5.2 MC simulation

The simulated data samples used in this analysis were produced as a part of the Run II Summer16 MiniAOD v2 - PU Morond 17 simulation campaign which has the collective tag:

$*/RunIISummer16MiniAODv2-PUMoriond17\_80X\_mcRun2\_asymptotic\_2016\_TrancheIV\_v6-v1$.

The most important background process is top quark pair production with additional jets. Next in importance is the tW production of single top (ST) quark process. These are followed by $Z+$jets and $W+$jets electroweak processes (EW), where only the leptonic decay modes of the bosons are considered. Next are rare processes involving multiple top (anti-) quarks and a Z, W, or Higgs bosons, namely, $t\bar{t}+Z/W/H$. Finally, $t\bar{t}$ production

in association with diboson pairs, $t\bar{t}WW$, $t\bar{t}WZ$, $t\bar{t}ZZ$, $t\bar{t}WH$, $t\bar{t}ZW$, $t\bar{t}HH$, and triple top quark production ($t\bar{t}t$+jets and $t\bar{t}tW$) are considered. These processes are collectively labeled as ttXY.

The Monte Carlo (MC) event generators used to simulate these processes includes POWHEG [33, 34, 35, 36, 37], MADGRAPH5_aMC@NLO [20, 38] and PYTHIA 8.212 [39, 40], as indicated in their corresponding sample names. All of the simulated MC samples use the CUETP8M2T4 tune [41, 42] for the parton-shower (PS) and underlying event (UE) modeling, except for the Z+jets electroweak processes, which uses CUETP8M1 tune. For the samples with next-to-leading order (NLO) matrix elements (MEs), the NNPDF3.0NLO PDFs [43] are used, while for the samples with leading order (LO) matrix elements (MEs), the corresponding NNPDF3.0LO PDFs are used. The parton shower (PS), hadronization, and underlying event (UE) models implemented in PYTHIA 8.212 are used to simulate higher-order processes and nonperturbative aspects of pp collisions. The NLO simulations use strong coupling constant values of $\alpha_S(M_Z) = 0.137$ and $\alpha_S(M_Z) = 0.113$ for the ME and PS modeling, and LO simulations use $\alpha_S(M_Z) = 0.130$ for the ME. In all simulations involving the top quark, a mass m_t of 172.5 GeV is used.

The `/TTTo2L2Nu_HT500Njet7_TuneCUETP8M2T4_13TeV-powheg-pythia8` sample was produced with generator level selection criteria to increase MC statistics in signal sensitive region for a better modeling of the background distribution, these criteria are: $HT_{\text{genjets}} \geq 500$ GeV, $N_{\text{genjets}} \geq 7$, $N_{\text{genleps}} = 2$, where HT_{genjets} is the p_{T} sum of al the jets at generator level, N_{genjets} is the number of jets at generator level in the event, and N_{genleps} is the number of leptons at generator level in the event.

The simulated signal and background data samples are listed in Table 5.3, the samples used to add more statistics to $t\bar{t}$ MC background are listed in Table 5.4. Samples used to estimate systematic uncertainties of $t\bar{t}$ background are listed in Table 5.5

Table 5.3: Simulated data samples, cross sections and event yields used in this analysis

Sample	σ (pb)	No of events
/TTTT_TuneCUETP8M2T4_13TeV-amcatnlo-pythia8	0.009	2455793
/TT_TuneCUETP8M2T4_13TeV-powheg-pythia8	831.8	65832468
/ST_tW_antitop_5f_inclusiveDecays_13TeV-powheg-pythia8_TuneCUETP8M2T4	35.8	998254
/ST_tW_top_5f_inclusiveDecays_13TeV-powheg-pythia8_TuneCUETP8M2T4	35.8	992006
/DYJetsToLL_M-50_TuneCUETP8M1_13TeV-madgraphMLM-pythia8	5075.6	18496085
/ttHTobb_M125_TuneCUETP8M2_ttHtranche3_13TeV-powheg-pythia8	0.2934	3845797
/ttWJets_13TeV_madgraphMLM	0.611	6971708
/ttZJets_13TeV_madgraphMLM	0.783	10782305
/TTWH_TuneCUETP8M2T4_13TeV-madgraph-pythia8	0.001572	
/TTWW_TuneCUETP8M2T4_13TeV-madgraph-pythia8	0.007882	
/TTWZ_TuneCUETP8M2T4_13TeV-madgraph-pythia8	0.002974	99141
/TTZZ_TuneCUETP8M2T4_13TeV-madgraph-pythia8	0.001572	98706
/TTZH_TuneCUETP8M2T4_13TeV-madgraph-pythia8	0.01253	97849
/TTHH_TuneCUETP8M2T4_13TeV-madgraph-pythia8	0.0007408	99990
/TTTW_TuneCUETP8M2T4_13TeV-madgraph-pythia8	0.007882	97222
/TTTJ_TuneCUETP8M2T4_13TeV-madgraph-pythia8	0.0004741	96282

Table 5.4: Extra $t\bar{t}$ samples used in the analysis to gain more MC background statistics, together with the number of events processed

Sample	No of events
/TT_TuneCUETP8M2T4_mtop1665_13TeV-powheg-pythia8	
/TT_TuneCUETP8M2T4_mtop1695_13TeV-powheg-pythia8	
/TT_TuneCUETP8M2T4_mtop1715_13TeV-powheg-pythia8	
/TT_TuneCUETP8M2T4_mtop1735_13TeV-powheg-pythia8	
/TT_TuneCUETP8M2T4_mtop1755_13TeV-powheg-pythia8	
/TT_TuneCUETP8M2T4_mtop1785_13TeV-powheg-pythia8	192450826
/TT_widthx0p2_TuneCUETP8M2T4_13TeV-powheg-pythia8	
/TT_widthx0p5_TuneCUETP8M2T4_13TeV-powheg-pythia8	
/TT_widthx0p8_TuneCUETP8M2T4_13TeV-powheg-pythia8	
/TT_widthx2_TuneCUETP8M2T4_13TeV-powheg-pythia8	
/TT_widthx4_TuneCUETP8M2T4_13TeV-powheg-pythia8	
/TT_widthx8_TuneCUETP8M2T4_13TeV-powheg-pythia8	111017631
/TTTo2L2Nu_HT500Njet7_TuneCUETP8M2T4_13TeV-powheg-pythia8	9243099

Table 5.5: Simulated data samples used in the analysis to estimate systematic uncertainties of $t\bar{t}$ background.

Sample	No of events
/TT_TuneCUETP8M2T4_13TeV-powheg-isrdown-pythia8	22054069
/TT_TuneCUETP8M2T4_13TeV-powheg-isrup-pythia8	49345094
/TT_TuneCUETP8M2T4_13TeV-powheg-fsrdown-pythia8	28986893
/TT_TuneCUETP8M2T4_13TeV-powheg-fsrup-pythia8	29056947
/TT_TuneCUETP8M2T4up_13TeV-powheg-pythia8	27598563
/TT_TuneCUETP8M2T4down_13TeV-powheg-pythia8	29309800
/TTTT_TuneCUETP8M2T4_13TeV-amcatnlo-isrdown-pythia8	1490180
/TTTT_TuneCUETP8M2T4_13TeV-amcatnlo-isrup-pythia8	1466201
/TTTT_TuneCUETP8M2T4_13TeV-amcatnlo-fsrdown-pythia8	1402872
/TTTT_TuneCUETP8M2T4_13TeV-amcatnlo-fsrup-pythia8	1378414

Chapter 6

Event Selection and Corrections

The event selection in this analysis focuses on dilepton final states and follows the recommendations of the Top Quark Physics Analysis Group (PAG) [44]. The selections are applied to the objects whose definitions are provided by dedicated Physics Object Groups (POGs). Events from the whole datasets (data and simulation) are first filtered by dedicated HLT paths [45] which perform a preliminary selection of the events of interest. In this case events with at least two isolated energetic leptons are retained. The surviving events are then filtered using software that does a selection on the primary vertex filter, to clean the events of machine or reconstruction deficiencies. Next, the full ID and Isolation requirements for leptons are applied and the events containing two high p_{T} leptons (leading leptons) of opposite charges are selected. The pair is also required to lie outside of a Z boson mass window (76-106 GeV) if they have the same flavor. Subsequent selection imposes requirements the number of jets and b tagged jets. These are discussed in more detail later in this chapter.

6.1 High level trigger

Trigger selection for this analysis is targeted at the final states with opposite-sign $\mu^+\mu^-$, $\mu^\pm e^\mp$, or e^+e^- dilepton pairs arising in the decay chain of the $t\bar{t}$ system when both daughter $W^\pm$ bosons decay semi-leptonically. Dilepton events were recorded using either the single lepton or dilepton triggers. In the case of dilepton triggers, the p_{T} thresholds for leading and sub-leading leptons for dimuon triggers are 17 GeV and 8 GeV, respectively. For dielectron triggers these are 23 GeV and 12 GeV, and for muon-electron triggers these are 23 and 8 GeV, regardless of the lepton flavor. The single-lepton triggers were used to increase the acceptance of offline event selection. This is necessary because a decrease of signal over noise ratio associated to loss of tracking has been observed in the tracker system affecting data during B to F data epochs. The single-lepton triggers add about 20% to the acceptance. Since the dilepton-trigger paths for the $\mu\mu$ and $e\mu$ triggers used in epochs B-G are prescaled in epoch H, dedicated trigger paths with the dz cut are used for epoch H. The full set of trigger paths is listed in Table 6.1, where M denotes single muon, E denotes single electron, MM denotes dimuon, ME denotes muon-electron and EE denotes dielectron.

The selection logic for simulated MC events is a simple "OR" of the trigger paths. An event is selected if it passes at least one of the trigger paths. For the data, an exclusive "OR" is used to avoid double counting. The detailed selection logic for each final state is listed in Table 6.2

Table 6.1: HLT trigger paths used to select data events and the runs to which they are applied.

Trigger path name	Data Runs	Trigger type
HLT_Mu17_TrkIsoVVL_Mu8_TrkIsoVVL_v	B–G	MM
HLT_Mu17_TrkIsoVVL_TkMu8_TrkIsoVVL_v	B–G	MM
HLT_Mu17_TrkIsoVVL_Mu8_TrkIsoVVL_DZ_v	H	MM
HLT_Mu17_TrkIsoVVL_TkMu8_TrkIsoVVL_DZ_v	H	MM
HLT_Mu23_TrkIsoVVL_Ele8_CaloIdL_TrackIdL_IsoVL_v	B–G	ME
HLT_Mu8_TrkIsoVVL_Ele23_CaloIdL_TrackIdL_IsoVL_v	B–G	ME
HLT_Mu23_TrkIsoVVL_Ele8_CaloIdL_TrackIdL_IsoVL_DZ_v	H	ME
HLT_Mu8_TrkIsoVVL_Ele23_CaloIdL_TrackIdL_IsoVL_DZ_v	H	ME
HLT_Ele23_Ele12_CaloIdL_TrackIdL_IsoVL_DZ_v	B–H	EE
HLT_IsoMu24_v	B–H	M
HLT_IsoTkMu24_v	B–H	M
HLT_Ele27_WPTigh_Gsf_v	B–H	E

Table 6.2: Trigger logic in data event selection.

Channel	Dataset	Selection logic
$\mu\mu$	/DoubleMuon	MM
	/SingleMuon	M && !MM
$e\mu$	/MuonEG	ME
	/SingleMuon	M && !ME
	/SingleElectron	E && !M && !ME
ee	/DoubleEG	EE
	/SingleElectron	E && !EE

6.2 Object selection

6.2.1 Muon

The muon objects [46] used in this analysis are the isolated muons that are not identified as jets. These meet the standard *loose muon* identification criteria provided by the CMS Muon POG [47]. They are required to satisfy the following criteria:

- Is a PF muon reconstructed either as Global Muon or as a Tracker Muon
- $p_{\mathrm{T}} \geq 25\,\mathrm{GeV}$ (leading) or $p_{\mathrm{T}} \geq 20\,\mathrm{GeV}$ (trailing)
- $|\eta| < 2.4$
- Number of valid layer hits in the tracker > 5
- Number of hits in the muon stations > 0
- Transverse impact parameter of the muon with respect to the leading primary vertex < 0.2 cm
- Distance in z-dimension between the leading primary vertex the muon track < 0.5 cm
- Number of pixel hits > 0
- Normalized χ^2 of track < 10
- Number of matched muon stations > 1
- Relative Isolation (defined below), $I_{\mathrm{PF}}^{\mathrm{rel}} < 0.15$

The Particle-Flow based relative isolation of leptons is defined as of Equation. 6.1 with a cone of size $\Delta R < 0.4$ in (η-ϕ) space:

$$I_{\mathrm{PF}}^{\mathrm{rel}} = \frac{1}{p_{\mathrm{T}}^{\mu}} \left(\sum_{ch.had\,from\,PV} p_{\mathrm{T}} + \max \left(0, \sum_{photon} E_{\mathrm{T}} + \sum_{neut.had} E_{\mathrm{T}} - 0.5 \times \sum_{ch.had\,from\,PU} p_{\mathrm{T}} \right) \right) \tag{6.1}$$

The charged hadrons which are associated to non-primary vertices are removed when calculating the isolation. A $\Delta\beta$ correction factor, which corresponds approximately to the ratio of neutral particle to charged hadron in pp collisions, is applied for PU mitigation

to suppress the effect of the corresponding neutral particles from non-primary vertices. Since the ratio of charged to neutral energy is ≈ 0.5, the neutral energy from primary vertices in a jet is thus approximated as $\sum_{neut.had} E_{\mathrm{T}} - 0.5 \times \sum_{ch.had from\, PU} p_{\mathrm{T}}$. The max() function is used to ensure that the corrected neutral hadronic energy is never assigned a negative value. The isolation requirement will help select prompt muons with higher efficiency.

6.2.2 Electron

Cut-based electron identification with the versioned identification (VID) framework [48] is used in this analysis. This follows the recommendation of CMS Electron/γ POG [49]. Different electron ID working points (WP) are available based on the selection criteria, as shown in Table 6.3 and Table 6.4. The loose WP is selected for use in this analysis due to rather low event statistics. Besides the loose WP selection criteria, electron candidates are also required to satisfy the impact parameter cuts shown in Table 6.5, in addition to $p_{\mathrm{T}} \geq 25\,\mathrm{GeV}$ for the leading electron and $p_{\mathrm{T}} \geq 20\,\mathrm{GeV}$ for the trailing electron, and $|\eta| < 2.4$. Electrons with η values corresponding to the detector-absence gap between the ECAL barrel and the endcap ($1.4442 < |\eta| < 1.566$) are excluded. The veto WP electrons are used to reject events containing more than two leptons.

6.2.3 Jets

The reconstructed jets are required to satisfy the standard *Loose Jet* identification criteria provided by the CMS Jet and Missing $\mathrm{E_T}$ (JME) POG [50] to be used in this analysis. Jets are retained if they satisfy $|\eta| < 2.4$ and $p_{\mathrm{T}} > 30\,\mathrm{GeV}$. Jets that are also

Table 6.3: The cut-based electron ID selection criteria for different WPs in barrel region, $|\eta| < 1.479$

Cuts in barrel region	Veto	Loose	Medium	Tight
full $5 \times 5\sigma_{i\eta i\eta}$ <	0.0115	0.011	0.00998	0.00998
$\lvert\Delta\eta_{in}^{seed}\rvert$ <	0.00749	0.00477	0.00311	0.00308
$\lvert\Delta\phi_{in}\rvert$ <	0.228	0.222	0.103	0.0816
$\frac{H}{E}$ <	0.356	0.298	0.253	0.0414
Rel. comb. PF iso with EA corr <	0.175	0.0994	0.0695	0.0588
$\left\lvert\frac{1}{E} - \frac{1}{p}\right\rvert$ <	0.299	0.241	0.134	0.0129
Expected missing Inner Hits <=	2	1	1	1
Pass conversion Veto	yes	yes	yes	yes

Table 6.4: The cut-based electron ID selection criteria for different WPs in endcap region, $|\eta| > 1.479$

Cut in endcap region	Veto	Loose	Medium	Tight
full $5 \times 5\sigma_{i\eta i\eta}$ <	0.037	0.0314	0.0298	0.0292
$\lvert\Delta\eta_{in}^{seed}\rvert$ <	0.00895	0.00868	0.00609	0.00605
$\lvert\Delta\phi_{in}\rvert$ <	0.213	0.213	0.045	0.0394
$\frac{H}{E}$ <	0.211	0.101	0.0878	0.0641
Rel. comb. PF iso with EA corr <	0.159	0.107	0.0821	0.0571
$\left\lvert\frac{1}{E} - \frac{1}{p}\right\rvert$ <	0.15	0.14	0.13	0.0129
Expected missing Inner Hits <=	3	1	1	1
Pass conversion Veto	yes	yes	yes	yes

Table 6.5: Impact parameter cuts for the cut-based electron ID in barrel region and endcap region.

	barrel (cm)	endcap (cm)
d_0 <	0.05	0.10
d_z <	0.10	0.20

reconstructed as leptons are excluded by requiring that each jet is separated from the nearest reconstructed loose working point lepton by $\Delta R > 0.3$. Table 6.6 shows the loose PF jets

identification requirements.

Table 6.6: Loose PF jet ID requirements for $\eta < 2.7$

Neutral Hadron Fraction	< 0.99
Neutral EM Fraction	< 0.99
Number of Constituents	> 1
Charged Hadron Fraction	> 0
Charged Multiplicity	> 0
Charged EM Fraction	< 0.99

6.2.4 *b*-tagged jets

The *b*-tagged jets (*b* jets) are the jets originating from the fragmentation and hadronization of b quarks. They pass the basic jet selection criteria with the additional requirement that the jet is tagged with a discriminant value by the Combined Secondary Vertex v2 (CSVv2) algorithm [51]. The *medium* and *loose* working points tagged jets are used in this analysis. For these the corresponding discriminant values are larger than 0.8484 and 0.5426, respectively. In this analysis the *medium* WP is used for *b* jet identification with a misidentification rate of approximately 10% for light-quark and gluon jets and a *b* tagging efficiency of about 70%, the *loose* WP is used as an input variable for event level discriminant as described in section 8.

6.3 Baseline event selection

A *baseline selection* is performed on the events passing the single- and multi-lepton triggers listed above. First, only events with a well reconstructed primary vertex are selected. The primary is required to have at least five degrees of freedom, $d_z < 24$ cm

and $d_{xy} < 2$ cm, where d is the longitudinal or transversal distance to the CMS coordinate system origin.

As this analysis focuses on the $\mu^+\mu^-$, $e^\pm\mu^\mp$, and e^+e^- channels, events containing a single oppositely charged pair of leptons defined above are selected using the criteria listed below. Events in which the lepton pair consists of two leptons of the same species, pairs originating from the decay of a Z-boson are rejected by applying a Z-veto cut, where the events lying within 30 GeV of the Z-boson invariant mass (76 to 106 GeV window) are excluded. Events originating from the decay of low mass resonances are also excluded by requiring that the invariant mass be greater than 20 GeV.

The event selection criteria are:

$\mu\mu$ **channel**:

- Exactly one opposite sign loose muon pair
- No additional muons or electrons passing the loose ID criteria
- The pair invariant mass must lie outside of the Z mass window (76 to 106 GeV) and have an invariant mass greater than 20 GeV
- A minimum of 4 jets, with $p_{\mathrm{T}} > 30$ GeV if they are not tagged as b jets
- Of the selected jets there should be at least 2 with $p_{\mathrm{T}} > 25$ GeV which pass the CSVv2M b-tagging criterion
- H_{T}, defined as scalar sum of all jet p_{T}, greater than 500 GeV

$e\mu$ **channel**:

- Exactly one opposite sign lepton pair consisting of a loose electron and a loose muon
- No additional muons or electrons passing the loose ID criteria
- A minimum of 4 jets with $p_{\mathrm{T}} > 30\,\mathrm{GeV}$ if they are not tagged as b jets
- Of the selected jets there should be at least 2 with $p_{\mathrm{T}} > 25\,\mathrm{GeV}$ which pass the CSVv2M b-tagging criterion
- $H_{\mathrm{T}} > 500\,\mathrm{GeV}$

ee **channel**:

- Exactly one opposite sign loose electron pair
- No additional muons or electrons passing the loose ID criteria
- The pair invariant mass must lie outside of the Z mass window (76 to 106 GeV) and have an invariant mass greater than 20 GeV
- A minimum of 4 jets with $p_{\mathrm{T}} > 30\,\mathrm{GeV}$ if they are not tagged as b jets
- Of the selected jets there should be at least 2 with $p_{\mathrm{T}} > 25\,\mathrm{GeV}$ which pass the CSVv2M b-tagging criterion
- $H_{\mathrm{T}} > 500\,\mathrm{GeV}$

The events passing this selection define the control samples which are used to validate the simulated samples and to provide the input samples for the analysis.

6.4 Event corrections

To better match simulated data and really data or correct for detector response, corrections are applied to either simulated events or real data events, or both. These are listed below:

6.4.1 Pile-up Reweighting

Since MC samples were produced before the real data taking, they are generated with number of pile-up interactions distribution that roughly covers, but does not exactly match the conditions of the real data-taking. To factorize this effect, the number of pile-up interactions from the MC simulation truth is reweighted to match the pile-up distribution for data. This is computed assuming a total pp inelastic cross-section of 69.2 mb for the 2016 data-taking period [52].

6.4.2 Lepton Corrections

In order to correct the difference between leptons reconstruction and selection efficiencies in data and simulation, lepton scale factors (SF) were applied to the simulation. They are defined as

$$SF = \frac{\epsilon_{data}}{\epsilon_{MC}} \tag{6.2}$$

and they are measured for the tracking, identification, isolation and trigger selection efficiencies as a dependent of both p_{T} and η. The overall lepton scale factor is given as

$$w_{overall} = SF_{id}(p_{\mathrm{T}}, \eta) SF_{iso}(p_{\mathrm{T}}, \eta) SF_{trig}(p_{\mathrm{T}}, \eta) SF_{track}(\eta) \tag{6.3}$$

where SF_{id} is identification scale factor, SF_{iso} is isolation scale factor, SF_{trig} is trigger efficiency scale factor, and SF_{track} is tracking efficiency scale factor. This is used to reweight each event in the simulation. The identification and isolation efficiencies are provided by the Muon Physics Object Group (POG) [47] and Electron/γ POG [49]. Electron reconstruction efficiency is taken into consideration as suggested by Electron/γ POG [49]. The scale factors of dilepton trigger efficiency are taken from [53] as a function of lepton transverse momentum and pseudorapidity.

6.4.3 Jet Energy Corrections

The detector response to particles is not linear and therefore it is not straightforward to translate the measured jet energy to the true particle or parton energy. Jet energy corrections are applied to map the measured jet energy deposition to the particle-level jet energy. The measured energy of the jets is corrected through two contributions: scale and resolution [54].

The scale of the jet energy is corrected in a factorized approach: L1 pile-up correction is to remove the energy coming from pile-up events, L2 relative is to correct jet dependence of η, L3 Absolute is to correct jet dependence of p_{T}, and the L2L3 residuals are to correct for remaining small differences (of the order of %) within jet response in data and MC. The set of corrections provided by JMET POG, labelled Summer16 23Sep2016V4, were applied to both MC and data, with the additional residual corrections applied only to data.

The jet energy resolution (JER) in data is worse than in the simulation, thus the reconstructed jets in simulation are smeared so that their p_{T} resolution matches the

one observed in data. If a matching particle-level jet is found, the four-momentum of the reconstructed jet is rescaled with a factor

$$c_{\mathrm{JER}} = 1 + (s_{\mathrm{JER}} - 1)\,\frac{p_{\mathrm{T}} - p_{\mathrm{T}}^{ptcl}}{p_{\mathrm{T}}} \tag{6.4}$$

where p_{T} is its transverse momentum, p_{T}^{ptcl} is the transverse momentum of the corresponding jet clustered from generator-level particles, and s_{JER} is the data-to-simulation scale factor. Otherwise the jet four-momentum is rescaled with a factor

$$c_{\mathrm{JER}} = 1 + \mathcal{N}(0, \sigma_{\mathrm{JER}})\sqrt{max(s_{\mathrm{JER}}^2 - 1, 0)} \tag{6.5}$$

where σ_{JER} is the relative p_{T} resolution in simulation, $\mathcal{N}(0, \sigma)$ denotes a random number sampled from a normal distribution with a zero mean and variance σ^2.

6.4.4 *b*-jet Reweighting

Significant differences exist between the b-tagging efficiencies measured by the BTV-POG [55] in data and those predicted by simulation[56]. The shape of the CSV discriminator value distribution needs to be corrected. A per-jet scale factor which is a function of CSV value, p_{T}, and η, is derived for each jet flavor as seen in equation 6.6.

$$SFjet_{\mathrm{B}}\,(\mathrm{CSV}, p_{\mathrm{T}}, \eta) = \frac{\mathrm{Data} - \mathrm{MC_A}}{\mathrm{MC_B}} \tag{6.6}$$

where A and B represent heavy flavour and light flavour or vice versa. For this method, the jet flavors are defined as heavy for bottom quarks and light for u, s, d, g whilst c-quarks are given $SF = 1$. An event weight is determined by taking the product of the per-jet scale factors, as shown in equation 6.7.

$$w_{\mathrm{total}} = \prod_{i}^{N_{\mathrm{j}}} SFjet_i \tag{6.7}$$

6.4.5 Top p_{T} Reweighting

The shape of the p_{T} spectrum of the individual top quarks in data is softer than predicted by the various simulations [57]. A strategy to deal with this discrepancy was derived from the differential p_{T} measurements. From the comparison of the data and simulation a scale factor is derived which can be applied to the POWHEG+PYTHIA8 value of the top p_{T}:

$$SF\left(p_{\mathrm{T}}\right) = \exp\left(0.0615 - 0.0005 p_{\mathrm{T}}\right) \tag{6.8}$$

The weight for a $t\bar{t}$ event is then defined as:

$$w = \sqrt{SF\left(p_{\mathrm{T}}, t\right) SF\left(p_{\mathrm{T}}, \bar{t}\right)} \tag{6.9}$$

6.4.6 Jet multiplicity correction

It has been shown [58] that there is an increasing trend of discrepancy of $t\bar{t}$ event yields between data and $t\bar{t}$ POWHEG predictions with respect to jet multiplicities, as shown in Figure 6.1 [58]. This is arising from the combination of the limited accuracy of the PYTHIA parton shower model and the lack of cross section calculations beyond NLO, both of which affect the region of the jet multiplicity.

In this analysis the same type of disagreement between the same dataset and simulation as a function of the jet multiplicity exists. Although the discrepancy is within uncertainties, this analysis focuses on very high jet multiplicity bins and it could significantly affect the background prediction from simulation. Jet multiplicity dependent corrections are applied to correct for this. The correction factors are determined from the postfit values

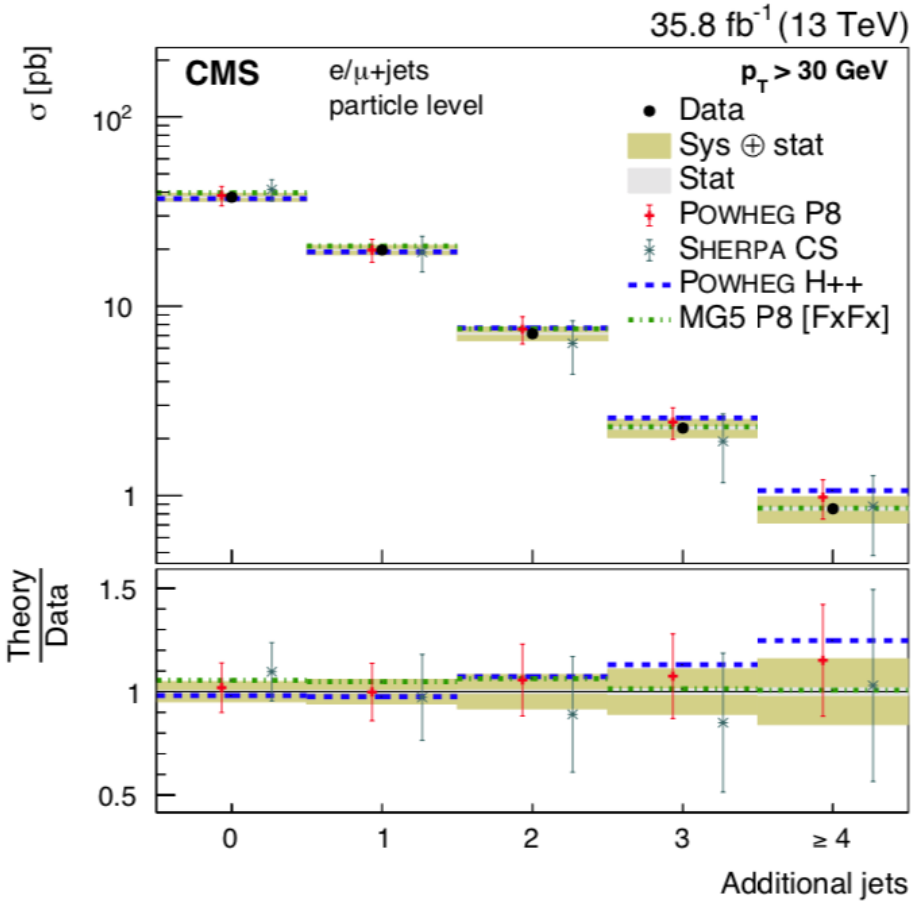

Figure 6.1: Absolute cross sections of jet multiplicities for jets with $p_{\mathrm{T}} > 30$ GeV. The data are shown as points with light (dark) bands indicating the statistical (statistical and sysstematic) uncertainties. The cross sections are compared to the predictions of POWHEG combined with PYTHIA8 (P8) or HERWIG++ (H++) and the multiparton simulations MG5 aMC@NLO (MG5)+PYTHIA8 FxFx and SHERPA. The ratios of the predictions to the measured cross sections are shown at the bottom of each panel.

of the floating parameter for these jet multiplicity categories by fitting data to SM predicted simulation in the control regions, and are shown in table 6.7

Table 6.7: Normalisation correction factors for different jet multiplicities.

Jet multiplicity category	normalisation correction factor	uncertainty
6	0.81	0.01
7	0.73	0.01
8+	0.73	0.07

Chapter 7

Data and Simulation Agreement

In this chapter the level of agreement between data and simulations after applying the selection criteria and corrections 6 is discussed.

To correctly match with simulations to experimental data, all the simulation samples are rescaled to the the same integrated luminosity as data, 35.8 fb^{-1}, with a scale factor:

$$SF_{lumi} = \frac{L_{Data}}{L_{Simulation}} \tag{7.1}$$

From Eq. 3.3, one can derive

$$L_{Simulation} = \frac{N_{Simulation}}{\sigma_{Simulation}} \tag{7.2}$$

where N denotes total number of events in the sample and σ denotes the cross-section value of the corresponding process. The aMC@NLO generator utilizes negatively weighted events to remove double counting of events between the lower and higher order QCD diagrams. Thus luminosity for samples generated with aMC@NLO is calculated with effective number

of events

$$N_{Simulation}^{Effective} = N_{Simulation}^{Positively\ weighted} - N_{Simulation}^{Negatively\ weighted} \tag{7.3}$$

7.1 Stitch Method

Two POWHEG $t\bar{t}$ samples were generated. The original inclusive sample and a filtered sample in which generator level selections ($N_{\text{genjet}} \geq 7$, $HT_{\text{genjets}} \geq 500\,\text{GeV}$ and $N_{\text{genleps}} = 2$) were applied to restrict the simulation to the large jet multiplicity region, most relevant to the analysis. The samples were 'stitched' together by rejecting events from inclusive sample that passed the generator level requirements of the filtered sample and by adding the events from the filtered sample with appropriate weights (see below).

When there was just the inclusive $t\bar{t}$ sample, we use the following weight for MC normalization:

$$n_i = N_i^{inc} \times \frac{\mathcal{L}^{data}}{\mathcal{L}^{inc}} = N_i^{inc} \times SF_1 = (N_i^{inc,veto} + N_i^{inc,filt}) \times SF_1 \tag{7.4}$$

where n_i is the number of weighted MC events in the histogram bin i; N_i^{inc} is the number of MC events in bin i that passed baseline selection; $N_i^{inc,veto}$ are the number of baseline selected MC events from inclusive sample that do not pass the generator level cuts, $N_i^{inc,filt}$ are the number of baseline selected MC events from inclusive sample that pass the generator level cuts. We replace the statistically limited events of $N_i^{inc,filt}$ with the filtered sample MC events $N_i^{new,filt}$ that passed baseline selection.

Denoting the filter efficiency by ϵ and taking into account that

$$\frac{N_i^{inc,filt}}{\epsilon N_{tot}^{inc}} = \frac{N_i^{new,filt}}{N_{tot}^{filt}} \tag{7.5}$$

where $N_{tot}^{inc/filt}$ is the total number of events originally produced in the inclusive/filtered sample. So we have

$$n_i = SF_1 \times (N_i^{inc,veto} + N_i^{inc,filt}) \tag{7.6}$$

$$= SF_1 \times (N_i^{inc,veto} + \frac{\epsilon N_{tot}^{inc}}{N_{tot}^{filt}} \times N_i^{new,filt}) \tag{7.7}$$

$$= SF_1 \times N_i^{inc,veto} + SF_2 \times N_i^{new,filt} \tag{7.8}$$

Therefore the normalization scale factors to be applied to the inclusive sample events after cutting off $N_i^{inc,filt}$ events is

$$SF_1 = \frac{\mathcal{L}^{data}}{\mathcal{L}^{inc}}, \tag{7.9}$$

and to the baseline selected filtered sample events is

$$SF_2 = \frac{\mathcal{L}^{data}}{\mathcal{L}^{inc}} \times \frac{\epsilon N_{tot}^{inc}}{N_{tot}^{filt}}. \tag{7.10}$$

7.1.1 Combined Sample Cross Checks

Here we compare distributions of generator level variables between the stitched and the original samples to verify the correctness of the stitching. Figure 7.1 and 7.2 show that normalization of the stitched sample is correctly handled according to formula above. Besides, plots show that statistical uncertainty in the tails is roughly 3 times smaller since we have about 10 times larger statistics from the filtered sample.

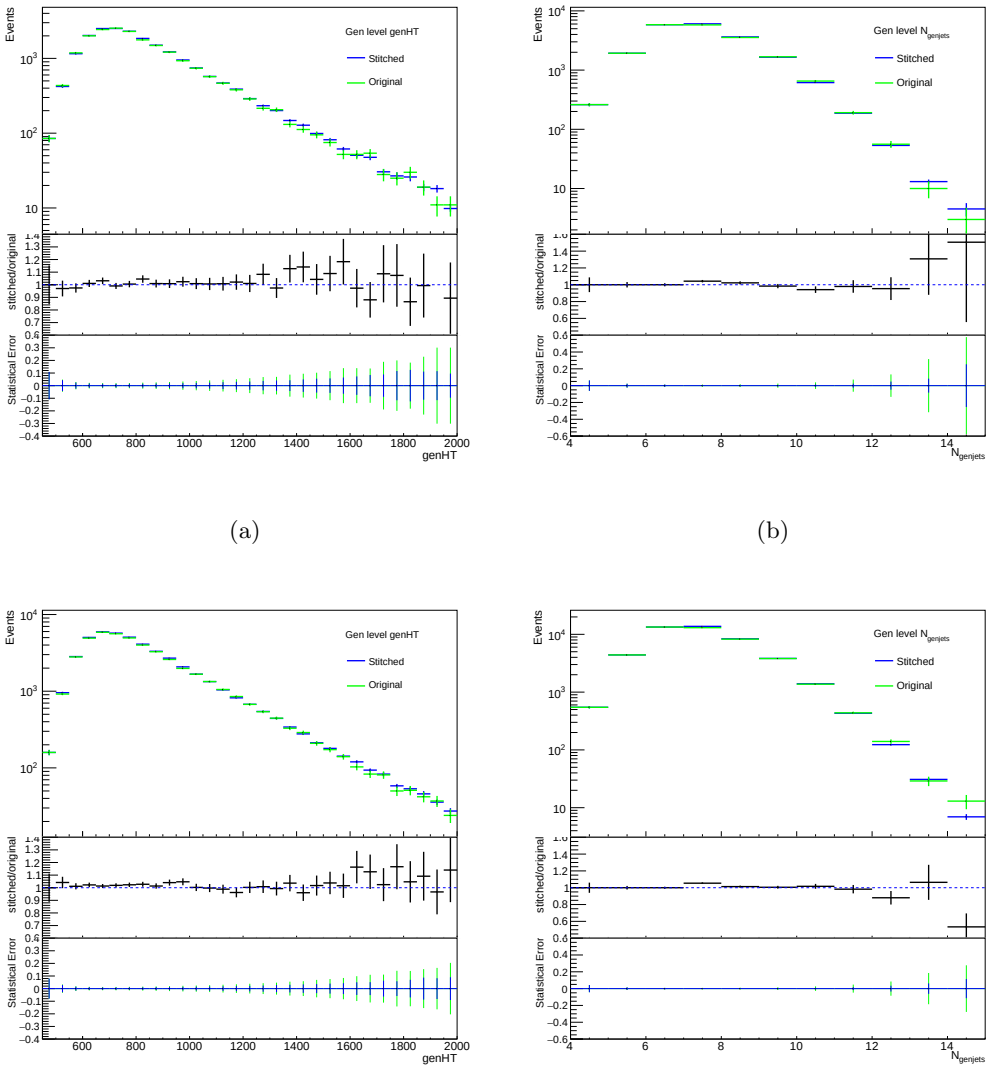

(a) (b)

(c) (d)

Figure 7.1: Comparison of generator level HT_{genjets} and jet multiplicity in $\mu\mu$ channel (upper row) and $e\mu$ channel (lower row) between original and combined samples

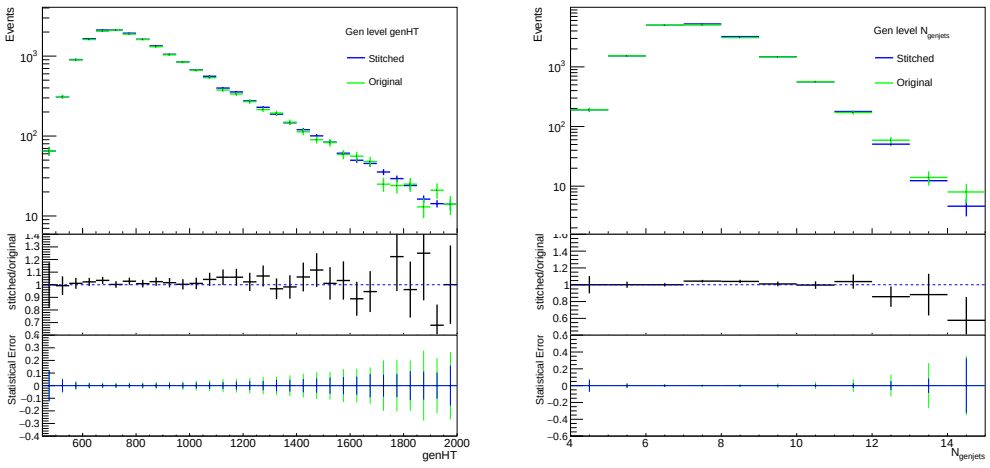

(a) (b)

Figure 7.2: Comparison of generator level HT_{genjets} and jet multiplicity in ee channel between original and combined samples

7.2 Pre-fit Control Distributions

Figs 7.3 to 7.17 show the inclusive pre-fit control distributions of the kinematics in the $\mu^+\mu^-, e^\pm\mu^\mp$ and e^+e^- channels. In all cases good agreement within the prefit uncertainty is observed between the observed and predicted distributions.

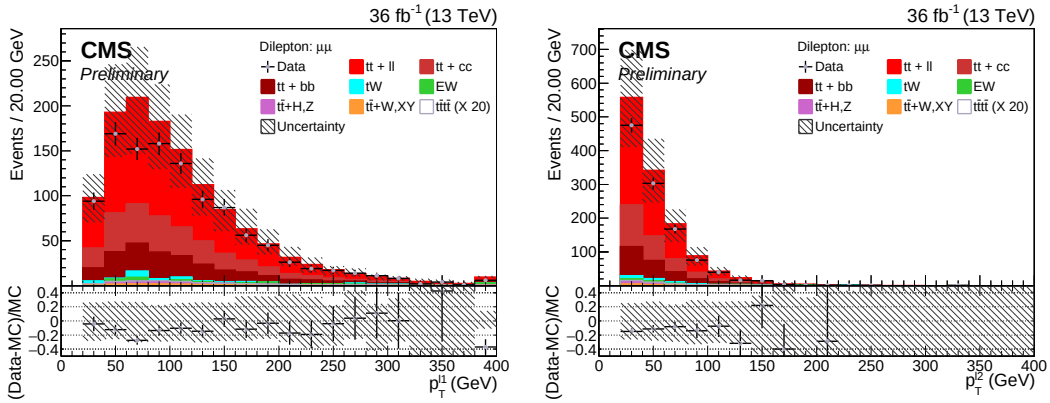

(a) (b)

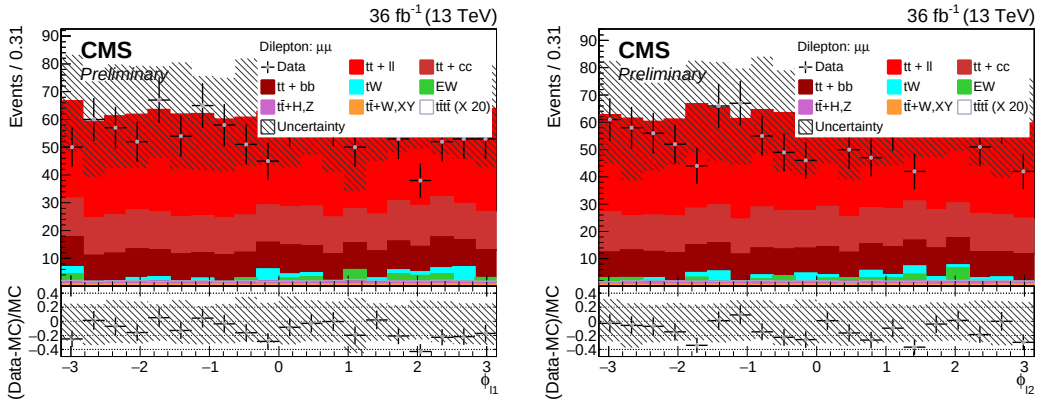

(c) (d)

Figure 7.3: Distributions of lepton kinematics in ($\mu\mu$ channel).

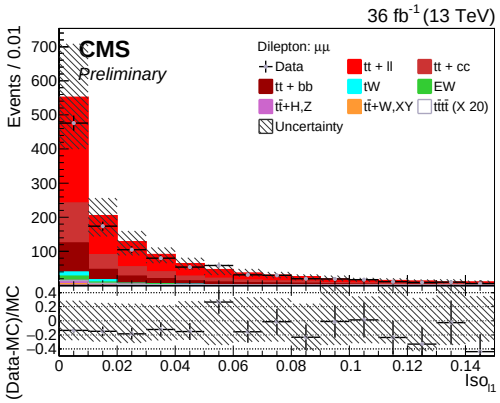

(a)

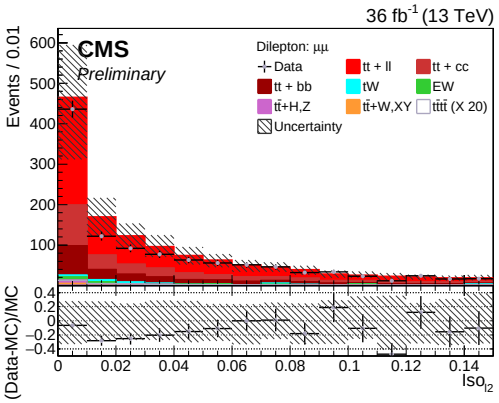

(b)

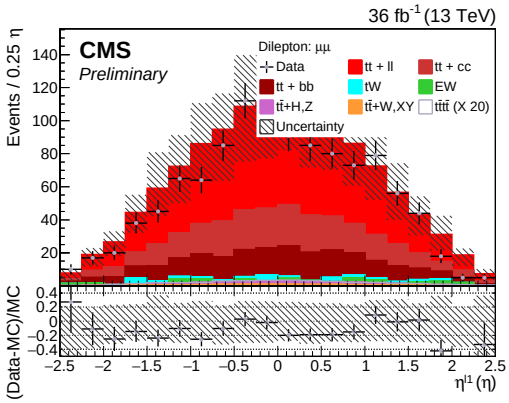

(c)

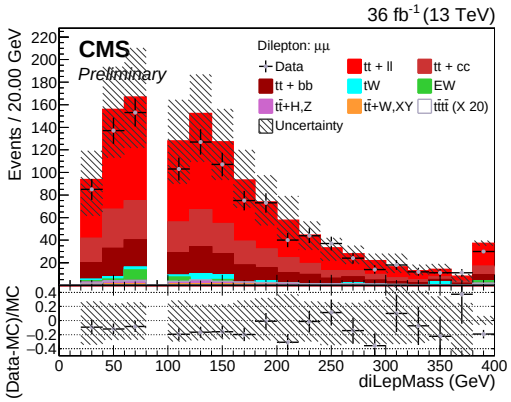

(d)

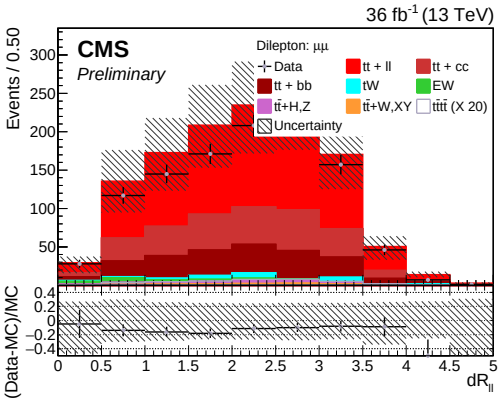

(e)

Figure 7.4: Distributions of lepton kinematics in ($\mu\mu$ channel).

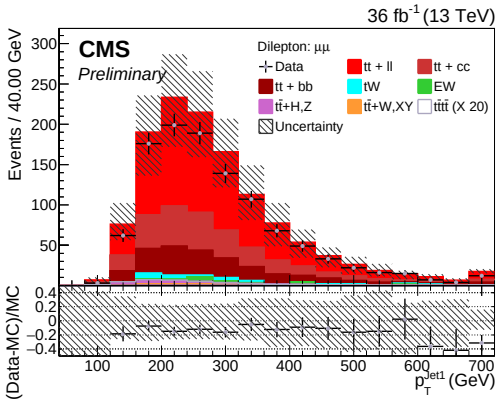

(a)

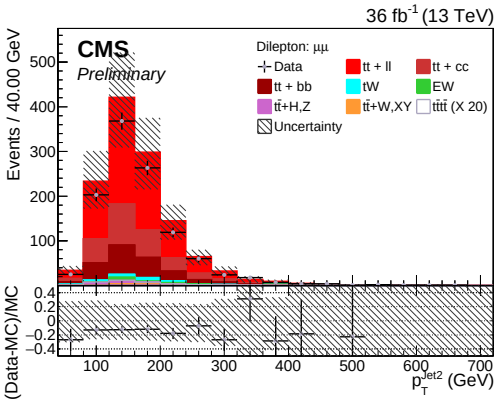

(b)

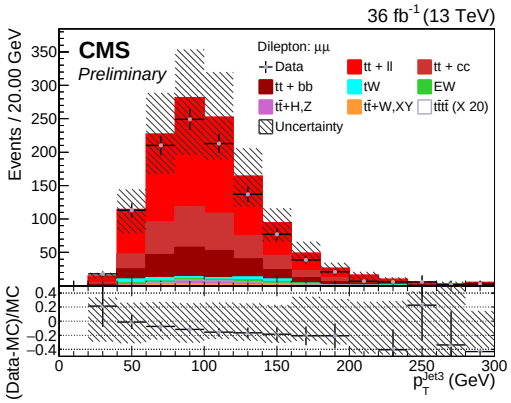

(c)

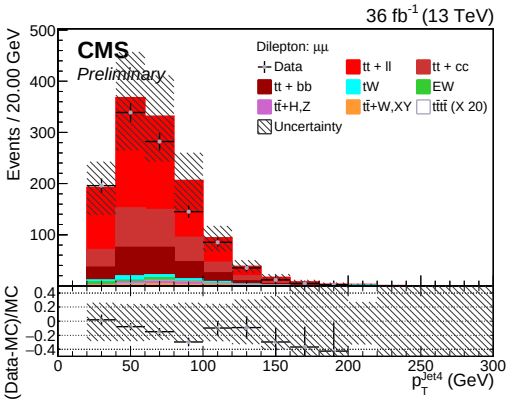

(d)

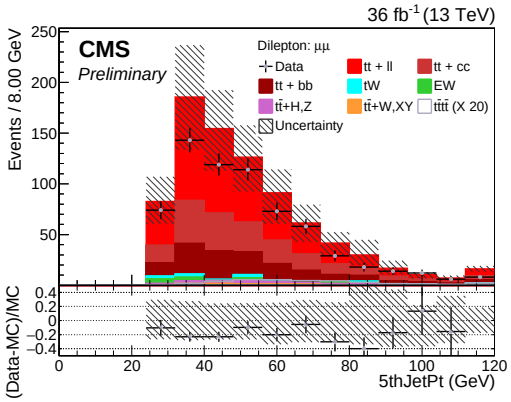

(e)

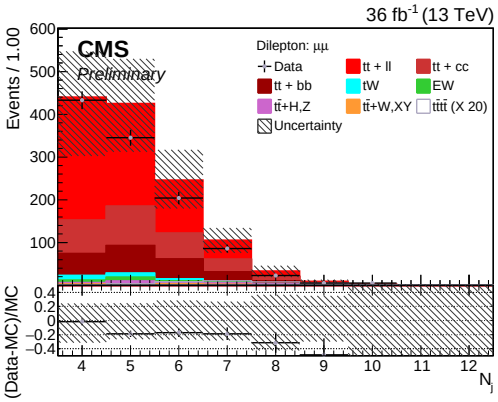

(f)

Figure 7.5: Distributions of jet kinematics in ($\mu\mu$ channel).

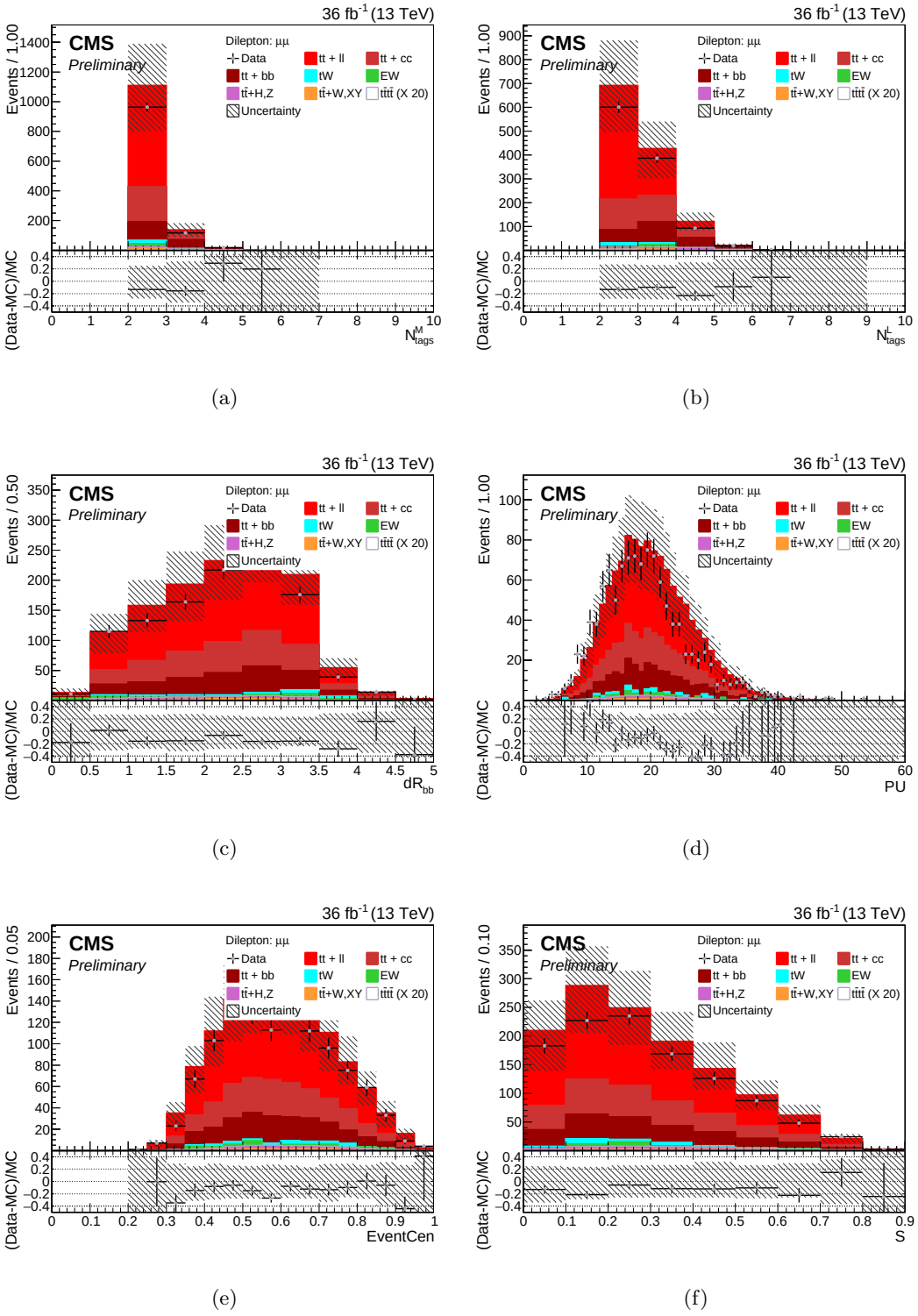

(a) (b)

(c) (d)

(e) (f)

Figure 7.6: Distributions of jet and event kinematics in ($\mu\mu$ channel).

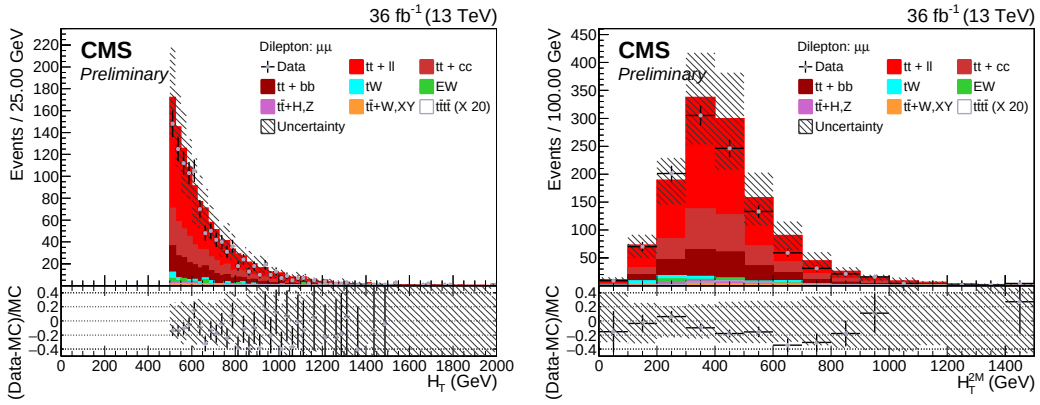

Figure 7.7: Distributions of event kinematics ($\mu\mu$ channel).

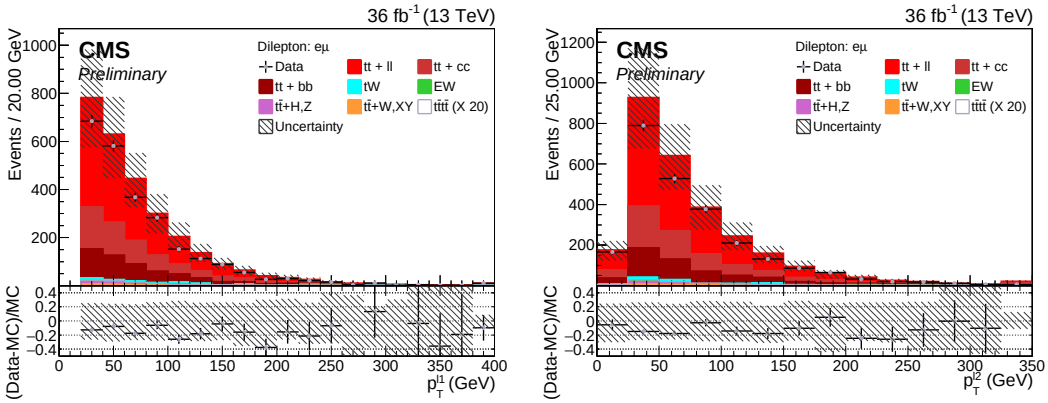

(a) (b)

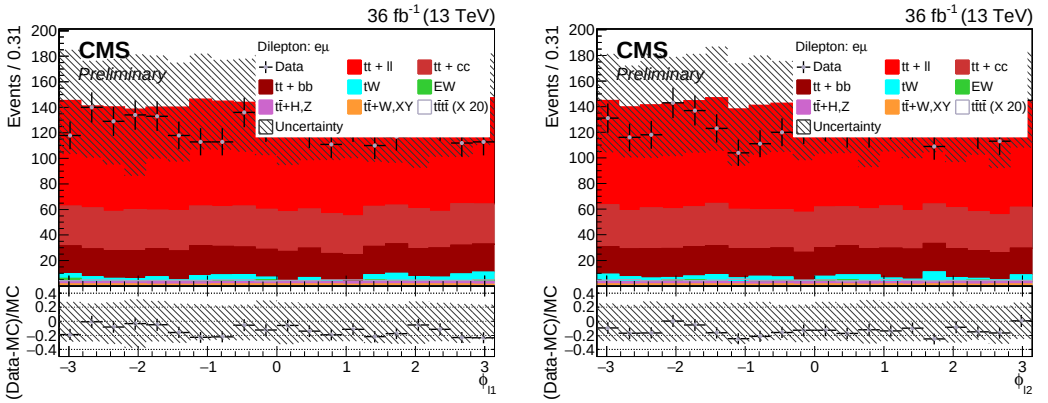

(c) (d)

Figure 7.8: Distributions of lepton kinematics in ($e\mu$ channel).

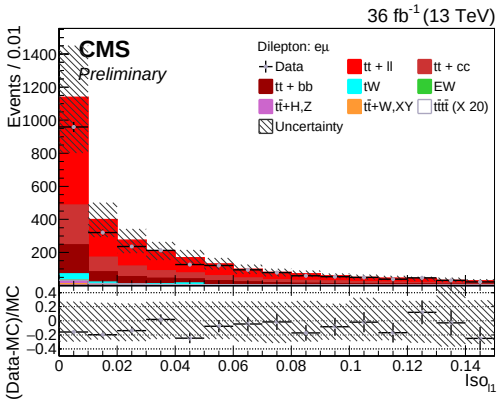

(a)

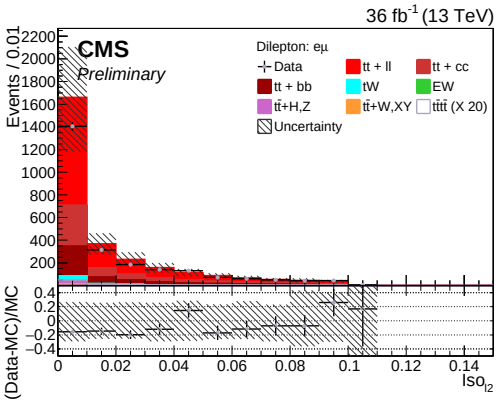

(b)

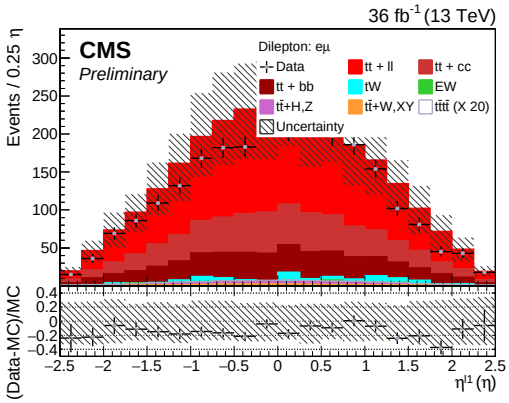

(c)

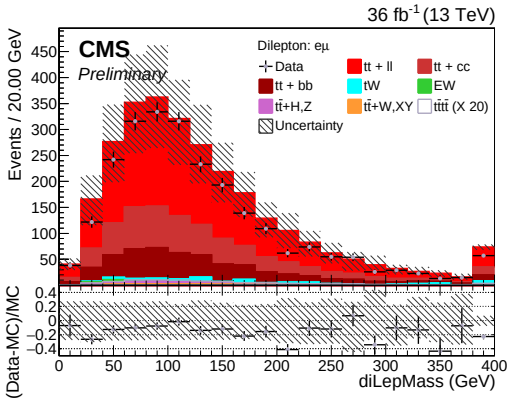

(d)

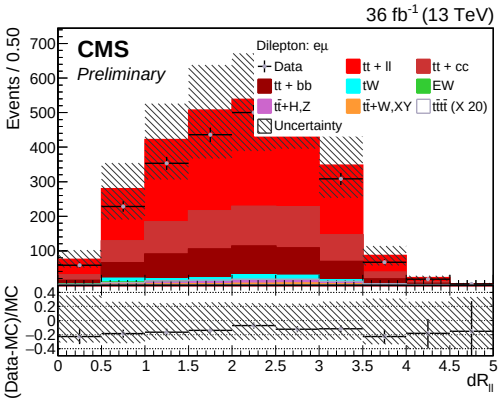

(e)

Figure 7.9: Distributions of lepton kinematics in ($e\mu$ channel).

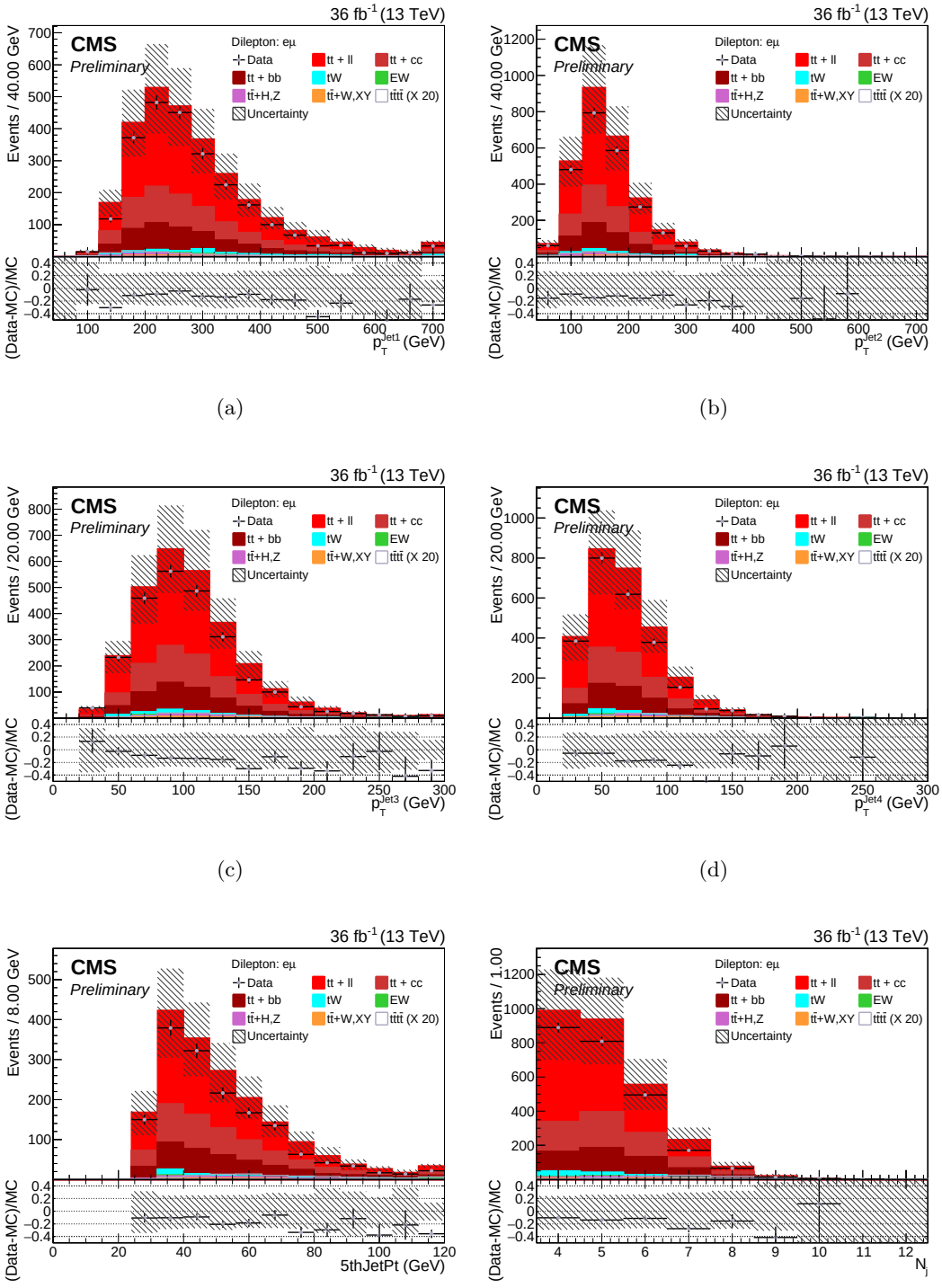

Figure 7.10: Distributions of jet kinematics in ($e\mu$ channel).

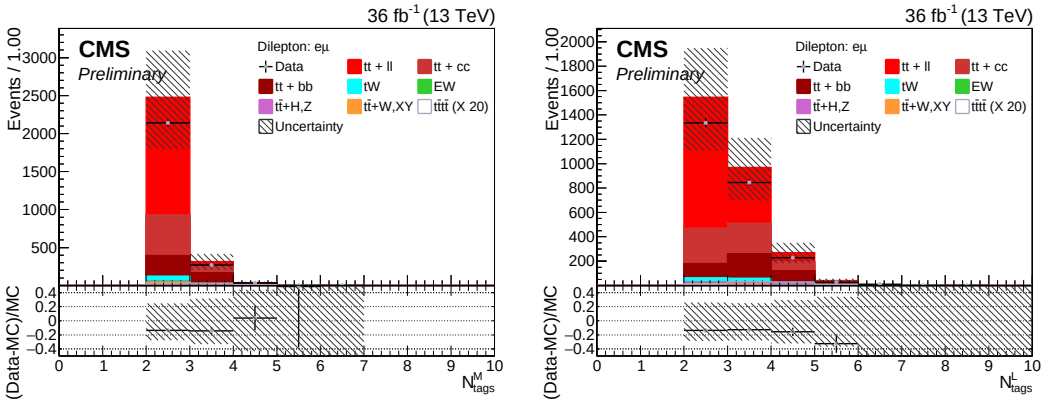

(a) (b)

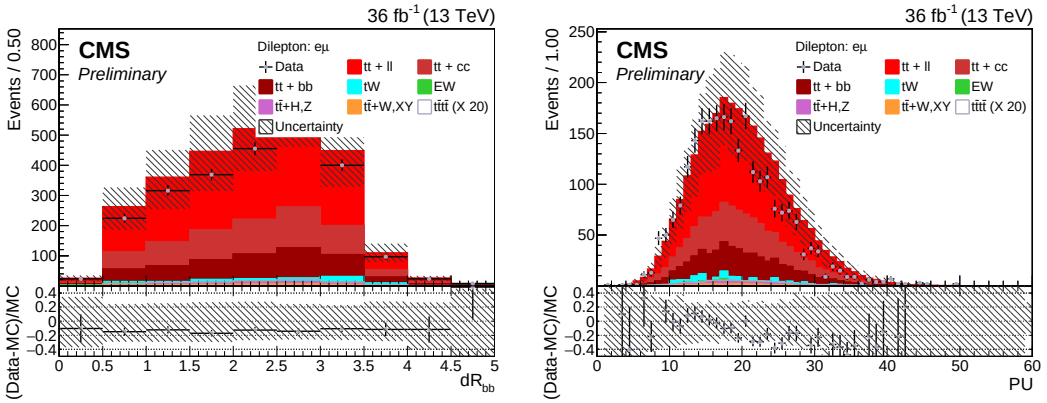

(c) (d)

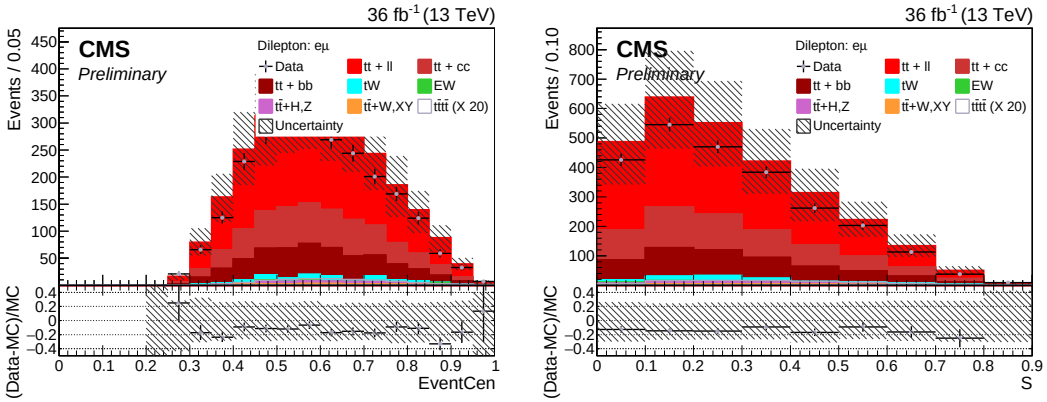

(e) (f)

Figure 7.11: Distributions of jet and event kinematics in ($e\mu$ channel).

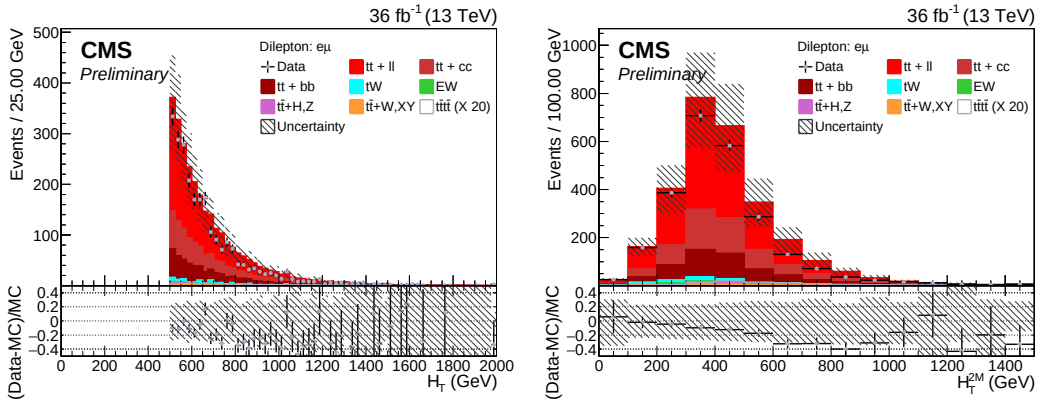

(a) (b)

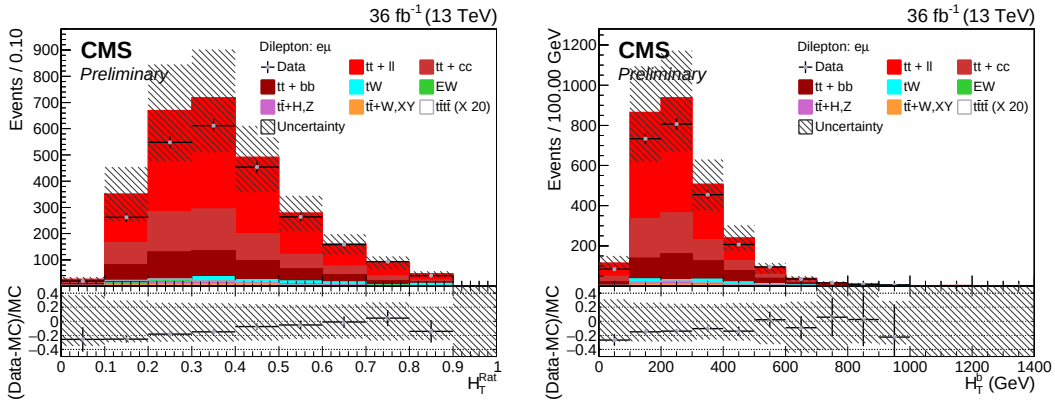

(c) (d)

Figure 7.12: Distributions of event kinematics ($e\mu$ channel).

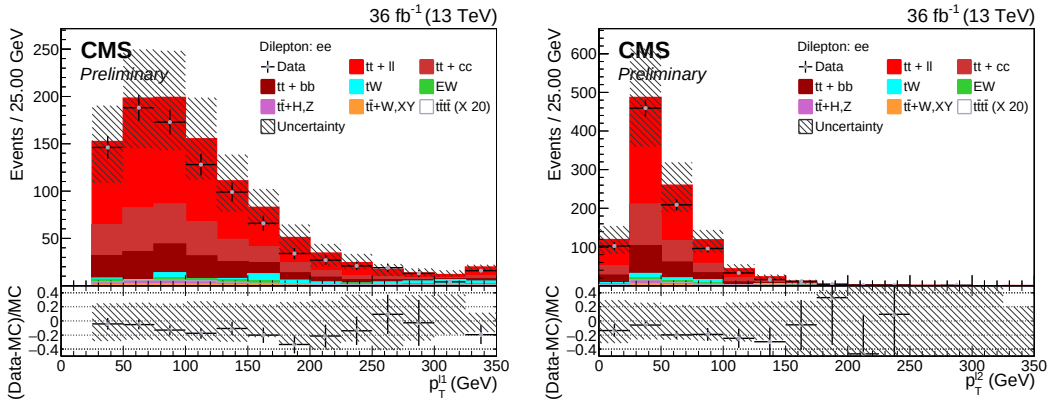

(a) (b)

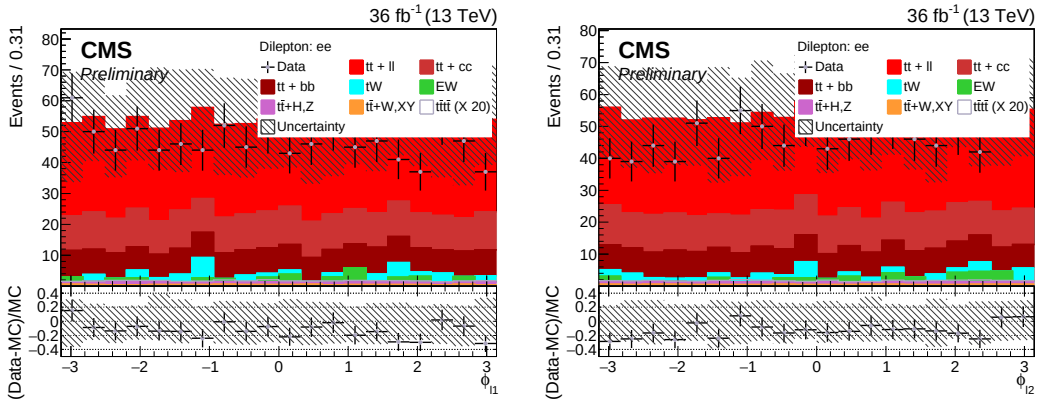

(c) (d)

Figure 7.13: Distributions of lepton kinematics in (ee channel).

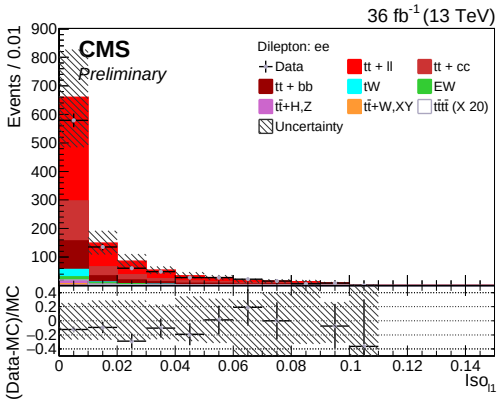

(a)

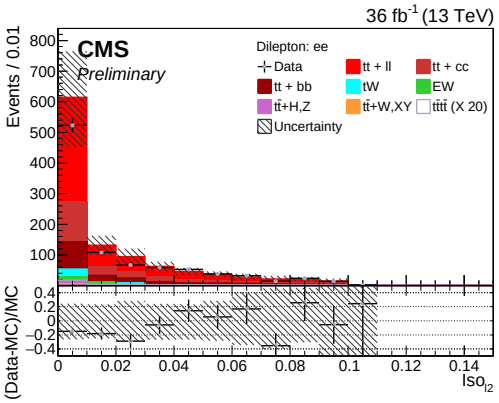

(b)

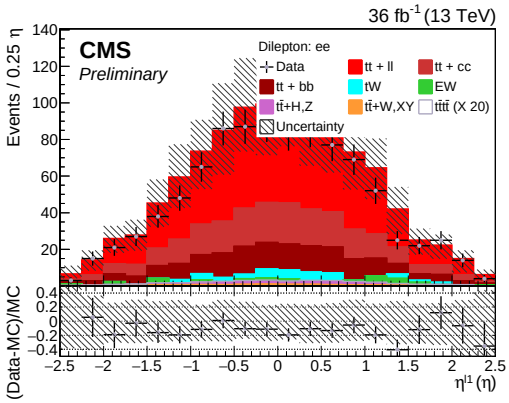

(c)

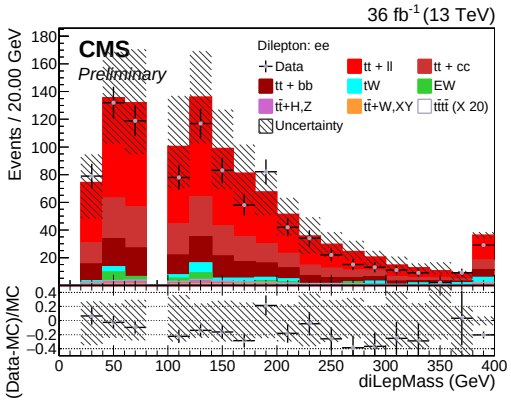

(d)

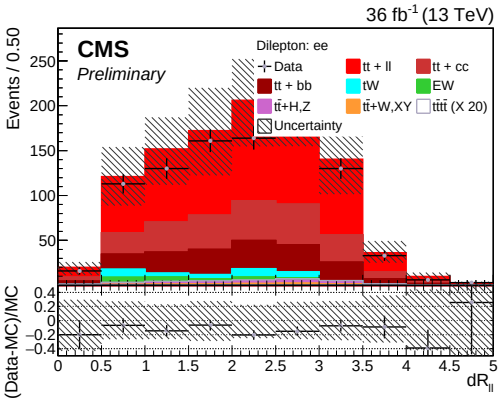

(e)

Figure 7.14: Distributions of lepton and event kinematics in (ee channel).

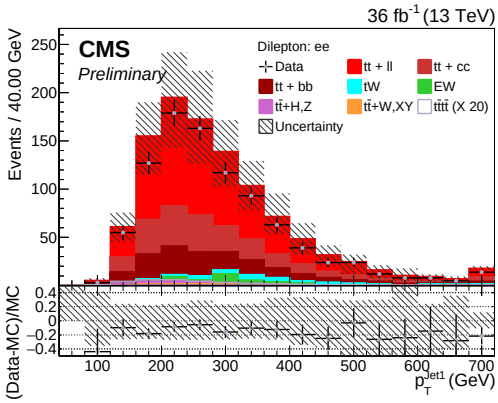

(a)

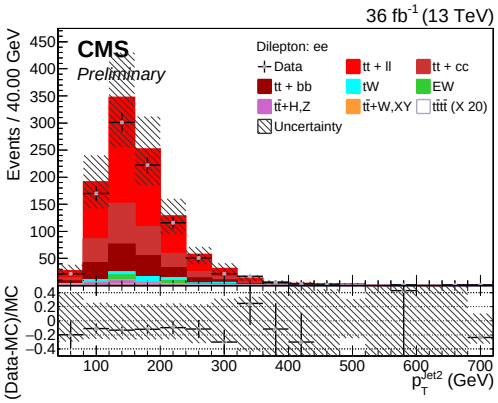

(b)

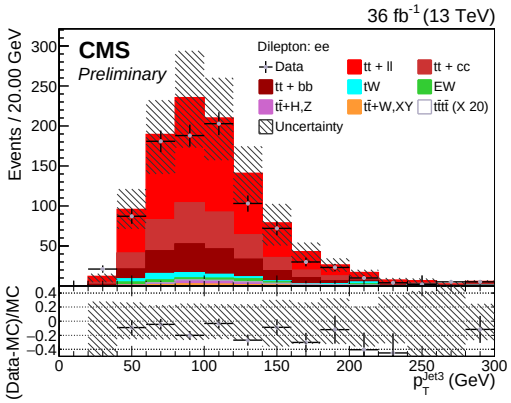

(c)

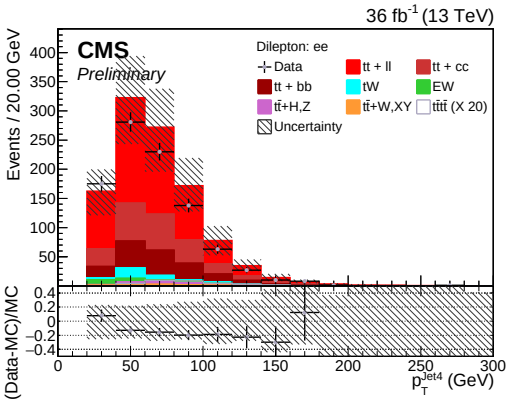

(d)

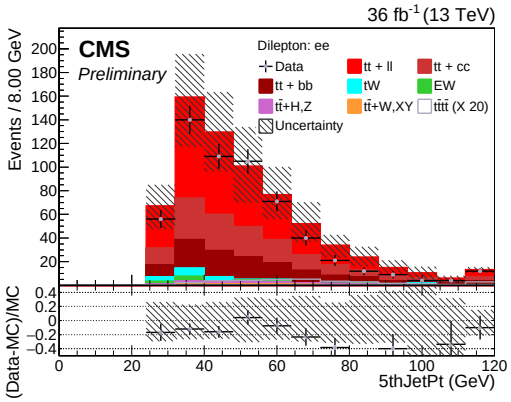

(e)

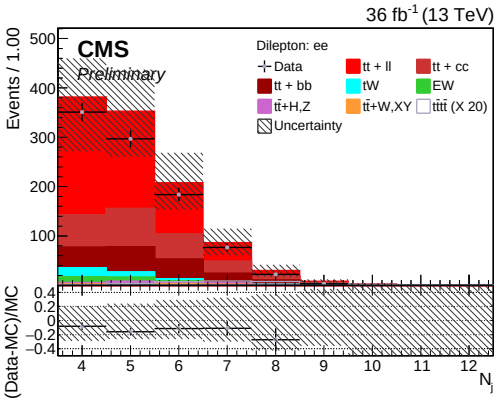

(f)

Figure 7.15: Distributions of jet kinematics in (ee channel).

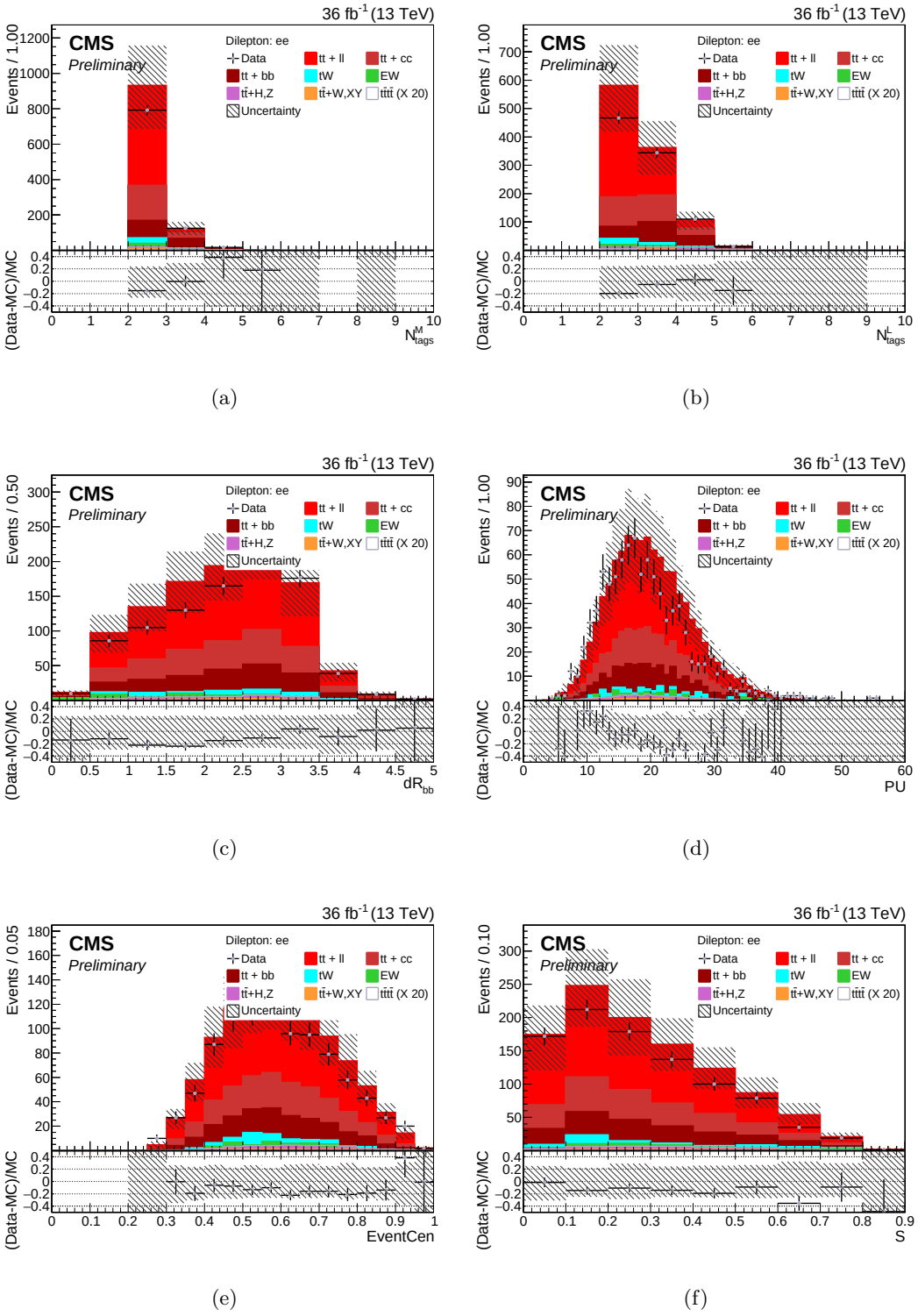

(a) (b) (c) (d) (e) (f)

Figure 7.16: Distributions of jet and event kinematics in (*ee* channel).

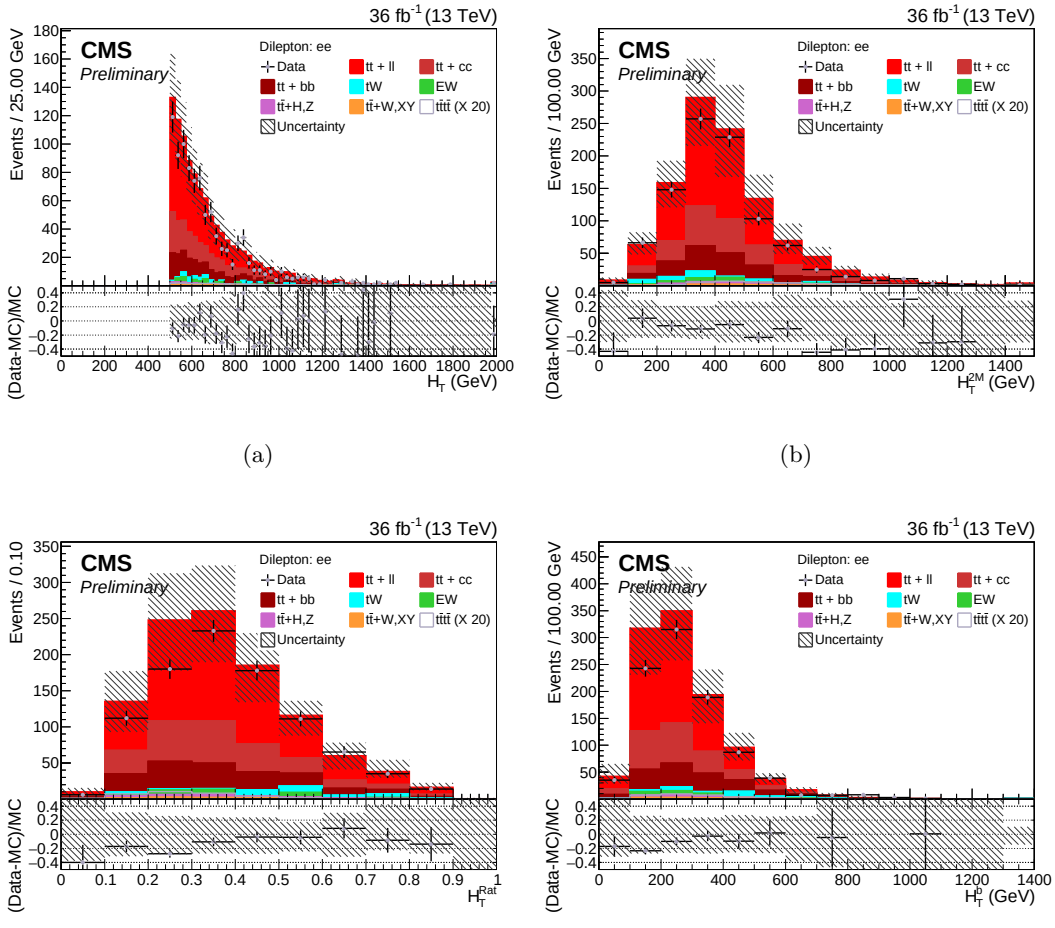

Figure 7.17: Distributions of event kinematics (*ee* channel).

7.3 Event Selection Cut-flow

The selected events are dominated by the $t\bar{t}$ background, with only small contributions from other processes. The numbers of data events selected and the number of simulated events expected after each step of the baseline selections for each channel is presented in Tables 7.1, 7.2 and 7.3. After the baseline selection has been applied, the $t\bar{t}$ events represent 93% of the total background events.

Table 7.1: Pre selection cut flow for the $\mu\mu$ channel (36.0 fb^{-1} of int. lumi.)

	Data	$t\bar{t}t\bar{t}$	ST	$Z + jets$	$TTRare$	$t\bar{t}$	Total MC
initial	1061717512	326.1	2.56847e+06	1.8182e+8	27825.9	2.9796e+07	214212622
Trigger/PV	527871933	90.4	376466	4.0362e+7	6466.3	4.2146e+06	44959622.7
2 OS Iso μ	26287705	4.9	18431.7	2.1450e+7	673.6	191717	21660827.2
Mass Veto	2410398	3.9	14183.9	1.6168e+6	270.6	146226	1777484.4
$\geq$ 4 Jets	23575	3.8	535.2	4046.1	153.4	17908.3	22646.8
$\geq$ 2 b-tags	6547	2.7	137.7	168.2	67.1	7045.1	7420.8
HT $\geq$ 500 GeV	1101	1.9	24.9	20.0	33.2	1184.5	1264.5

Table 7.2: Preselection cut flow for the $e\mu$ channel (36.0 fb^{-1} of int. lumi.)

	Data	$t\bar{t}t\bar{t}$	ST	$Z + jets$	$TTRare$	$t\bar{t}$	Total MC
initial	953423996	326.1	2.56847e+06	1.8182e+08	27825.9	2.9796e+07	214212622
Trigger/PV	517420715	96.2	393825	3.8990e+07	6850.9	4.4143e+06	43805072.1
1 Iso. μ	361469669	63.5	335362	1.7023e+07	4705.3	3.6399e+06	21003030.8
1 Iso. e	512101	12.5	29043.3	72503	725.0	301139	403422.8
$\geq$ 4 Jets	36378	12.4	1096.4	415.5	392.5	37901.6	39818.4
$\geq$ 2 b-tags	13145	8.7	300.1	19.8	169.0	14799.4	15297
HT $\geq$ 500 GeV	2450	4.5	68.8	8.7	64.6	2684.1	2830.7

Table 7.3: Preselection cut flow for the ee channel (36.0 fb^{-1} of int. lumi.)

	Data	$t\bar{t}t\bar{t}$	ST	$Z + jets$	$TTRare$	$t\bar{t}$	Total MC
initial	474084027	326.1	2.56847e+06	1.8182e+8	27828.9	2.9796e+07	214212625
Trigger/PV	39765633	17.6	27749.2	2.10075e+7	1446.7	330465	21367178.5
2 OS Iso μ	15016125	3.6	11315.2	1.32165e+7	475.0	117628	13345921.8
Mass Veto	1101731	3.0	9024.3	799597	190.4	91450.6	900265.3
$\geq$ 4 Jets	14499	2.9	393.7	2408.7	109.2	11774.7	14689.2
$\geq$ 2 b-tags	4218	2.1	117.5	88.5	47.6	4594.4	4850.1
HT $\geq$ 500 GeV	934	1.7	35.0	12.9	27.0	984.8	1061.4

Chapter 8

Analysis Methodology

8.1 Multivariate Analysis

The data sample consists of two types of events: signal and background. In order to classify events into the right type, information such as kinematic variables, event properties, topology or detector response can be used as discriminating variables. The signal or background classification will depend on the set of cuts on these variables that it satisfies (see Figure 8.1). This analysis uses a multivariate analysis method which takes the information as input variables and builds it into a signal discriminating variable (classifier). The optimal decision boundaries on the input variables are found from supervised machine learning with training data.

The implementation of multivariate analysis is done in the TMVA framework [59], whose code flow is shown in Figure 8.2. The Boosted Decision Trees (BDTs) [60, 61] method with the Adaptive boosting (AdaBoost) algorithm [62] is used for classifier training and

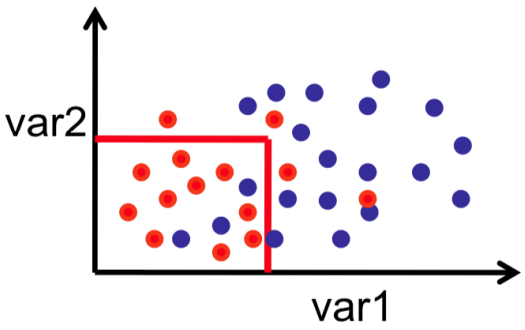

Figure 8.1: A simple demonstration of event classification defined by cuts on two variables. Red dots represent signal data while blue dots represent background data.

application. The decision tree is a sequential application of cuts on the discriminating variables x_i that splits data into nodes, where the final nodes (leaves) classify an event as either signal (S) or background (B). Figure 8.3 shows a schematic view of a decision tree. The Boosted Decision Trees combine a forest of Decision Trees derived from the same sample with different event weights and the AdaBoost algorithm reweights events misclassified by the classifier from previous Decision Trees by weight

$$w = \frac{1 - f_{err}}{f_{err}} \tag{8.1}$$

where f_{err} is misclassification rate. Figure 8.4 shows a schematic view of the Boosting flow.

8.2 BDT Discriminant

To achieve good discrimination between signal and background, two BDT classifiers implemented with the TMVA library are used. The first classifier, $\mathrm{BDT}_{\mathrm{trijet1}}$, is used to identify the hadronically decaying top quarks and the second classifier, $D^{DL}_{\bar{t}t\bar{t}t}$, is used as

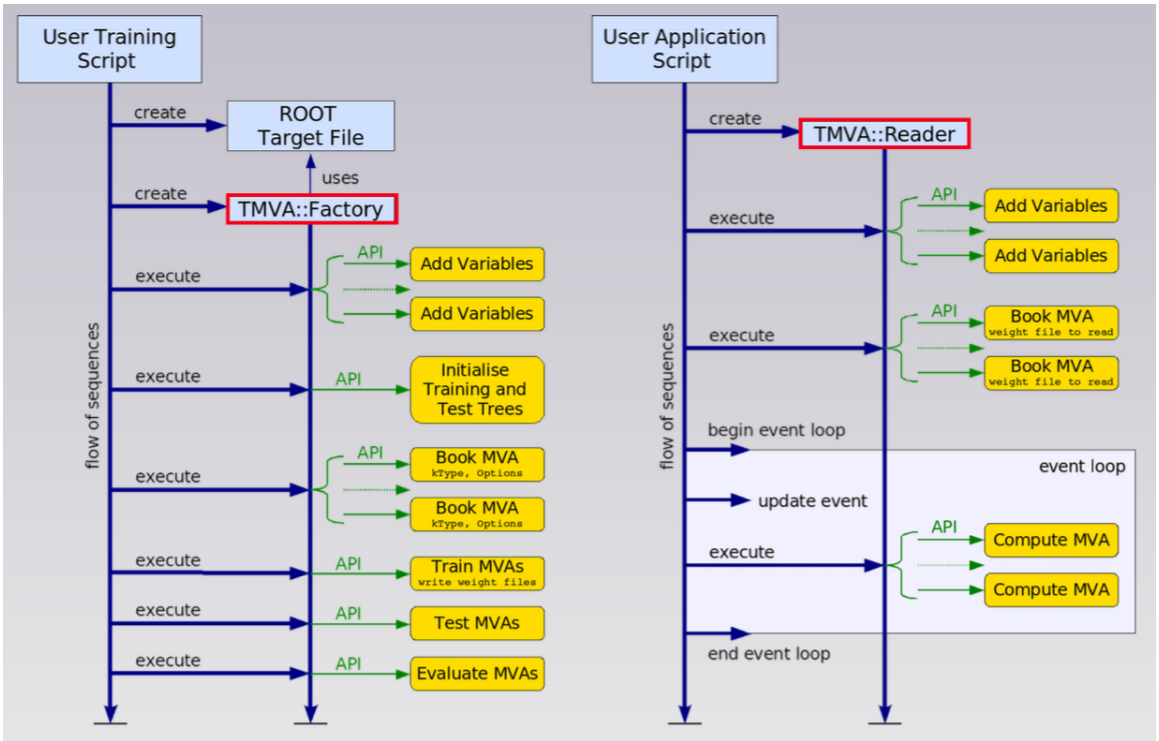

Figure 8.2: Code Flow for training classifiers using data samples with known signal and background composition and apply classifiers to classify unknown data samples with TMVA framework.

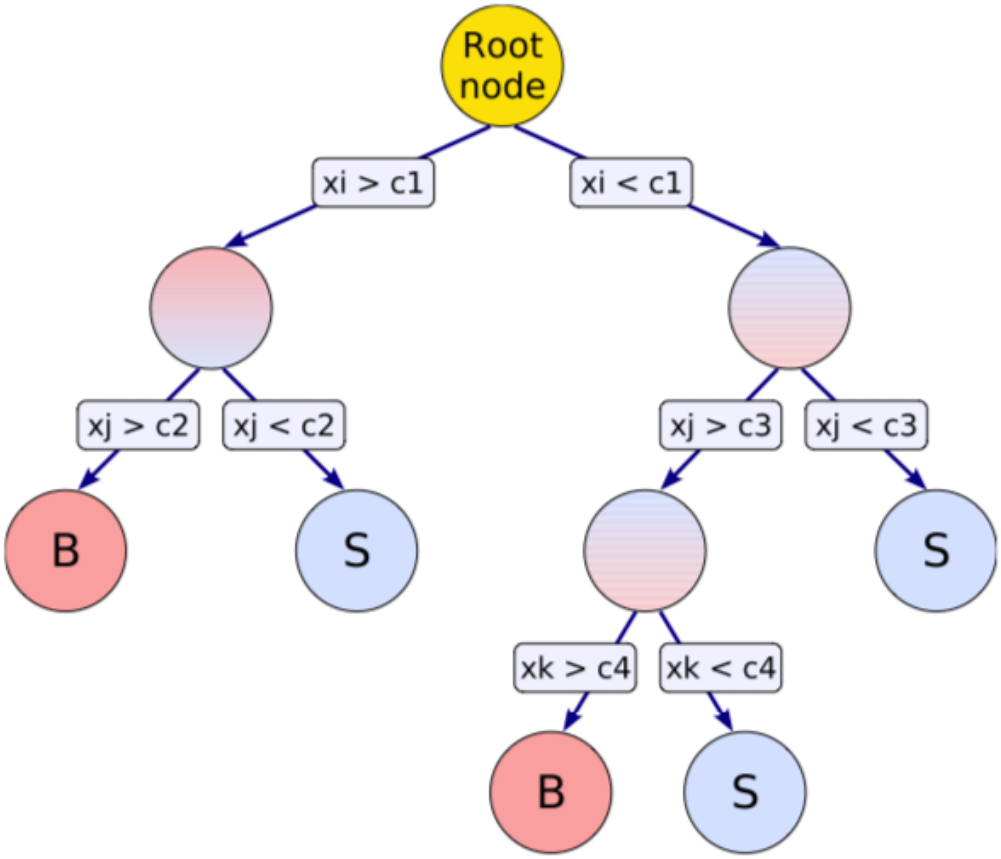

Figure 8.3: Schematic view of a decision tree. The leaf nodes are labeled "S" for signal and "B" for background depending on the majority of events in the respective nodes.

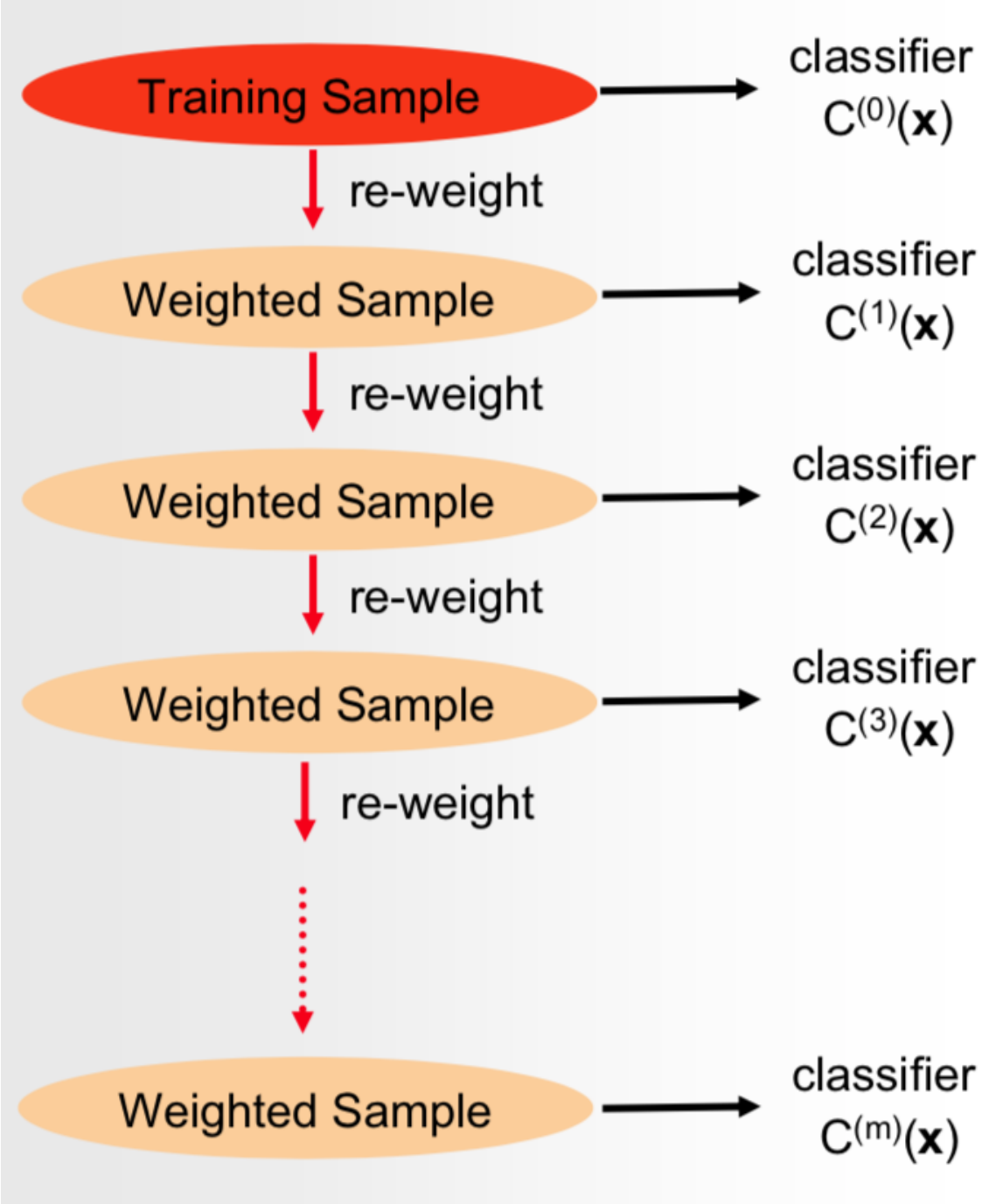

Figure 8.4: Schematic view of Boost Decision Trees flow.

a discriminant variable between signal and background.

8.2.1 Top Quark Discriminant $\mathrm{BDT_{trijet1}}$

The BDT discriminant used to identify hadronically decaying top quarks classifies the three jet permutation (trijets) of the jets in an event based on how well the trijets resemble a hadronically decaying top quark ($t \to bW \to bq\bar{q}$). The input variables consists of b tagging information, the invariant dijet and trijet masses, the angles between the three jets, and ratio of the reconstructed topp_{T} to the sum of the three jets. Each of these is detailed below.

- **Trijet invariant mass** This variable exploits the fact that invariant mass distribution for good trijets (as from top quark decay) peaks sharply close to the top mass while the distribution for bad trijets has a less pronounced peak.

- **Dijet invariant mass** A hadronically decaying top quark produces a hadronically decaying W boson. Thus a good trijet should contain a dijet with an invariant mass consistent with the W mass. The dijet is formed from the two jets in the trijet which have the smallest ΔR separation. An alternative method of selecting the dijet would have been to take the two jets with the lowest values of the CSVv2 b-tagging discriminant to exploit the fact that W bosons decay very rarely to b quarks. However, this method is rejected so as not to bias the CSV discriminant value of the jet not included in the dijet which is used later in the kinematic reconstruction. The distribution for good dijets peaks sharply close to the W mass while the distribution for bad dijets has a less pronounced peak and a tail extending to large values.

- $\boldsymbol{p_{\mathrm{T}}^{Rat}}$ This variable is defined as the ratio of the vectorial p_{T} of the trijet to the scalar sum of the p_{T} of the jets in the trijet. This variable is seen to provide significant discrimination.

- $\boldsymbol{\Delta\phi_{T-W}}$ This variable is defined as the transverse angle between the trijet system and the constituent dijet system used in the dijet invariant mass.

- $\boldsymbol{\Delta\phi_{T-b}}$ This variable is defined as the transverse angle between the trijet system and the jet that is not used in the dijet invariant mass.

- ***b*-tag information** CSVv2 discriminant value of the jet that is not included in the dijet system.

There are many trijet combinations in each event due to the high jet multiplicity in our selection requirements. For each event the trijet permutations are ranked according to their discriminant values, from highest to lowest. The higher the discriminant value, the more likely the trijet combination originates from a hadronic top quark. In the dilepton channel, there are two hadronically decaying top quarks in $t\bar{t}t\bar{t}$ events while no hadronically decaying top quarks in $t\bar{t}$ events. Thus the BDT discriminant with the highest ranked value ($\mathrm{BDT}_{\mathrm{trijet1}}$) is used as the classifier and as an input variable for the second BDT discriminant.

8.2.2 Event Level BDT $D_{t\bar{t}t\bar{t}}^{DL}$

The input variables for the second BDT discriminant can be grouped into five categories, based on the underlying physical characteristics that they exploit: top quark

content ($\mathrm{BDT}_{\mathrm{trijet1}}$ as described above), event activity, event topology, b quark content and lepton content. These variables are listed below and their discriminating power are discussed in the next section.

8.2.2.1 Event Activity

The principal differences between $t\bar{t}t\bar{t}$ and $t\bar{t}$ production are in the jet multiplicity and the number of b jets. SM theory predicts there to be eight hard jets in the di-leptonic final state of $t\bar{t}t\bar{t}$ events compared to two in di-leptonic $t\bar{t}$ events. This difference is exploited to pose the variables below, which are used as the input parameters for the second BDT:

- $\boldsymbol{N}_{\mathrm{j}}$, the number of selected jets presented in the event.
- $\boldsymbol{H}_{\mathrm{T}}^{\mathrm{b}}$, the scalar sum of the p_{T} of all b tagged jets in the event, identified using the medium working point. $t\bar{t}t\bar{t}$ events should have four b quark jets originating from top quark decay while $t\bar{t}$ events should have two b jets from top decay and other b jets from gluon splitting. As b jets originating from top quark decay tends to have larger p_{T}values, $H_{\mathrm{T}}^{\mathrm{b}}$ should have larger values for $t\bar{t}t\bar{t}$ events than for $t\bar{t}$ events.
- $\boldsymbol{H}_{\mathrm{T}}^{\mathrm{Rat}}$, the ratio of the H_{T} of the two leading jets in the event in the dilepton channel to the H_{T} of the other jets in the event.
- $\boldsymbol{H}_{\mathrm{T}}^{\mathrm{2M}}$, the H_{T} in the event minus the E_{T} of the two selected b jets.
- $\boldsymbol{p}_{\mathrm{T}}^{\mathrm{Jet3}}$ and $\boldsymbol{p}_{\mathrm{T}}^{\mathrm{Jet4}}$, the p_{T} values of the 3rd and 4th largest p_{T} jets in the event. The reason to use these is that in di-leptonic $t\bar{t}$ events these jets come from bremsstrahlung or gluon splitting processes and thus, they have different spectra from jets coming from

top quark decay in $t\bar{t}t\bar{t}$ events.

8.2.2.2 Event Topology

- Event Sphericity $\boldsymbol{S}$ [63], calculated from all of the jets in the event in terms of the tensor $S^{\alpha\beta} = \frac{\sum_i p_i^\alpha p_i^\beta}{\sum_i |\vec{p_i}|^2}$, where α and β refer to the three-components of the momentum of the i^{th} jet. The sphericity is then $S = \frac{3}{2}(\lambda_2 + \lambda_3)$, where λ_2 and λ_3 are the two smallest eigenvalues of $S^{\alpha\beta}$. The sphericity in $t\bar{t}t\bar{t}$ events should differ from that in background $t\bar{t}$ events of the same energy. The $t\bar{t}$ decays will be less spherically distributed as they are boosted by the additional jet activity in the event (eg. ISR).

- Hadronic centrality $\boldsymbol{C}$, the value of H_{T} divided by the sum of the energies of all jets in the event.

8.2.2.3 b jet Content

The analysis assumes that the top quark decays with the SM branching ratio of $\mathcal{B}(t \to bW) = 1$. Hence four b quarks from top quark decays should be expected in the di-leptonic final state of $t\bar{t}t\bar{t}$ events compared to two b quarks for the du-leptonic $t\bar{t}$ events. Therefore the multiplicity of b quark jets is a source of discriminating power. Based on b quark jet content the following variables are selected as input for the second BDT:

- $\boldsymbol{N}^{\text{M}}_{\text{tags}}$, the number of b jets tagged by the CSV algorithm operating at its medium working point

- $\boldsymbol{N}^{\text{L}}_{\text{tags}}$, the number of b jets tagged by the CSV algorithm operating at its loose working point.

- $\boldsymbol{dR}_{\mathrm{bb}}$, the angular separation between the two b-tagged jets with highest CSV discriminant values.

8.2.2.4 Lepton Content

The previous variables rely only on the hadronic information in the event. To exploit lepton information in the event, the following variables are added:

- $\boldsymbol{p}_{\mathrm{T}}^{\mathrm{l1}}$ the p_{T} values of the highest-p_{T} lepton in the event.
- $\boldsymbol{\eta}^{\mathrm{l1}}$ the η values of the highest-p_{T} lepton in the event.
- $\boldsymbol{dR}_{\mathrm{ll}}$ the angular difference between the two selected leptons.

The control distributions of these input variables are shown in section 7.

8.3 BDT Training

Training and evaluation of the BDT discriminator is carried out in $\mu\mu, e\mu, ee$ channels separately using version 4.2.0 of the TMVA package with the AdaBoost boosting algorithm. A forest of 400 decision trees are generated using the Gini Index to determine separation at each node. The trees are restricted to a maximum depth of 3 cuts with a minimum amount of events per node of 5% of the total input samples. The aggregate, weighted response of the forest is used to output the discriminator value. All events provided to the BDT training are assigned a unity weight. Any mis-modeling from this choice will be smaller than other dominant sources of systematic uncertainty.

TMVA separates the input events into a training and test sample in order to test that the forest has not been over-trained and learned to pick out individual fluctuations in the training sample. If the forest has not been over-trained, then the output discriminator distributions of the test and training sample should be the same assuming there are enough events to populate the bins sufficiently. Figure 8.5 shows that the response of the signal and background for both the test and training samples agrees quite well. Additionally, the separation is quite good.

The event-level variables described in section 8.2 were used as input features in the event-level, BDT discriminator. Input distributions for these features can be seen in Figure 8.6. The event level BDT is trained on each final state separately.

Figure 8.7 shows the correlation matrix from the BDT training for the signal sample and background sample.

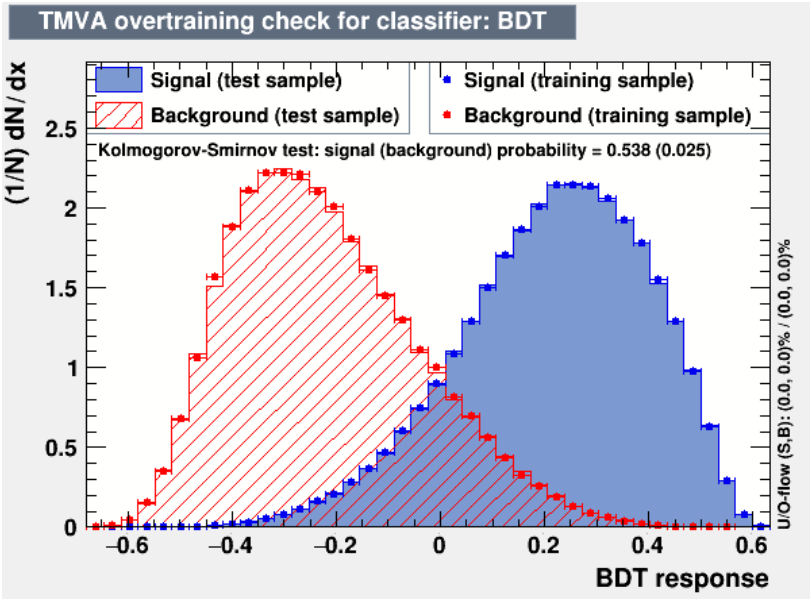

Figure 8.5: Classifier response for the trained BDT in $\mu\mu, e\mu, ee$ channels separately.

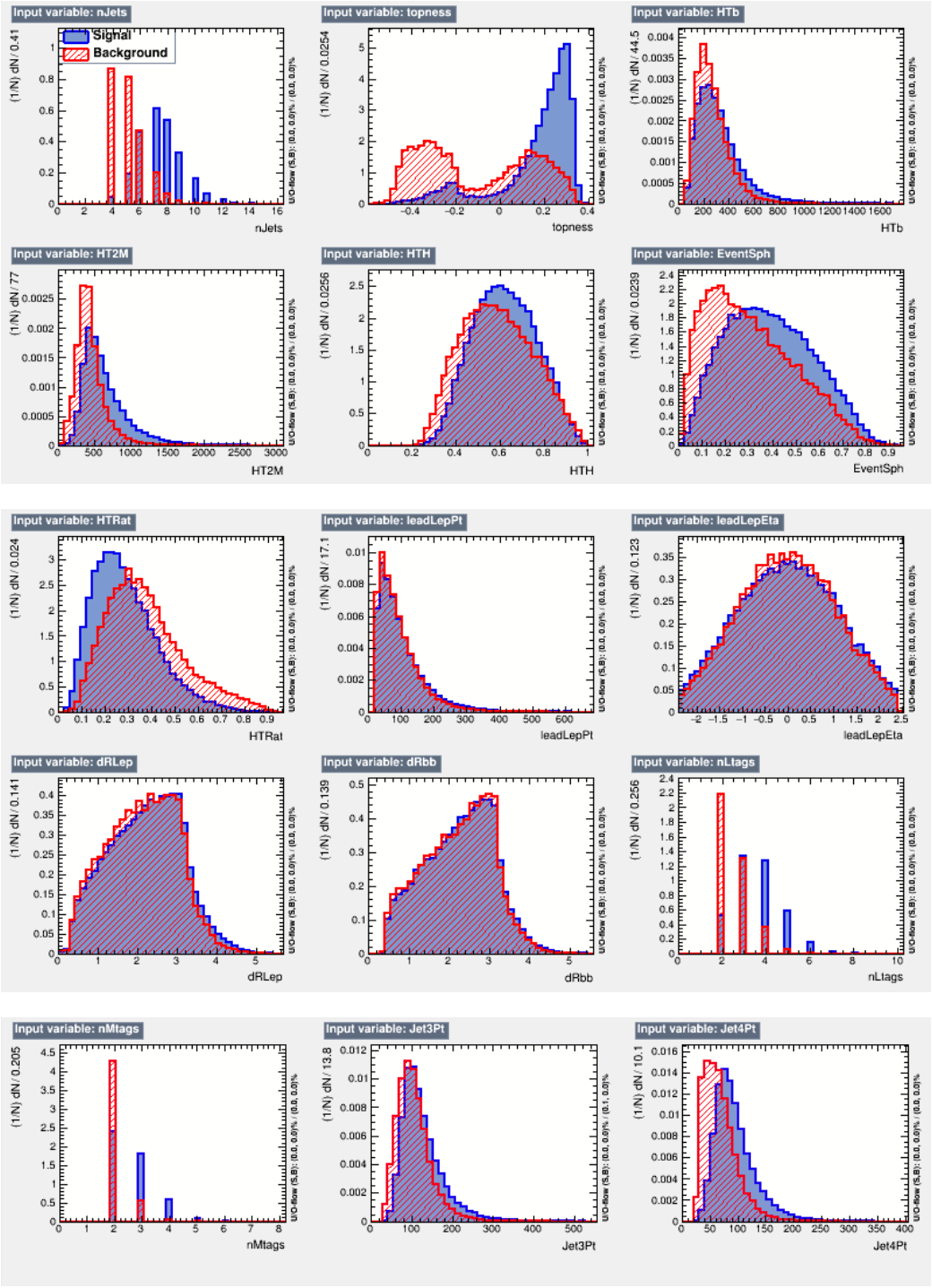

Figure 8.6: Input feature distributions to the BDT for signal (blue) and background (red) in $\mu\mu$ channel.

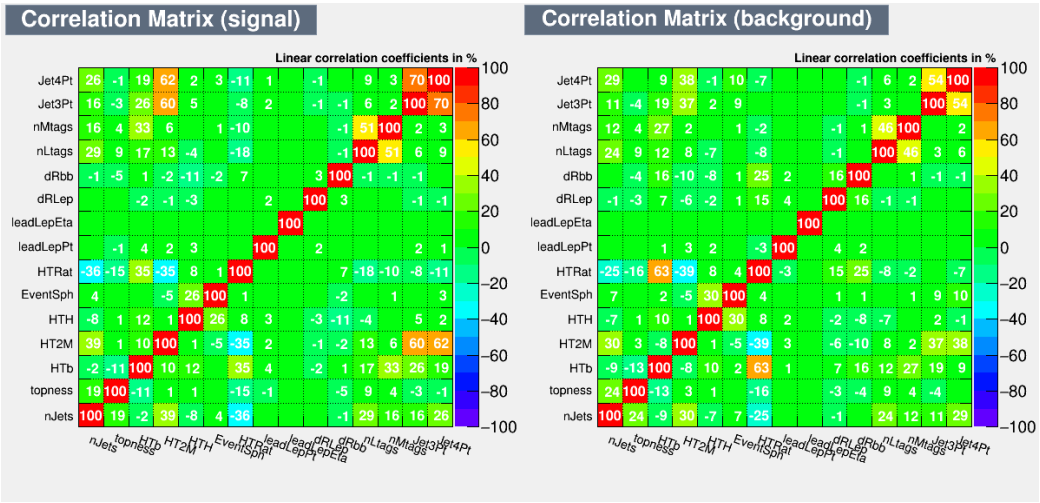

Figure 8.7: Correlation Matrix for Signal and Background in $\mu\mu$ channel.

The discrimination power of the features used in the BDT and are shown in Table 8.1.

8.4 Event Categorization

The variables described above are combined using the second BDT ($D^{DL}_{t\bar{t}t\bar{t}}$). To maximize the sensitivity, the events are divided into exclusive jet multiplicity categories corresponding to $N_{\mathrm{j}} = 4-5, 6-7, and \geq 8$, then further split into exclusive b jet multiplicity categories of $N^{\mathrm{M}}_{\mathrm{tags}} = 2, and \geq 3$ in each N_{j} category.

Fig 8.8, 8.11, 8.16 show BDT distributions for the different jet and b-tag categories for each channel. The first and last few bins in each category have been combined into one bin, so that there are no bins with zero MC background events. This is done to avoid bias

Table 8.1: Rankings of the features used in the BDT training.

Rank	Feature Name	Feature Frequency
1	N_{j}	1.443e-01
2	$\mathrm{BDT}_{\mathrm{trijet1}}$	1.105e-01
3	$H_{\mathrm{T}}^{\mathrm{2M}}$	7.987e-02
4	$p_{\mathrm{T}}^{\mathrm{Jet4}}$	7.687e-02
5	$N_{\mathrm{tags}}^{\mathrm{L}}$	7.574e-02
6	$H_{\mathrm{T}}^{\mathrm{Rat}}$	6.869e-02
7	$H_{\mathrm{T}}^{\mathrm{b}}$	6.812e-02
8	S	5.945e-02
9	dR_{bb}	5.618e-02
10	$N_{\mathrm{tags}}^{\mathrm{M}}$	5.548e-02
11	dR_{ll}	5.140e-02
12	C	4.979e-02
13	$p_{\mathrm{T}}^{\mathrm{Jet3}}$	3.681e-02
14	$p_{\mathrm{T}}^{\mathrm{l1}}$	3.455e-02
15	η^{l1}	3.218e-02

when the distributions are fitted.

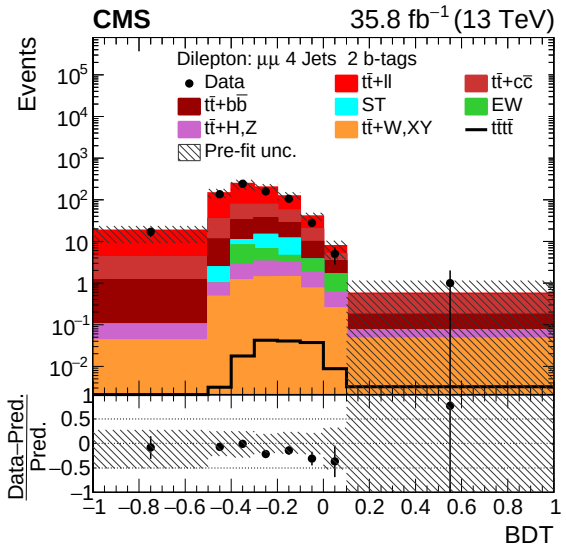

(a) 4-5jets 2b

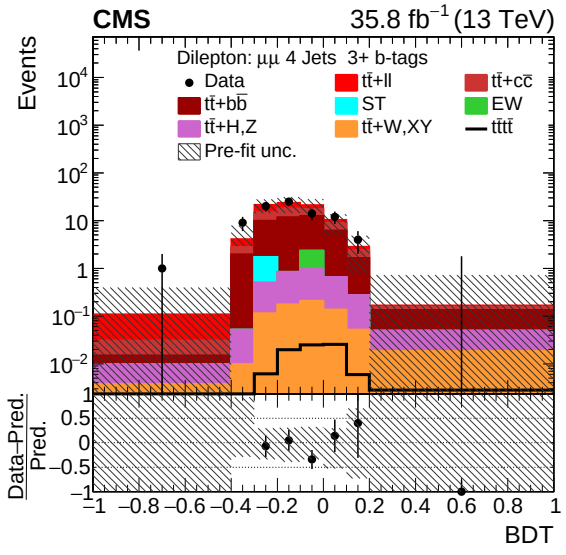

(b) 4-5jets 3+b

Figure 8.8: BDT distribution for $N_{\mathrm{j}} = 4-5$ and $N_{\mathrm{tags}}^{\mathrm{M}} = 2, \geq 3$ categories in the $\mu^{+}\mu^{-}$ channel.

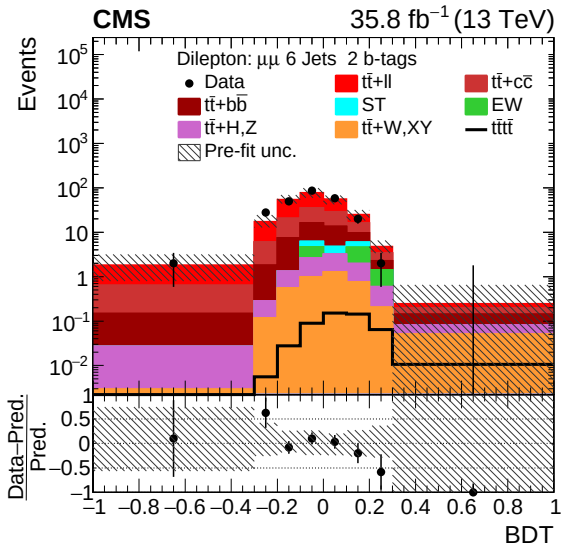

(a) 6-7jets 2b

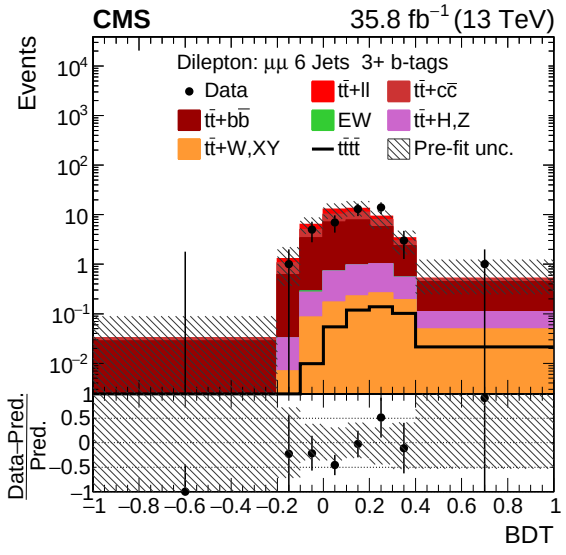

(b) 6-7jets 3+b

Figure 8.9: BDT distribution for $N_{\mathrm{j}} = 6-7$ and $N_{\mathrm{tags}}^{\mathrm{M}} = 2, \geq 3$ categories in the $\mu^{+}\mu^{-}$ channel.

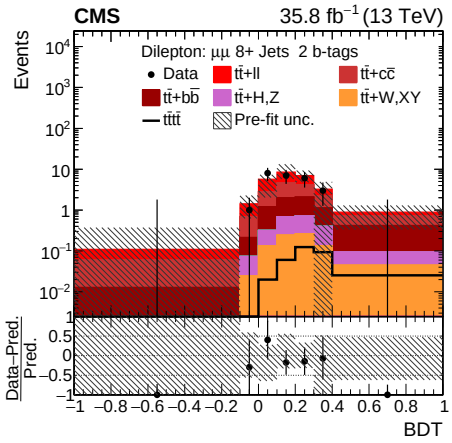

(a) 8+jets 2b

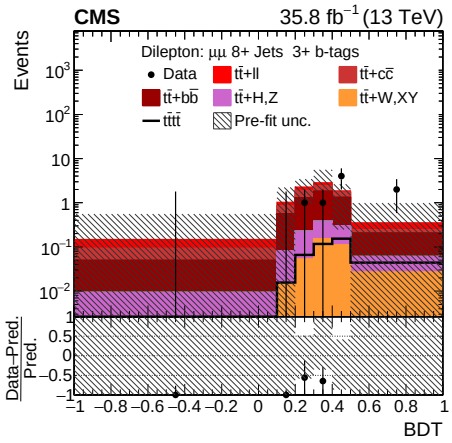

(b) 8+jets 3+b

Figure 8.10: BDT distribution for $N_{\mathrm{j}} \geq 8$ and $N_{\mathrm{tags}}^{\mathrm{M}} = 2, \geq 3$ categories in the $\mu^{+}\mu^{-}$ channel.

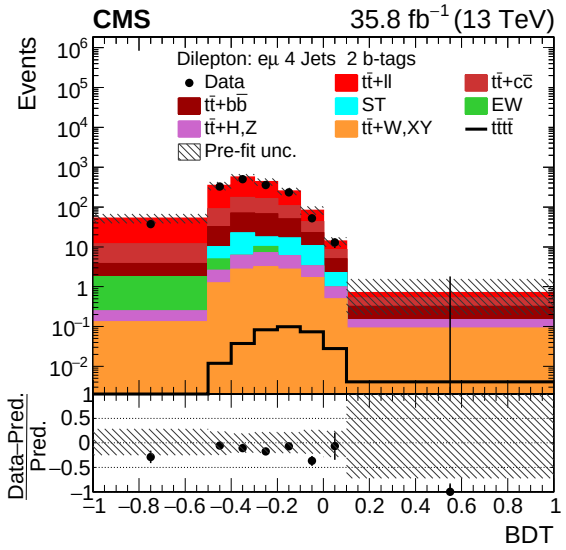

(a) 4-5jets 2b

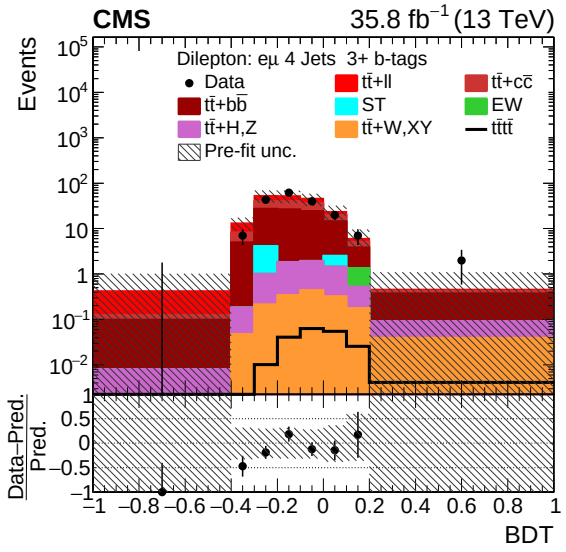

(b) 4-5jets 3+b

Figure 8.11: BDT distribution for $N_{\mathrm{j}} = 4-5$ and $N_{\mathrm{tags}}^{\mathrm{M}} = 2, \geq 3$ categories in the $e^{\pm}\mu^{\mp}$ channel.

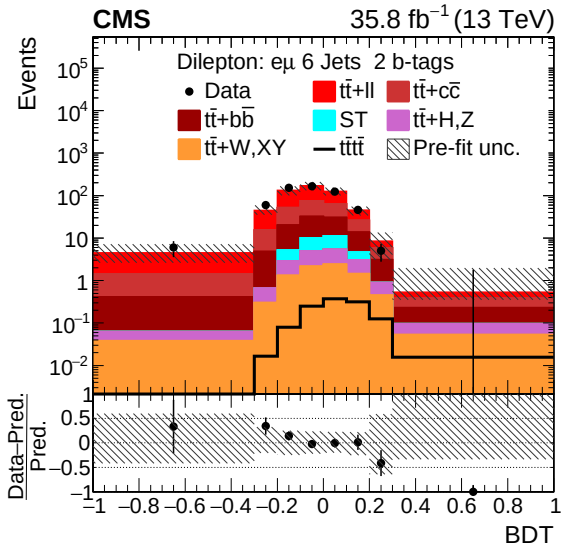

(a) 6-7jets 2b

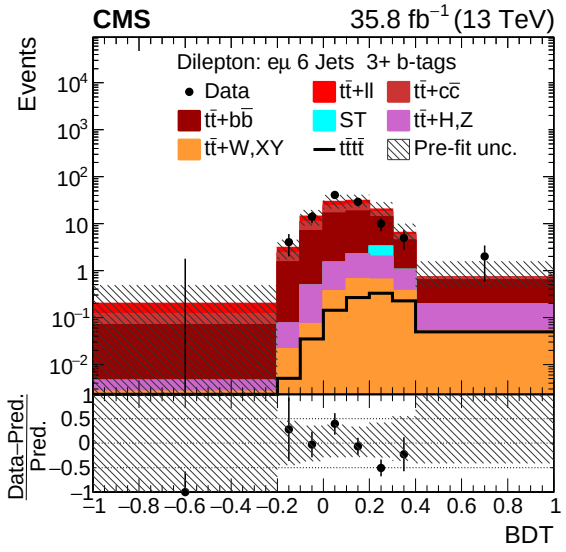

(b) 6-7jets 3+b

Figure 8.12: BDT distribution for $N_{\mathrm{j}} = 6-7$ and $N_{\mathrm{tags}}^{\mathrm{M}} = 2, \geq 3$ categories in the $e^{\pm}\mu^{\mp}$ channel.

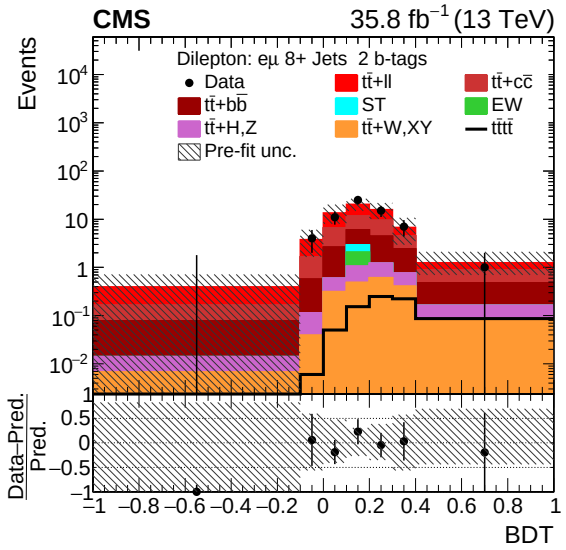

(a) 8+jets 2b

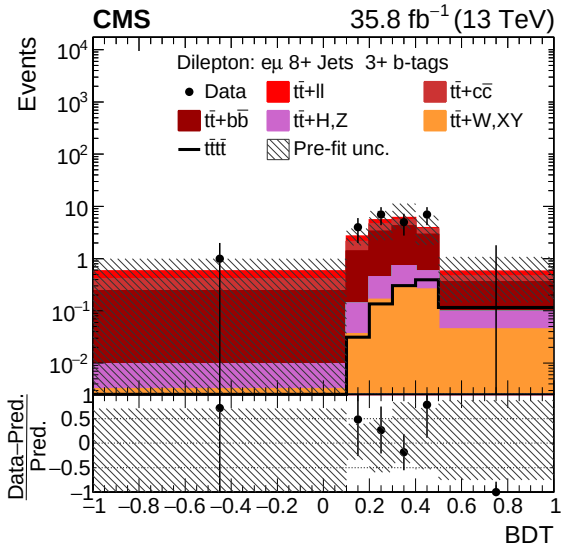

(b) 8+jets 3+b

Figure 8.13: BDT distribution for $N_{\mathrm{j}} \geq 8$ and $N_{\mathrm{tags}}^{\mathrm{M}} = 2, \geq 3$ categories in the $e^{\pm}\mu^{\mp}$ channel.

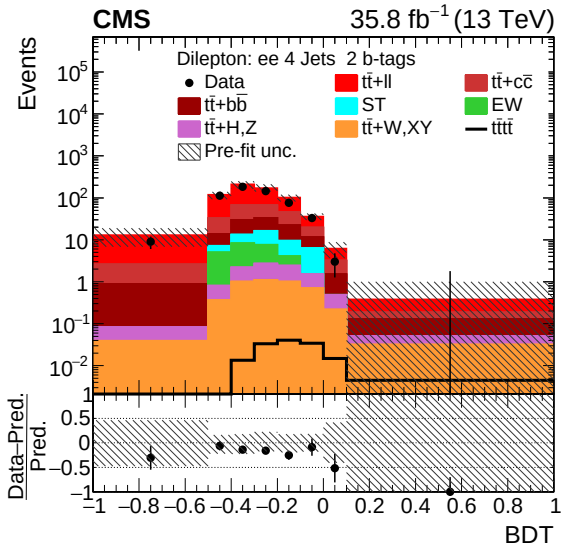

(a) 4-5jets 2b

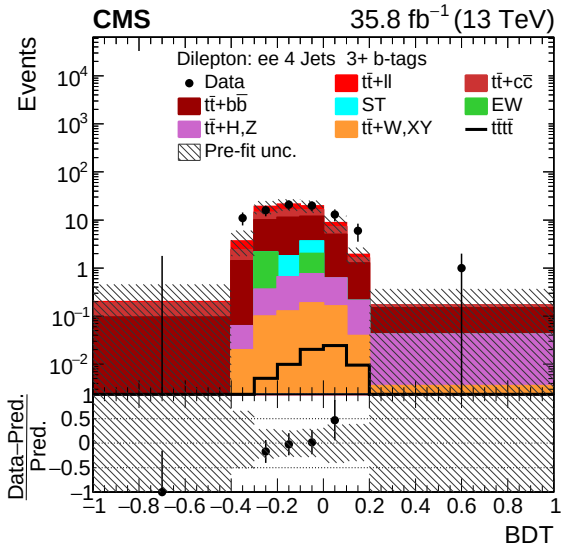

(b) 4-5jets 3+b

Figure 8.14: BDT distribution for $N_{\mathrm{j}} = 4-5$ and $N_{\mathrm{tags}}^{\mathrm{M}} = 2, \geq 3$ categories in the $e^{+}e^{-}$ channel.

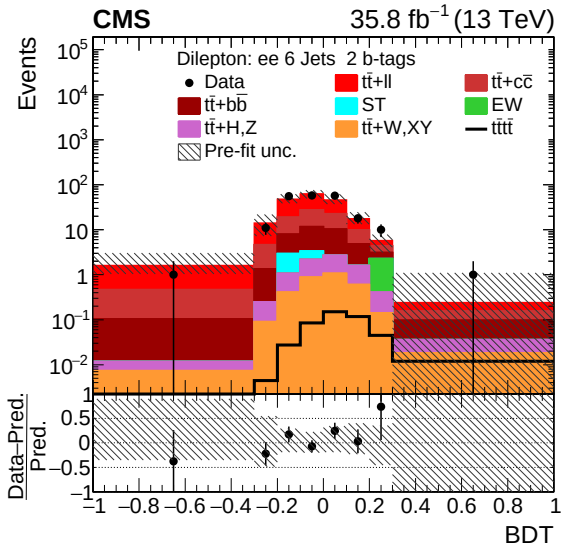

(a) 6-7jets 2b

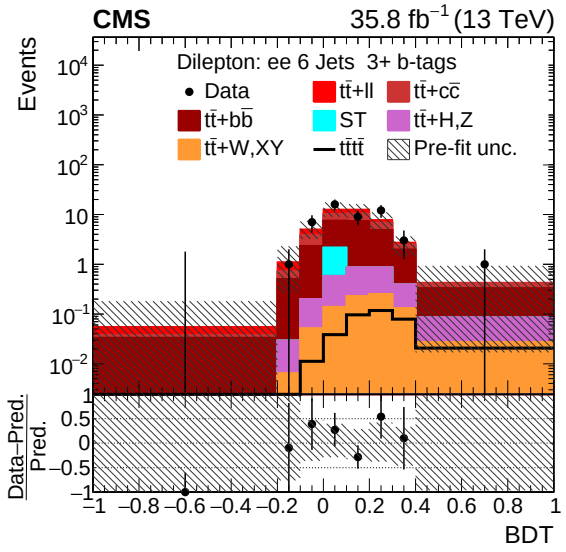

(b) 6-7jets 3+b

Figure 8.15: BDT distribution for $N_{\mathrm{j}} = 6-7$ and $N_{\mathrm{tags}}^{\mathrm{M}} = 2, \geq 3$ categories in the $e^{+}e^{-}$ channel.

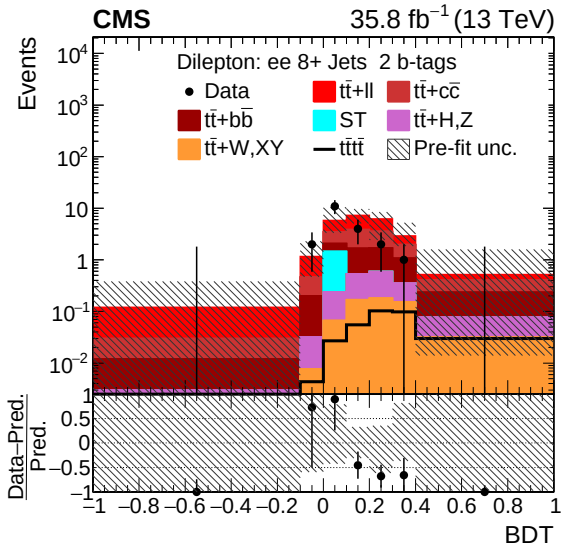

(a) 8+jets 2b

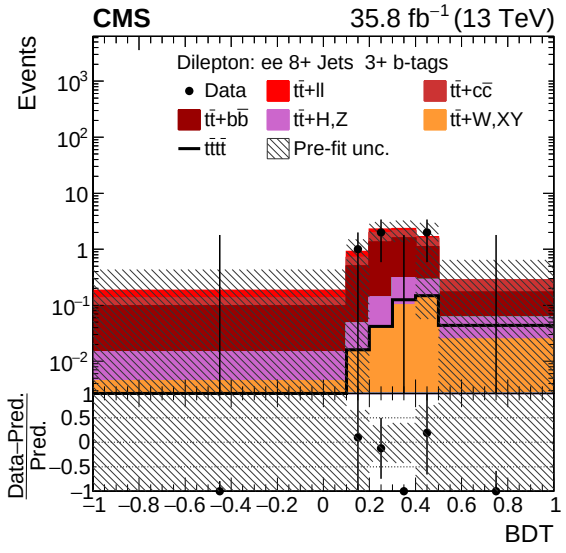

(b) 8+jets 3+b

Figure 8.16: BDT distribution for $N_{\mathrm{j}} \geq 8$ and $N_{\mathrm{tags}}^{\mathrm{M}} = 2, \geq 3$ categories in the $e^{+}e^{-}$ channel.

Chapter 9

Uncertainties

9.1 Sources of Systematic Uncertainties

The systematic uncertainties considered in this analysis can be categorized into two types: the ones that affect the normalization of the discriminant distributions, and those that affect the shape of the discriminant distributions. Table 9.1 characterizes all of these systematic uncertainties. Each systematic uncertainty is modeled by one nuisance parameter in the fit used to set the cross section limits.

Luminosity: The uncertainty on the luminosity scale for the 2016 CMS data is 2.5% [64].

Simulation processes cross sections: As the $t\bar{t}$ process dominates the events selected by the baseline selection, the cross section uncertainty on this process will also give the dominant cross section uncertainty. The uncertainty in the NLO $t\bar{t}$ cross section [65, 66, 67, 68, 69, 70, 71] is based on Powheg ME+PDF weights. The uncertainties in the cross

Table 9.1: Systematic uncertainties considered in this analysis. Their effects on the normalization of the datasets and shapes of the discriminant distribution are denoted by X

Uncertainty sources	Normalization	Shape
Integrated luminosity	X	
Simulation processes cross-section	X	
Pileup modeling	X	X
Lepton reconstruction and identification	X	
Jet energy corrections	X	X
b tagging	X	X
Ren. and fact. scales	X	X
PS scales	X	
ME-PS matching	X	
UE	X	
Jet multiplicity correction	X	
Parton density functions	X	X
Top quark p_T reweighting		X
Heavy flavor reweighting	X	X

sections for the other backgrounds were also included and found to be negligible.

Pile up: The number of pileup events in the simulation is matched to that of the data. The uncertainty due to this correction is estimated by varying the total inelastic pp collision cross section by ±4.6% [72].

Lepton reconstruction and identification: The uncertainty coming from the baseline selections choice of the lepton identification, the reconstruction criteria, and the trigger are included in a single nuisance parameter. A conservative constant 3% normalization uncertainty is assigned to the sum of these sources.

Jet energy corrections: The uncertainties due to limited knowledge of the jet energy scale (JES) and the jet energy resolution (JER) are estimated by varying the η- and p_T-dependent JES and JER corrections for all of the jets by ±1 standard deviation [73]. In

the case of JES uncertainty, this was split into 6 components, each representing a quadratic sum of subsets of jet energy correction uncertainty sources. The effect of each component is evaluated separately. The list of components are:

- SubTotalPileUp: sum of pile-up uncertainties.
- SubTotalRelative: eta-dependence uncertainties
- SubTotalPt: high/low p_{T} extrapolation
- SubTotalScale: flat scale uncertainties
- Flavor[QCD] : jet flavor. Based on Pythia6 Z2/Herwig++2.3 differences in uds/c/b-quark and gluon responses
- TimePtEta : JEC time dependence between BCD, EF, G and H.

***b*-tagging:** The uncertainty associated with the b tagging efficiency is estimated by varying the corrections for the b tagging CSVv2 [74] discriminator up and down by their corresponding uncertainties. These variations correspond to uncertainties in the jet energy scale, the background contamination of the samples used to derive them, and the statistical uncertainties of these data samples. They are parameterized as a function of p_{T}, η, and flavor of the jets.

Renormalization and factorization scales: The uncertainty from the choice of the factorization and renormalization scales in the calculation of the matrix element of the hard-scattering process, is estimated by varying each scale by a factor of 1/2 and 2 to calculate the envelope around the central value. The unphysical anti-correlated combina-

tions are excluded due to the large logarithmic corrections $|ln(\mu_R/\mu_F)| > 1$, Only the effects on the $t\bar{t}t\bar{t}$ and the $t\bar{t}$ components are considered. These are assumed to be uncorrelated.

Parton shower scales: The evolution scale in the initial- and final-state parton showers was separately varied by a factor of 2 and $\sqrt{2}$ up and down relative to their normal values, in order to estimate the uncertainty attributed to the shower model. Dedicated simulation samples with these varied scale choices were used in the uncertainty determination.

The limited number of events of these systematic samples yield large statistical fluctuations and thus unrealistic variations of the templates of the final distributions. Following the same approach adopted by the CMS TTH analysis [75], a conservative rate uncertainty is estimated per PS process and per jet multiplicity bin, by comparing the total event yields of the nominal and varied samples. If the observed differences are in opposite direction, i.e. if the yield increases for one variation and decreases for the other, the differences are assigned as uncertainty in each direction. In cases where this difference is smaller than the statistical uncertainty of the MC yields, the latter is used instead. If the yield changes are in the same direction, the larger of the two differences is compared to the statistical uncertainty, where again the larger of the two is used as uncertainty in that direction For the other direction, the statistical uncertainty of the MC yields is used, to ensure a 'two-sided' effect.

ME-PS matching: To estimate the uncertainty coming from ME-PS matching scale, the POWHEG parton-shower scale parameter, $h_{damp} = 1.581^{+0.658}_{-0.585}$ [39], was varied by $\pm 1\sigma$ to check the effects on both the shape and the normalization of the background.

Underlying event: The uncertainty from the UE tune of the $t\bar{t}$ event gen-

erator is evaluated by using simulations with varied parameters that are related to the CUETP8M2T4 tune. Due to the limited number of events of these samples, the same procedure as described above for the parton-shower scale uncertainty was used to estimate the impact by means of a jet-multiplicity dependent rate uncertainty.

PDFs uncertainty: The PDF uncertainty [76] in $t\bar{t}$ production is estimated by evaluating the shape difference between the nominal simulation and simulations based on the central NNPDF [43], MMHT14 [77], and CT10 [78] PDF sets.

Jet multiplicity norm uncertainty: Due to imperfect modeling of POWHEG $t\bar{t}$+jets simulation at high jet multiplicity, scale factors are derived from control samples in low jet multiplicity regions, and applied to simulation in high jet multiplicity regions. The uncertainty resulting from this correction is about 10%. This is estimated only for the $t\bar{t}$ process.

Top p_{T} reweight uncertainty: The uncertainty from the corrections made to the shape of the top quark p_{T} distribution is estimated by allowing the correction function to vary within a ± 1 standard deviation uncertainty [58, 79]. This is estimated only for the $t\bar{t}$ process.

$t\bar{t}$ Heavy flavor uncertainty: Since the analysis relies heavily on b-tagging information, $t\bar{t}$ events which have radiated a gluon which splits into a $b\bar{b}$ pair (termed $t\bar{t}b\bar{b}$ events) will closely resemble signal events. A study in [80] shows that the ratio $\sigma_{t\bar{t}b\bar{b}}/\sigma_{t\bar{t}jj}$ in $t\bar{t}$ MC is not correctly predicted by the POWHEG event generator. The result of the study on fitting the control regions in which the non-$t\bar{t}b\bar{b}$ contributions were not re-scaled and only the overall $t\bar{t}b\bar{b}$ normalization was left floating, shows consistency with [58, 80].

This uncertainty is taken into account by leaving $t\bar{t}b\bar{b}$ component floating and assigning to it a 35% uncertainty.

9.2 Size of Systematic Uncertainties

The aforementioned sources of systematic uncertainties are examined individually by comparing the alternative discriminant distribution derived from varying only the systematic certainty source under examination by 1 standard deviation up and down with the nominal discriminant distribution. The shape and normalization change of $t\bar{t}$ background related uncertainties are shown in Figures 9.1 to 9.9. The $t\bar{t}t\bar{t}$ signal-related uncertainties are shown in Figures 9.10 to 9.18. The CSV reshaping and theoretical systematics form relatively flat envelopes around the nominal $t\bar{t}$ sample. JER and split JES systematics deviates very little from the nominal distribution. TUNE systematics in Figures 9.19 to 9.24 show large fluctuations which is reasonable since these samples have limited statistics.

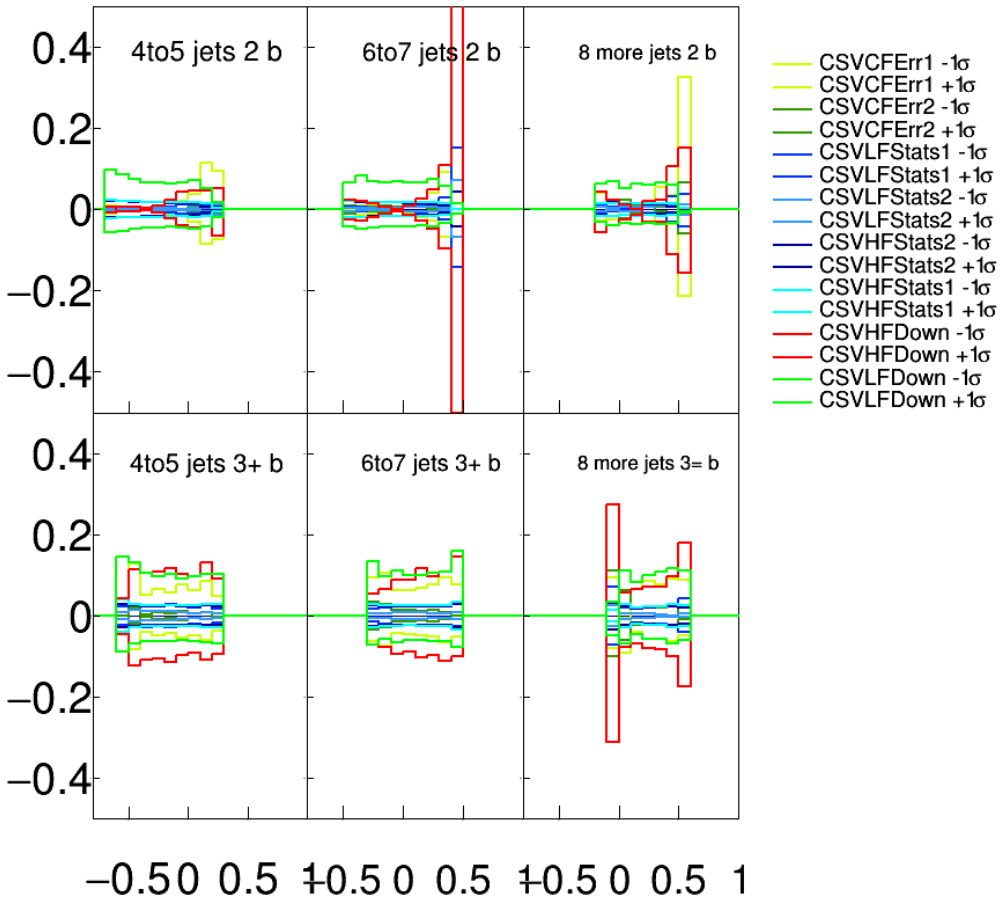

Figure 9.1: Variation of b-tagging systematic uncertainties in $t\bar{t}$ MC in $\mu^+\mu^-$ channel.

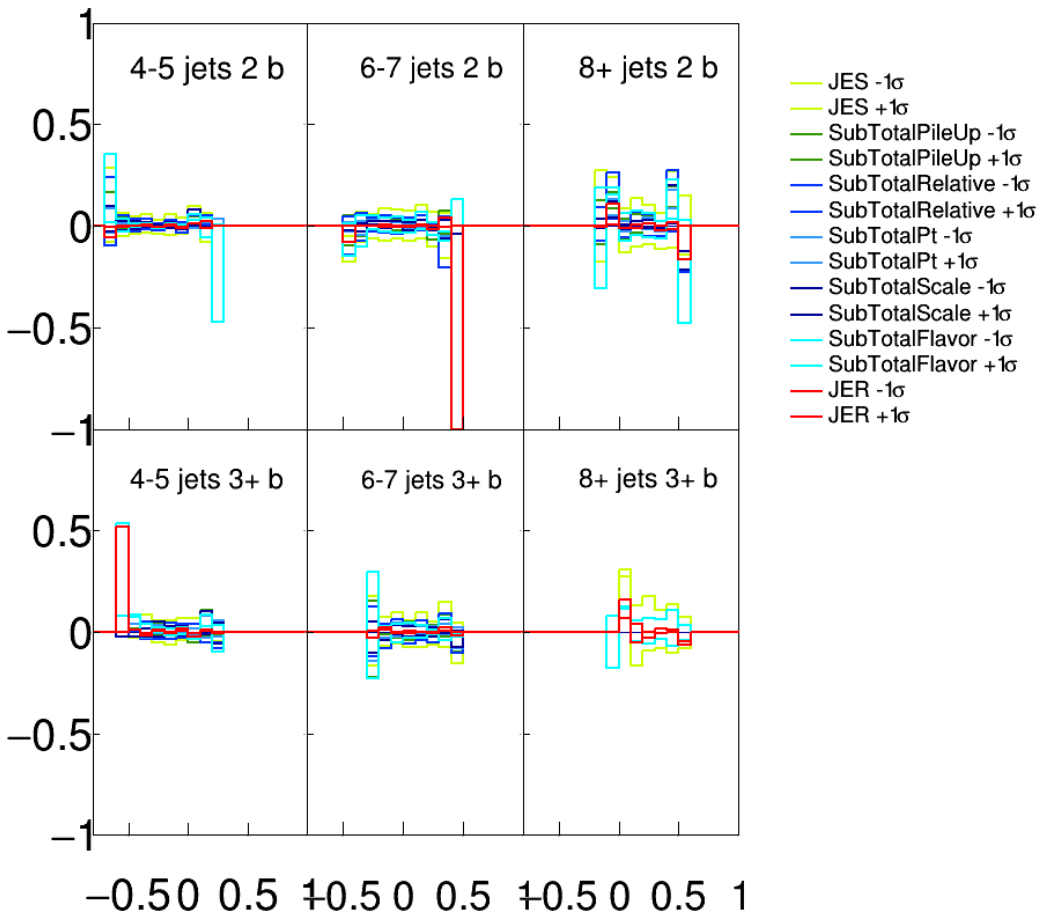

Figure 9.2: Variation of JES systematic uncertainties in $t\bar{t}$ MC in $\mu^+\mu^-$ channel.

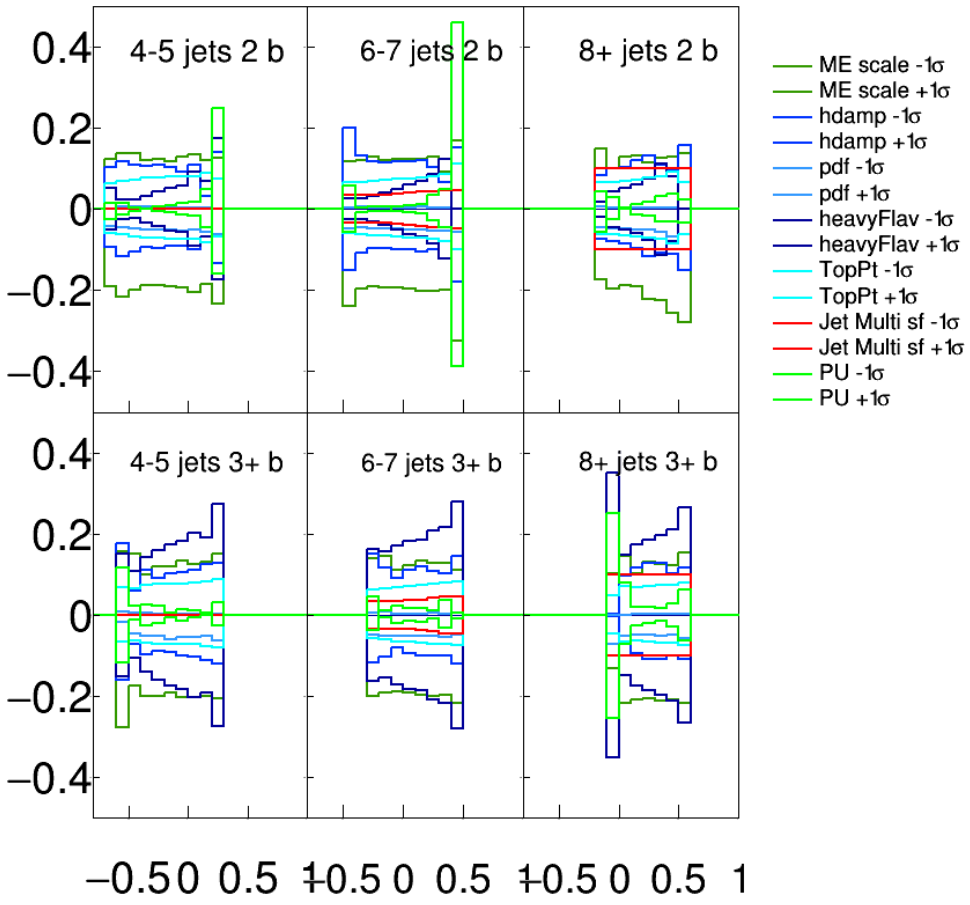

Figure 9.3: Variation of theoretical systematic uncertainties in $t\bar{t}$ MC in $\mu^+\mu^-$ channel.

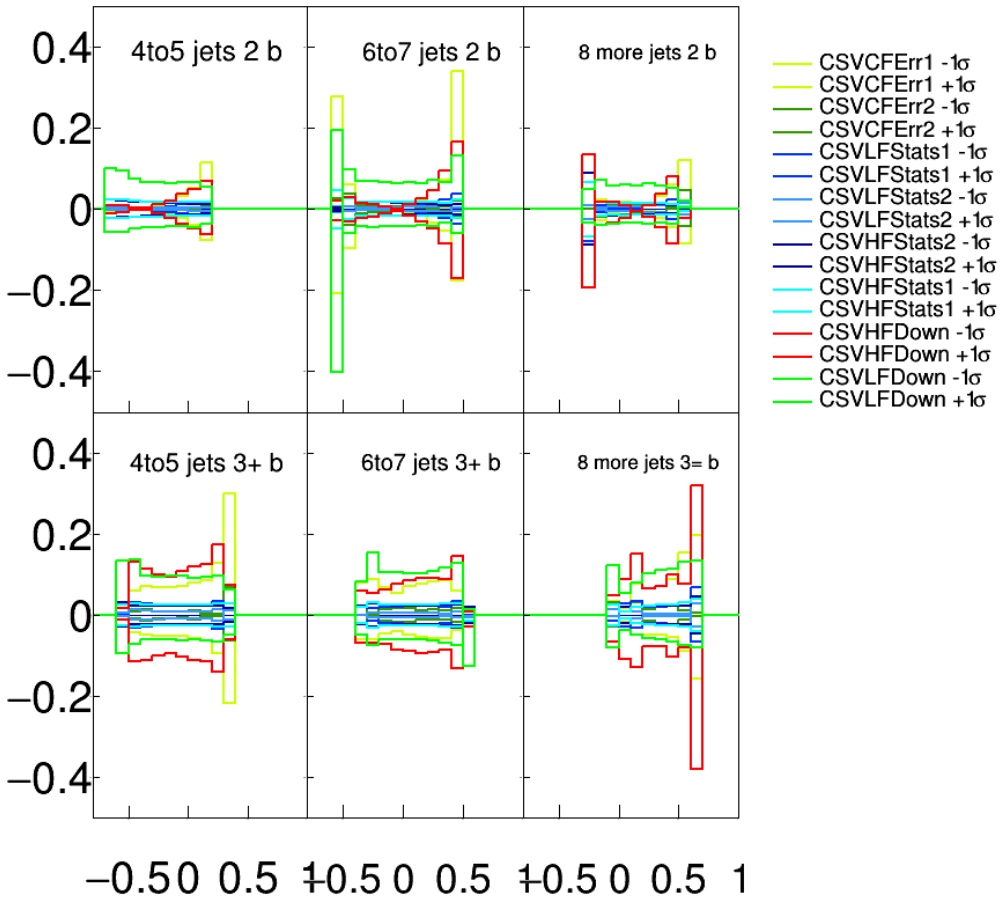

Figure 9.4: Variation of b-tagging systematic uncertainties in $t\bar{t}$ MC in $e^{\pm}\mu^{\mp}$ channel.

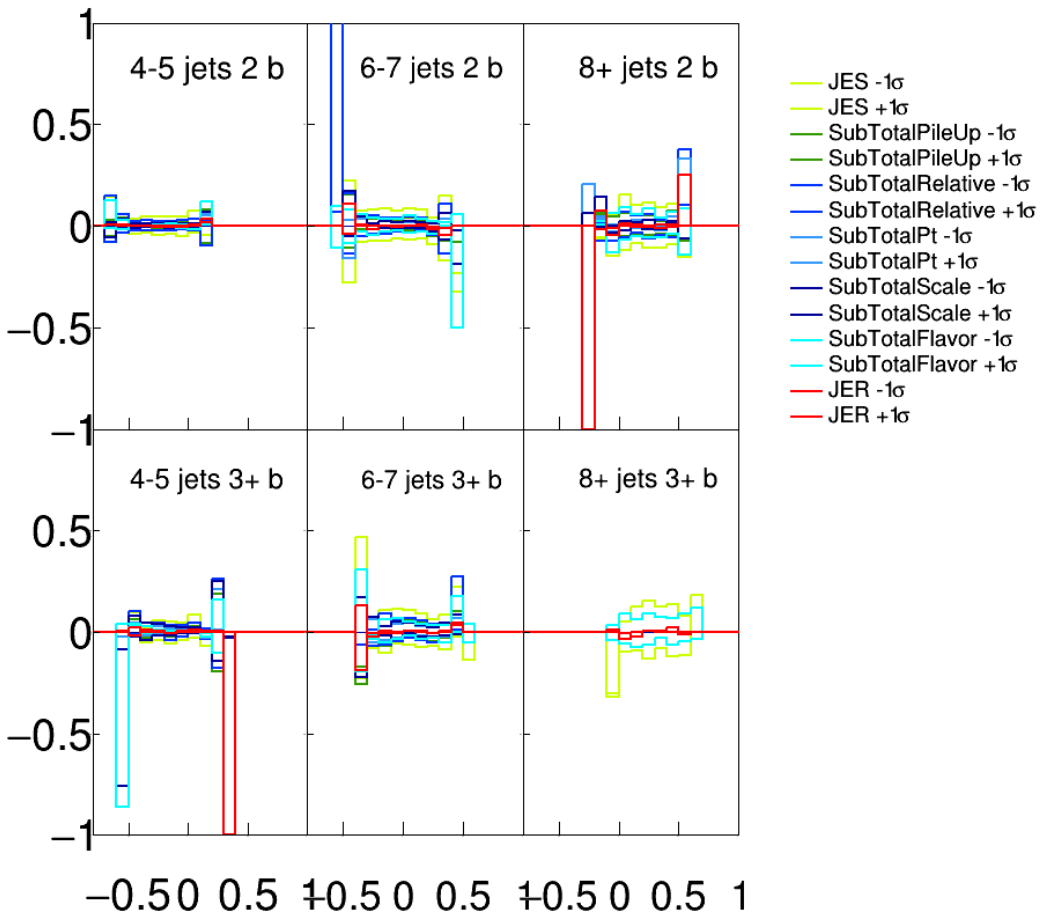

Figure 9.5: Variation of JES systematic uncertainties in $t\bar{t}$ MC in $e^{\pm}\mu^{\mp}$ channel.

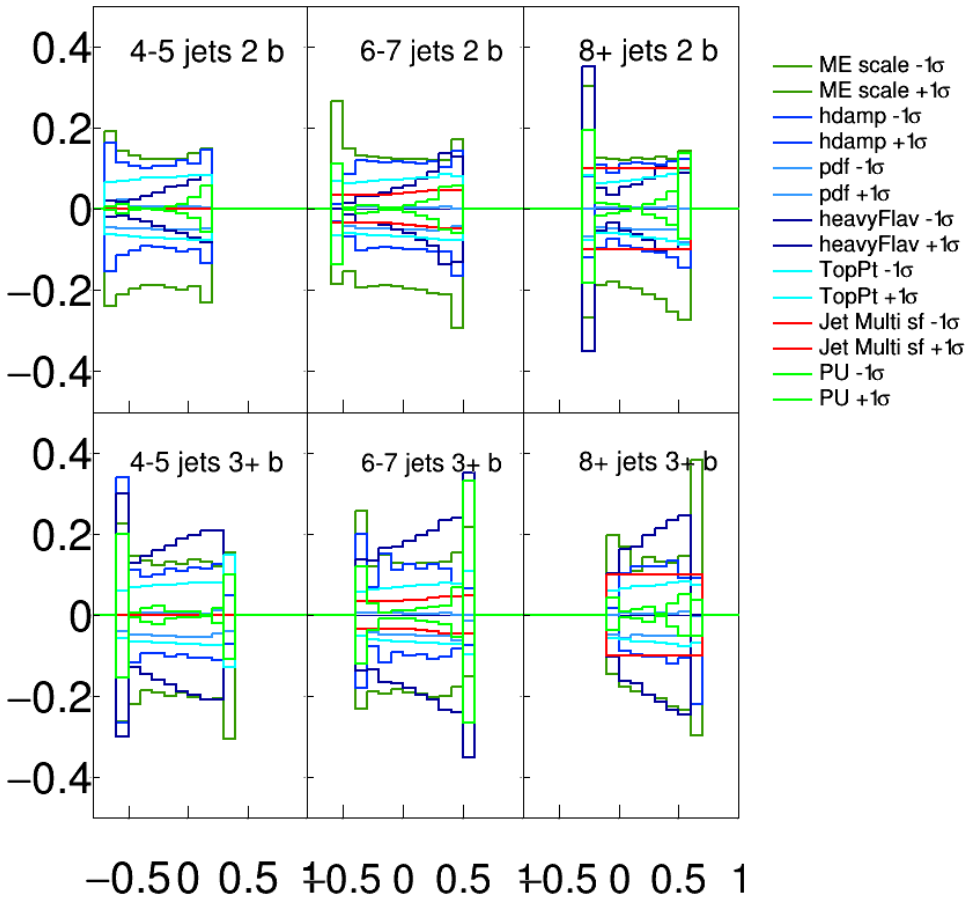

Figure 9.6: Variation of theoretical systematic uncertainties in $t\bar{t}$ MC in $e^{\pm}\mu^{\mp}$ channel.

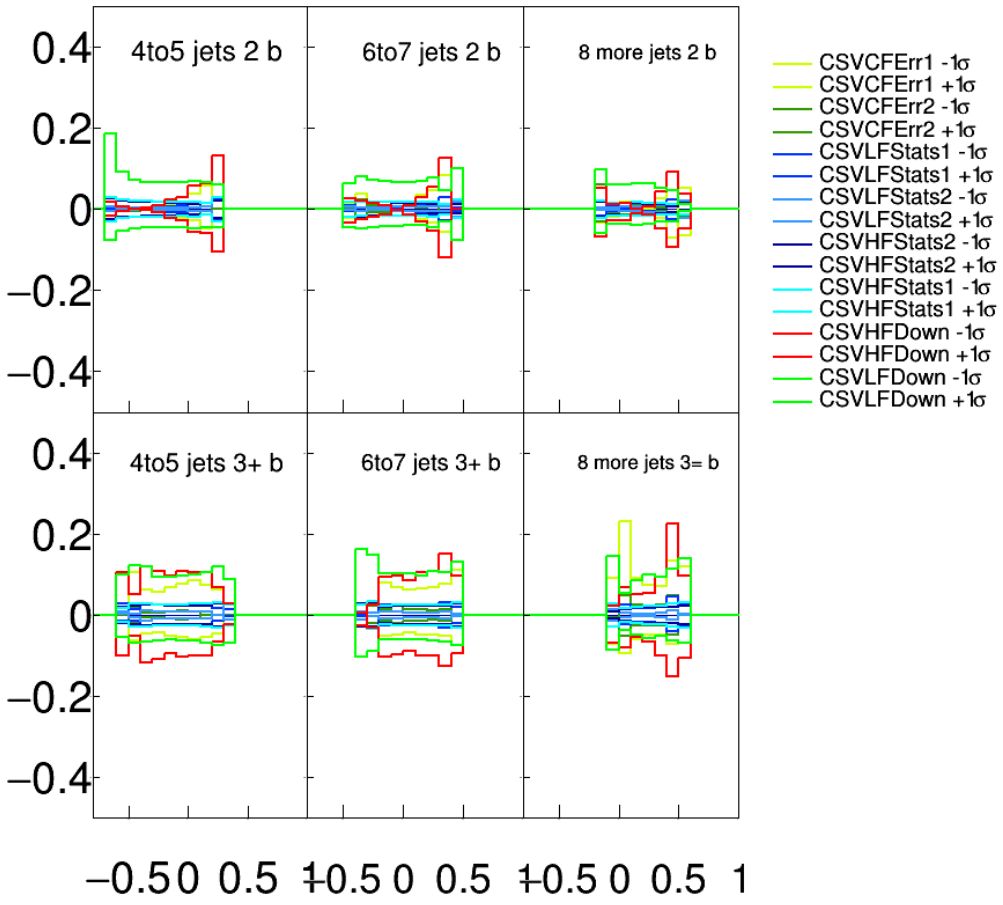

Figure 9.7: Variation of b-tagging systematic uncertainties in $t\bar{t}$ MC in e^+e^- channel.

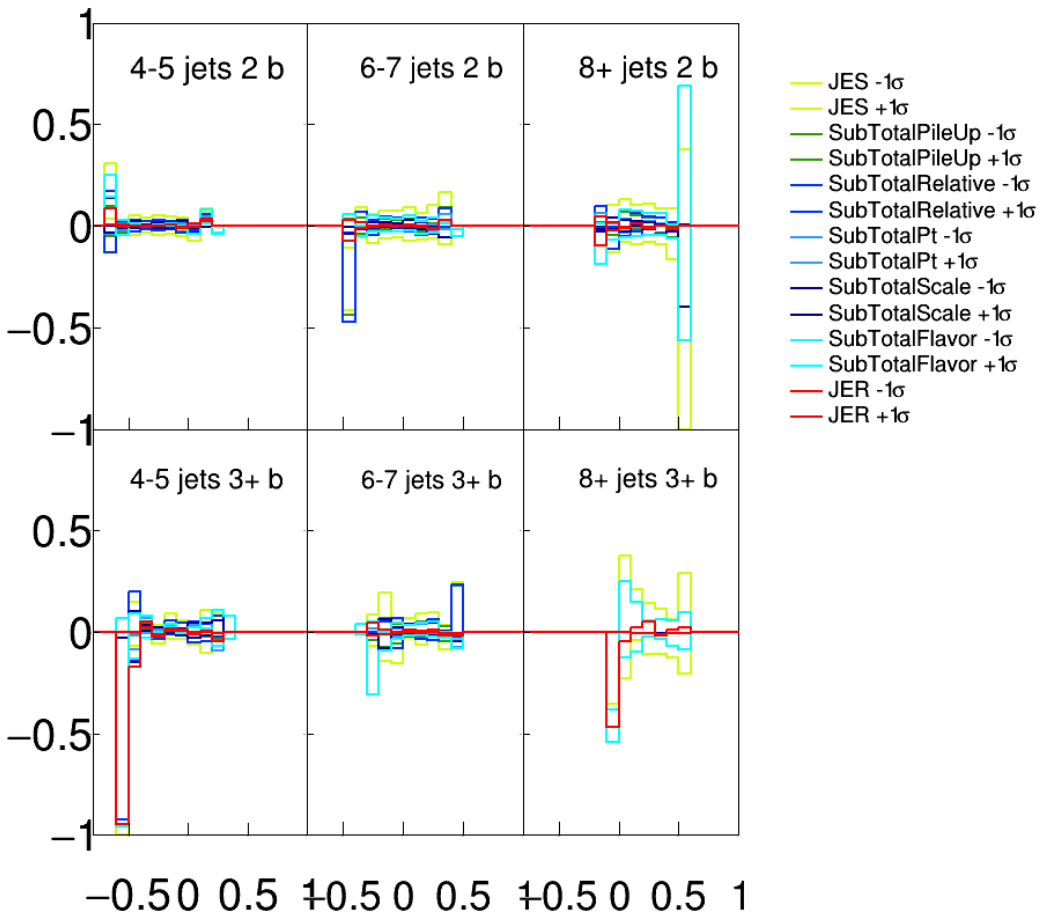

Figure 9.8: Variation of JES systematic uncertainties in $t\bar{t}$ MC in e^+e^- channel.

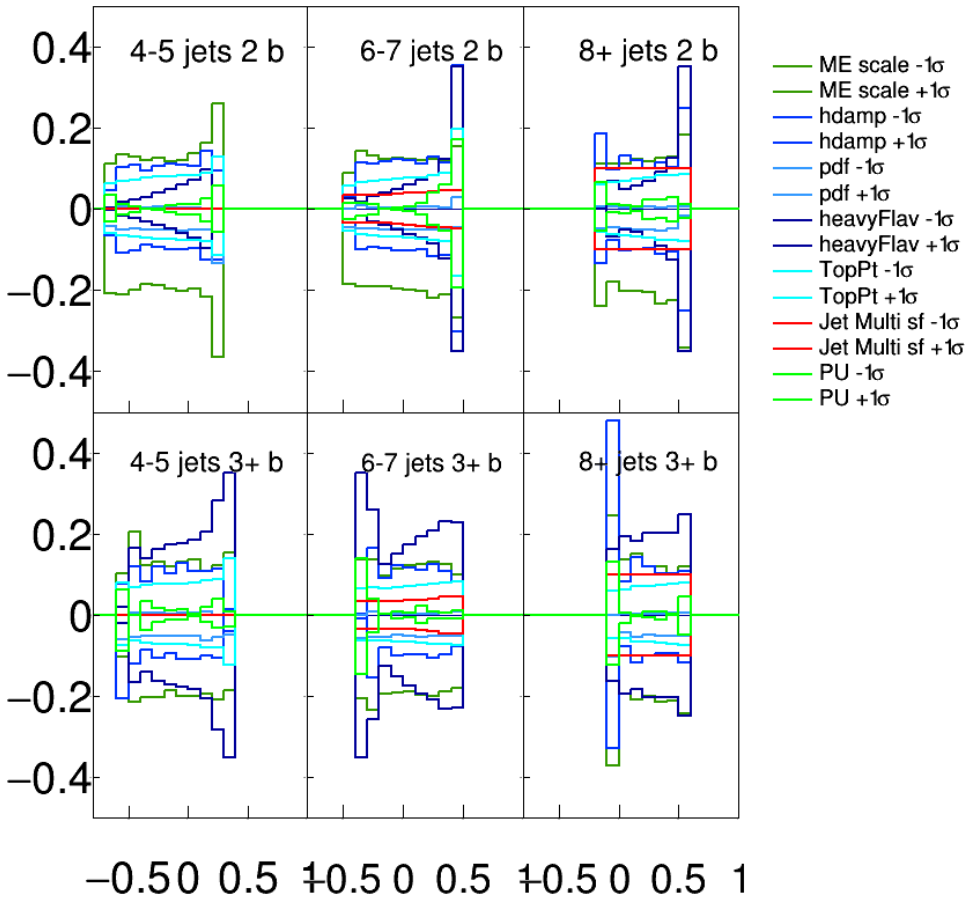

Figure 9.9: Variation of theoretical systematic uncertainties in $t\bar{t}$ MC in e^+e^- channel.

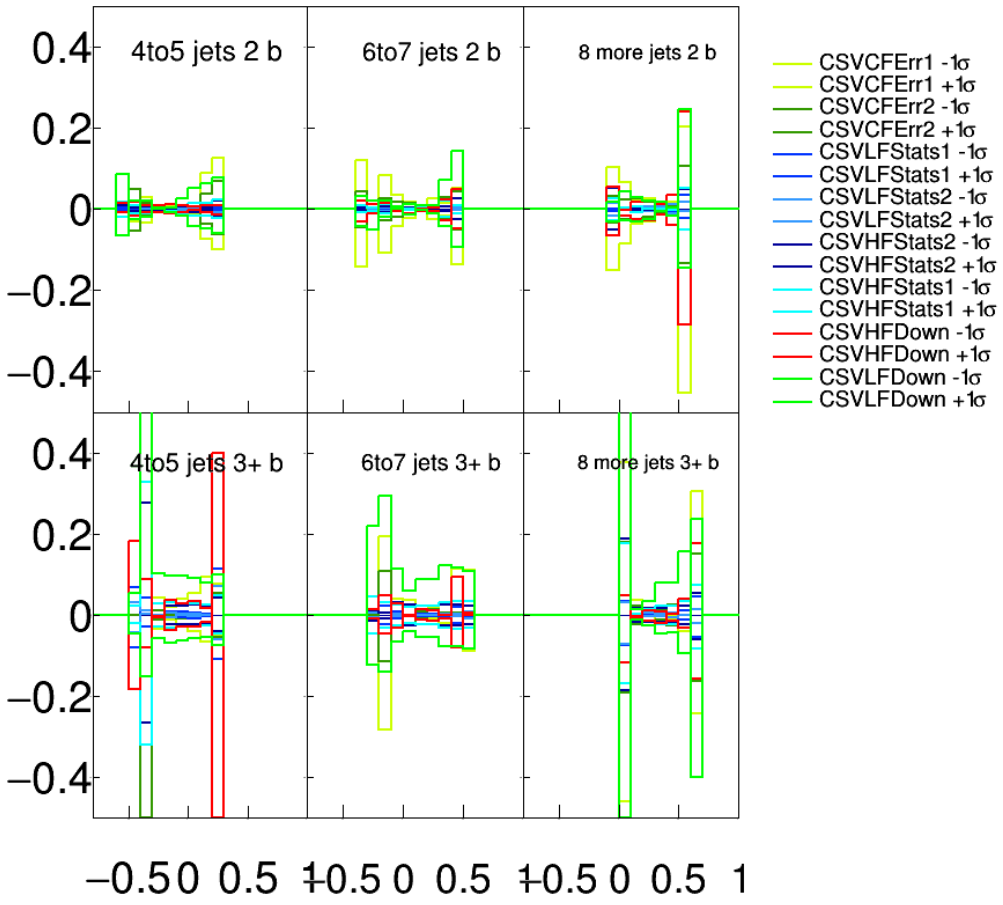

Figure 9.10: Variation of b-tagging systematic uncertainties in $t\bar{t}t\bar{t}$ MC in $\mu^+\mu^-$ channel.

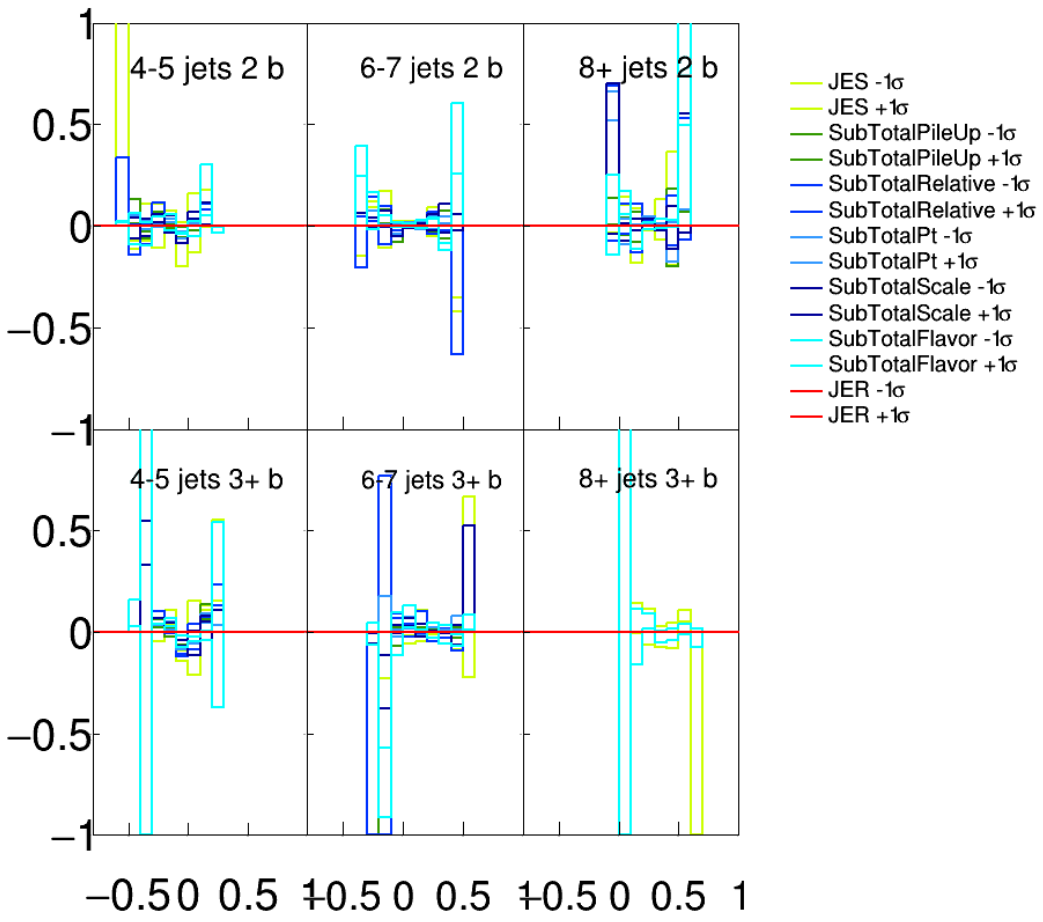

Figure 9.11: Variation of JES systematic uncertainties in $t\bar{t}t\bar{t}$ MC in $\mu^+\mu^-$ channel.

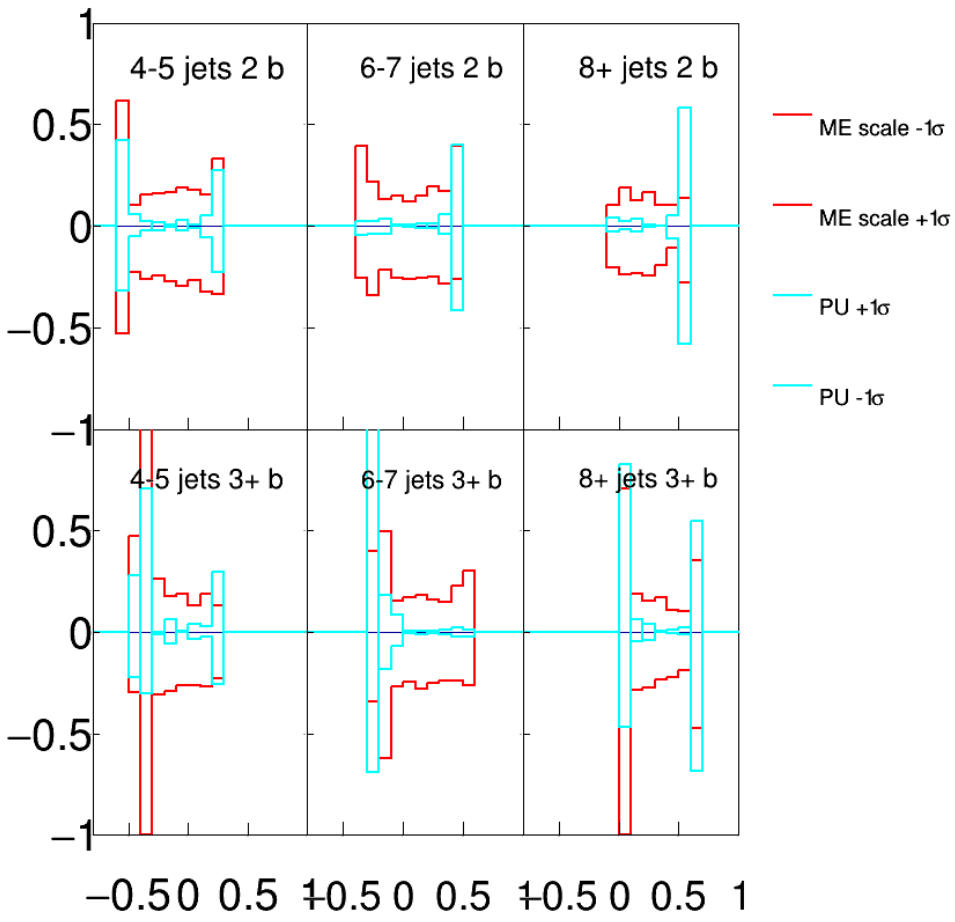

Figure 9.12: Variation of theoretical systematic uncertainties in $t\bar{t}t\bar{t}$ MC in $\mu^+\mu^-$ channel.

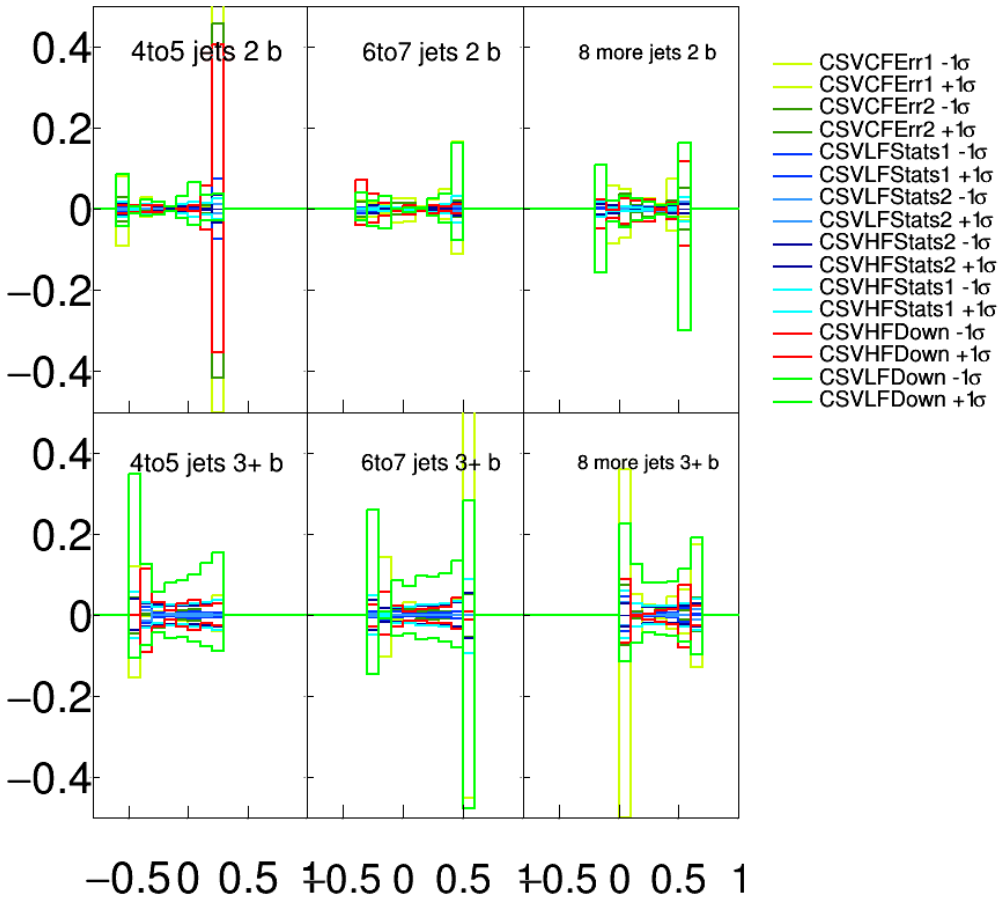

Figure 9.13: Variation of b-tagging systematic uncertainties in $t\bar{t}t\bar{t}$ MC in $e^{\pm}\mu^{\mp}$ channel.

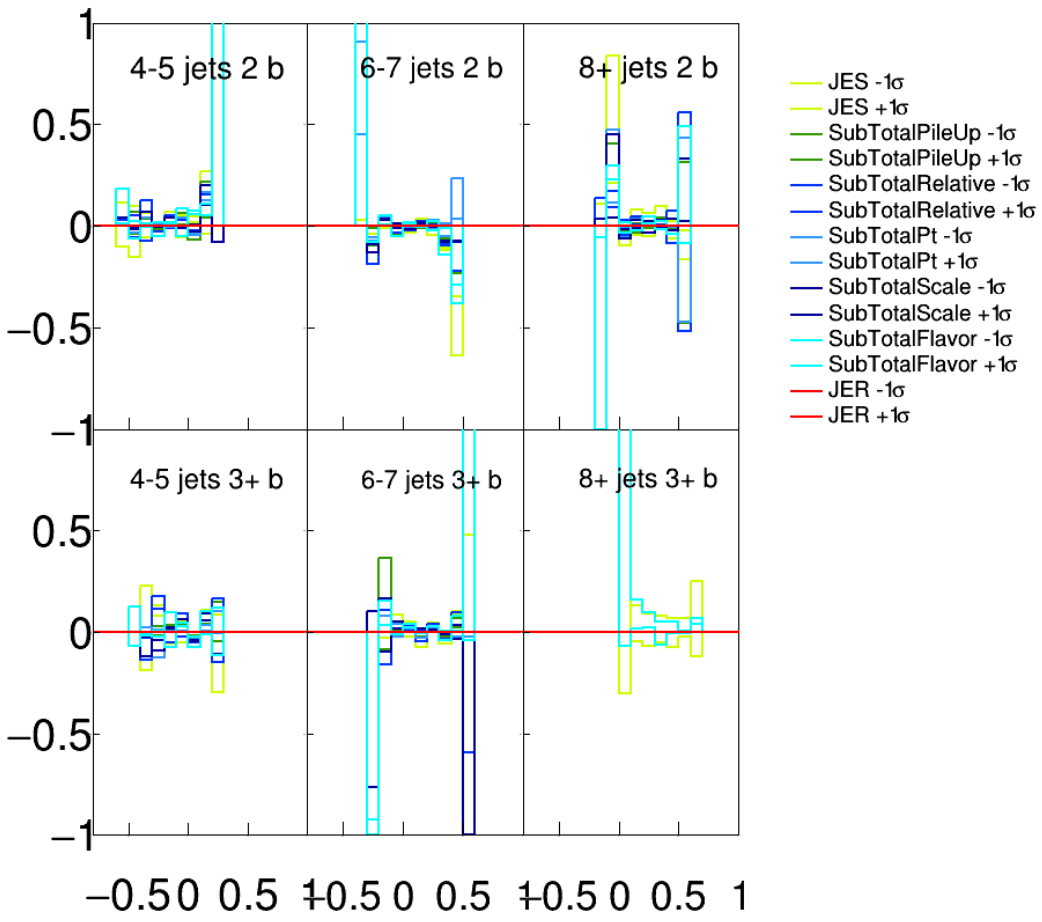

Figure 9.14: Variation of JES systematic uncertainties in $t\bar{t}t\bar{t}$ MC in $e^{\pm}\mu^{\mp}$ channel.

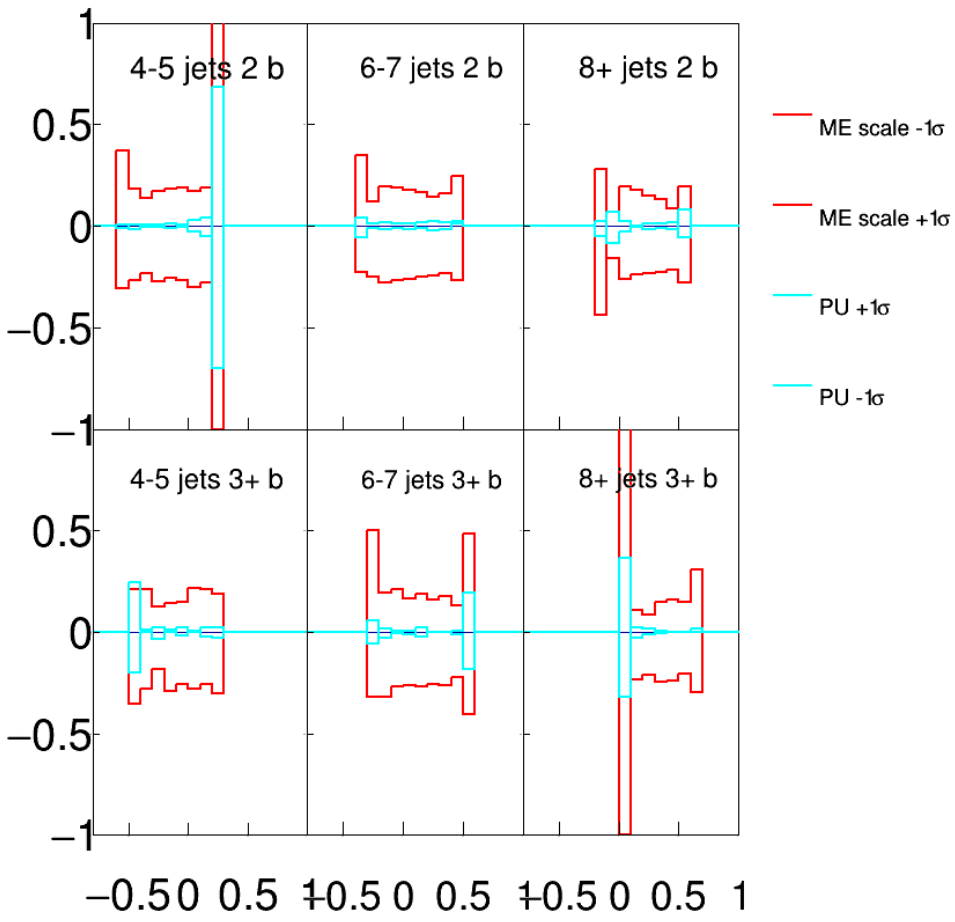

Figure 9.15: Variation of theoretical systematic uncertainties in $t\bar{t}t\bar{t}$ MC in $e^{\pm}\mu^{\mp}$ channel.

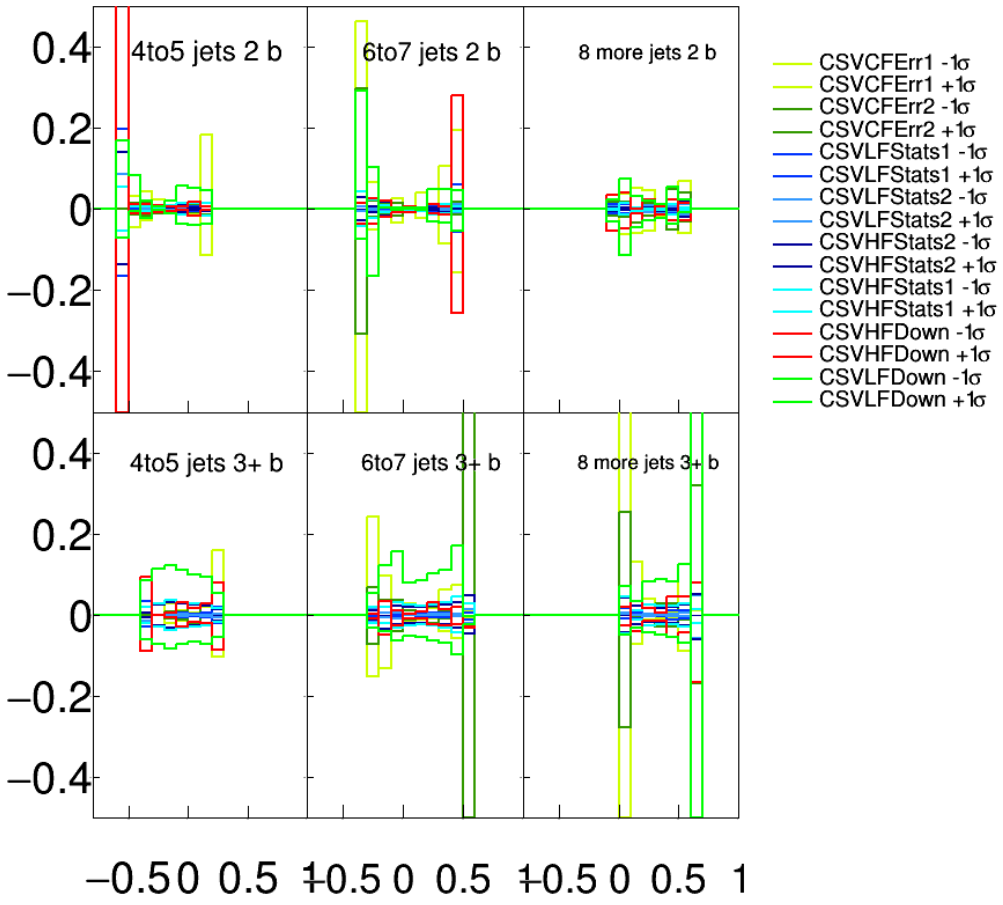

Figure 9.16: Variation of b-tagging systematic uncertainties in $t\bar{t}t\bar{t}$ MC in e^+e^- channel.

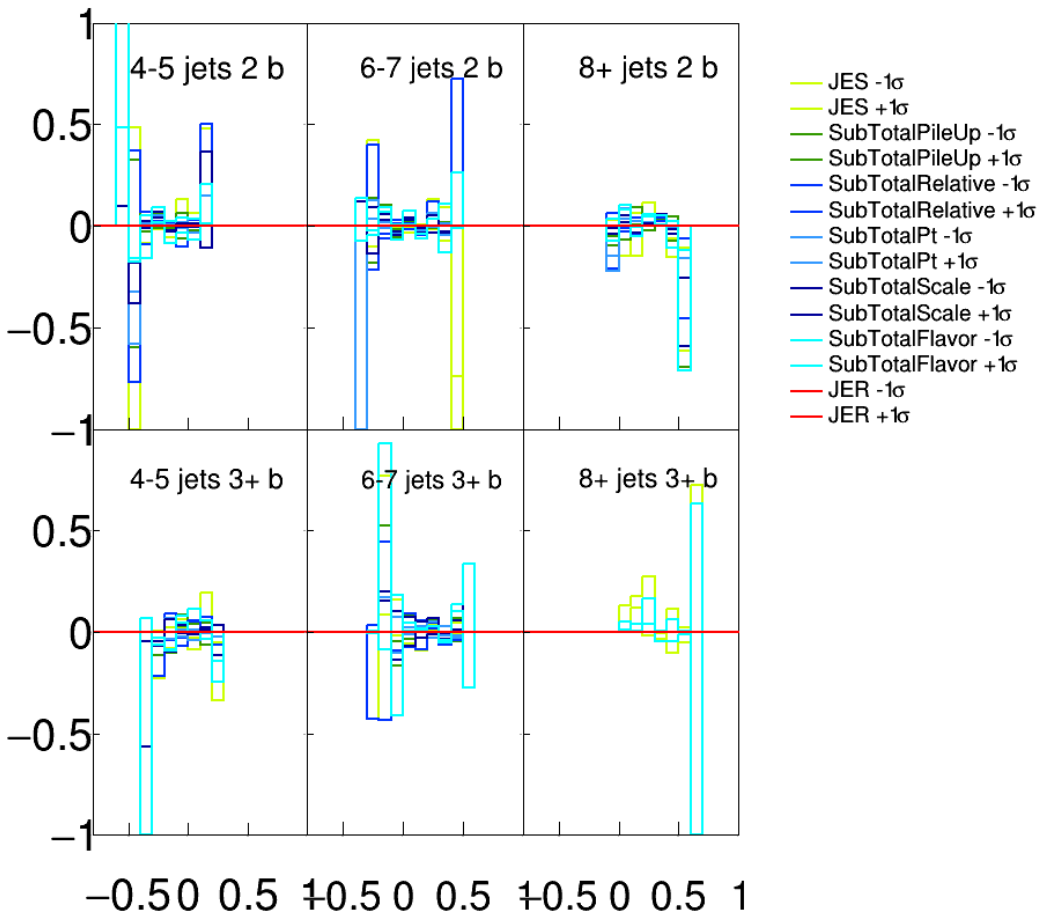

Figure 9.17: Variation of JES systematic uncertainties in $t\bar{t}t\bar{t}$ MC in e^+e^- channel.

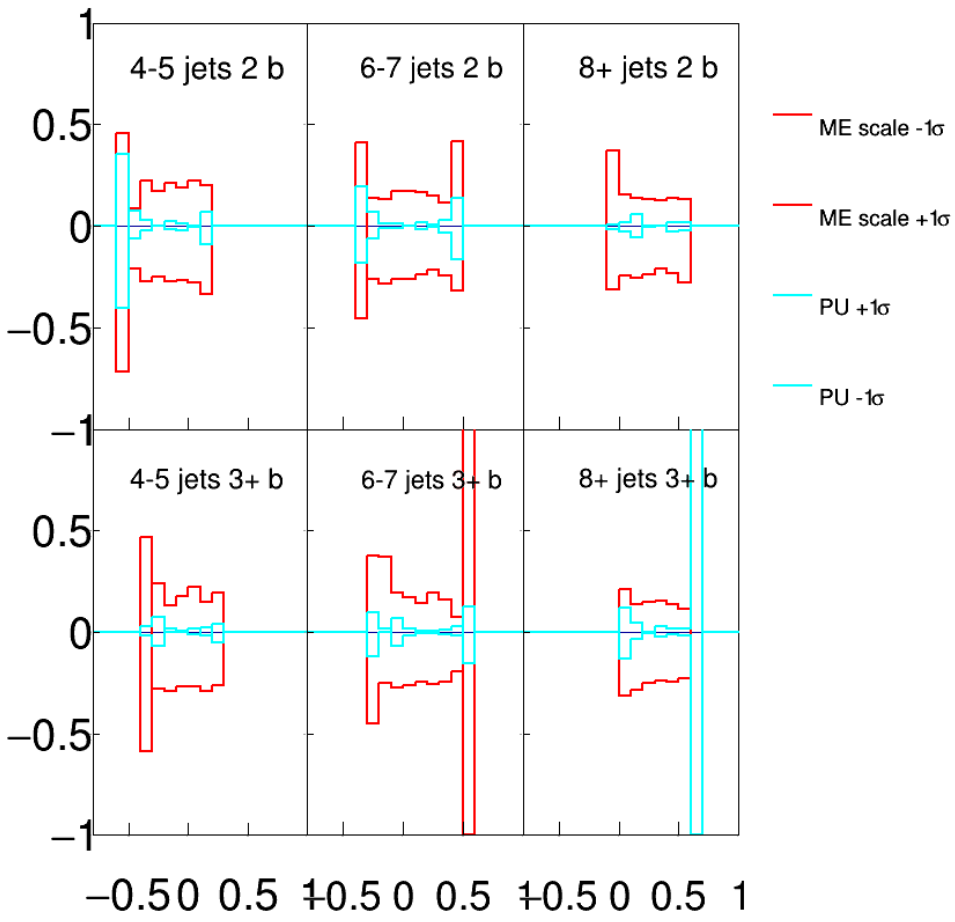

Figure 9.18: Variation of theoretical systematic uncertainties in $t\bar{t}t\bar{t}$ MC in e^+e^- channel.

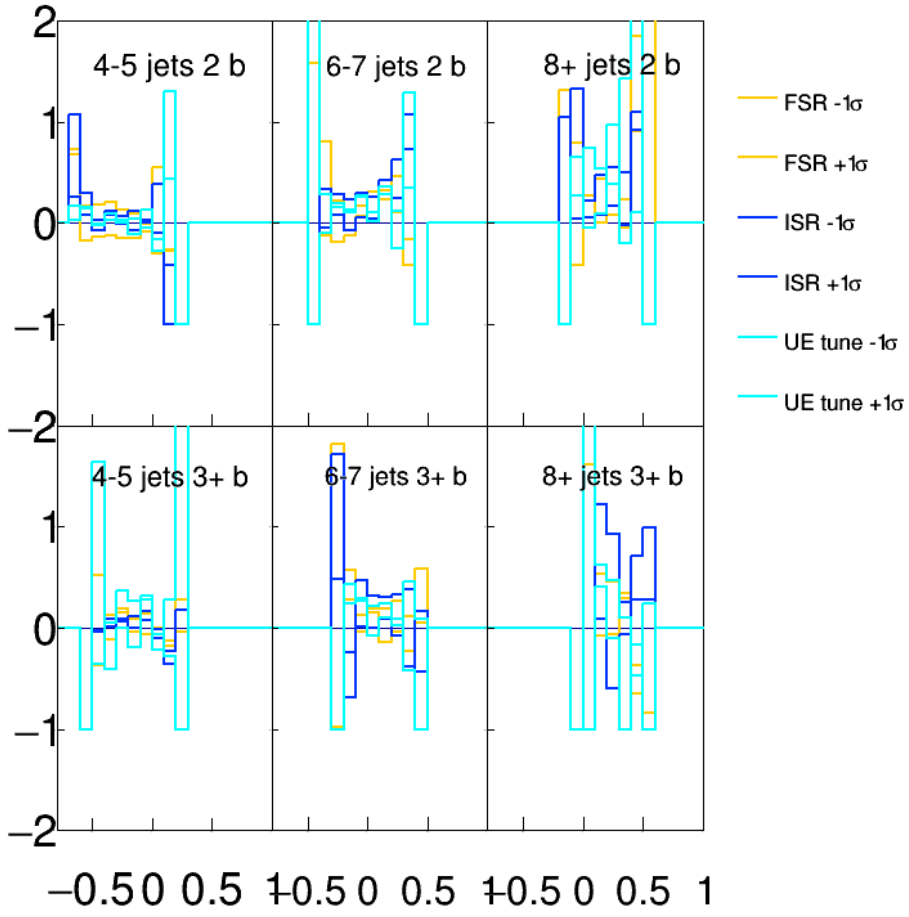

Figure 9.19: Variation of parton shower tune systematic uncertainties in $t\bar{t}$ MC $\mu^+\mu^-$ channel

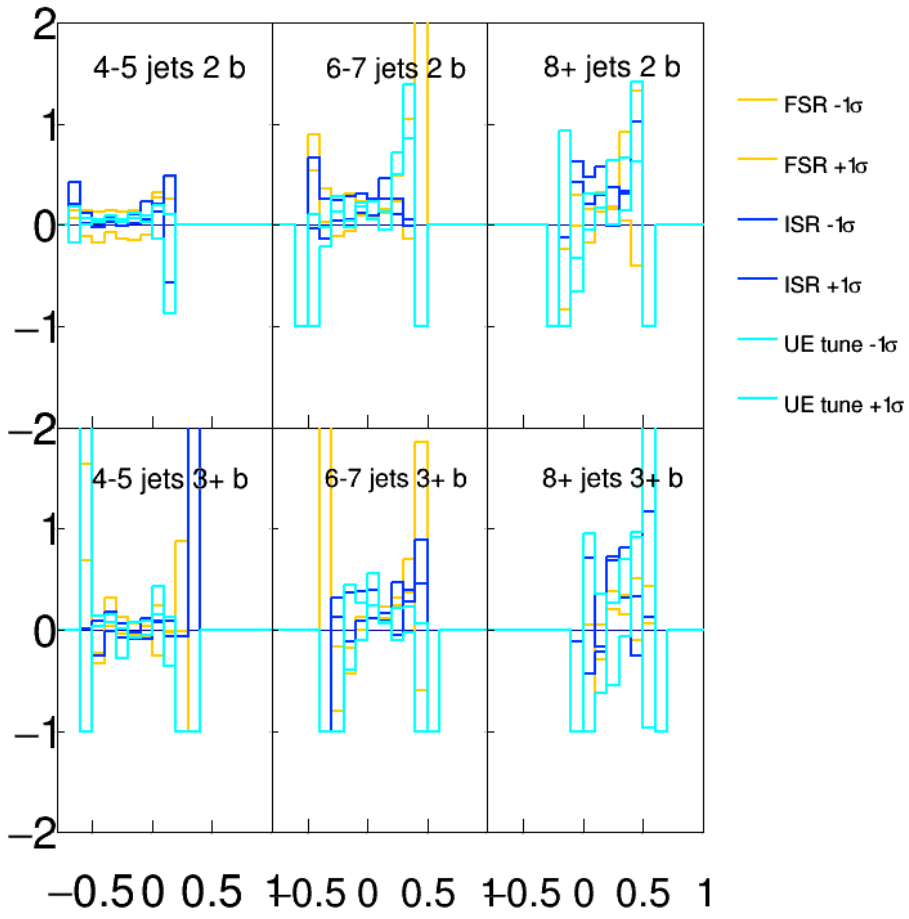

Figure 9.20: Variation of parton shower tune systematic uncertainties in $t\bar{t}$ MC $e^{\pm}\mu^{\mp}$ channel

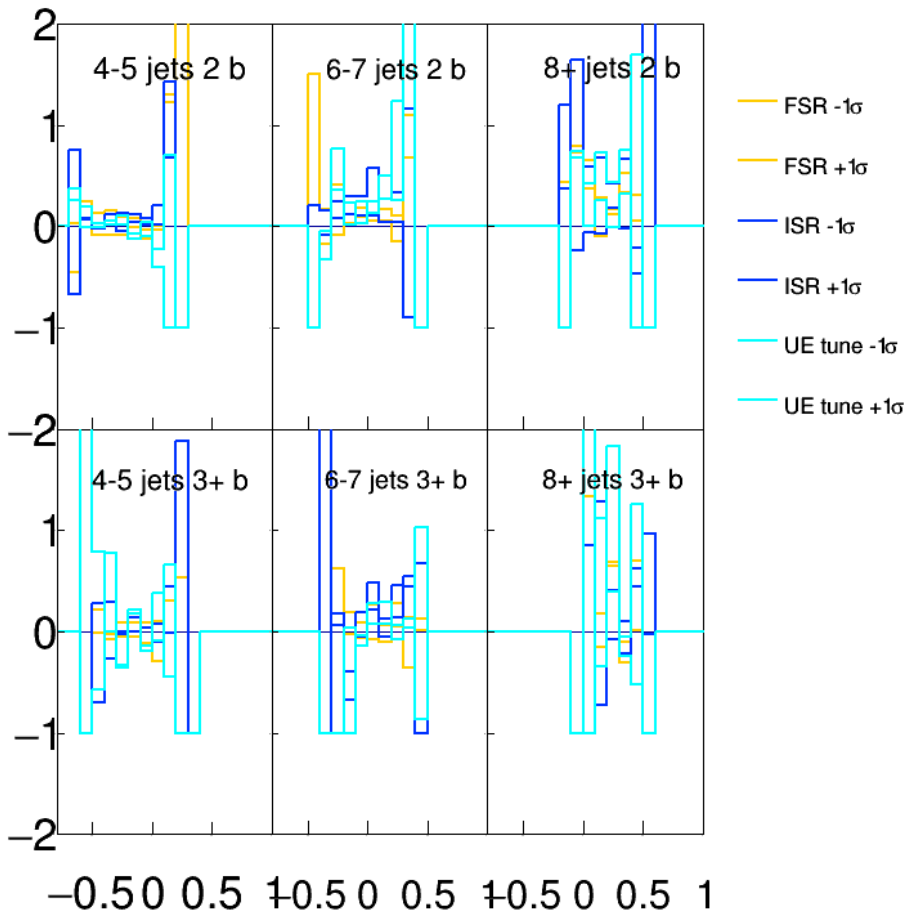

Figure 9.21: Variation of parton shower tune systematic uncertainties in $t\bar{t}$ MC e^+e^- channel

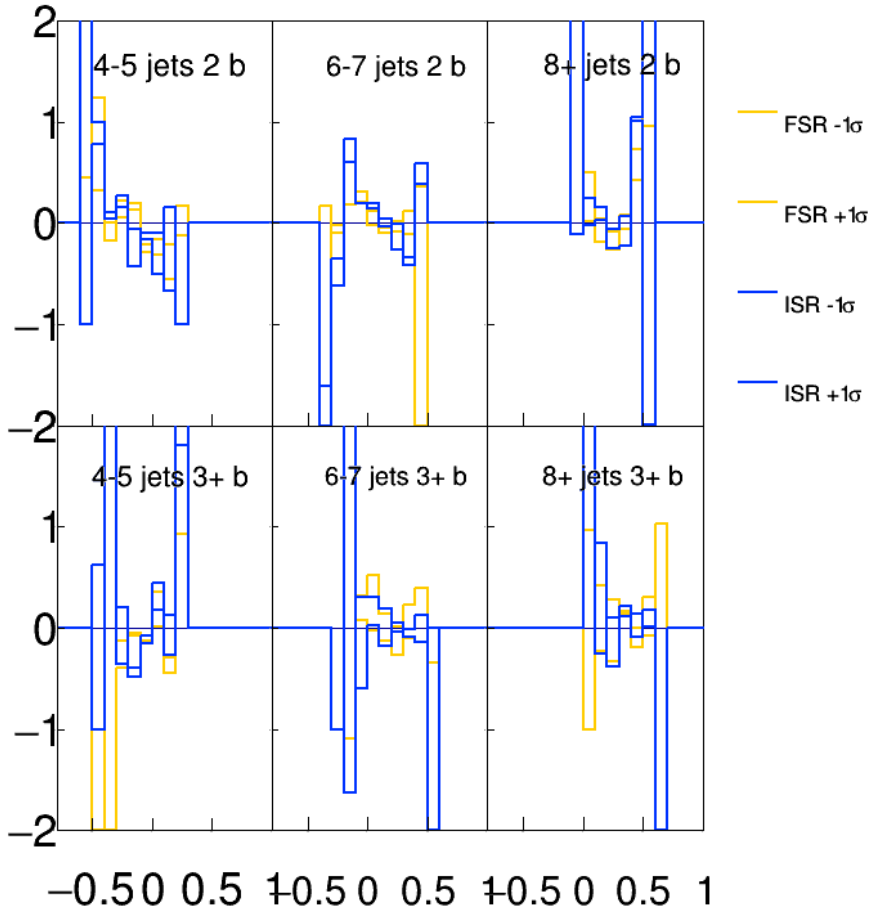

Figure 9.22: Variation of parton shower tune systematic uncertainties in $t\bar{t}t\bar{t}$ MC in $\mu^+\mu^-$ channel

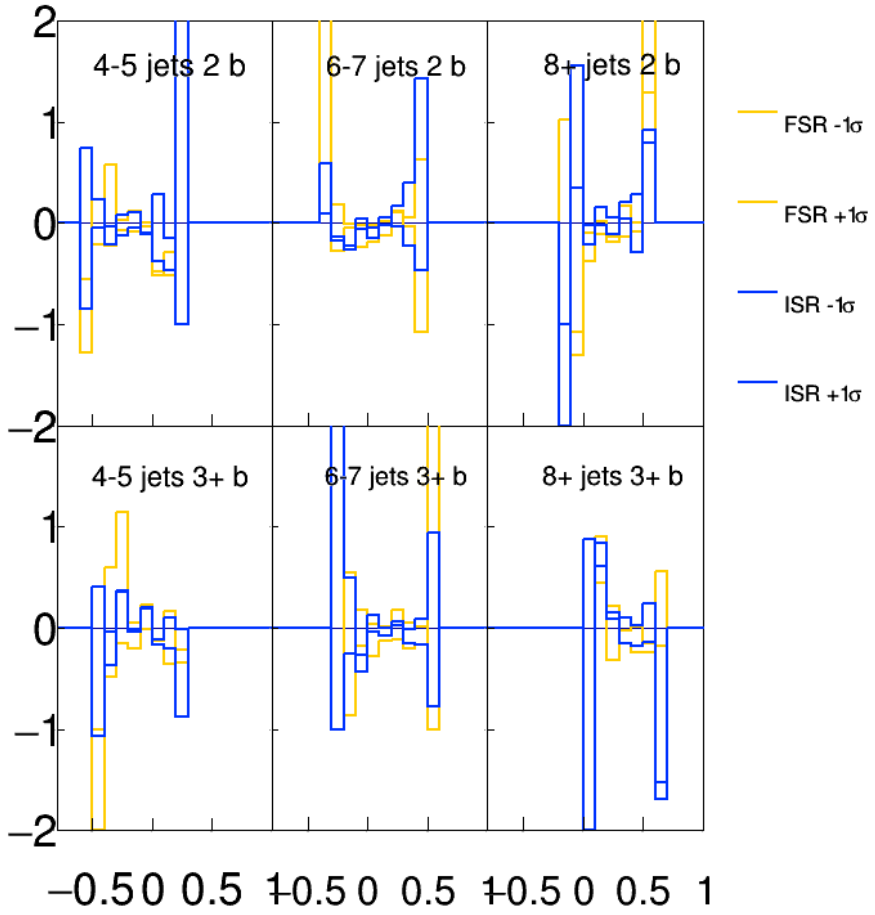

Figure 9.23: Variation of parton shower tune systematic uncertainties in $t\bar{t}t\bar{t}$ MC in $e^{\pm}\mu^{\mp}$ channel

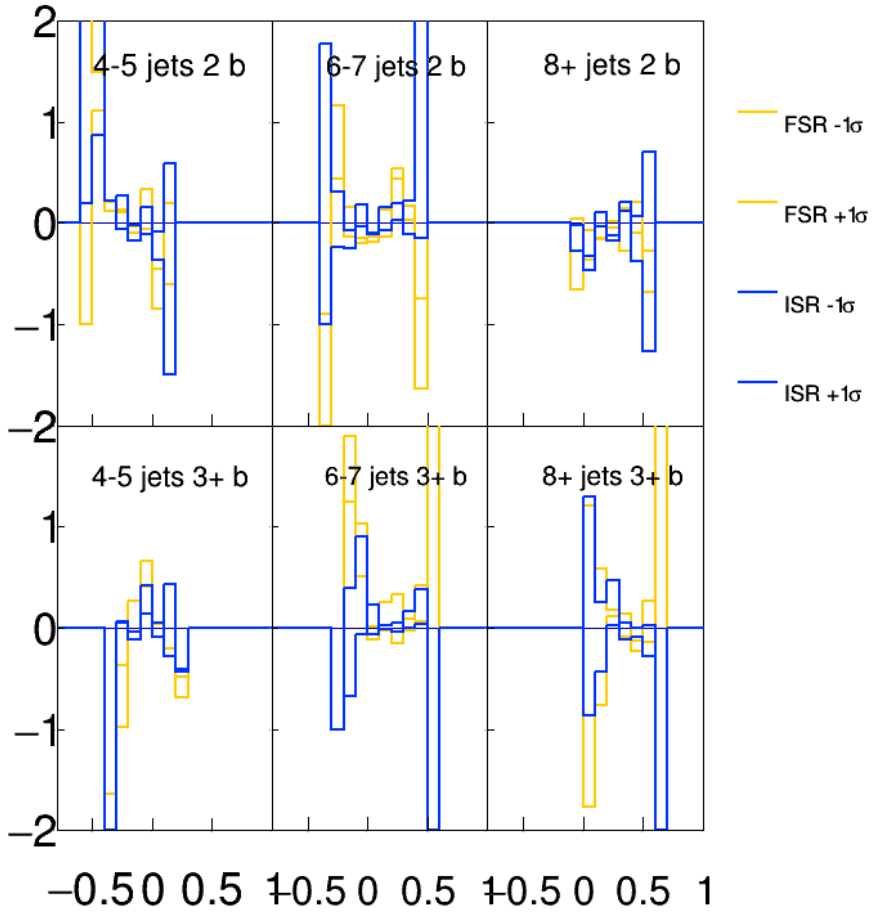

Figure 9.24: Variation of parton shower tune systematic uncertainties in $t\bar{t}t\bar{t}$ MC in e^+e^- channel

Chapter 10

Signal-strength Extraction and Limit Setting

10.1 Maximum likelihood method and signal strength

Given that s is the number of hypothesis predicted signal counts, and b is the number background counts for different bins, The standard model hypothesis is that of signal:

$$s = L \times \sigma_{signal}^{SM} \tag{10.1}$$

where L is the luminosity and σ_{signal}^{SM} is the standard model predicted cross-section of signal production rate. The signal strength μ is defined as

$$\mu = \frac{\sigma_{signal}}{\sigma_{signal}^{SM}} \tag{10.2}$$

The number of total event counts is then

$$n = L \times \sigma_{signal} + b \tag{10.3}$$

$$= L \times \mu * \sigma^{SM}_{signal} + b \tag{10.4}$$

$$= \mu \times s + b \tag{10.5}$$

For a binned shape analysis, the mean value of the number of events in the i^{th} bin is $E[n_i] = \mu s_i + b_i$. Rewriting $b_i = \theta f_{b,i}$, where $f_{b,i}$ is the probability to find a background event in bin i, θ is a nuisance parameter that gives the total expected number of background events. The likelihood function can then be written as

$$L(\mu, \theta) = \prod_{i=1}^{N} \frac{(\mu s_i + \theta f_{b,i})^{n_i}}{n_i!} e^{-(\mu s_i + \theta f_{b,i})} \tag{10.6}$$

For a given binned dataset $(n_1, ..., n_N)$, the signal strength is evaluated from the maximum likelihood estimation

$$\mu = \hat{\mu} \tag{10.7}$$

where the likelihood function is maximized at values $\hat{\mu}, \hat{\theta}$.

In this analysis there are 35 nuisance parameters in the likelihood function which incorporate the systematic uncertainties in the signal and background, and one nuisance parameter to account for the bin-wise statistical uncertainty for each bin containing at least one simulated event. The normalization uncertainties are included assuming a log-normal distribution for the nuisance parameters and the shape uncertainties are included as Gaussian-distributed parameters.

10.2 CL_s method and upper limit

In statistics, a confidence interval (CI) is an interval estimate of a parameter, and how likely the CI is to contain the true value of the parameter is determined by the confidence level (CL). Denote the probability density function for the background-only hypothesis as $f(q_\mu|H_0)$, and the probability density function for signal + background hypothesis as $f(q_\mu|H_\mu)$, where the test statistics $q_\mu = L(s+b)/L(b)$ is the ratio of likelihood functions for the two hypotheses of interest. Figure 10.1 shows the p-value for a signal hypothesis determined from and observed test statistics $q_{\mu,obs}$:

$$p_\mu = \int_{q_{\mu,obs}}^{+\infty} f(q_\mu|H_\mu)dq_\mu \tag{10.8}$$

$CL_b = 1 - p_b$ is thus the compatibility of the background with the background only hypothesis, and $CL_{s+b} = p_\mu$ is the confidence level of accepting the alternative hypothesis.

When a signal is very small compared to background ($\mu s + b \sim b$), the signal + background hypothesis can be rejected, but at the same time the background hypothesis can also be almost rejected is there is a downward fluctuation of the background. A CL_s method [81, 82, 83, 84] is proposed with

$$CL_s = \frac{CL_{s+b}}{CL_b} = \frac{p_\mu}{1 - p_b} \tag{10.9}$$

Here a signal with a very small cross section will never be excluded even when the experiment is not sensitive to the signal.

By iterating and finding the $\mu = \mu_{up}$ for which $CL_s = 5\%$, a confidence interval of the signal strength $[0, \mu_{up}]$ with CL = 95% can be found, and μ_{up} gives the upper limit

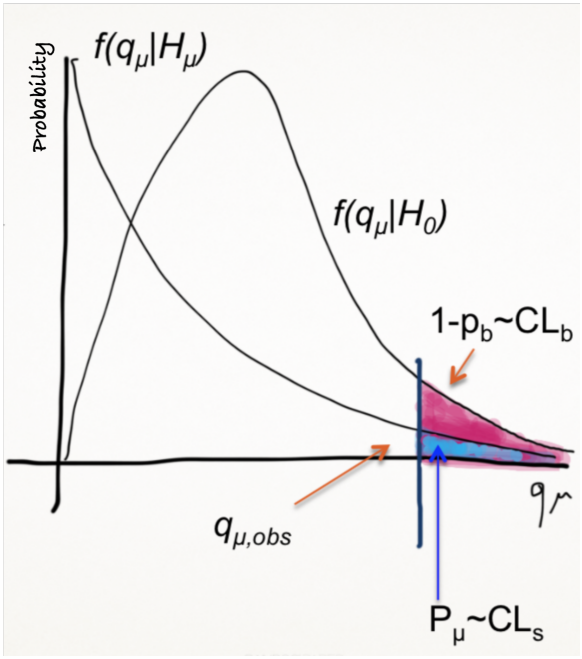

Figure 10.1: Probability density functions for null hypothesis H_0 and alternative hypothesis H_μ

of signal.

10.3 Fits to signal depleted region

10.3.1 Signal injection test

As a first step, a test of the fit stability was conducted by determining the variance of signal strength parameter for different assumptions of injected signal. For each signal strength testing point 100 randomized Asimov toy datasets (i.e. the datasets in which all observed quantities are set equal to their expected values) are used, each with nuisance parameters fluctuated according to the pre-fit uncertainties and they are fitted using a maximum likelihood method. The injection test in which the $\mu^+\mu^-$, $\mu^\pm e^\mp$ and e^+e^- channels

are fitted simultaneously is shown in Fig. 10.2. General good stability is found during the fitting procedure, and more than 90% of the toys converged to the injected signal strength. Good linearity of the average fit was also observed.

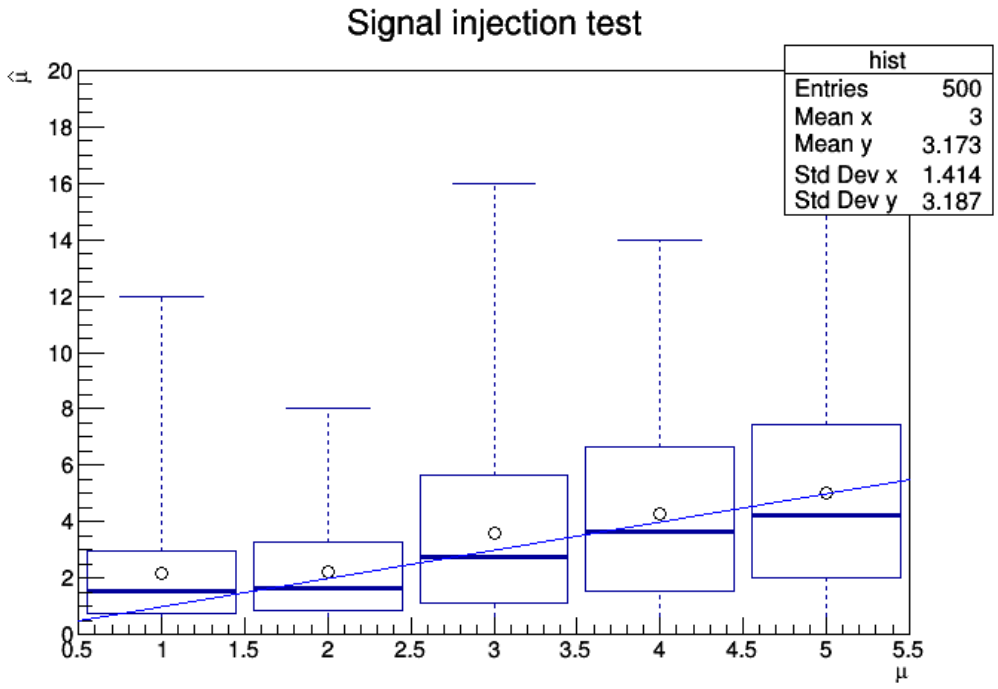

Figure 10.2: Signal injection test with randomized Asimov toy datasets in the combined channels fit. The open circles are the expected average signal strength from the 100 Asimov toy datasets, the horizontal lines are the median values of the expected signal strength, the open boxes include 50% of the expected signal strength values with the same median and the vertical dashed lines include 75% of the expected signal strength values with the same median.

10.3.2 Blinded fit

A fit to a signal depleted region is performed in each sub-channel and in all sub-channels simultaneously. The signal sensitive region is defined to be $N_{\mathrm{j}} \geq 8$, $N_{\mathrm{tags}}^{\mathrm{M}} \geq 3$ category, and the other jet and tag multiplicity categories are considered signal depleted regions. In the first step, these are used to determine the values of the nuisance parameters in a signal-blinded fit. The expected upper limits and signal significances calculated with CL_s method for each fit are summarized in Table 10.1.

Table 10.1: Summary of expected upper limits, expected upper cross section with CL=95% and signal significance of $t\bar{t}t\bar{t}$ production with bin-to-bin statistical uncertainty on MC predictions.

Channel	Expected limit $\times\sigma_{t\bar{t}t\bar{t}}^{SM}$	Expected cross section fb^{-1}	Expected signal significance (s.d.)
$\mu\mu$	$15.8^{+9.6}_{-5.4}$	$143.8^{+87.4}_{-49.1}$	0.16
μe	$9.3^{+5.9}_{-3.3}$	$84.6^{+53.7}_{-30.0}$	0.28
ee	$16.6^{+10.7}_{-5.9}$	$151.1^{+99.2}_{-53.7}$	0.16
OS DL Combined	$7.2^{+4.4}_{-2.5}$	$65.5^{+40.0}_{-22.8}$	0.34

The signal strength from maximum likelihood fit in these regions are found to be extremely small, ~ 0, as expected, and verifies the choice of the signal depleted region. The post-fit distributions of the discriminant show good data/simulation agreement, and provide good constraints on the rare processes backgrounds ($t\bar{t} + Z/W/H$, ttXY), as can be seen from Figures 10.3 to 10.5. Figure 10.6 to 10.9 show that all of the post-fit nuisance parameter values from the blinded fit are consistent with their initial values to well within

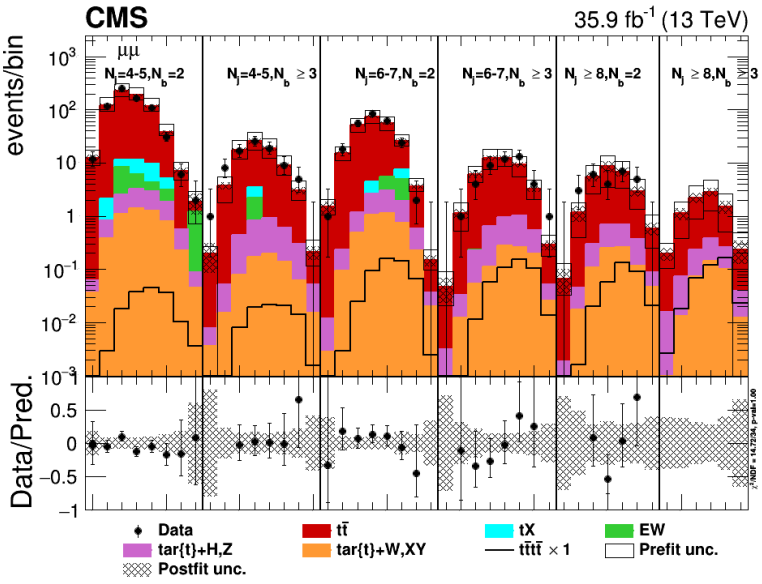

Figure 10.3: Postfit control distributions from signal region blinded fit in $\mu\mu$ channel.

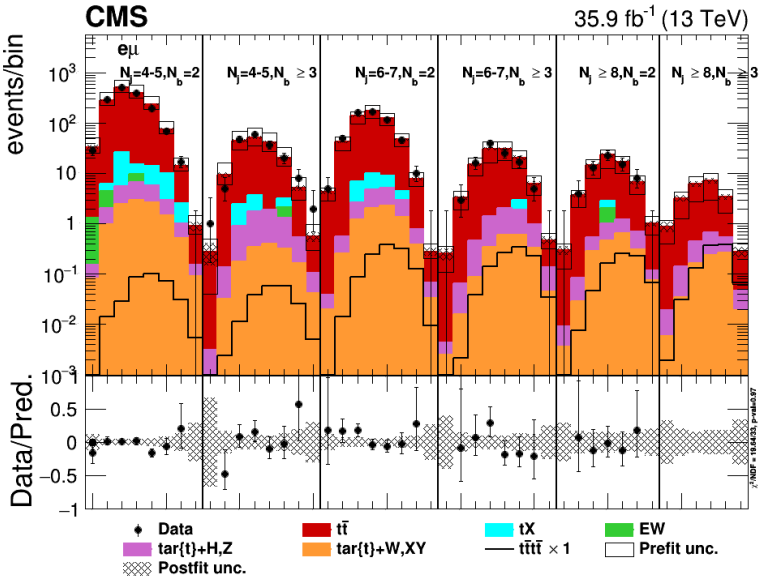

Figure 10.4: Postfit control distributions from signal region blinded fit in $e\mu$ channel.

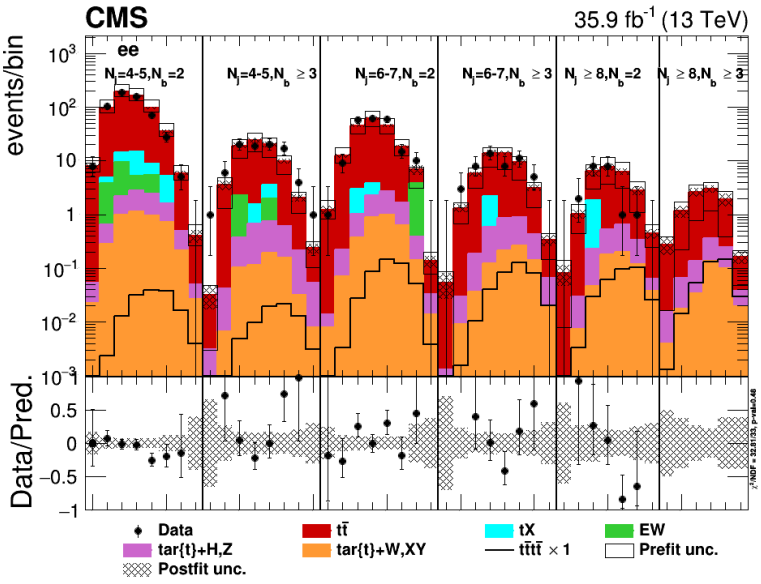

Figure 10.5: Postfit control distributions from signal region blinded fit in *ee* channel.

their estimated uncertainties.

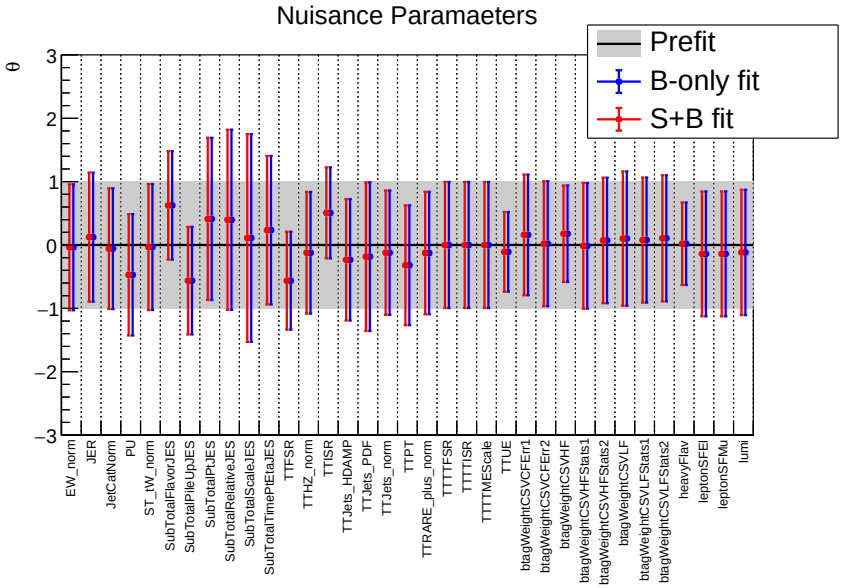

Figure 10.6: Pulls of the nuisance parameters from signal region blinded fit in $\mu\mu$ channel.

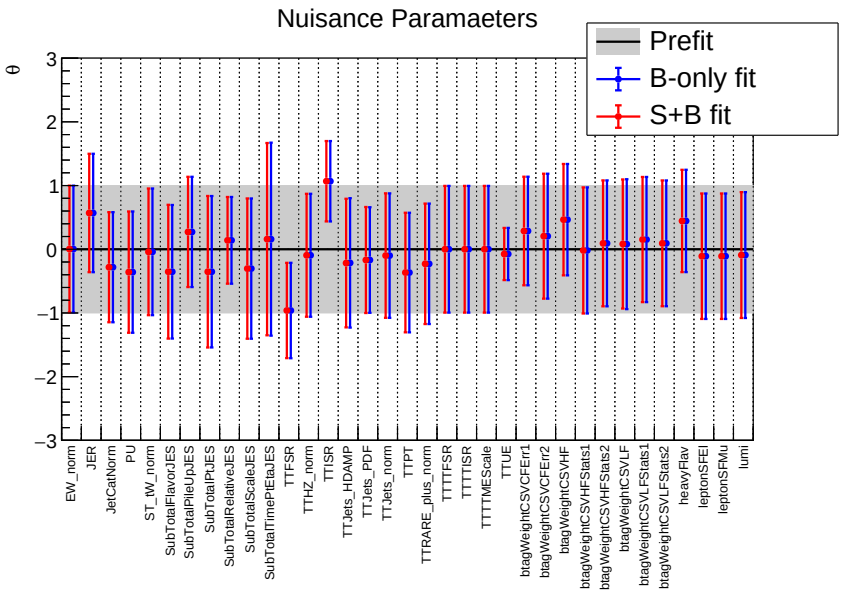

Figure 10.7: Pulls of the nuisance parameters from signal region blinded fit in $e\mu$ channel.

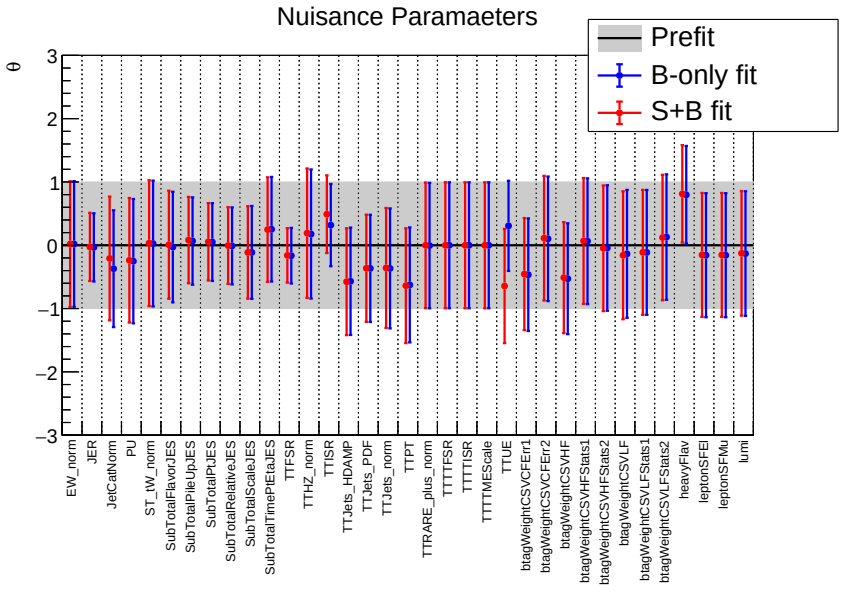

Figure 10.8: Pulls of the nuisance parameters from signal region blinded fit in ee channel.

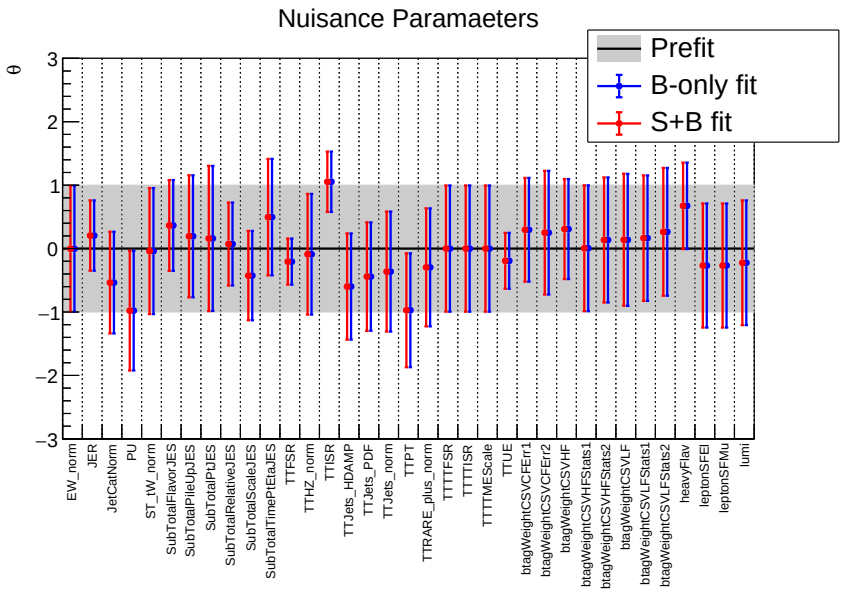

Figure 10.9: Pulls of the nuisance parameters from signal region blinded fit combining three channels.

10.4 Unblinding

As no problems were observed with the blinded fit, the signal region was unblinded and the fit repeated to search for a signal. This was done separately in each sub-channel as well as simultaneously in all three sub-channels. No signal event was observed. The maximum-likelihood signal strength of $t\bar{t}t\bar{t}$ production was found to be $\mu = 0^{+2.7}$ with zero observed significance, where the upper uncertainty is the 1 standard deviation value. The fit was used to set a 95% CL upper-limit on the $t\bar{t}t\bar{t}$ cross section. The results from an asymptotic CL_s calculation are summarized in Table 10.2. The corresponding post-fit discriminant distributions are shown in Figures 10.10 and 10.11, and the post-fit nuisance parameter values are shown in Figures 10.12 to 10.15. Again, all of the nuisance parameters

are consistent with their initial values to well within their estimated uncertainties.

Table 10.2: Summary of expected upper limits, expected upper cross section, observed upper limits and observed upper cross section of $t\bar{t}t\bar{t}$ production with CL=95% in OS DL channel.

Channel	Expected limit $\times\sigma^{SM}_{t\bar{t}t\bar{t}}$	Expected cross section fb^{-1}	Observed limit $\times\sigma^{SM}_{t\bar{t}t\bar{t}}$	Observed cross section fb^{-1}
$\mu\mu$	$15.6^{+9.3}_{-5.3}$	$143.5^{+85.6}_{-48.8}$	20.2	185.8
μe	$10.0^{+6.3}_{-3.5}$	$92.0^{+58.0}_{-32.2}$	8.2	75.4
ee	$16.6^{+10.7}_{-5.9}$	$152.7^{+98.4}_{-54.3}$	11.9	109.5
Combined	$7.3^{+4.5}_{-2.5}$	$67.2^{+41.4}_{-23.0}$	6.9	63.5

10.5 Combination with single-lepton, same-sign dilepton and multilepton channels

Independent searches for the SM $t\bar{t}t\bar{t}$ production have been performed in single-lepton (SL) channels and same-sign (SS) dilepton/multilepton channels [85]. A combination of the results with these orthogonal channels was performed for the complementarity of the search. The combination is based on the product of the likelihood functions from each channel, and the systematic uncertainties are treated as uncorrelated because of their independent feature [86]. The combined cross section on the $t\bar{t}t\bar{t}$ production is 13^{+11}_{-9} fb with an observed significance of 1.4 standard deviations, and the combined expected and observed 95% CL upper limits on the $t\bar{t}t\bar{t}$ production are 20^{+10}_{-6} fb and 33 fb, respectively. A

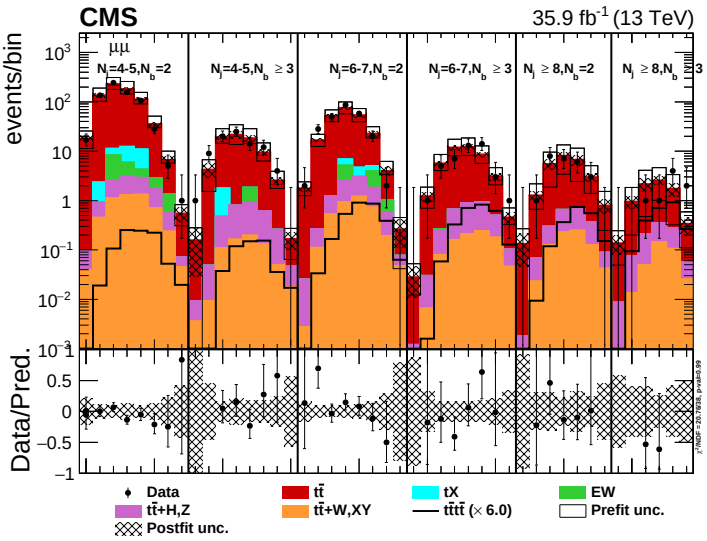

(a) $\mu\mu$

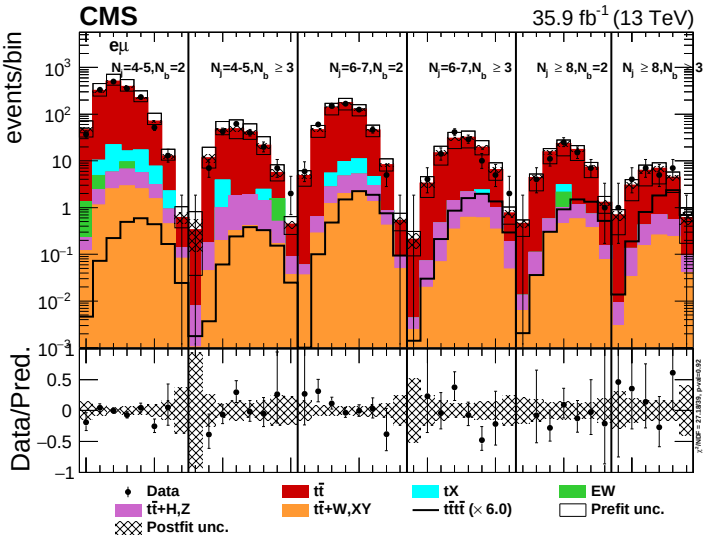

(b) $e\mu$

Figure 10.10: Postfit discriminant distributions for events passing $\mu^+\mu^-$ sub-channel (top) and $\mu^\pm e^\mp$ sub-channel (bottom) baseline selections in all multiplicity categories.

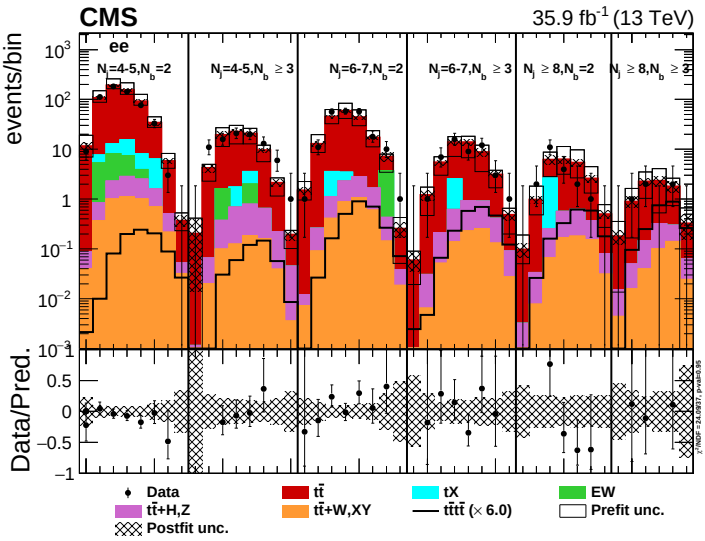

(a) ee

Figure 10.11: Postfit discriminant distributions for events passing e^+e^- sub-channel baseline selection in all multiplicity categories.

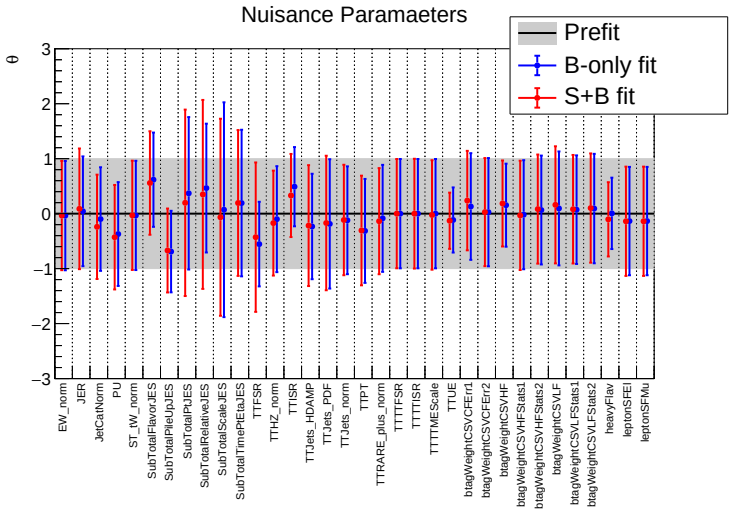

Figure 10.12: Pulls of the nuisance parameters from unblided fit in $\mu\mu$ channel.

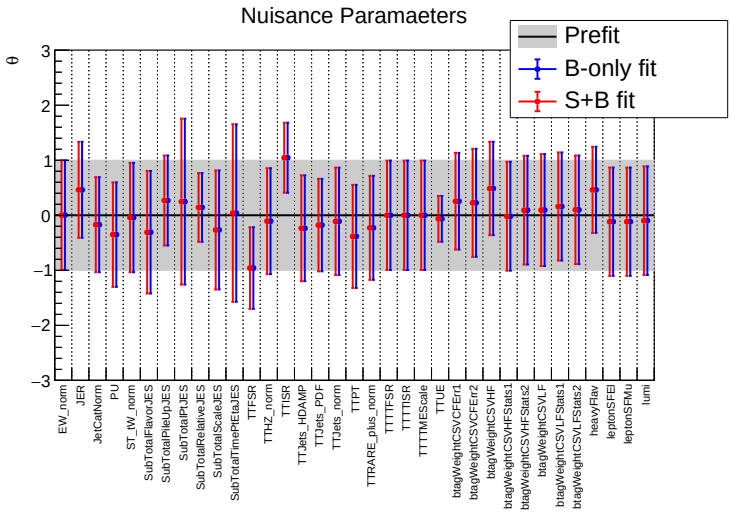

Figure 10.13: Pulls of the nuisance parameters from unblinded fit in $e\mu$ channel.

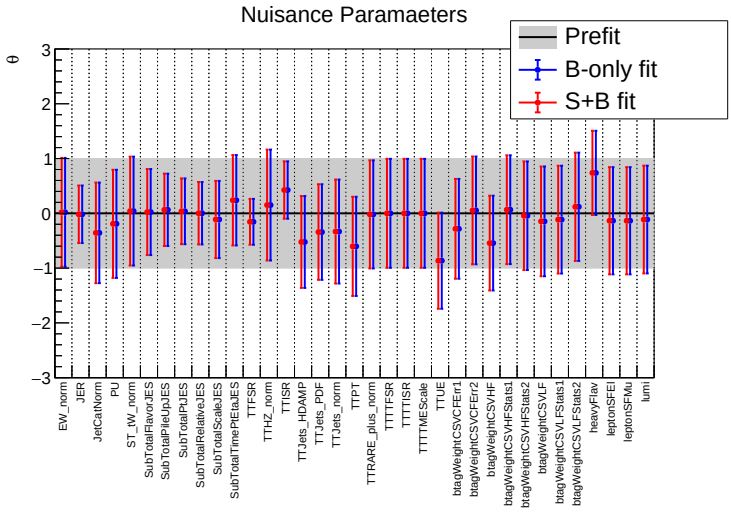

Figure 10.14: Pulls of the nuisance parameters from unblinded fit in ee channel.

summary of the cross section upper limits in each channel and combined is shown Table 10.3

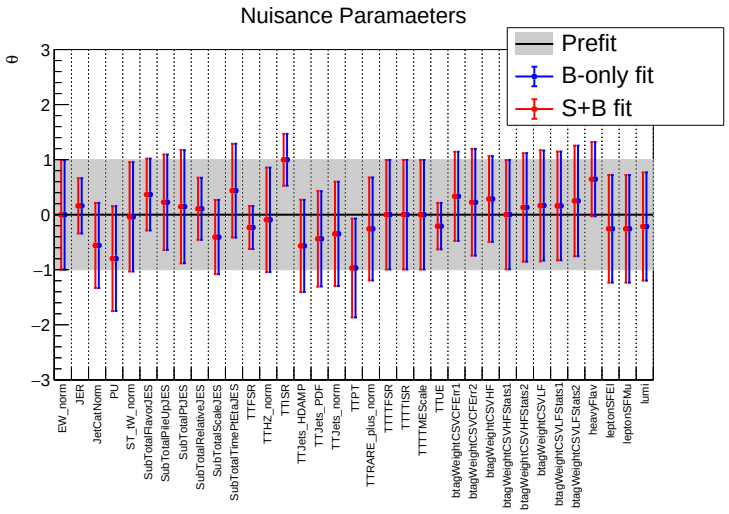

Figure 10.15: Pulls of the nuisance parameters from unblinded fit combining three channels.

Table 10.3: Expected and observed 95% CL upper limits on SM $t\bar{t}t\bar{t}$ production.

Channel	Expected limit ($\times\sigma^{SM}_{t\bar{t}t\bar{t}}$)	Observed limit ($\times\sigma^{SM}_{t\bar{t}t\bar{t}}$)	Expected limit (fb)	Observed limit (fb)
Single lepton	$9.4^{+4.4}_{-2.9}$	10.6	86^{+40}_{-26}	97
Dilepton	$7.3^{+4.5}_{-2.5}$	6.9	67^{+41}_{-23}	64
SL+DL Combined	$5.7^{+2.9}_{-1.8}$	5.2	52^{+26}_{-17}	48
Combined	$2.2^{+1.1}_{-0.7}$	3.6	20^{+10}_{-6}	33

Chapter 11

Conclusions

A search for the process of four top quark production has been performed with multi-variant techniques using the data collected by the CMS experiment during year 2016 corresponding to an integrated luminosity of 35.8 fb^{-1}. The analysis was carried out in opposite-sign dilepton final state. The signal strength has been extracted from a maximum-likelihood fit and no significant deviation was observed from the predicted background. An upper limit on the SM $t\bar{t}t\bar{t}$ production cross-section is set to be $7.3^{+4.5}_{-2.5} \times \sigma^{SM}_{t\bar{t}t\bar{t}}$ at CL=95% using the asymptotic CL_s method. Combining this analysis with single-lepton channel and same-sign/multilepton channels, the resulting cross section is 13^{+11}_{-9} fb with an observed significance of 1.4 standard deviations.

This combined result poses one of the most stringent constraints to date on $t\bar{t}t\bar{t}$ production. At this stage, this analysis is still heavily affected by large statistical uncertainty. With ~ 4 times more data collected by the CMS experiment during 2017 and 2018, there are more opportunities to refine the MVA method, and to improve the systematic

uncertainties, making it highly possible to give an evidence (3 standard deviation) for the SM $t\bar{t}t\bar{t}$ production.

Bibliography

[1] J. J. Thomson. Cathode rays. *Phil. Mag. Ser.5*, 44:293–316, 1897.

[2] E. Rutherford. Collision of α particles with light atoms. IV. An anomalous effect in nitrogen. *Phil. Mag. Ser.6*, 37:581–587, 1919. [Phil. Mag.90,no.sup1,31(2010)].

[3] N. Bohr. On the Constitution of Atoms and Molecules. *Phil. Mag. Ser.6*, 26:1–24, 1913.

[4] Albert Einstein. Concerning an heuristic point of view toward the emission and transformation of light. *Annalen Phys.*, 17:132–148, 1905.

[5] Louis Victor Pierre Raymond de Broglie. Recherches sur la théorie des quanta. *Annals Phys.*, 2:22–128, 1925.

[6] J. Chadwick. Possible Existence of a Neutron. *Nature*, 129:312, 1932.

[7] E. Radermacher. The Experimental Discovery of the Intermediate Vector Bosons W^+, W^- and Z^0 at the CERN $p\bar{p}$ Collider. *Prog. Part. Nucl. Phys.*, 14:231–328, 1985.

[8] Francis Halzen and Alan D. Martin. *Quarks and Leptons: An introductory Course in Modern Particle Physics*. Wiley, 1984.

[9] M. Tanabashi, K. Hagiwara, K. Hikasa, K. Nakamura, Y. Sumino, F. Takahashi, J. Tanaka, K. Agashe, G. Aielli, C. Amsler, M. Antonelli, D. M. Asner, H. Baer, Sw. Banerjee, R. M. Barnett, T. Basaglia, C. W. Bauer, J. J. Beatty, V. I. Belousov, J. Beringer, S. Bethke, A. Bettini, H. Bichsel, O. Biebel, K. M. Black, E. Blucher, O. Buchmuller, V. Burkert, M. A. Bychkov, R. N. Cahn, M. Carena, A. Ceccucci, A. Cerri, D. Chakraborty, M.-C. Chen, R. S. Chivukula, G. Cowan, O. Dahl, G. D'Ambrosio, T. Damour, D. de Florian, A. de Gouvêa, T. DeGrand, P. de Jong, G. Dissertori, B. A. Dobrescu, M. D'Onofrio, M. Doser, M. Drees, H. K. Dreiner, D. A. Dwyer, P. Eerola, S. Eidelman, J. Ellis, J. Erler, V. V. Ezhela, W. Fetscher, B. D. Fields, R. Firestone, B. Foster, A. Freitas, H. Gallagher, L. Garren, H.-J. Gerber, G. Gerbier, T. Gershon, Y. Gershtein, T. Gherghetta, A. A. Godizov, M. Goodman, C. Grab, A. V. Gritsan, C. Grojean, D. E. Groom, M. Grünewald, A. Gurtu, T. Gutsche, H. E. Haber, C. Hanhart, S. Hashimoto, Y. Hayato, K. G. Hayes,

A. Hebecker, S. Heinemeyer, B. Heltsley, J. J. Hernández-Rey, J. Hisano, A. Höcker, J. Holder, A. Holtkamp, T. Hyodo, K. D. Irwin, K. F. Johnson, M. Kado, M. Karliner, U. F. Katz, S. R. Klein, E. Klempt, R. V. Kowalewski, F. Krauss, M. Kreps, B. Krusche, Yu. V. Kuyanov, Y. Kwon, O. Lahav, J. Laiho, J. Lesgourgues, A. Liddle, Z. Ligeti, C.-J. Lin, C. Lippmann, T. M. Liss, L. Littenberg, K. S. Lugovsky, S. B. Lugovsky, A. Lusiani, Y. Makida, F. Maltoni, T. Mannel, A. V. Manohar, W. J. Marciano, A. D. Martin, A. Masoni, J. Matthews, U.-G. Meißner, D. Milstead, R. E. Mitchell, K. Mönig, P. Molaro, F. Moortgat, M. Moskovic, H. Murayama, M. Narain, P. Nason, S. Navas, M. Neubert, P. Nevski, Y. Nir, K. A. Olive, S. Pagan Griso, J. Parsons, C. Patrignani, J. A. Peacock, M. Pennington, S. T. Petcov, V. A. Petrov, E. Pianori, A. Piepke, A. Pomarol, A. Quadt, J. Rademacker, G. Raffelt, B. N. Ratcliff, P. Richardson, A. Ringwald, S. Roesler, S. Rolli, A. Romaniouk, L. J. Rosenberg, J. L. Rosner, G. Rybka, R. A. Ryutin, C. T. Sachrajda, Y. Sakai, G. P. Salam, S. Sarkar, F. Sauli, O. Schneider, K. Scholberg, A. J. Schwartz, D. Scott, V. Sharma, S. R. Sharpe, T. Shutt, M. Silari, T. Sjöstrand, P. Skands, T. Skwarnicki, J. G. Smith, G. F. Smoot, S. Spanier, H. Spieler, C. Spiering, A. Stahl, S. L. Stone, T. Sumiyoshi, M. J. Syphers, K. Terashi, J. Terning, U. Thoma, R. S. Thorne, L. Tiator, M. Titov, N. P. Tkachenko, N. A. Törnqvist, D. R. Tovey, G. Valencia, R. Van de Water, N. Varelas, G. Venanzoni, L. Verde, M. G. Vincter, P. Vogel, A. Vogt, S. P. Wakely, W. Walkowiak, C. W. Walter, D. Wands, D. R. Ward, M. O. Wascko, G. Weiglein, D. H. Weinberg, E. J. Weinberg, M. White, L. R. Wiencke, S. Willocq, C. G. Wohl, J. Womersley, C. L. Woody, R. L. Workman, W.-M. Yao, G. P. Zeller, O. V. Zenin, R.-Y. Zhu, S.-L. Zhu, F. Zimmermann, P. A. Zyla, J. Anderson, L. Fuller, V. S. Lugovsky, and P. Schaffner. Review of particle physics. *Phys. Rev. D*, 98:030001, Aug 2018.

[10] Georges Aad et al. Observation of a new particle in the search for the Standard Model Higgs boson with the ATLAS detector at the LHC. *Phys. Lett.*, B716:1–29, 2012.

[11] Claudio Campagnari and Melissa Franklin. The Discovery of the top quark. *Rev. Mod. Phys.*, 69:137–212, 1997.

[12] Albert M Sirunyan et al. Measurement of the top quark mass with lepton+jets final states using p p collisions at $\sqrt{s} = 13\,\text{TeV}$. *Eur. Phys. J.*, C78(11):891, 2018.

[13] Hans Peter Nilles. Supersymmetry, supergravity and particle physics. *Phys. Rep.*, 110:1, 1984.

[14] Stephen P. Martin. A supersymmetry primer. In Gordon L. Kane, editor, *Perspectives on Supersymmetry II*, page 1. World Scientific, 2010. Adv. Ser. Direct. High Energy Phys., vol. 21.

[15] Giacomo Cacciapaglia, Haiying Cai, Aldo Deandrea, Thomas Flacke, Seung J. Lee, and Alberto Parolini. Composite scalars at the LHC: the Higgs, the sextet and the octet. *JHEP*, 11:201, 2015.

[16] Kunal Kumar, Tim M. P. Tait, and Roberto Vega-Morales. Manifestations of top compositeness at colliders. *JHEP*, 05:022, 2009.

[17] Giacomo Cacciapaglia, Aldo Deandrea, and Jérémie Llodra-Perez. A dark matter candidate from Lorentz invariance in 6D. *JHEP*, 03:083, 2010.

[18] Otilia Ducu, Lucien Heurtier, and Julien Maurer. LHC signatures of a Z' mediator between dark matter and the SU(3) sector. *JHEP*, 03:006, 2016.

[19] G. Bevilacqua and M. Worek. Constraining BSM physics at the LHC: four top final states with NLO accuracy in perturbative QCD. *JHEP*, 07:111, 2012.

[20] J. Alwall, R. Frederix, S. Frixione, V. Hirschi, F. Maltoni, O. Mattelaer, H. S. Shao, T. Stelzer, P. Torrielli, and M. Zaro. The automated computation of tree-level and next-to-leading order differential cross sections, and their matching to parton shower simulations. *JHEP*, 07:079, 2014.

[21] Rikkert Frederix, Davide Pagani, and Marco Zaro. Large NLO corrections in $t\bar{t}W^{\pm}$ and $t\bar{t}t\bar{t}$ hadroproduction from supposedly subleading EW contributions. *JHEP*, 02:031, 2018.

[22] Rudiger Voss and Amos Breskin, editors. *The CERN Large Hadron Collider, accelerator and experiments*. 2009.

[23] S. Chatrchyan et al. The CMS experiment at the CERN LHC. *JINST*, 3:S08004, 2008.

[24] G. L. Bayatian et al. CMS Physics. 2006.

[25] M. A. Shah et al. The CMS RPC Detector Performance and Stability during LHC RUN-2. In *14th Workshop on Resistive Plate Chambers and Related Detectors (RCP2018) Puerto Vallarta, Jalisco State, Mexico, February 19-23, 2018*, 2018.

[26] CMS Collaboration. The Phase-2 Upgrade of the CMS Muon Detectors. Technical Report CERN-LHCC-2017-012. CMS-TDR-016, CERN, Geneva, Sep 2017. This is the final version, approved by the LHCC.

[27] A. M. Sirunyan et al. Particle-flow reconstruction and global event description with the CMS detector. *JINST*, 12(10):P10003, 2017.

[28] Wolfgang Adam, Boris Mangano, Thomas Speer, and Teddy Todorov. Track Reconstruction in the CMS tracker. Technical Report CMS-NOTE-2006-041, CERN, Geneva, Dec 2006.

[29] Wolfgang Adam, R. Frühwirth, Are Strandlie, and T. Todor. Reconstruction of Electrons with the Gaussian-Sum Filter in the CMS Tracker at the LHC. 2005.

[30] E. Chabanat and N. Estre. Deterministic annealing for vertex finding at CMS. In *Computing in high energy physics and nuclear physics. Proceedings, Conference, CHEP'04, Interlaken, Switzerland, September 27-October 1, 2004*, pages 287–290, 2005.

[31] Matteo Cacciari, Gavin P. Salam, and Gregory Soyez. The anti-k_{T} jet clustering algorithm. *JHEP*, 04:063, 2008.

[32] Matteo Cacciari, Gavin P. Salam, and Gregory Soyez. FastJet user manual. *Eur. Phys. J. C*, 72:1896, 2012.

[33] Stefano Frixione, Giovani Ridolfi, and Paolo Nason. A positive-weight next-to-leading-order Monte Carlo for heavy flavour hadroproduction. *JHEP*, 09:126, 2007.

[34] Paolo Nason. A new method for combining NLO QCD with shower Monte Carlo algorithms. *JHEP*, 11:040, 2004.

[35] Stefano Frixione, Paolo Nason, and Carlo Oleari. Matching NLO QCD computations with parton shower simulations: the POWHEG method. *JHEP*, 11:070, 2007.

[36] Simone Alioli, Paolo Nason, Carlo Oleari, and Emanuele Re. A general framework for implementing NLO calculations in shower Monte Carlo programs: the POWHEG BOX. *JHEP*, 06:043, 2010.

[37] Simone Alioli, Sven-Olaf Moch, and Peter Uwer. Hadronic top-quark pair-production with one jet and parton showering. *JHEP*, 01:137, 2012.

[38] Michelangelo L. Mangano, Mauro Moretti, Fulvio Piccinini, and Michele Treccani. Matching matrix elements and shower evolution for top-quark production in hadronic collisions. *JHEP*, 01:013, 2007.

[39] CMS Collaboration. Investigations of the impact of the parton shower tuning in Pythia 8 in the modelling of $\mathrm{t\bar{t}}$ at $\sqrt{s} = 8$ and 13 TeV. CMS Physics Analysis Summary CMS-PAS-TOP-16-021, 2016.

[40] Torbjörn Sjöstrand, Stefan Ask, Jesper R. Christiansen, Richard Corke, Nishita Desai, Philip Ilten, Stephen Mrenna, Stefan Prestel, Christine O. Rasmussen, and Peter Z. Skands. An introduction to PYTHIA 8.2. *Comput. Phys. Commun.*, 191:159, 2015.

[41] Vardan Khachatryan et al. Event generator tunes obtained from underlying event and multiparton scattering measurements. *Eur. Phys. J. C*, 76:155, 2016.

[42] Peter Skands, Stefano Carrazza, and Juan Rojo. Tuning PYTHIA 8.1: the Monash 2013 tune. *Eur. Phys. J. C*, 74:3024, 2014.

[43] Richard D. Ball et al. Parton distributions for the LHC Run II. *JHEP*, 04:040, 2015.

[44] CMS. Top pag: Top reference selections and recommendations (run2). Technical Report , 2015.

[45] CMS. Top pag: Top trigger (run2). Technical Report , 2016.

[46] A. M. Sirunyan et al. Performance of the CMS muon detector and muon reconstruction with proton-proton collisions at $\sqrt{s} = 13$ TeV. *JINST*, 13:P06015, 2018.

[47] CMS Muon POG. Cms muon id run2 wiki. Technical Report , 2015.

[48] Vardan Khachatryan et al. Performance of electron reconstruction and selection with the CMS detector in proton-proton collisions at $\sqrt{s} = 8$ TeV. *JINST*, 10:P06005, 2015.

[49] CMS EGM POG. Instructions for applying electron and photon id. Technical Report , 2015.

[50] CMS JME POG. Instructions for applying jet id. Technical Report , 2017.

[51] A. M. Sirunyan et al. Identification of heavy-flavour jets with the CMS detector in pp collisions at 13 TeV. *JINST*, 13:P05011, 2018.

[52] CMS. Utilities for accessing pileup information for data. Technical Report , 2015.

[53] Till Arndt, Carmen Diez Pardos, Andreas Meyer. Measurement of the 2016 Trigger Efficiencies for a dilepton selection for a ttbar analysis. CMS AN-16-392.

[54] CMS. Jet energy resolution. Technical Report , 2015.

[55] CMS b Tag and Vertexing POG. b tag & vertexing physics object group. Technical Report , 2016.

[56] CMS BTV-POG. Methods to apply b-tagging efficiency scale factors. Technical Report , 2013.

[57] Martin Goerner. Top p_T reweighing wiki. Technical Report , 2013.

[58] Albert M Sirunyan et al. Measurement of differential cross sections for the production of top quark pairs and of additional jets in lepton+jets events from pp collisions at $\sqrt{s} = 13$ TeV. *Phys. Rev.*, D97(11):112003, 2018.

[59] Helge Voss, Andreas Höcker, Jörg Stelzer, and Fredrik Tegenfeldt. TMVA, the toolkit for multivariate data analysis with ROOT. In *XIth International Workshop on Advanced Computing and Analysis Techniques in Physics Research (ACAT)*, page 40, 2007. [PoS(ACAT)040].

[60] Leo Breiman, Jerome Friedman, R. A. Olshen, and Charles J. Stone. *Classification and regression trees*. Chapman and Hall/CRC, 1984.

[61] Jerome H. Friedman. Recent advances in predictive (machine) Learning. *J. Classif.*, 23:175, 2006.

[62] Yoav Freund and Robert E. Schapire. A decision-theoretic generalization of on-line learning and an application to boosting. *J. Comput. Syst. Sci.*, 55:119, 1997.

[63] J. D. Bjorken and Stanley J. Brodsky. Statistical model for electron-positron annihilation into hadrons. *Phys. Rev. D*, 1:1416, 1970.

[64] CMS Collaboration. CMS luminosity measurements for the 2016 data taking period. CMS Physics Analysis Summary CMS-PAS-LUM-17-001, 2017.

[65] Michal Czakon and Alexander Mitov. Top++: A program for the calculation of the top-pair cross-section at hadron colliders. *Comput. Phys. Commun.*, 185:2930, 2014.

[66] M. Beneke, P. Falgari, S. Klein, and C. Schwinn. Hadronic top-quark pair production with NNLL threshold resummation. *Nucl. Phys. B*, 855:695, 2012.

[67] Matteo Cacciari, Michal Czakon, Michelangelo Mangano, Alexander Mitov, and Paolo Nason. Top-pair production at hadron colliders with next-to-next-to-leading logarithmic soft-gluon resummation. *Phys. Lett. B*, 710:612, 2012.

[68] Peter Bärnreuther, Michal Czakon, and Alexander Mitov. Percent level precision physics at the Tevatron: first genuine NNLO QCD corrections to $q\bar{q} \to t\bar{t} + X$. *Phys. Rev. Lett.*, 109:132001, 2012.

[69] Michal Czakon and Alexander Mitov. NNLO corrections to top-pair production at hadron colliders: the all-fermionic scattering channels. *JHEP*, 12:054, 2012.

[70] Michal Czakon and Alexander Mitov. NNLO corrections to top pair production at hadron colliders: the quark-gluon reaction. *JHEP*, 01:080, 2013.

[71] Michał Czakon, Paul Fiedler, and Alexander Mitov. Total top-quark pair-production cross section at hadron colliders through $\mathcal{O}(\alpha_S^4)$. *Phys. Rev. Lett.*, 110:252004, 2013.

[72] A. M. Sirunyan et al. Measurement of the inelastic proton-proton cross section at $\sqrt{s} = 13$ TeV. *JHEP*, 07:161, 2018.

[73] Vardan Khachatryan et al. Jet energy scale and resolution in the CMS experiment in pp collisions at 8 TeV. *JINST*, 12:P02014, 2017.

[74] CMS Collaboration. Identification of b quark jets at the CMS experiment in the LHC Run 2. CMS Physics Analysis Summary CMS-PAS-BTV-15-001, 2016.

[75] Search for ttH production in the H-to-bb decay channel with leptonic tt decays in proton-proton collisions at sqrt(s) = 13 TeV with the CMS detector. Technical Report CMS-PAS-HIG-17-026, CERN, Geneva, 2018.

[76] Jon Butterworth et al. PDF4LHC recommendations for LHC Run II. *J. Phys. G*, 43:023001, 2016.

[77] L. A. Harland-Lang, A. D. Martin, P. Motylinski, and R. S. Thorne. Parton distributions in the LHC era: MMHT 2014 PDFs. *Eur. Phys. J. C*, 75:204, 2015.

[78] Sayipjamal Dulat, Tie-Jiun Hou, Jun Gao, Marco Guzzi, Joey Huston, Pavel Nadolsky, Jon Pumplin, Carl Schmidt, Daniel Stump, and C. P. Yuan. New parton distribution functions from a global analysis of quantum chromodynamics. *Phys. Rev. D*, 93:033006, 2016.

[79] Albert M Sirunyan et al. Measurements of $t\bar{t}$ differential cross sections in proton-proton collisions at $\sqrt{s} = 13$ TeV using events containing two leptons. *JHEP*, 02:149, 2019.

[80] Albert M Sirunyan et al. Measurements of $t\bar{t}$ cross sections in association with b jets and inclusive jets and their ratio using dilepton final states in pp collisions at $\sqrt{s} = 13$ TeV. *Phys. Lett. B*, 776:355, 2018.

[81] T. Junk. Confidence level computation for combining searches with small statistics. *Nucl. Instrum. Meth. A*, 434:435, 1999.

[82] A. L. Read. Presentation of search results: the CL_s technique. *J. Phys. G*, 28:2693, 2002.

[83] L. Moneta, K. Belasco, K. S. Cranmer, A. Lazzaro, D. Piparo, G. Schott, W. Verkerke, and M. Wolf. The RooStats project. In *13th international workshop on advanced computing and analysis techniques in physics research (ACAT2010)*, page 057, 2010. PoS(ACAT2010)057.

[84] G. Cowan, K. Cranmer, E. Gross, and O. Vitells. Asymptotic formulae for likelihood-based tests of new physics. *Eur. Phys. J. C.*, 71:1554, 2011.

[85] Albert M Sirunyan et al. Search for standard model production of four top quarks with same-sign and multilepton final states in proton-proton collisions at $\sqrt{s} = 13$ TeV. *Eur. Phys. J. C*, 78:140, 2017.

[86] ATLAS and CMS Collaborations and the LHC Higgs combination group. Procedure for the LHC Higgs boson search combination in summer 2011. Technical Report CMS-NOTE-2011-005, ATL-PHYS-PUB-2011-11, 2011.

[87] Matteo Cacciari, Gavin P. Salam, and Gregory Soyez. The catchment area of jets. *JHEP*, 04:005, 2008.

[88] Pileup removal algorithms. CMS Physics Analysis Summary CMS-PAS-JME-14-001, 2014.

Appendix A

QCD Background Estimation

"Fake" isolated leptons are defined as the reconstructed leptons misidentified from heavy-flavor decays, misidentified hadrons, muons from in flight pion/kion decays, or electrons from unidentified photon conversions.

The lepton fake rate is estimated in the exclusive dilepton baseline region with inverted reliso cut on one lepton. The kinematics between measurement and application region are very much alike because of the baseline cuts, then we extrapolate the fake rate from the non-isolated region.

Table A.1: Isolation region definition

	Isolated region	Non-isolated region
μ	$RelIso < 0.15$	$0.15 < RelIso < 0.35$
barrel e	$RelIso < 0.0994$	$0.1 < RelIso < 0.3$
endcap e	$RelIso < 0.107$	$0.12 < RelIso < 0.3$

A.1 Muon fakes

Table A.2 and Fig A.1 show fake muon estimation in signal sensitive baseline regions in $\mu\mu$ channel. We see no evidence of fake muons that originate from QCD multi-jet events, and the data is consistent with $t\bar{t}$ prediction. The same conclusion can be drawn for muons in $e\mu$ channel from table A.3 and Fig A.2.

Table A.2: Fake muons counts in high jet/tag regions in $\mu\mu$ channel

	8+ jets 2 btags	8+ jets 3+ btags
Data	$8.0^{+2.8}_{-2.8}$	$2.0^{+1.4}_{-1.4}$
$t\bar{t}$	$6.0^{+0.3}_{-0.3}$	$1.9^{+0.2}_{-0.2}$

Table A.3: Fake muons counts in high jet/tag regions in $e\mu$ channel

	8+ jets 2 btags	8+ jets 3+ btags
Data	$9.0^{+3.0}_{-3.0}$	$2.0^{+1.4}_{-1.4}$
$t\bar{t}$	$7.2^{+0.4}_{-0.4}$	$2.7^{+0.2}_{-0.2}$

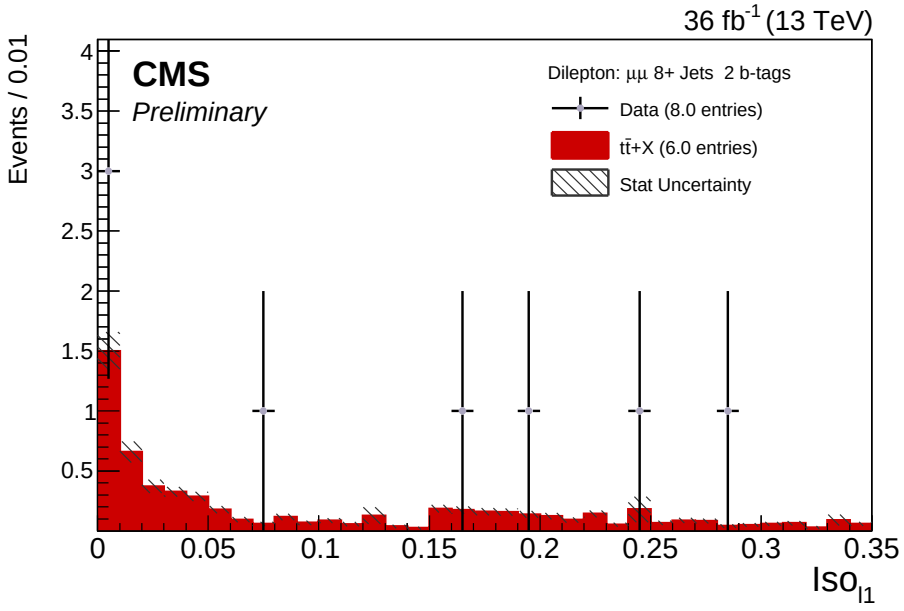

(a)

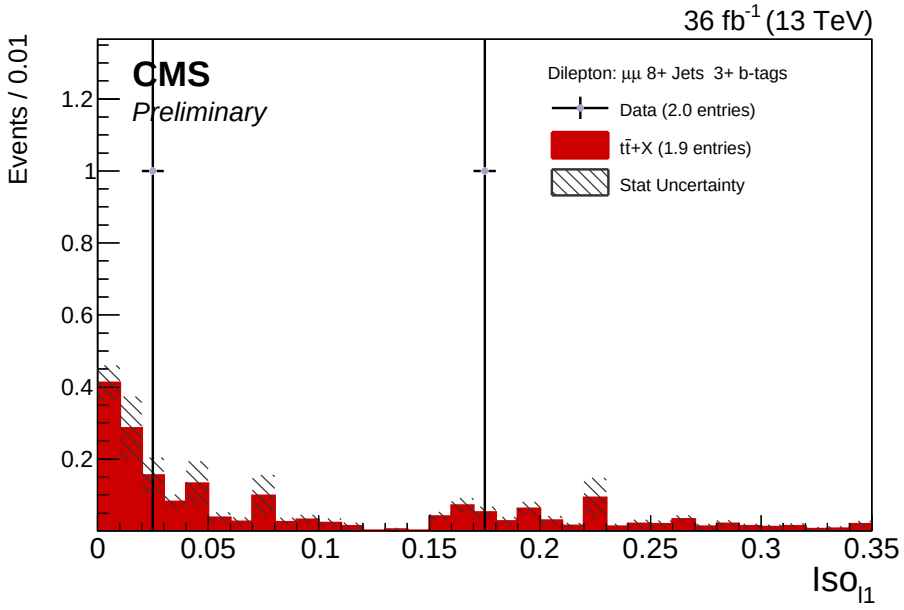

(b)

Figure A.1: Isolation distribution of the muon with the largest p_T in a $\mu\mu$ event with one non-isolated muon, in signal sensitive baseline regions

A.2 Electron fakes

Table A.4 and Fig A.3 show fake electron estimation in signal sensitive baseline regions in ee channel. Within statistical uncertainties, we see no evidence of fake muons coming from QCD multi-jet events, and the data is consistent with $t\bar{t}$ prediction. The same conclusion can be drawn for electrons in $e\mu$ channel from table A.5 and Fig A.4.

Table A.4: Fake electrons counts in high jet/tag regions in ee channel

	8+ jets 2 btags	8+ jets 3+ btags
Data	$6.0^{+2.4}_{-2.4}$	$5.0^{+2.2}_{-2.2}$
$t\bar{t}$	$5.7^{+0.4}_{-0.4}$	$2.0^{+0.2}_{-0.2}$

Table A.5: Fake electrons counts in high jet/tag regions in $e\mu$ channel

	8+ jets 2 btags	8+ jets 3+ btags
Data	$7.0^{+2.6}_{-2.6}$	$1.0^{+1.0}_{-1.0}$
$t\bar{t}$	$8.8^{+0.5}_{-0.5}$	$2.6^{+0.3}_{-0.3}$

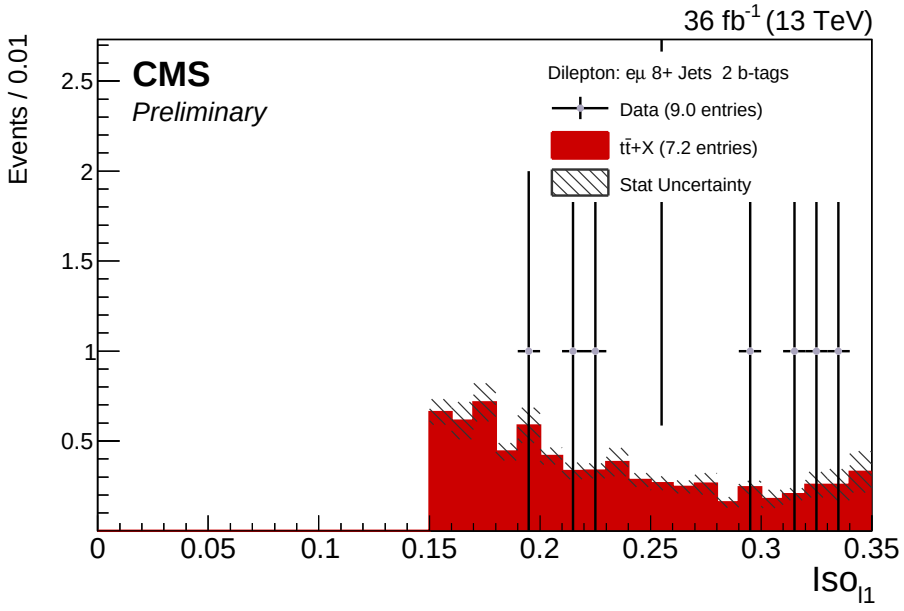

(a)

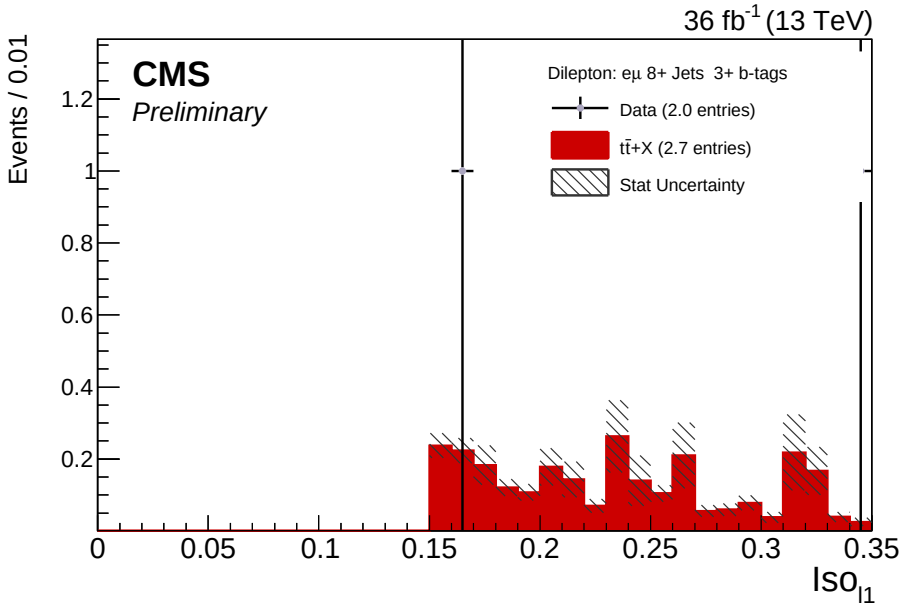

(b)

Figure A.2: Muon isolation distribution in a $e\mu$ event with one non-isolated electron, in signal sensitive baseline regions

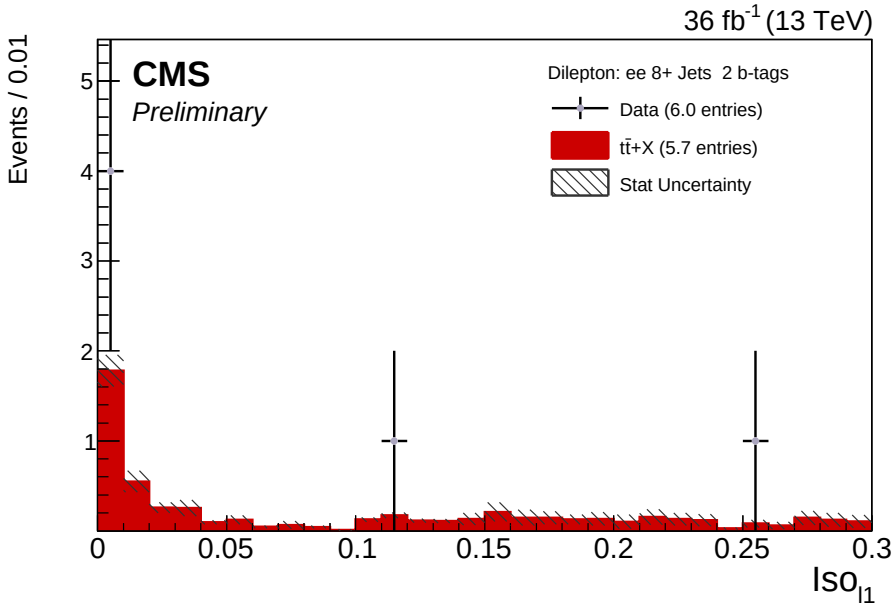

(a)

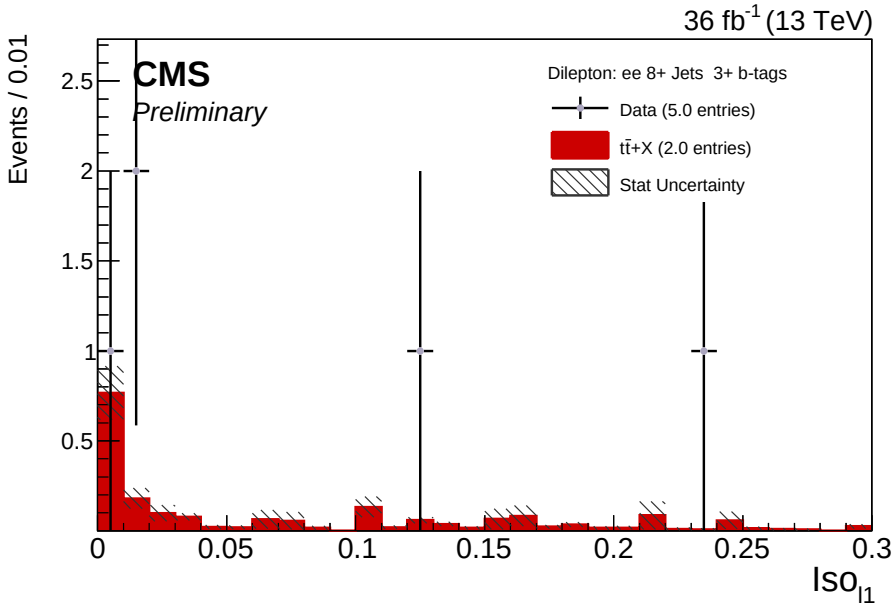

(b)

Figure A.3: Isolation distribution of the electron with the largest p_T in a *ee* event with one non-isolated electron, in signal sensitive baseline regions

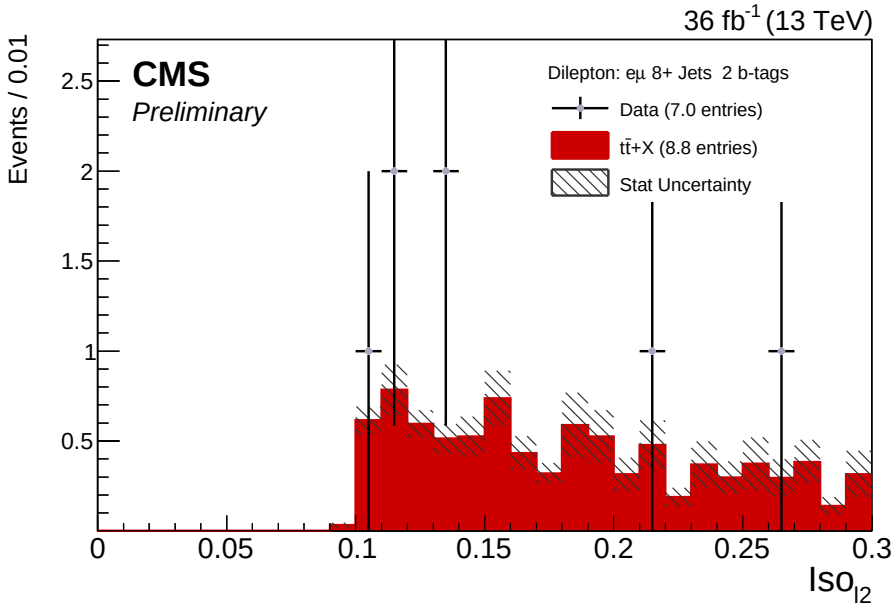

(a)

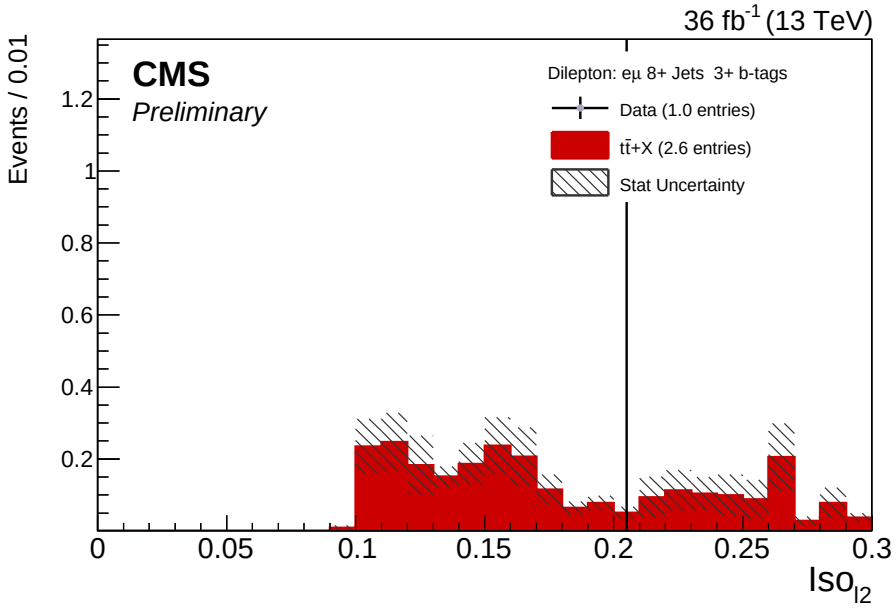

(b)

Figure A.4: Electron isolation distribution in a $e\mu$ event with one non-isolated muon, in signal sensitive baseline regions

Appendix B

Studies of the sensitivity to the $t\bar{t}c\bar{c}$ component of $t\bar{t}$+jets

B.1 Impact of splitting $t\bar{t}c\bar{c}$ from $t\bar{t}$+jets

The original systematic uncertainty treatment of $t\bar{t}c\bar{c}$ component in the $t\bar{t}$+jets event was obtained by fully correlating it with $t\bar{t}$+light flavor jets. In this study, the effects of splitting $t\bar{t}c\bar{c}$ component from $t\bar{t}$+light flavor jets is examined. The normalization of $t\bar{t}c\bar{c}$ component and $t\bar{t}b\bar{b}$ component are allowed to float in the fit with the same prefit uncertainty of either 35% or 50%.

Figure B.1 shows the BDT discriminant sensitivity to the $t\bar{t}c\bar{c}$ and $t\bar{t}b\bar{b}$ uncertainties in each category in $e\mu$ channel. In the signal-sensitive region, $t\bar{t}c\bar{c}$ component shows little variation, tending to have a small decrease for discriminant values larger than 0, while $t\bar{t}b\bar{b}$ component has a significant sensitivity to the discriminant value and has a bigger effect.

$t\bar{t}c\bar{c}$ has very small influence on the high BDT values.

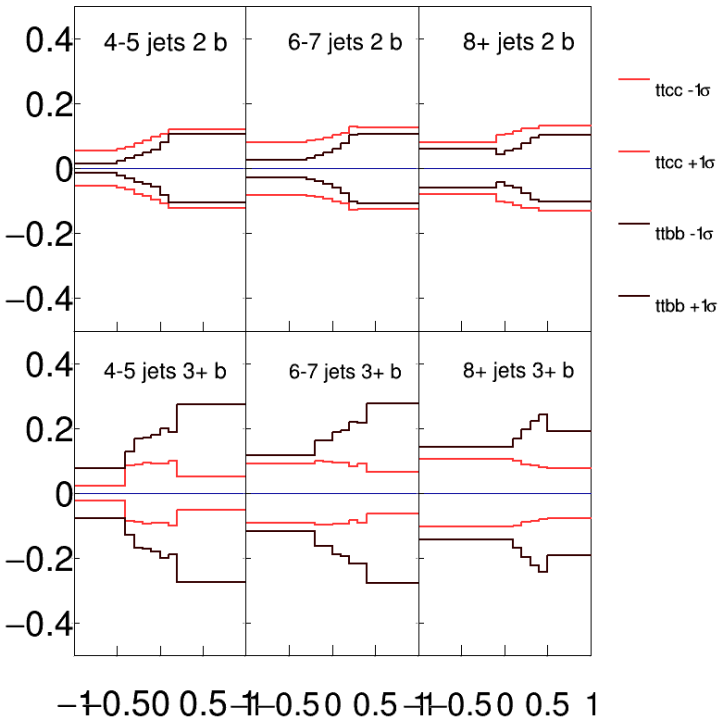

Figure B.1: Comparison of systematic templates, when $t\bar{t}c\bar{c}$ and $t\bar{t}b\bar{b}$ components are varied up and down by 1 sigma. Assuming 35% uncertainties on both $t\bar{t}c\bar{c}$ and $t\bar{t}b\bar{b}$.

The fit results for the two approaches are compared (original approach as fully correlated with $t\bar{t}$+light flavor, split with 35% uncertainty, slit with 50% uncertainty) and in Table B.1. The table shows upper limits from blind fit in signal depleted regions for the two $t\bar{t}c\bar{c}$ treatments. The change in expected limits is less than 1% comparing to the original approach in the analysis, from which it can be concluded that the fit is insensitive to different methods and uncertainties of $t\bar{t}c\bar{c}$ component treatment.

Table B.1: Expected limits from data blinded fit with different $t\bar{t}c\bar{c}$ treatment approaches.

Channel	Original approach $\times\sigma^{SM}_{t\bar{t}t\bar{t}}$	Split $t\bar{t}c\bar{c}$ (35% unc.) $\times\sigma^{SM}_{t\bar{t}t\bar{t}}$	Split $t\bar{t}c\bar{c}$ (50% unc.) $\times\sigma^{SM}_{t\bar{t}t\bar{t}}$
$\mu\mu$	$15.8^{+9.6}_{-5.4}$	$15.8^{+9.7}_{-5.4}$	$15.9^{+9.6}_{-5.4}$
μe	$9.3^{+5.9}_{-3.3}$	$9.3^{+6.0}_{-3.3}$	$9.3^{+6.0}_{-3.3}$
ee	$16.6^{+10.7}_{-5.9}$	$16.6^{+10.7}_{-5.9}$	$16.6^{+10.7}_{-5.9}$
Combined	$7.2^{+4.4}_{-2.5}$	$7.3^{+4.5}_{-2.5}$	$7.3^{+4.5}_{-2.5}$

Figure B.2 shows the nuisance pulls with 35% uncertainty on $t\bar{t}c\bar{c}$ normalization from signal region blinded fit and unblinded fit respectively. The comparison shows almost no change in all the nuisance parameters after including signal bins in the fit. This shows that the fit is very stable going from background to the signal region. Comparing to the original $t\bar{t}c\bar{c}$ treatment, there are marginal changes in all nuisance parameters when $t\bar{t}c\bar{c}$ is split from $t\bar{t}$+jets.

B.2 Post-fit Plots of Event Level BDT Splitting $t\bar{t}$+jets

Figure B.3 and B.4 show the post-fit distributions of the event level BDT with the $t\bar{t}$+jets background split into three components ($t\bar{t}$+light flavor jets, $t\bar{t}c\bar{c}$ and $t\bar{t}b\bar{b}$) discussed

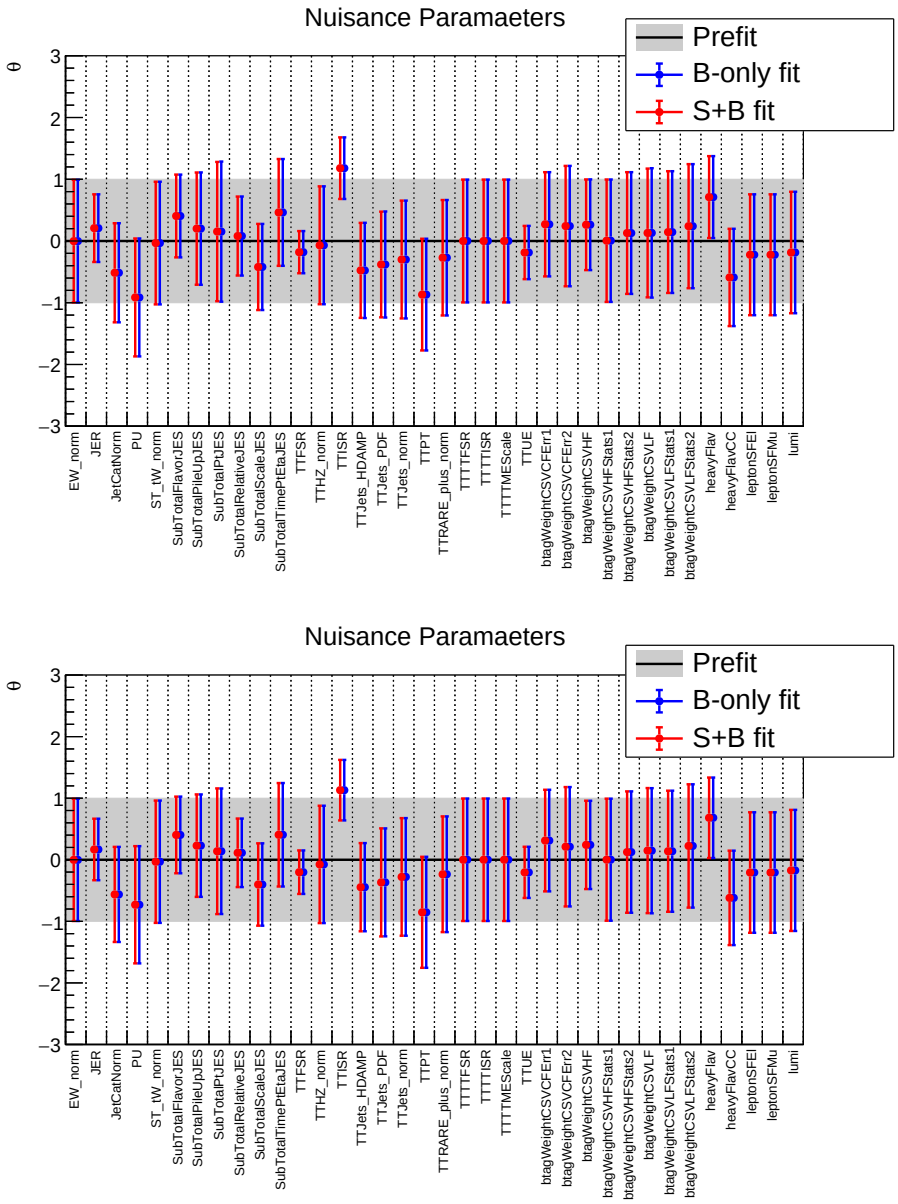

Figure B.2: Pulls of nuisance parameters from maximum-likelihood fit with 35% uncertainty on $t\bar{t}c\bar{c}$ normalization. Upper figure represents signal region blinded fit, lower figure represents unblinded fit.

in the previous section.

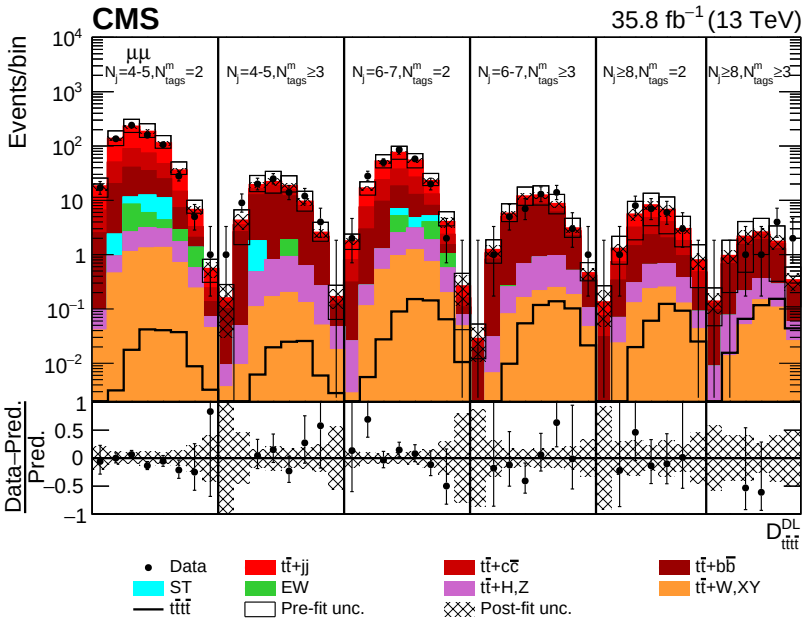

Figure B.3: Postfit discriminant distributions for events passing $\mu^+\mu^-$ sub-channel baseline selections in all multiplicity categories.

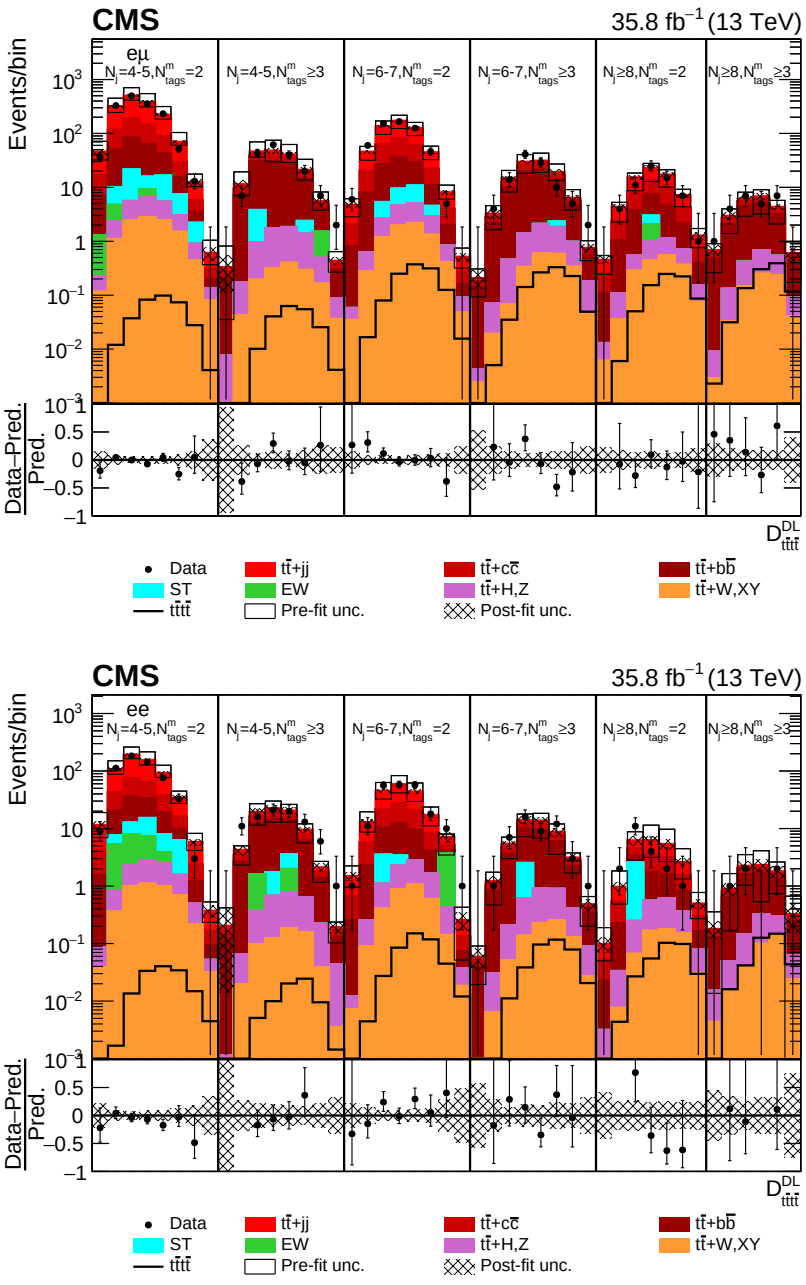

Figure B.4: Postfit discriminant distributions for events passing $\mu^{\pm}e^{\mp}$ sub-channel (top) and $e^{+}e^{-}$ sub-channel (bottom) baseline selection in all multiplicity categories.

Appendix C

GIF++ CSC Longevity Studies

The new CERN Gamma Irradiation Facility (GIF++) is used to expose detectors to an intense gamma field from a 14 TBq ^{137}Cs source, and to high energy charged particle beams. This allows the detectors to accumulate doses equivalent to high-luminosity LHC (HL-LHC) experimental conditions in a reasonable time, and allows the study of the performance and stability of detectors at the LHC and future upgrade systems. Two CSC chambers had been installed in GIF++ for longevity studies, an ME1/1 chamber and an ME2/1 chamber. The differences between these CSC chambers are shown in Figure C.1. Aging studies of the CSC chambers include the relative gain, the dark rates and dark current, the reference current, Malter test, strip-to-strip resistance and so on. In this appendix, dark rate studies and strip-to-strip resistance studies are presented.

C.1 CSC Electronics

The CSC chambers are constructed in trapezoidal shape with the electronics mounted on top. Figure C.2 shows a schematic view of the CSC electronics system.

The Anode Front-End Boards (AFEBs) amplify signals from the anode wires and send hits to the Anode Local Charged Track boards (ALCTs), where the anode hits patterns consistent with muon stubs among the six layers are recognized and the two with the most layer hits are sent to the Trigger MotherBoard (TMB). The Cathode Front-End Boards (CFEBs) amplifies signals from the cathode strips, sends primitive trigger information (Cathode Local Charged Tracks) to the TMB, and, upon receiving a level 1 acceptance (L1A), digitizes the strip signal waveforms and sends them to the Data acquisition MotherBoard (DMB). The TMB sends coincided Local Charged Tracks (LCT) between cathode hit patterns and hit patterns to the Muon Port Card (MPC), and upon receiving an L1A, to the DMB as well. The DMB collects anode, cathode, and trigger information and sends it to the Detector-Dependent Unit (DDU) upon receiving an L1A. Upon arrival of L1A, DDU collects data from all DMBs and sends the information to the global DAQ path.

C.2 Dark Rate Studies

The stability and performance of each detector is monitored using the TMB LCT hit rates from either anodes or cathodes or the coincidence between them when there is no radiation source. These are referred to as the dark rates. Ideally, the dark rates shouldn't change if chamber wires and strips are stable after accumulating radiation, thus any change

of the dark rates would give a hint for aging.

The two CSC test chambers (ME1/1 and ME2/1) were irradiated between 2016 and 2018, with both accumulating large doses. The monitored ALCT dark rates and ALCT*CLCT coincidence dark rates as a function of the accumulated charge are shown in Figures C.3 and C.4 respectively for each chamber. As indicated by the red, there is peak structure of the ALCT rate in ME1/1, this is understood because of a malfunctioning wire group turning noisy. The red circle shows the ALCT rates after subtracting this noisy wire group from the total. After correcting the ALCT rate by subtracting this noisy wire group, we can see both the ALCT rate and the coincided LCT rate stay stable as the accumulated charge increase for both ME1/1 and ME2/1. Figures C.5 and C.6 show the dark ALCT hit rates normalized to unit wire length in each wire group for each of the 6 layers in each chamber with respect to the accumulated charge. As can be seen from the plots, most wire groups have stable and uniformed distribution of dark ALCT rates. No evidence for aging behavior in either chamber was observed.

One of the motivations for this study was to test the possibility of reducing or eliminating the usage of CF_4 gas in the CSC chambers, as it is a green-house gas and detrimental to environment when leaked. Currently, CF_4 is used as a protection gas for anode wires and cathode strips. Figure C.3 and C.5 also show that a percentage drop of CF_4 from 10 % to 2 % does not induce change of dark rates.

C.3 Strip-to-strip Resistance Studies

When high energy particles ionize the working gas, the positively charged ionized particles are attracted to the cathode strips, and attach to them, thus causing the strips to grow. This growth can be reflected by the resistance between two adjacent strips, making it another indicator for detector aging. In this study the strip-to-strip resistance in each layer of the two chambers were monitored as a function of the accumulated charge. To measure the resistance between two adjacent strips, a 300 V voltage is applied on them. The current that goes through the two strips is monitored continuously by a current amplifier, and an exponential fit to the measured currents as a function of time is performed. The asymptote of the exponential function is then the predicted stable current under 300 V, and is used to calculate the resistance between the two strips. The results of the resistances in terms of accumulated charge are shown in Figures C.8 and C.9 for the chambers ME1/1 and ME2/1, respectively. A very small decreasing trend of the resistance shown in the plots is expected. However, overall, the resistances are stable in each layer. Again, no aging behavior of the CSC chambers was observed.

Chamber parameters. Wire/strip #s fixed 5-17-2001

Parameter	ME1/1	ME1/2	ME1/3	ME2/1	ME3/1	ME4/1	ME234/2
Basic single plane parameters							
full gas gap (2h), mm	6	9.5					
wire diameter, m	30	50					
wire spacing, mm	2.5	3.16	3.16	3.12	3.12	3.12	3.16
Active area							
width (top), mm	487	819	933	1254	1254	1254	1270
width (bottom), mm	201	511	630	534	617	685	666
length, mm	1505	1635	1735	1900	1680	1500	3215
Wires							
wire tilt	25°	0°					
wires per plane	600	528	560	620	550	492	1028
wires per wire group	11-12	11	12	5, 6	5, 6	5	16
wire group width, mm	27.5-30	35	38	16, 19	16, 19	16	51
wire group cap., pF	60-150	40-70	50-80	20-60	20-60	25-45	80-150
wire channels per plane	48	64	32	112	96	96	64
Strips							
(single strip), mrad	2.96	2.33	2.16	4.65	4.65	4.65	2.33
width (top), mm	7.6	10.4	14.9	15.6	15.6	15.6	16.0
width (bottom), mm	3.15	6.6	11.1	6.8	7.8	8.6	8.5
gap between strips, mm	0.35	0.5					
strip capacitance, pF	90-140	110	145	145	130	120	250
radial split of strips	@ =2.0	none					
strip channels per plane	64/48	80	64	80	80	80	80
HV							
Operating HV [kV]	~3.0	4.1					
HV segments per plane	1 or 2	2	3	3	3	3	5
Overall chamber parameters							
Number of chambers	72	72	72	36	36	36	216
Planes/chamber	6						
-coverage, degrees	10°	10°	10°	20°	20°	20°	10°
-overlap, strips	5	5	none	5	5	5	5
-coverage	1.5-2.4	1.2-1.6	0.9-1.1	1.6-2.4	1.75-2.4	1.85-2.4	varies
-overlap	none						
Length, mm	1680	1800	1900	2065	1845	1665	3380
Width (top), mm	613	1078	1192	1534	1534	1534	1530
Width (bottom), mm	311	740	859	751	835	903	895
Chamber thickness, mm	148	250					
Chamber weight, kg	~60	150	160	190	180	160	276

Figure C.1: CSC chamber parameters.

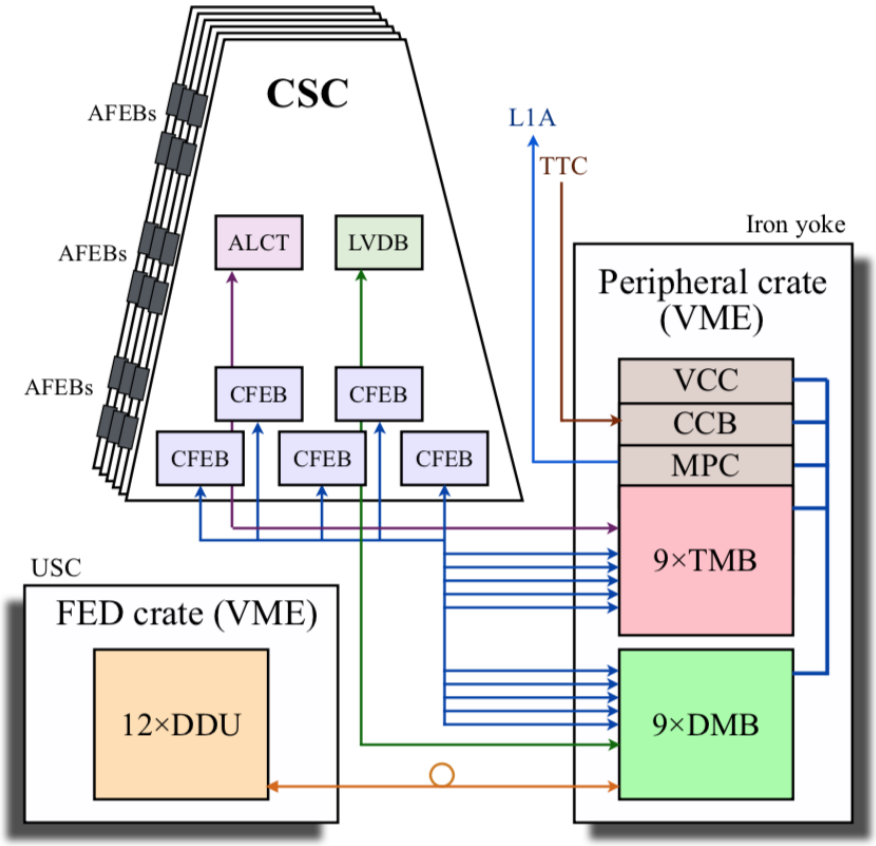

Figure C.2: Overview of CSC electronics system.

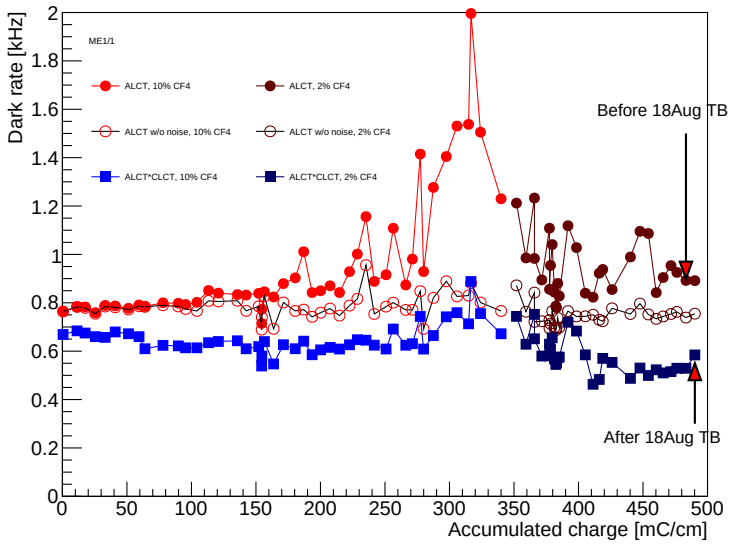

Figure C.3: Dark rates in the whole ME1/1 chamber with respect to accumulated charges.

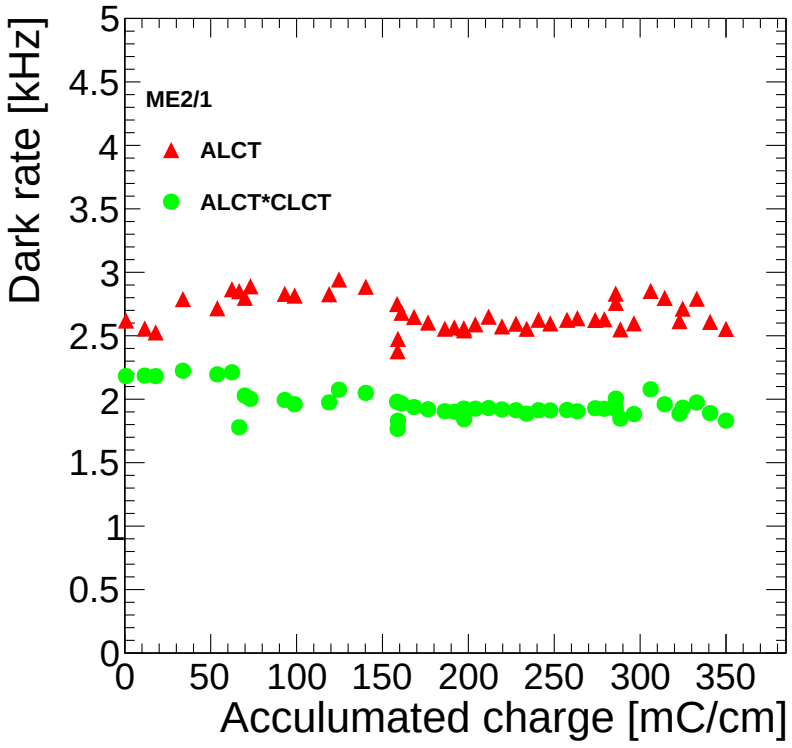

Figure C.4: Dark rates in the whole ME2/1 chamber with respect to accumulated charges.

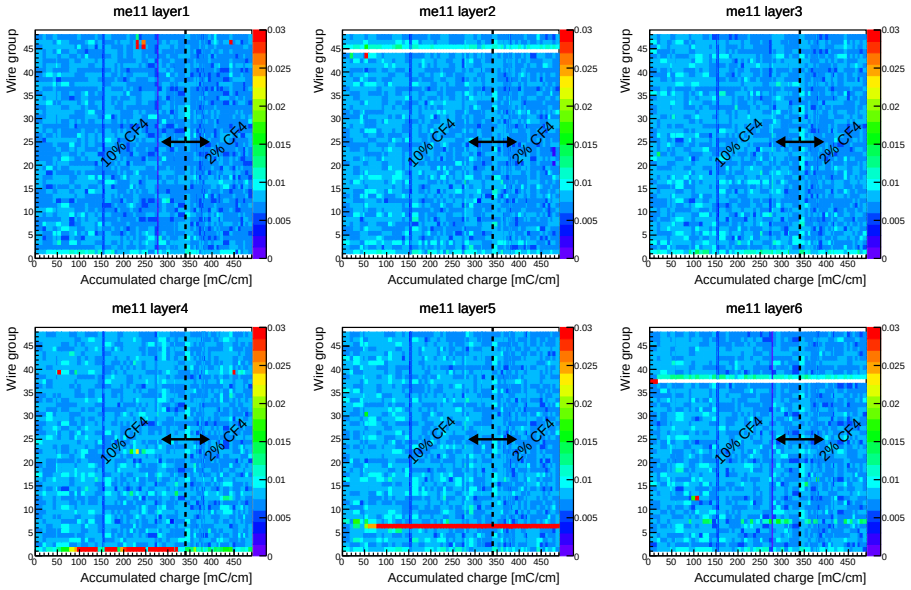

Figure C.5: Dark ALCT rates in each wire group in ME1/1 chamber.

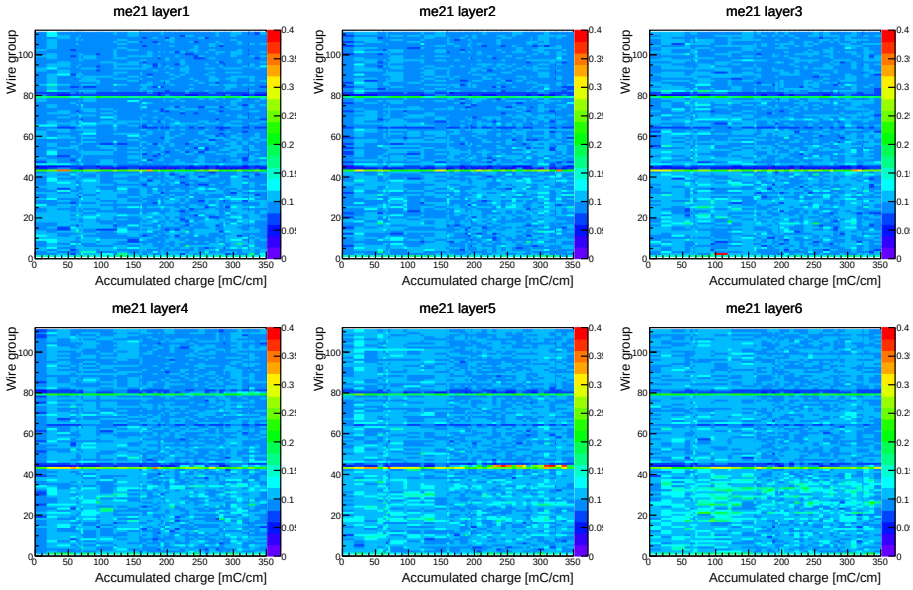

Figure C.6: Dark ALCT rates in each wire group in ME2/1 chamber.

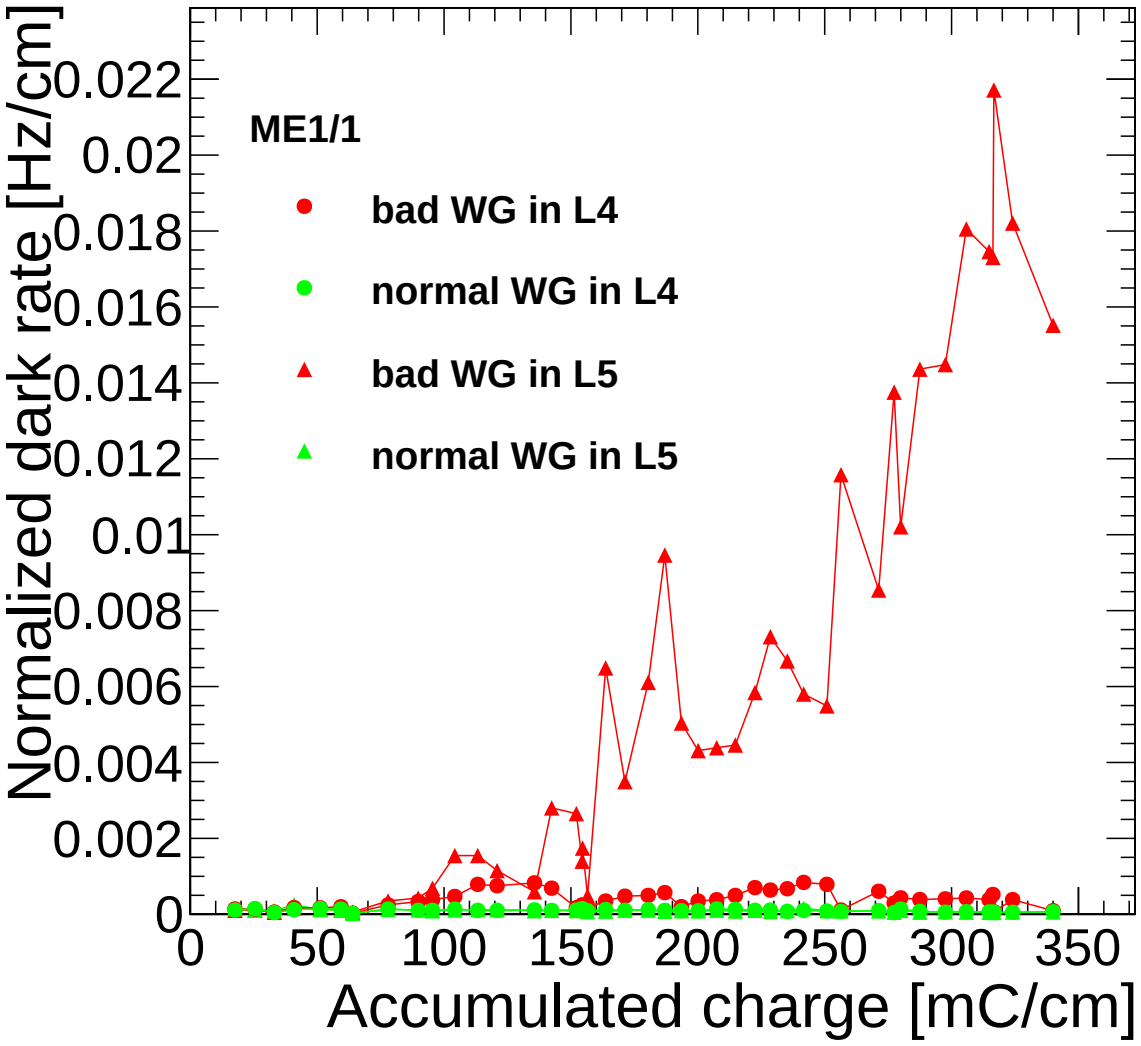

Figure C.7: Dark ALCT rates normalized to unit wire length in the two noisy wire groups (WG) in layer 4 (L4) and layer 5 (L5) in ME1/1.

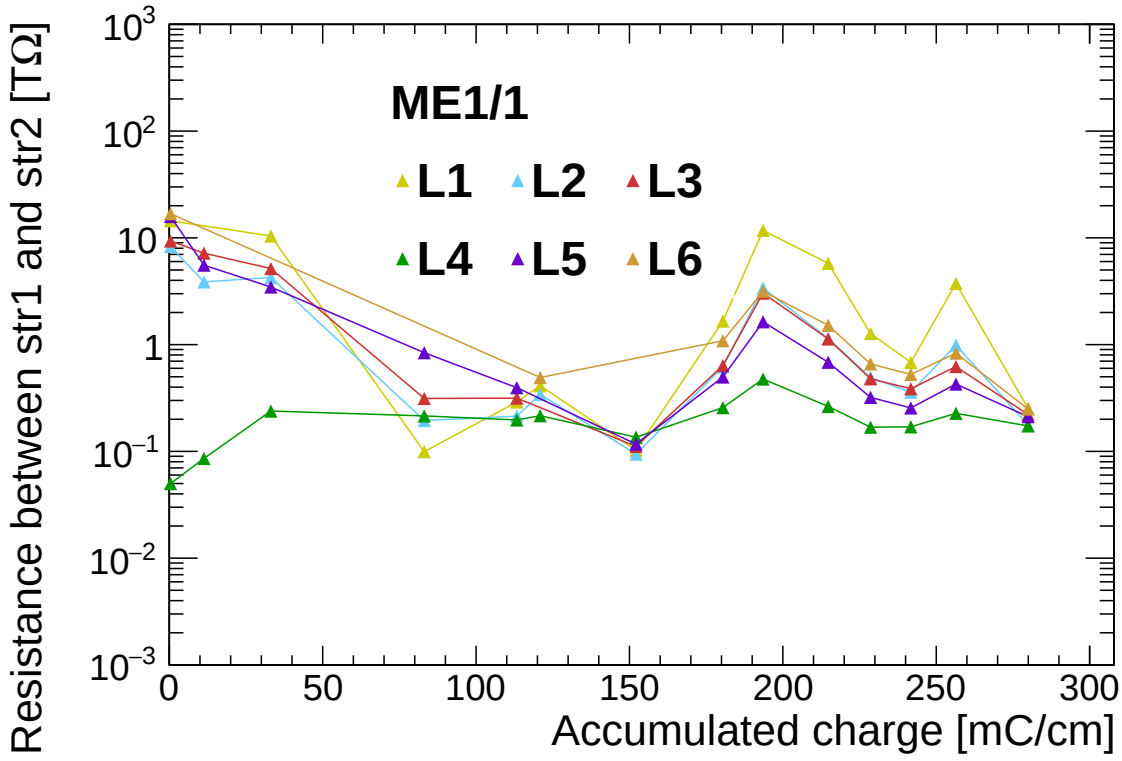

Figure C.8: Resistance between the first and second strips in each layer of ME1/1 chamber as a dependent of accumulated charge.

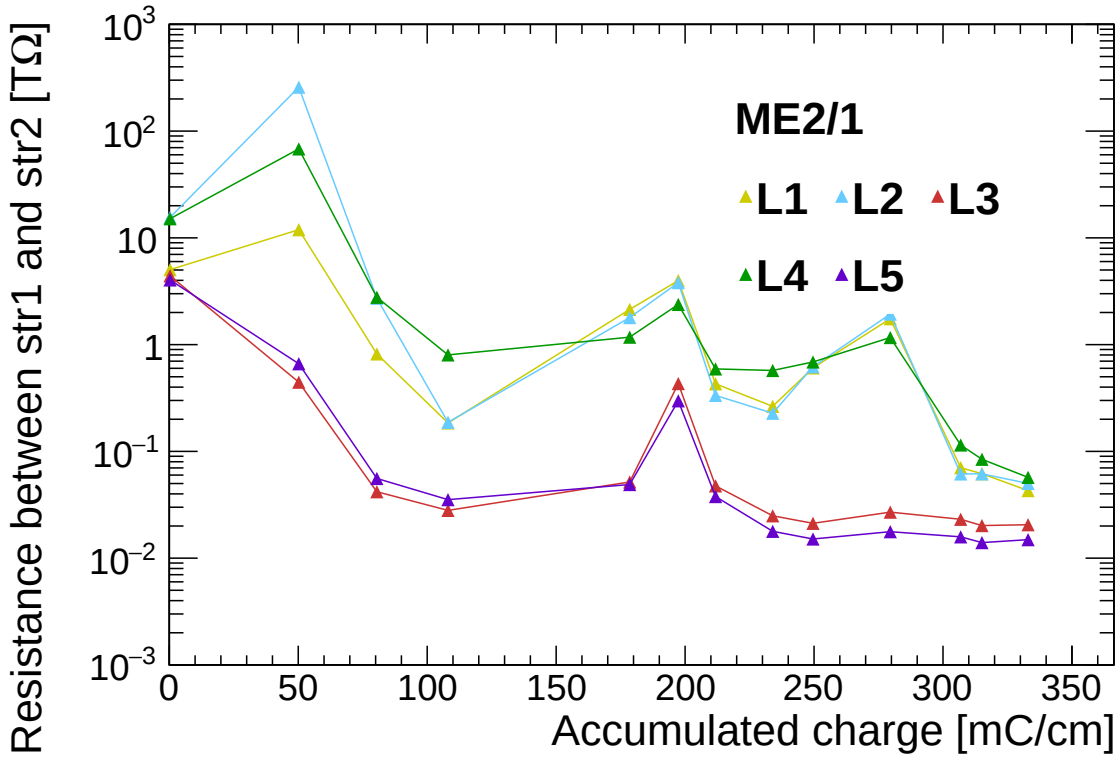

Figure C.9: Resistance between the first and second strips in each layer of ME2/1 chamber as a dependent of accumulated charge.